IntechOpen

Superfluids and Superconductors

Edited by Roberto Zivieri

SUPERFLUIDS AND SUPERCONDUCTORS

Edited by **Roberto Zivieri**

Superfluids and Superconductors
http://dx.doi.org/10.5772/intechopen.71107
Edited by Roberto Zivieri

Contributors

Wenka Zhu, Jifeng Shao, Nick Verhelst, Jacques Tempere, Wout Van Alphen, Giovanni Lombardi, Serghei Klimin, Supeng Kou, Vladimir Kozhevnikov, Abdelhakim Nafidi, Conrado Rillo, Javier Sesé, Miguel Gabal, Stefano Spagna, Roberto Zivieri

© The Editor(s) and the Author(s) 2018
The rights of the editor(s) and the author(s) have been asserted in accordance with the Copyright, Designs and Patents Act 1988. All rights to the book as a whole are reserved by INTECHOPEN LIMITED. The book as a whole (compilation) cannot be reproduced, distributed or used for commercial or non-commercial purposes without INTECHOPEN LIMITED's written permission. Enquiries concerning the use of the book should be directed to INTECHOPEN LIMITED rights and permissions department (permissions@intechopen.com).
Violations are liable to prosecution under the governing Copyright Law.

Individual chapters of this publication are distributed under the terms of the Creative Commons Attribution 3.0 Unported License which permits commercial use, distribution and reproduction of the individual chapters, provided the original author(s) and source publication are appropriately acknowledged. If so indicated, certain images may not be included under the Creative Commons license. In such cases users will need to obtain permission from the license holder to reproduce the material. More details and guidelines concerning content reuse and adaptation can be foundat http://www.intechopen.com/copyright-policy.html.

Notice

Statements and opinions expressed in the chapters are these of the individual contributors and not necessarily those of the editors or publisher. No responsibility is accepted for the accuracy of information contained in the published chapters. The publisher assumes no responsibility for any damage or injury to persons or property arising out of the use of any materials, instructions, methods or ideas contained in the book.

First published in London, United Kingdom, 2018 by IntechOpen
eBook (PDF) Published by IntechOpen, 2019
IntechOpen is the global imprint of INTECHOPEN LIMITED, registered in England and Wales, registration number: 11086078, The Shard, 25th floor, 32 London Bridge Street
London, SE19SG – United Kingdom
Printed in Croatia

British Library Cataloguing-in-Publication Data
A catalogue record for this book is available from the British Library

Additional hard and PDF copies can be obtained from orders@intechopen.com

Superfluids and Superconductors
Edited by Roberto Zivieri

p. cm.

Print ISBN 978-1-78923-204-2

Online ISBN 978-1-78923-205-9

eBook (PDF) ISBN 978-1-83881-513-4

Meet the editor

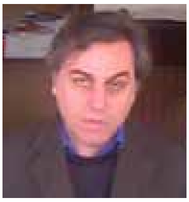

Roberto Zivieri is a theoretical condensed matter physicist. He got his master's degrees in Medicine and Surgery and in Physics (with honors) and his PhD degree in Physics from the University of Modena, Italy (grade excellent). He is an author of more than 200 scientific contributions in condensed matter and biological physics and electric engineering in international reputed journals and conferences. He has been serving as an editorial board member, and he makes part of organizing committees in international conferences. He is a member of the APS, ACS, and Italian Societies of Mathematical Physics and Magnetism. He is the winner of the APS Award "Outstanding Referees 2016." He is the editor in chief of the book series *Theoretical and Computational Models in Condensed Matter Physics* (Aracne Rome).

Contents

Preface XI

Section 1 Introduction 1

Chapter 1 **Introductory Chapter 3**
Roberto Zivieri

Section 2 Superfluidity: Theory and Observation 5

Chapter 2 **An Effective Field Description for Fermionic Superfluids 7**
Wout Van Alphen, Nick Verhelst, Giovanni Lombardi, Serghei Klimin and Jacques Tempere

Chapter 3 **Topological Interplay between Knots and Entangled Vortex-Membranes 33**
Su-Peng Kou

Chapter 4 **"Clean" Liquid Helium 67**
Miguel Gabal, Javier Sesé, Conrado Rillo and Stefano Spagna

Section 3 Superconductivity: Modelling and Experiment 87

Chapter 5 **Intermediate State in Type-I Superconductors 89**
Vladimir Kozhevnikov

Chapter 6 **Emerging Superconductivity and Topological States in Bismuth Chalcogenides 111**
Jifeng Shao and Wenka Zhu

Chapter 7 **Effects of Isovalent Substitutions and Heat Treatments on Tc, Orthorhombicity, Resistivity, AC Magnetic Shielding and Irreversibility Line in High-Tc Superconductors 129**
Abdelhakim Nafidi

Preface

Two of the main phenomena occurring in condensed matter systems are superfluidity and superconductivity. The two phenomena can be considered as two faces of the same coin. Indeed, superfluidity is the property of a fluid with zero viscosity and no losses of fluid kinetic energy, while superconductivity occurs as the property of a conductor having zero electrical resistance and exhibiting the total expulsion of a magnetic field. Below a critical temperature, viscosity in a superfluid and resistance in a superconductor drop to zero. In the former case, there is the appearance of a superfluid phase, while in the latter case, a superconducting phase arises.

Since the first discovery of superfluidity in the two isotopes of helium, helium-3 and helium-4, and the observation of superconductivity, many efforts have been done to understand the underlying physics characterizing these two remarkable phenomena. A step forward for the comprehension of superfluidity on a microscopic level has been the connection between superfluid helium-4 and a boson particle and between superfluid helium-3 and a fermion particle with the pairing between two helium-3 atoms occurring at low temperatures and leading to the superfluid phase below the critical temperature. The pairing mechanism represents the analogous of the electron Cooper pairs that are at the basis of the microscopic theory of superconductivity for superconductors of the first kind and allows a superfluid behavior below a critical temperature with zero resistance. The discovery of superconductors of the second kind exhibiting a higher critical temperature and two critical values for the external magnetic field has been an important advancement in the field of superconductivity. Finally, for both phenomena, one of the most important implications is the formation of vortex configurations that are linked to their topological properties.

I would like to thank all the authors for their efforts in writing the chapters included in this book. Each of them contains the recent advances in the topics of superfluidity and superconductivity both from the theoretical and experimental points of view catching the attention not only of specialists but also of nonspecialists working in the field of condensed matter physics. Special thanks go to the Publishing Process Manager, Mr. Julian Virag, for his kind help and for his precious and devoted assistance during all the production steps. I would also like to acknowledge the National Institute of Advanced Mathematics (INdAM) and the National Group for the Mathematical Physics (GNFM) in Rome for their kind support offered to me during this project.

Prof. Roberto Zivieri
INdAM and GNFM, Rome
Department of Mathematical and Computer Sciences
Physical Sciences and Earth Sciences
Messina University, Messina, Italy

Section 1

Introduction

Introductory Chapter

Roberto Zivieri

Additional information is available at the end of the chapter

http://dx.doi.org/10.5772/intechopen.77318

1. Generalities on superfluidity and superconductivity

This book deals with the recent advancements in two topical subjects of condensed matter physics, superfluidity, and superconductivity. In principle, the two phenomena are very similar because they occur as a function of temperature and in the presence of the vanishing of a physical quantity marking a phase transition below a critical temperature. A superfluid is a fluid having zero viscosity while a superconductor is a conductor with zero resistance. Superfluidity occurs in liquid helium and in ultracold atomic gases while superconductivity is typical of elements like niobium and lead, of some niobium alloys, or compounds like yttrium barium and copper oxide and compounds containing iron. Regarding the latter, since the first discoveries, the interplay between superconductivity and magnetism has also been investigated finding that the magnetic state of superconductors can be described as ideal diamagnetism. The behaviour toward the external magnetic field allows to distinguish between first- and second-type superconductors. Instead, the critical temperature in correspondence of which superconductivity arises allows to distinguish between low- and high-critical temperature superconductors. After their initial discovery, superfluidity was explained as a quantum mechanical phenomenon, while superconductivity was described first according to a phenomenological and classical theory and only in a second moment in terms of a microscopic quantum mechanical theory.

2. Topological properties of superfluids and superconductors

Recently, there has been a growing interest in both fields for the important implications of the two phenomena in terms of their topological properties. In particular, if stirred, superfluids form cellular vortices that rotate indefinitely. On the other hand, also multiply-connected superconductors form vortices giving rise to flux quantization that can be just like the quantization of

IntechOpen

circulation in multiply-connected superfluids. Quantized vortex structures are characterized by a singularity in the center and the vortex core is quantified by means of vorticity, a topological charge otherwise called winding number characterizing the strength of a vortex and identifying superfluid and superconducting vortices as topological defects. This description is an important step forward in both fields because the study of the topological properties is crucial to fully understand the underlying physics in the systems exhibiting either superconductivity or superfluidity.

3. Contents and organization of the book

In the next six chapters of the book, some of the recent novelties in the two fields of superconductivity and superfluidity are reviewed both from a theoretical and an experimental point of view. The book is organized into two sections: (1) the first section contains three chapters dealing with the recent developed theoretical models and measurements carried out in superconductors and (2) the last three chapters contained in the second section report on the theoretical advancement together with the most sophisticated experimental techniques in superfluidity. In more detail, Chapter 2 reviews the main properties of the intermediate state in type-I superconductors and the main theoretical models to interpret it. Chapter 3 reports the recent experiments on some emerging superconductors, the bismuth chalcogenides, and the BiS_2-based layered superconductors with special regard to the correlation between crystal structure and superconductivity. Chapter 4 reports on the effect of isovalent substitutions and heat treatments on some physical properties of high-critical temperature superconductors by means of advanced experimental techniques. Chapter 5 presents an advanced theory in the field of superfluids on the Kelvin wave and knot dynamics on three-dimensional deformed knot-crystal and its relation with deformed space-time. Chapter 6 outlines an effective field theory applied to study vortices and solitons in superfluid Fermi gases. Chapter 7 describes an experimental technique that is able to produce hydrogen-free liquid helium and illustrates how to solve the flow impedance blocking issue.

Acknowledgements

Finally, I would like to express my personal gratitude to all authors who have contributed with their efforts to this book. I am sure that all the contributions can give interesting insights into the condensed matter physics scientific community.

Author details

Roberto Zivieri

Address all correspondence to: roberto.zivieri@unife.it

INdAM-GNFM Rome, Department of Mathematical and Computer Sciences, Physical Sciences and Earth Sciences, Messina University, Messina, Italy

Section 2

Superfluidity: Theory and Observation

Chapter 2

An Effective Field Description for Fermionic Superfluids

Wout Van Alphen, Nick Verhelst,
Giovanni Lombardi, Serghei Klimin and
Jacques Tempere

Additional information is available at the end of the chapter

http://dx.doi.org/10.5772/intechopen.73058

Abstract

In this chapter, we present the details of the derivation of an effective field theory (EFT) for a Fermi gas of neutral dilute atoms and apply it to study the structure of both vortices and solitons in superfluid Fermi gases throughout the BEC-BCS crossover. One of the merits of the effective field theory is that, for both applications, it can provide some form of analytical results. For one-dimensional solitons, the entire structure can be determined analytically, allowing for an easy analysis of soliton properties and dynamics across the BEC-BCS interaction domain. For vortices on the other hand, a variational model has to be proposed. The variational parameter can be determined analytically using the EFT, allowing to also study the vortex structure (variationally) throughout the BEC-BCS crossover.

Keywords: fermionic superfluids, superfluidity, effective field theory, solitons, vortices

1. Introduction

When cooling down a dilute cloud of fermionic atoms to ultralow temperatures, particles of different spin type can form Cooper pairs and condense into a superfluid state. The properties and features of these superfluid Fermi gases have been the subject of a considerable amount of theoretical and experimental research [1, 2]. The opportunity to investigate a whole continuum of inter-particle interaction regimes and the possibility to create a population imbalance result in an even richer physics than that of superfluid Bose gases. In this chapter, we present an effective field theory (EFT) suitable for the description of ultracold Fermi gases across the BEC-BCS interaction regime in a wide range of temperatures. The merits of this formalism mainly lie in the fact that it is computationally much less requiring than the Bogoliubov-de Gennes method, and that, in some cases, it can provide exact analytical solutions for the problem at hand. In Section 2, we give a short overview of the path integral theory that forms the basis for the EFT. In Section 3, we study the associated mean field theory for the description of homogeneous superfluids. In Section 4, we go beyond the mean-field approximation and describe the framework of the EFT. Sections 5 and 6 are dedicated to the application of the EFT to two important topological excitations: dark solitons and vortices.

2. Path integral theory and bosonification

The effective field theory for fermionic superfluids presented in this chapter is based on the path integral formalism of quantum field theory. The advantage of this formalism lies in the fact that the operators are replaced by fields, which can yield a more intuitive interpretation for the physics of the system. Moreover, the fact that there are no operators make working with functions of the quantum fields a lot easier.

In this section, the path integral description for ultracold Fermi gases will be briefly introduced. Using the Hubbard-Stratonovich identity, the fermionic degrees of freedom can be integrated out, resulting in an effective bosonic action. This effective bosonic action is the object of interest of this chapter and will lie at the basis of the effective field theory. An extended discussion of this section and the mean-field theory of the next section are given in an earlier publication [3]. Comprehensive introductions to the path integral method include [4] (Quantum Field Theory with Path Integrals), [5, 6] (The "classical" Path Integral), and [7] (General review book on the Path Integrals and most of its applications).

2.1. A brief introduction to the path integral formalism

The partition function of a system described by the quantum field action functional $S\left[\phi(\mathbf{x},t),\overline{\phi}(\mathbf{x},t)\right]$ can be expressed as a path integral [7]:

$$\mathcal{Z}=\int\mathcal{D}\overline{\phi}_{\mathbf{x},\tau}\mathcal{D}\phi_{\mathbf{x},\tau}\exp\left(-S_E\left[\phi_{\mathbf{x},\tau},\overline{\phi}_{\mathbf{x},\tau}\right]\right). \tag{1}$$

Here, $\mathcal{D}\phi_{\mathbf{x},\tau}$ represents a sum over all possible space-time configurations of the field $\phi(\mathbf{x},\tau)$, and $\tau=it$ indicates imaginary times running from $\tau=0$ to $\tau=\hbar\beta$ with $\beta=1/(k_BT)$. The Euclidian action $S_E(\beta)$ of the system is found from the real-time action functional $S(t_b,t_a)$ through the substitution

$$t\rightarrow-i\tau\Rightarrow S(t_b,t_a)\rightarrow iS_E(\beta). \tag{2}$$

For systems with an Euclidean action which is at most quadratic in the fields, the path integral (1) can be calculated analytically. In particular, two distinct cases can be considered:

Bosonic path integral: The path integral sums over a bosonic (scalar, complex valued) field $\Psi(\mathbf{x},\tau)$:

$$\mathcal{Z}_B = \int \mathcal{D}\overline{\Psi}\mathcal{D}\Psi \exp\left(-\int d\tau \int d\mathbf{x} \int d\tau' \int d\mathbf{x}' \left[\overline{\Psi}(\mathbf{x},\tau)\mathbb{A}\left(\mathbf{x},\tau;\mathbf{x}',\tau'\right)\Psi\left(\mathbf{x}',\tau'\right)\right]\right) = \frac{1}{\det(\mathbb{A})}, \tag{3}$$

For the case of a quadratic bosonic path integral, the integration over the complex field Ψ reduces to a convolution of Gaussian integrals, which reduces to the inverse of the determinant of the matrix $\mathbb{A}$ containing the coefficients of the quadratic form.

Fermionic path integral: The path integral sums over a fermionic (Grassmann, complex valued) field $\psi(\mathbf{x},\tau)$:

$$\mathcal{Z}_F = \int \mathcal{D}\overline{\psi} \int \mathcal{D}\psi \exp\left(-\int d\tau \int d\mathbf{x} \int d\tau' \int d\mathbf{x}' \left[\overline{\psi}(\mathbf{x},\tau)\mathbb{A}\left(\mathbf{x},\tau;\mathbf{x}',\tau'\right)\psi\left(\mathbf{x}',\tau'\right)\right]\right) = \det(\mathbb{A}), \tag{4}$$

In the case of spin-dependent fermionic fields, the matrix $\mathbb{A}$ becomes slightly more complex since the spinor fields have multiple components[1] to account for the spin degree of freedom. The spinors ψ are described by anti-commuting Grassmann numbers [4, 8], thus satisfying $\psi^2 = 0$. For the quadratic case, the fermionic path integral simply returns the determinant of the matrix $\mathbb{A}$.

Using the trace-log formula, these results can also be rewritten as:

$$\mathcal{Z}_B = \exp\left(-\mathrm{Tr}[\ln(\mathbb{A})]\right), \tag{5}$$

$$\mathcal{Z}_F = \exp\left(+\mathrm{Tr}[\ln(\mathbb{A})]\right). \tag{6}$$

Partition functions with quadratic action functionals form the basis of the path integral formalism. The usual approach for solving path integrals with higher order action functionals is to reduce them to the quadratic forms given above by the means of transformations and/or approximations.

In this chapter, the system of interest is an ultracold Fermi gas in which fermionic particles of opposite pseudo-spin interact via an s-wave contact potential. The Euclidian action functional for this system is given by

$$\begin{aligned} S_{\mathrm{E}} = & \int_0^{\hbar\beta} d\tau \int d\mathbf{x} \sum_{\sigma\in\{\uparrow,\downarrow\}} \left[\overline{\psi}_\sigma(\mathbf{x})\left(\hbar\partial_\tau - \frac{\hbar^2}{2m_\mathbf{x}}\nabla_\mathbf{x}^2 - \mu_\sigma\right)\right]\psi_\sigma(\mathbf{x}) \\ & + \int_0^{\hbar\beta} d\tau \int d\mathbf{x} \int d\mathbf{y} \overline{\psi}_\uparrow(\mathbf{x})\overline{\psi}_\downarrow(\mathbf{y}) g\delta(\mathbf{x}-\mathbf{y})\psi_\downarrow(\mathbf{y})\psi_\uparrow(\mathbf{x}), \end{aligned} \tag{7}$$

where $\sigma \in \{\uparrow,\downarrow\}$ denotes the spin components of the fermionic spinor fields, the chemical potentials μ_σ fix the amount of particles of each spin population, and g is the renormalized interaction strength [9, 10], linking the interaction potential to the s-wave scattering length a_s:

---

[1] The matrix $\mathbb{A}$ can be thought of as an infinite matrix composed of either 2×2 or 4×4 matrices, depending on whether the spin-dependence of the fermionic field is considered in the theory.

$$\frac{1}{g} = \frac{m}{4\pi\hbar^2 a_s} - \int \frac{d\mathbf{k}}{(2\pi)^3} \frac{m}{\hbar^2 k^2}. \tag{8}$$

For the remainder of the chapter, the units

$$\hbar = k_B = k_F = 2m = 1 \tag{9}$$

will be used, meaning that we work in the natural units of k_F, E_F, $\omega_F = E_F/\hbar$, and $T_F = E_F/k_B$. Consequentially, the partition function of the ultracold Fermi gas can be written down as

$$\begin{aligned} \mathcal{Z} = \; & \int \mathcal{D}\overline{\psi}_\sigma \mathcal{D}\psi_\sigma \exp\left[-\int_0^\beta d\tau \int d\mathbf{x} \left(\sum_{\sigma \in \{\uparrow,\downarrow\}} \overline{\psi}_\sigma(\mathbf{x},\tau) \left(\frac{\partial}{\partial\tau} - \nabla_{\mathbf{x}}^2 - \mu_\sigma \right) \psi_\sigma(\mathbf{x},\tau) \right.\right. \\ & \left.\left. + g\overline{\psi}_\uparrow(\mathbf{x},\tau)\overline{\psi}_\downarrow(\mathbf{x},\tau)\psi_\downarrow(\mathbf{x},\tau)\psi_\uparrow(\mathbf{x},\tau) \right) \right], \end{aligned} \tag{10}$$

where the label σ was explicitly added to the integration measure to show that the path integration is performed also over both spin components of the spinor ψ. As noted above, only quadratic path integrals can be solved analytically, meaning that an additional trick is needed[2] to calculate the above partition sum (10). In the present treatment, this trick will be the Hubbard-Stratonovich transformation.

2.2. Bosonification: the Hubbard-Stratonovich transformation

Using the Hubbard-Stratonovich identity [11–14],

$$\exp\left(-g \int d^3x g\overline{\psi}_\uparrow\overline{\psi}_\downarrow\psi_\downarrow\psi_\uparrow \right) = \int \mathcal{D}\overline{\Psi}\mathcal{D}\Psi \exp\left(\int d^3\mathbf{x} \left[\frac{|\Psi|^2}{g} + \overline{\psi}_\uparrow\overline{\psi}_\downarrow\Psi + \psi_\downarrow\psi_\uparrow\overline{\Psi} \right] \right), \tag{11}$$

it is possible to rewrite the action in a form that is quadratic in the fermionic fields ψ and $\overline{\psi}$, allowing for the fermionic degrees of freedom to be integrated out. The price of this transformation is the introduction of a new (auxiliary) bosonic field $\Psi(\mathbf{r},\tau)$, which can be interpreted as the field of the Cooper pairs that will form the superfluid state. Diagramatically, the Hubbard-Stratonovich identity removes the four-point vertex (quartic interaction term) and replaces it with two three-point vertices (quadratic terms), as illustrated in **Figure 1**. It is important to note that, although the Hubbard-Stratonovich transformation is an exact identity, further calculations will require approximations for which the choice of collective field (or "channel") becomes important. Whereas the bosonic pair field is suitable for the superfluid state, it will fail when one tries to use it to take into account interactions in the normal state. It should therefore be pointed out that alternatives exist, notably Kleinert's variational

---

[2] Of course, it is always possible, given sufficient computational resources and time, to calculate the partition sum numerically.

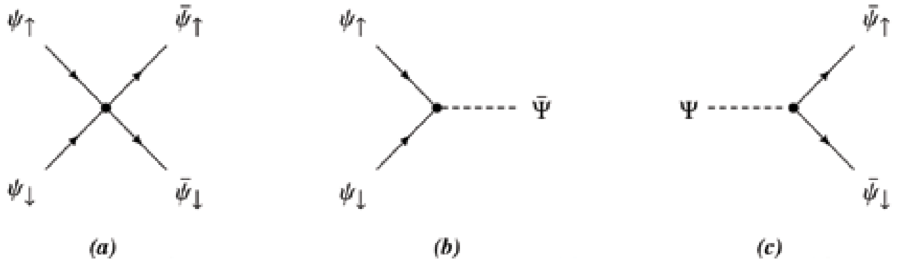

Figure 1. A diagrammatic representation of the different terms in the Hubbard-Stratonovich identity (11).

perturbation theory, in which a classical collective field rather than a quantum collective field is used. This allows for the simultaneous treatment of multiple collective fields [15], for example, the pair field and the density field. For our present purposes, however, it is sufficient to restrict ourselves to the superfluid state and describe it with a single collective field.

After applying the Hubbard-Stratonovich identity (11) to expression (10), the partition function becomes

$$\mathcal{Z} = \int \mathcal{D}\overline{\psi}_\sigma \mathcal{D}\psi_\sigma \int \mathcal{D}\overline{\Psi}\mathcal{D}\Psi \exp\left[-\int_0^\beta d\tau \int d\mathbf{x} \left(\sum_{\sigma\in\{\uparrow,\downarrow\}} \overline{\psi}_\sigma(\mathbf{x},\tau)\left(\frac{\partial}{\partial\tau} - \nabla_\mathbf{x}^2 - \mu_\sigma\right)\psi_\sigma(\mathbf{x},\tau) \right.\right.$$
$$\left.\left. - \frac{|\Psi(\mathbf{x},\tau)|^2}{g} - \overline{\psi}_\uparrow(\mathbf{x},\tau)\overline{\psi}_\downarrow(\mathbf{x},\tau)\Psi(\mathbf{x},\tau) - \psi_\downarrow(\mathbf{x},\tau)\psi_\uparrow(\mathbf{x},\tau)\overline{\Psi}(\mathbf{x},\tau)\right)\right] \tag{12}$$

2.3. The resulting bosonic path integral

Since the path integral over the fermionic fields ψ and $\overline{\psi}$ is now quadratic, it can be performed analytically using formula (4), resulting in the effective bosonic path integral [3]

$$\mathcal{Z} = \int \mathcal{D}\overline{\Psi}\mathcal{D}\Psi \exp\left[-\left(-\int_0^\beta \int d\mathbf{x} \frac{|\Psi(\mathbf{x},\tau)|^2}{g} - \mathrm{Tr}\left[\ln\left(-\mathbb{G}^{-1}\right)\right]\right)\right], \tag{13}$$

where the components of the inverse Green's function matrix $-\mathbb{G}^{-1}$ are given by

$$-\mathbb{G}^{-1}(\mathbf{x},\tau) = \begin{pmatrix} \frac{\partial}{\partial\tau} - \nabla_\mathbf{x}^2 - \mu_\uparrow & -\Psi(\mathbf{x},\tau) \\ -\overline{\Psi}(\mathbf{x},\tau) & \frac{\partial}{\partial\tau} + \nabla_\mathbf{x}^2 + \mu_\downarrow \end{pmatrix} \tag{14}$$

Since $-\mathbb{G}^{-1}$ depends on the bosonic field $\Psi(\mathbf{x},\tau)$, the action in the exponent is not quadratic, and hence, the remaining bosonic path integral can still not be solved analytically. In order to obtain a workable solution, two different approximations will be considered. First, a mean field approximation (using a constant value for Ψ) will be discussed in Section 3. Subsequently, this mean field theory will form the basis for a finite temperature effective field theory, which also takes into account *slow* fluctuations of the pair field $\Psi(\mathbf{x},\tau)$. This theory will be presented in Section 4.

3. The mean field theory

At first sight, the introduction of the auxiliary bosonic fields $\Psi(\mathbf{x},\tau)$ and $\overline{\Psi}(\mathbf{x},\tau)$ through the Hubbard-Stratonovich transformation seems to have been of little use; while the transformation enables us to perform the path integrals over the fermionic fields, we end up with path integrals for $\Psi(\mathbf{x},\tau)$ and $\overline{\Psi}(\mathbf{x},\tau)$ that still cannot be calculated exactly. The advantage of switching to the bosonic pair fields, however, lies in the fact that they allow us to make a physically plausible approximation based on our knowledge of the system. If we want to investigate the superfluid state, we can assume that the most important contribution to the path integral will come from the configuration in which all the bosonic pairs are condensed into the lowest energy state of the system and form a homogeneous superfluid. This assumption is most easily expressed in momentum-frequency representation $\{\mathbf{q}, m\}$:

$$\Psi(\mathbf{q},m) \to \sqrt{\beta V}\delta(\mathbf{q})\delta_{m,0} \times \Delta, \tag{15}$$

$$\overline{\Psi}(\mathbf{q},m) \to \sqrt{\beta V}\delta(\mathbf{q})\delta_{m,0} \times \Delta^*, \tag{16}$$

where m characterizes the bosonic Matsubara frequencies $\tilde{\omega}_m = 2m\pi/\beta$, and V represents the volume of the system. This approximation, which is called the saddle-point approximation for the bosonic path integral, comes down to assuming that the pair field $\Psi(\mathbf{x},\tau)$ takes on a constant value Δ. By applying this approximation to the bosonic path integral in expression (12) (i.e., after performing the Hubbard-Stratonovich transformation but before performing the Grassmann integration over the fermionic fields), the resulting fermionic path integral can be solved analytically using formula (4) to find the saddle-point expression for the partition function:

$$\mathcal{Z}_{\text{sp}} = \exp\left\{\frac{|\Delta|^2}{g} - \sum_{\mathbf{k},n} \ln\left[(i\omega_n - E_{\mathbf{k}} + \zeta)(-i\omega_n - E_{\mathbf{k}} - \zeta)\right]\right\}. \tag{17}$$

where ω_n are the fermionic Matsubara frequencies $\omega_n = (2n+1)\pi/\beta$. We have also introduced the single-particle excitation energy $E_{\mathbf{k}} = \sqrt{\xi_{\mathbf{k}}^2 + \Delta^2}$ with $\xi_{\mathbf{k}} = k^2 - \mu$, and we have defined the average chemical potential μ and the imbalance chemical potential ζ as

$$\mu = \frac{\mu_\uparrow + \mu_\downarrow}{2} \quad \text{and} \quad \zeta = \frac{\mu_\uparrow - \mu_\downarrow}{2}. \tag{18}$$

The parameter ζ determines the population imbalance between the two spin populations. For $\zeta = 0$, the numbers of particles of each spin type are equal, while for non-zero values of ζ, there will be more spin-up than spin-down particles or vice versa. The saddle-point partition function can now be rewritten in terms of the saddle-point thermodynamic potential per unit volume Ω_{sp} as

$$\mathcal{Z}_{\text{sp}} = \exp\left\{-\beta V \Omega_{\text{sp}}\right\}. \tag{19}$$

After performing the Matsubara summation over n [3] and replacing the sum over $\mathbf{k}$ by a continuous integral in expression (17), we finally find for Ω_{sp}:

$$\Omega_{\text{sp}} = -\frac{|\Delta|^2}{8\pi k_F a_s} - \int \frac{d\mathbf{k}}{(2\pi)^3} \left\{ \frac{1}{\beta} \left[2\cosh\left(\beta E_{\mathbf{k}}\right) + 2\cosh\left(\beta\zeta\right) \right] - \xi_{\mathbf{k}} - \frac{|\Delta|^2}{2k^2} \right\} \tag{20}$$

The saddle-point value Δ_{sp} for the pair field is found through the requirement that Δ_{sp} minimizes Ω_{sp}, which yields the gap equation:

$$\left.\frac{\partial \Omega_{\text{sp}}}{\partial \Delta}\right|_{T,\mu,\zeta} = 0 \tag{21}$$

This is illustrated in **Figure 2**, which shows the thermodynamic potential Ω_{sp} as a function of Δ for several values of the imbalance chemical potential ζ. The superfluid state exists when Ω_{sp} reaches its minimum at a nonzero value of Δ. As ζ is increased, the normal state at $\Delta = 0$ develops and becomes the global minimum above a critical imbalance level. This transition from the superfluid to the normal state under influence of increasing population imbalance is known as the Clogston phase transition [16].

When working with a fixed number of particles, the chemical potential μ and the imbalance chemical potential ζ have to be related to the fermion density n_{sp} and density difference δn_{sp} (between the two spin populations) through the number equations

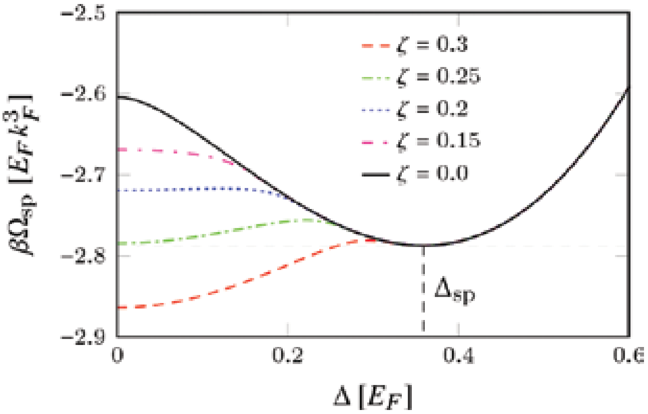

Figure 2. The thermodynamic potential Ω_{sp} in function of Δ for several values of the imbalance chemical potential ζ, at temperature $T/T_F = 0.01$ and chemical potential $\mu = 1.3E_F$. The evolution of the normal state at $\Delta = 0$ as ζ increases illustrates the Clogston phase transition.

$$n_{\mathrm{sp}} = -\left.\frac{\partial \Omega_{\mathrm{sp}}}{\partial \mu}\right|_{T,\zeta,\Delta} \tag{22}$$

$$\delta n_{\mathrm{sp}} = -\left.\frac{\partial \Omega_{\mathrm{sp}}}{\partial \zeta}\right|_{T,\mu,\Delta} \tag{23}$$

Since in our units $k_F = 1$, the particle density n_{sp} is fixed by $n_{\mathrm{sp}} = 1/\left(3\pi^2\right)$. Given the input parameters β, ζ, and a_s, the values Δ and μ can then be found from the coupled set of Eqs. (21) and (22), while (23) fixes δn_{sp} as a function of ζ. Solutions for Δ_{sp} and μ across the BEC-BCS crossover are shown in **Figure 3a** and **b**.

4. The effective field theory

While the saddle-point approximation is a suitable model for the qualitative description of homogeneous Fermi superfluids, it does not account for the effects of fluctuations of the order parameter, nor does it include any excitations other than the single-particle Bogoliubov excitations. To study the properties and dynamics of non-homogeneous systems, one needs to go beyond the limitations of a mean field theory. In this section, we formulate an effective field theory (EFT) for the pair field $\Psi(\mathbf{r}, t)$ that can describe nonhomogeneous Fermi superfluids in the BEC-BCS crossover at finite temperatures. To this end, we return to the path integral expression (13) for the partition function, which was obtained after performing the Hubbard-Stratonovich transformation and integrating out the fermionic degrees of freedom. Since the exponent of this partition function only depends on the fields $\Psi(\mathbf{r}, t)$ and $\overline{\Psi}(\mathbf{r}, t)$, we can define an effective bosonic action for the pair field given by

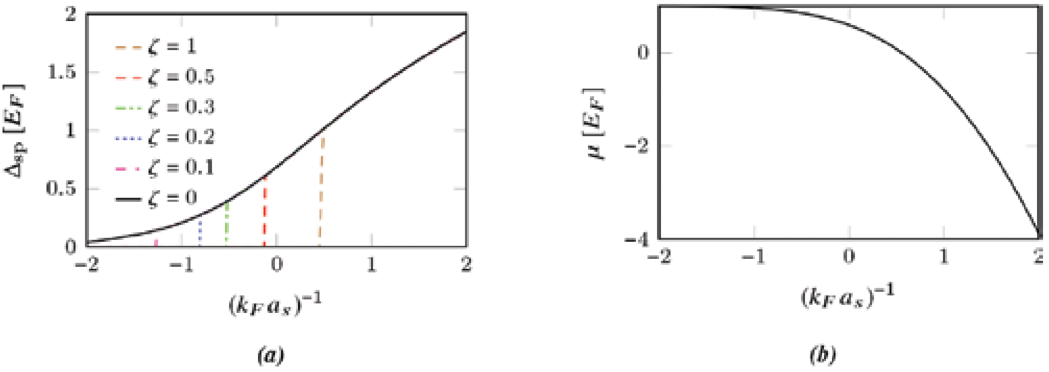

(a) *(b)*

Figure 3. Solutions for the pair field Δ and the average chemical potential μ in function of the interaction strength $(k_F a_s)^{-1}$ at temperature $T/T_F = 0.01$. The solution for Δ is shown for several values of the imbalance chemical potential ζ, illustrating the transition from the superfluid to the normal state under influence of population imbalance.

$$S_{\text{eff}} = S_B - \text{Tr}\left[\ln\left(-\mathbb{G}^{-1}\right)\right], \tag{24}$$

where $S_B = -\int_0^\beta \int d\mathbf{x} \frac{|\Psi(\mathbf{x},\tau)|^2}{g}$ is the action for free bosonic fields. The inverse Green's function matrix $-\mathbb{G}^{-1}$ for interacting fermions, which was defined in expression (14), can be separated into its diagonal and off-diagonal components

$$\begin{aligned} -\mathbb{G}^{-1}(\mathbf{x},\tau) &= -\mathbb{G}_0^{-1}(\mathbf{x},\tau) + \mathbb{F}(\mathbf{x},\tau) \\ &= \begin{pmatrix} \frac{\partial}{\partial\tau} - \nabla_{\mathbf{x}}^2 - \mu_\uparrow & 0 \\ 0 & \frac{\partial}{\partial\tau} + \nabla_{\mathbf{x}}^2 + \mu_\downarrow \end{pmatrix} + \begin{pmatrix} 0 & -\Psi(\mathbf{x},\tau) \\ -\overline{\Psi}(\mathbf{x},\tau) & 0 \end{pmatrix}, \end{aligned} \tag{25}$$

where $-\mathbb{G}_0^{-1}$ describes free fermionic fields, while $\mathbb{F}$ describes the pairing of the fermions. Using this decomposition, we can write the effective bosonic action functional (24) as

$$\begin{aligned} S_{eff} &= S_B - Tr[\ln(-\mathbb{G}_0^{-1} + \mathbb{F})] \\ &= S_B - Tr[\ln(-\mathbb{G}_0^{-1})] - Tr[\ln(1 - \mathbb{G}_0\mathbb{F})] \\ &= S_B + S_0 + \sum_{p=1}^{\infty} \frac{1}{p} Tr[(\mathbb{G}_0\mathbb{F})^p]. \end{aligned} \tag{26}$$

While, in general, this infinite sum over all powers of the pair field cannot be calculated analytically, there exist many possible approximations that lead to various theoretical treatments of the ultracold Fermi gas. For example, the mean field saddle-point approximation from the previous section can be retrieved by simply setting

$$\mathbb{F}(\mathbf{x},\tau) \approx \mathbb{F}_{\text{sp}} = \begin{pmatrix} 0 & -\Delta \\ -\overline{\Delta} & 0 \end{pmatrix} \tag{27}$$

in (26) and calculating the whole sum over p. In the Ginzburg-Landau (GL) treatment for ultracold Fermi gases, the action is approximated by assuming small fluctuations of the pair field $\Psi(\mathbf{x},\tau)$ around the normal state $\Psi = 0$. This assumption comes down to keeping only terms up to $p = 2$ in the sum in (26) and approximating $\mathbb{F}(\mathbf{x},\tau)$ by the following gradient expansion

$$\begin{aligned} \mathbb{F}(\mathbf{x},\tau) \approx \mathbb{F}_0 + (\mathbf{x} - \mathbf{x}_0) \cdot \nabla_{\mathbf{x}}\mathbb{F}\big|_{\mathbf{x}_0} + \frac{1}{2} \sum_{i,j=x,y,z} (x_i - x_{0,i})\left(x_j - x_{0,j}\right) \frac{\partial^2\mathbb{F}}{\partial x_i \partial x_j}\bigg|_{\mathbf{x}_0} \\ + (\tau - \tau_0)\frac{\partial\mathbb{F}}{\partial\tau}\bigg|_{\tau_0} + \frac{1}{2}(\tau - \tau_0)^2 \frac{\partial^2\mathbb{F}}{\partial\tau^2}\bigg|_{\tau_0}, \end{aligned} \tag{28}$$

with $\mathbb{F}_0 \to 0$. The result is an effective field treatment which is valid close to the critical temperature T_c of the superfluid phase transition. Inspired by the GL formalism, we will now present a beyond saddle-point EFT that is capable of describing Fermi superfluids in the BEC-BCS crossover at finite temperatures. This theory is based on the assumption that the pair field $\Psi(\mathbf{x},\tau)$ exhibits *slow* variations in space and time around a constant bulk value. Since this is a weaker condition than the GL assumption of small variations, it is ultimately expected to lead to a larger applicability domain. The assumption of slow fluctuations is implemented through a gradient expansion of the pair field around its saddle-point value, similar to (28) but with $\mathbb{F}_0 \rightarrow \mathbb{F}_{\text{sp}}$. Subsequently, we consider the full infinite sum in (26):

$$\sum_{p=1}^{\infty}\frac{1}{p}\text{Tr}[(\mathbb{G}_0\mathbb{F})^p] = \sum_{p=1}^{\infty}\frac{1}{p}\text{Tr}\left[\underbrace{\mathbb{G}_0\mathbb{F}\mathbb{G}_0\mathbb{F}\ldots\mathbb{G}_0\mathbb{F}}_{p\ \text{ factors}}\right]. \tag{29}$$

In every term of this sum, we replace (at most) two occurrences of $\mathbb{F}(\mathbf{x},\tau)$ by its gradient expansion and substitute all remaining factors $\mathbb{F}(\mathbf{x},\tau)$ by $\mathbb{F}_{\text{sp}}$. Afterward, the entire sum over p can be calculated analytically. The result of this calculation, the details of which can be found in [17], is an explicit expression for the Euclidian action functional that governs the dynamics of the pair field $\Psi(\mathbf{x},\tau)$ of a three-dimensional (3D) superfluid Fermi gas:

$$\begin{aligned} S_{\text{EFT}} = \ & \int_0^{\beta} d\tau \int d\mathbf{x} \left[\frac{D}{2}\left(\bar{\Psi}\frac{\partial\Psi}{\partial\tau} - \frac{\partial\bar{\Psi}}{\partial\tau}\Psi\right) + \Omega_s + \frac{C}{2m}\left(\nabla_{\mathbf{x}}\bar{\Psi}\cdot\nabla_{\mathbf{x}}\Psi\right) - \frac{E}{2m}\left(\nabla_{\mathbf{x}}|\Psi|^2\right)^2 \right. \\ & \left. + Q\frac{\partial\bar{\Psi}}{\partial\tau}\frac{\partial\Psi}{\partial\tau} - R\left(\frac{\partial|\Psi|^2}{\partial\tau}\right)^2\right]. \end{aligned} \tag{30}$$

The EFT coefficients Ω_s, C, D, E, Q and R are given by

$$\Omega_s = -\frac{1}{8\pi k_F a_s}|\Delta|^2 - \int\frac{d\mathbf{k}}{(2\pi)^3}\left\{\frac{1}{\beta}\ln\left[2\cosh\left(\beta E_{\mathbf{k}}\right) + 2\cosh\left(\beta\zeta\right)\right] - \xi_{\mathbf{k}} - \frac{|\Delta|^2}{2k^2}\right\} \tag{31}$$

$$C = \int\frac{d\mathbf{k}}{(2\pi)^3}\frac{k^2}{3m}f_2(\beta,E_{\mathbf{k}},\zeta) \tag{32}$$

$$D = \int\frac{d\mathbf{k}}{(2\pi)^3}\frac{\xi_{\mathbf{k}}}{|\Psi|^2}\left[f_1(\beta,\xi_{\mathbf{k}},\zeta) - f_1(\beta,E_{\mathbf{k}},\zeta)\right] \tag{33}$$

$$E = 2\int\frac{d\mathbf{k}}{(2\pi)^3}\frac{k^2}{3m}\,\xi_{\mathbf{k}}^2 f_4(\beta,E_{\mathbf{k}},\zeta) \tag{34}$$

$$Q = \frac{1}{2|\Psi|^2}\int\frac{d\mathbf{k}}{(2\pi)^3}\left[f_1(\beta,E_{\mathbf{k}},\zeta) - (E_{\mathbf{k}}^2 + \xi_{\mathbf{k}}^2)f_2(\beta,E_{\mathbf{k}},\zeta)\right] \tag{35}$$

$$\begin{aligned} R = \frac{1}{2|\Psi|^2}\int\frac{d\mathbf{k}}{(2\pi)^3} & \left[\frac{f_1(\beta,E_{\mathbf{k}},\zeta) + (E_{\mathbf{k}}^2 - 3\xi_{\mathbf{k}}^2)f_2(\beta,E_{\mathbf{k}},\zeta)}{3|\Psi|^2}\right. \\ & \left. + \frac{4(\xi_{\mathbf{k}}^2 - 2E_{\mathbf{k}}^2)}{3}f_3(\beta,E_{\mathbf{k}},\zeta) + 2E_{\mathbf{k}}^2|\Psi|^2 f_4(\beta,E_{\mathbf{k}},\zeta)\right], \end{aligned} \tag{36}$$

where the functions $f_p(\beta, \varepsilon, \zeta)$ are recursively defined as

$$f_1(\beta, \epsilon, \zeta) = \frac{1}{2\epsilon} \frac{\sinh(\beta\epsilon)}{\cosh(\beta\epsilon) + \cosh(\beta\zeta)} \tag{37}$$

$$f_{p+1}(\beta, \epsilon, \zeta) = -\frac{1}{2p\epsilon} \frac{\partial f_p(\beta, \epsilon, \zeta)}{\partial \epsilon} \tag{38}$$

In general, each of these EFT coefficients depends on the modulus squared of the order parameter $|\Psi(\mathbf{x}, \tau)|^2$. In practice, however, we will assume that the coefficients associated with the second order derivatives of the pair field can be kept constant and equal to their bulk value, since retaining their full space-time dependence would strictly speaking lead us beyond the second-order approximation of the gradient expansion. This means that in expressions (32), (34), (35), and (36) for the coefficients C, E, Q, and R, we set $|\Psi(\mathbf{x}, \tau)|^2 = |\Psi_\infty|^2$ and $E_\mathbf{k} = \sqrt{\xi_\mathbf{k}^2 + |\Psi_\infty|^2}$, where $|\Psi_\infty|^2$ is the saddle-point value of the pair field for a uniform system. For the coefficients Ω_s and D on the other hand, the full space-time dependence of $|\Psi(\mathbf{x}, \tau)|^2$ is preserved.

The effective action functional (30) forms the basis of our EFT description of superfluid Fermi gases. The validity and limitations of the formalism are largely determined by the main assumption that the order parameter varies slowly in space and time, which corresponds to the condition that the pair field should vary over a spatial region much larger than the Cooper pair correlation length. A detailed study of the limitations imposed by this condition was carried out in [18]. In the following chapters, we will demonstrate some of the ways in which the EFT can be employed by applying it to the description of two important topological excitations of the superfluid: dark solitons and vortices.

5. Application 1: Soliton dynamics

In this section, we will use the EFT that was developed in Section 4 to study the properties of dark solitons in Fermi superfluids.

5.1. What is a dark soliton?

Solitons are nonlinear solitary waves that maintain their shape while propagating through a medium at a constant velocity. They are found as the solution of nonlinear wave equations and emerge in a wide variety of physical systems, including optical fibers, classical fluids, and plasmas. More recently, they have also become a subject of interest in superfluid quantum gases [19–23]. In these systems, solitons appear most often in the form of *dark* solitons, which are characterized by a localized density dip in the uniform background and a jump in the phase profile of the order parameter. The magnitude of this density dip and phase jump are intrinsically connected to the velocity v_s with which the soliton propagates through the superfluid, as illustrated in **Figure 4**. The higher the soliton velocity, the smaller the phase jump and

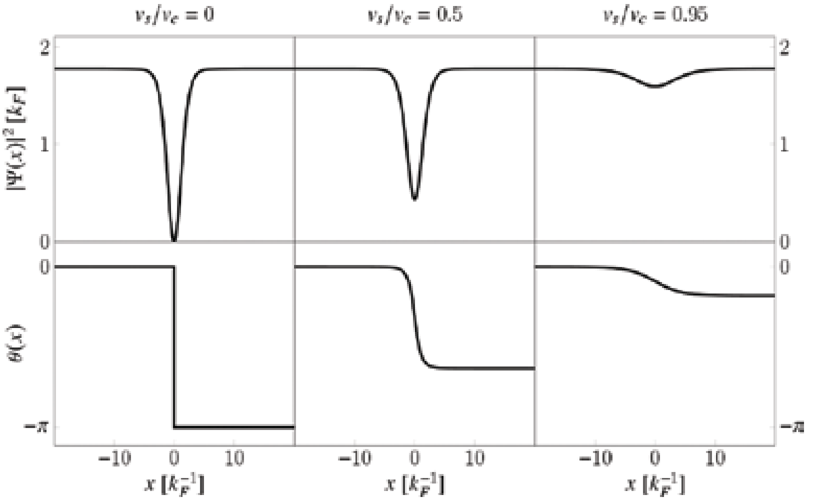

Figure 4. Example of the density profile (upper row) and phase profile (lower row) of a dark soliton for different soliton velocities v_s relative to the critical velocity v_c.

soliton depth become. Above a certain critical velocity v_c, the phase jump and density dip will disappear completely and a dark soliton solution no longer exists.

5.2. Solution for a one-dimensional dark soliton

For the case of a dark soliton in a one-dimensional (1D) Fermi superfluid with a uniform background, the EFT provides an exact analytical solution for the pair field [24]. To describe the dynamics of the system, it is necessary to move from the imaginary-time action functional (30) to the real-time one, using the formal replacements.

$$\tau \rightarrow it \tag{39}$$

$$S_{\text{EFT}}(\beta) \rightarrow -iS_{\text{EFT}}(t_b, t_a). \tag{40}$$

From the relation between the real-time action functional and the Lagrangian density $\mathcal{L}$,

$$S_{\text{EFT}}(t_b, t_a) = \int_{t_a}^{t_b} \mathrm{d}t \int \mathrm{d}\mathbf{x}\,\mathcal{L}, \tag{41}$$

we subsequently find the following expression for $\mathcal{L}$:

$$\begin{aligned} \mathcal{L} = i\frac{D}{2}\left(\overline{\Psi}\frac{\partial\Psi}{\partial t} - \frac{\partial\overline{\Psi}}{\partial t}\Psi\right) - \Omega_s - \frac{C}{2m}\left(\nabla_{\mathbf{x}}\overline{\Psi}\cdot\nabla_{\mathbf{x}}\Psi\right) + \frac{E}{2m}\left(\nabla_{\mathbf{x}}|\Psi|^2\right)^2 \\ +Q\frac{\partial\overline{\Psi}}{\partial t}\frac{\partial\Psi}{\partial t} - R\left(\frac{\partial|\Psi|^2}{\partial t}\right)^2, \end{aligned} \tag{42}$$

where the Hamiltonian density $\mathcal{H}$ is defined as

$$\mathcal{H} = \Omega_s + \frac{C}{2m}\left(\nabla_{\mathbf{x}}\overline{\Psi}\cdot\nabla_{\mathbf{x}}\Psi\right) - \frac{E}{2m}\left(\nabla_{\mathbf{x}}|\Psi|^2\right)^2 + Q\frac{\partial\overline{\Psi}}{\partial t}\frac{\partial\Psi}{\partial t} - R\left(\frac{\partial|\Psi|^2}{\partial t}\right)^2. \tag{43}$$

As mentioned above, a dark soliton in a superfluid is mainly characterized by a jump in the phase profile and a dip in the amplitude profile of the order parameter. Therefore, it is convenient to write the pair field $\Psi(\mathbf{x}, t)$ as

$$\Psi(\mathbf{x}, t) = |\Psi(\mathbf{x}, t)|e^{i\theta(\mathbf{x},t)}. \tag{44}$$

Moreover, since a soliton is a localized perturbation, we write the modulus as a product of the constant background value $|\Psi_\infty|$ and a relative amplitude $a(\mathbf{x}, t)$ that modifies the background value at the position of the soliton:

$$|\Psi(\mathbf{x}, t)| = |\Psi_\infty|a(\mathbf{x}, t). \tag{45}$$

Substituting this form for the pair field in the field Lagrangian (42), we find

$$\begin{aligned}\mathcal{L} = &-\kappa(a)a^2\frac{\partial\theta}{\partial t} - [\Omega_s(a) - \Omega_s(a_\infty)] - \frac{1}{2}\rho_{\text{qp}}(a)(\nabla_{\mathbf{x}}a)^2 - \frac{1}{2}\rho_{\text{sf}}(a)(\nabla_{\mathbf{x}}\theta)^2\\ &+\left(Q - 4R|\Psi_\infty|^2a^2\right)|\Psi_\infty|^2\left(\frac{\partial a}{\partial t}\right)^2 + Q|\Psi_\infty|^2a^2\left(\frac{\partial\theta}{\partial t}\right)^2,\end{aligned} \tag{46}$$

with

$$\kappa(a) = D(a)|\Psi_\infty|^2, \tag{47}$$

$$\rho_{\text{qp}}(a) = \frac{C - 4E|\Psi_\infty|^2a^2}{m}|\Psi_\infty|^2, \tag{48}$$

$$\rho_{\text{sf}}(a) = \frac{C}{m}|\Psi_\infty|^2a^2. \tag{49}$$

Here, we added $\Omega_s(a_\infty)$ to the original Lagrangian to obtain a regularized Lagrangian density in which energy values are considered with respect to the energy of the uniform system. The superfluid density ρ_{sf} determines how much the pair condensate resists gradients in its phase field, while the quantum pressure ρ_{qp} is a consequence of the fact that the condensate also resists gradients in the pair density. We will further limit ourselves to a 1D problem in which the soliton propagates with constant speed v_s in the x-direction on a uniform background. This assumption can be implemented through the condition that the space-time dependence of the pair field satisfies the relation $f(x, t) = f(x - v_st)$. We then perform a change of variables $x' = x - v_st$ and $t' = t$, corresponding to a transformation to the frame of reference that moves along with the soliton and has its origin at the soliton center. It follows that

$$f(x - v_st) = f(x'), \qquad \frac{\partial}{\partial x} = \frac{\partial}{\partial x'}, \qquad \frac{\partial}{\partial t} = \frac{\partial}{\partial t'} - v_s\frac{\partial}{\partial x'}. \tag{50}$$

If we further drop the primes, the Lagrangian density (46) in the soliton frame of reference can be written as

$$\mathcal{L} = \kappa(a)a^2 v_s \frac{\partial \theta}{\partial x} - [\Omega_s(a) - \Omega_s(a_\infty)] - \frac{1}{2}\tilde{\rho}_{\text{qp}}(a)\left(\frac{\partial a}{\partial x}\right)^2 - \frac{1}{2}\tilde{\rho}_{\text{sf}}(a)\left(\frac{\partial \theta}{\partial x}\right)^2. \tag{51}$$

with the modified superfluid density and quantum pressure

$$\tilde{\rho}_{\text{qp}}(a) = \frac{C - 4E|\Psi_\infty|^2 a^2}{m}|\Psi_\infty|^2 - 2\Big(Q - 4R|\Psi_\infty|^2 a^2\Big)|\Psi_\infty|^2 v_s^2, \tag{52}$$

$$\tilde{\rho}_{\text{sf}}(a) = \frac{C}{m}|\Psi_\infty|^2 a^2 - 2Q|\Psi_\infty|^2 a^2 v_s^2. \tag{53}$$

From the above expression for $\mathcal{L}(a, \theta)$, we can now find the equations of motion for the relative amplitude field $a(x)$ and the phase field $\theta(x)$:

$$\frac{\partial}{\partial t}\left(\frac{\partial \mathcal{L}}{\partial(\partial_t a)}\right) + \frac{\partial}{\partial x}\left(\frac{\partial \mathcal{L}}{\partial(\partial_x a)}\right) = \frac{\partial \mathcal{L}}{\partial a}, \tag{54}$$

$$\frac{\partial}{\partial t}\left(\frac{\partial \mathcal{L}}{\partial(\partial_t \theta)}\right) + \frac{\partial}{\partial x}\left(\frac{\partial \mathcal{L}}{\partial(\partial_x \theta)}\right) = \frac{\partial \mathcal{L}}{\partial \theta}. \tag{55}$$

Starting with the equation for the phase field, we easily find:

$$\frac{\partial}{\partial x}\left(\kappa(a)a^2 v_s - \tilde{\rho}_{\text{sf}}(a)\frac{\partial \theta}{\partial x}\right) = 0 \tag{56}$$

$$\Leftrightarrow \quad \frac{\partial \theta}{\partial x} = \frac{\kappa(a)a^2 v_s + \alpha}{\tilde{\rho}_{\text{sf}}(a)}. \tag{57}$$

The integration constant α can be determined through the boundary condition for a dark soliton:

$$\frac{\partial \theta}{\partial x} \to 0 \quad \text{for} \quad x \to \pm\infty. \tag{58}$$

which yields $\alpha = -v_s \kappa_\infty$ with $\kappa_\infty = \kappa(a_\infty)$ and thus

$$\frac{\partial \theta}{\partial x} = \frac{v_s}{\tilde{\rho}_{\text{sf}}(a)}\big(\kappa(a)a^2 - \kappa_\infty\big). \tag{59}$$

If we set $\theta(-\infty) = 0$, the phase profile of the superfluid is given by

$$\theta(x) = v_s \int_{-\infty}^{x} \frac{\kappa(a(x'))a^2(x') - \kappa_\infty}{\tilde{\rho}_{\text{sf}}(a(x'))}\, dx'. \tag{60}$$

Next, we derive the equation of motion for $a(x)$:

$$\frac{\partial}{\partial x}\left(-\tilde{\rho}_{\text{qp}}(a)\frac{\partial a}{\partial x}\right) = \frac{\partial}{\partial a}\left(\kappa(a)a^2\right)v_s\frac{\partial \theta}{\partial x} - \frac{\partial \Omega_s}{\partial a} - \frac{1}{2}\frac{\partial \tilde{\rho}_{\text{qp}}}{\partial a}\left(\frac{\partial a}{\partial x}\right)^2 - \frac{1}{2}\frac{\partial \tilde{\rho}_{\text{sf}}}{\partial a}\left(\frac{\partial \theta}{\partial x}\right)^2. \tag{61}$$

Inserting the solution for the derivative of the phase field (59) and defining

$$X(a) = \Omega_s(a) - \Omega_s(a_\infty), \tag{62}$$

$$Y(a) = \frac{\left(\kappa(a)a^2 - \kappa_\infty\right)^2}{2\tilde{\rho}_{\text{sf}}(a)}, \tag{63}$$

we find

$$\frac{1}{2}\frac{\partial\tilde{\rho}_{\text{qp}}}{\partial a}\left(\frac{\partial a}{\partial x}\right)^2 + \tilde{\rho}_{\text{qp}}(a)\frac{\partial^2 a}{\partial x^2} = \frac{\partial}{\partial a}\left(X(a) - v_s^2 Y(a)\right). \tag{64}$$

While the above equation does not allow for a straightforward solution for a as a function of the position x, it can be solved for x as a function of a instead. Using the boundary conditions for a dark soliton

$$\left.\frac{\partial a}{\partial x}\right|_{x\to\pm\infty} = 0 \quad \text{and} \quad a(x)|_{x\to\pm\infty} = 1, \tag{65}$$

we find that (64) can be integrated, yielding:

$$\frac{1}{2}\tilde{\rho}_{\text{qp}}(a)\left(\frac{\partial a}{\partial x}\right)^2 = X(a) - v_s^2 Y(a), \tag{66}$$

$$\Leftrightarrow \left(\frac{\partial x}{\partial a}\right)^2 = \frac{1}{2}\frac{\tilde{\rho}_{\text{qp}}(a)}{X(a) - v_s^2 Y(a)}, \tag{67}$$

$$\Leftrightarrow x = \pm\frac{1}{\sqrt{2}}\int_{a_0}^{a}\frac{\sqrt{\tilde{\rho}_{\text{qp}}(a')}}{\sqrt{X(a') - v_s^2 Y(a')}}da'. \tag{68}$$

Here, $a_0 = a(x = 0)$ is the relative amplitude at the center of the soliton, which is found as the solution of

$$X(a_0) - v_s^2 Y(a_0) = 0. \tag{69}$$

For given values of the interaction parameter $(k_F a_s)^{-1}$, the temperature T/T_F, the imbalance chemical potential ζ, and the soliton velocity v_s, formulae (60) and (68) allow us to calculate the complete pair field profile of the dark soliton. For example, the soliton density and phase profiles in **Figure 4** were calculated using the above expressions.

5.3. Dark solitons in imbalanced Fermi gases

The dark soliton solution derived in the previous section has been employed in the description of various soliton phenomena in superfluid Fermi gases. For instance, adding a small two-dimensional perturbation to the exact 1D solution allows for a description of the snake instability mechanism [25], which makes the soliton decay into vortices if the radial width of the system is too large [23, 26]. We have also studied collisions between dark solitons by numerically evolving two counter-propagating 1D solitons in time [27]. As an example of an application, we will give a short description of the influence of *spin-imbalance* on dark solitons, a topic that was studied in detail in [18].

In ultracold Fermi gases, the amount of atoms in each spin population can be tuned experimentally, allowing for the possibility of having unequal amounts of spin-up and spin-down particles [28, 29]. In that case, when particles of different spin type pair up and form a superfluid state, an excess of unpaired particles will remain in the normal state, which in turn can have interesting effects on other phenomena in the system, including dark solitons. In the context of the EFT, we control the population imbalance by setting the value of the imbalance chemical potential ζ, defined in (18). **Figure 5a** and **b** shows respectively the fermion particle density $n(x)$ and spin-population density difference $\delta n(x)$ (both with respect to the bulk density n_∞) along a stationary dark soliton for $(k_F a_s)^{-1} = 0$ (unitarity), $T = 0.1\,T_F$, and for different values of ζ. The density and density difference profiles are calculated using formulas (22) and (23) in a mean-field local density approximation. From the left figure, we observe that as we raise the imbalance chemical potential, the fermion density at the soliton center increases and the soliton broadens. However, we also know that, for a stationary dark soliton, the pair density at the center is always zero (as shown in the upper left panel of **Figure 4**), which means that the particles filling up the soliton are unpaired particles. This is confirmed by the right figure, which shows that the density difference between spin-up and spin-down particles in the soliton center increases with ζ. The same effects are observed across the whole BEC-BCS crossover.

As the imbalance between the spin components in the Fermi gas increases, so does the amount of unpaired particles that cannot participate in the superfluid state of pairs. While some of these normal state particles can coexist with the pair condensate as a thermal gas, it is energetically favorable for the remaining excess to be spatially separated from the superfluid. In this context, the soliton dip is a very suitable location to accommodate the excess particles and consequently fills up with an increasing amount of unpaired particles as the imbalance gets higher. Also, the broadening of the soliton with increasing imbalance might be a way of

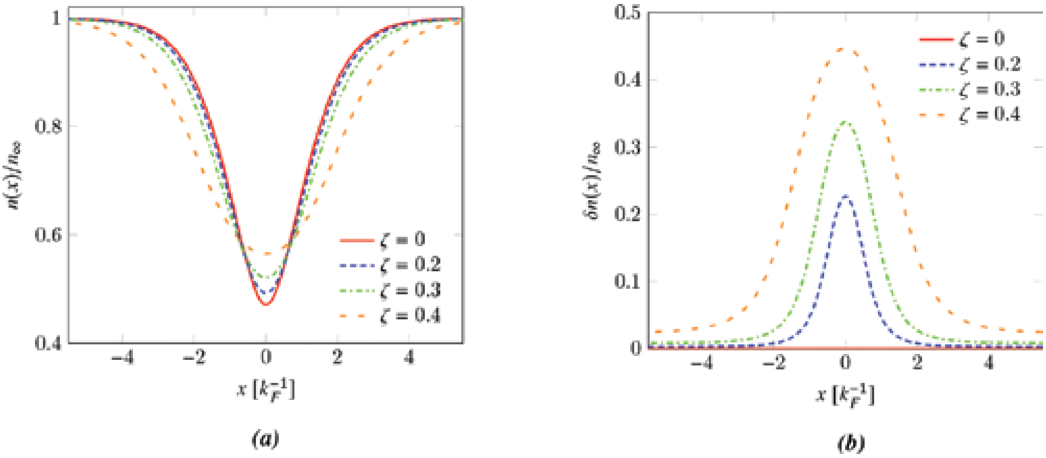

Figure 5. Fermion density (left figure) and density difference (right figure) profiles of a dark soliton for $(k_F a_S)^{-1} = 0$ at temperature $T/T_F = 0.1$, for different values of the imbalance chemical potential ζ. The densities are given with respect to the bulk density n_∞.

providing the system with more space to store the excess component. The fact that a dark soliton in an imbalanced superfluid Fermi gas has to drag along additional particles changes its effective mass, which in turn influences its general dynamical properties [18]. Moreover, since a soliton plane provides more space to accommodate the excess component than a vortex core, the presence of spin imbalance has been found to stabilize dark solitons with respect to the snake instability [25].

6. Application 2: the vortex structure

As a second application, the time-independent version of the theory is considered in order to derive the stable vortex structure. For the description of the vortex, the quantum velocity field $\mathbf{v}$ will be used, defined as:

$$\mathbf{v} = \frac{\hbar}{m} \nabla_{\mathbf{x}} \theta, \tag{70}$$

where θ is the phase field from the hydrodynamical description (44). In the time-independent case, the action (30) reduces to the free energy (times the inverse temperature), which is given by:

$$F = \int d\mathbf{r} \mathcal{F}(a, \nabla_{\mathbf{x}} a, \mathbf{x}) \quad \text{with} \quad \mathcal{F}(a, \nabla_{\mathbf{x}} a, \mathbf{x}) = X(a) + \frac{1}{8} \rho_{\text{sf}}(a) v^2(\mathbf{x}) + \frac{1}{2} \rho_{\text{qp}}(a) |\nabla_{\mathbf{x}} a|^2. \tag{71}$$

The free energy was written in a more compact[3] form using the hydrodynamical description (48), (49), (62) and (70). As an application of the effective field theory, the general structure of a superfluid vortex will be numerically determined and compared with the commonly used variational hyperbolic tangent. A more detailed description on vortices in superfluids and their behavior can be found in [30].

6.1. What is a vortex?

Both in the classical and the quantum sense, a vortex is defined as a line in the fluid around which there is a circulating flow. In order to quantify this rotation around an axis, the circulation κ is defined as:

$$\kappa = \oint_{\gamma} \mathbf{v}(\mathbf{r}) \cdot d\mathbf{s}, \tag{72}$$

where γ is a closed contour and $\mathbf{v}$ the superfluid velocity field (70). A distinct feature of superfluids[4] is that the circulation κ is only allowed to take on values which are integer multiples of the circulation quantum h/m. In superfluids, circulation is always carried by quantized vortices.

This quantization of the circulation can be derived using the definition of the velocity field (70). Upon substitution, the circulation (72) can be written as:

---

[3] Where again the free energy at infinity was subtracted to obtain a well behaved free energy.

[4] In the case of a superconductor, the quantized value is given by the magnetic flux.

$$\kappa = \frac{\hbar}{m}\oint_\gamma \nabla_{\mathbf{x}}\theta \cdot d\mathbf{s} = n\frac{h}{m} \quad \text{with} \quad n \in \mathbb{Z}, \tag{73}$$

where the gradient theorem was used together with the fact that the phase field θ is a periodic function (period 2π).

As the bulk superfluid itself is irrotational, any loop with nonzero circulation must encircle a node in the superfluid order parameter. As a consequence, the superfluid pair density must go to zero along the entire vortex line, resulting in a vortex "core" region with a radius comparable to the healing length. Important to note is that vortices of a single circulation quantum are energetically more favorable than multiply quantized vortices in a homogeneous condensate (which is the type of condensate that will be considered in this chapter) [9]. For the remainder of this application, only singly quantized vortices will thus be studied.

6.2. About the structure of a quantum vortex

The most natural coordinate system to describe vortices are the polar coordinates $\mathbf{x} = (r, \phi)$. The origin of the polar coordinates will be chosen in the center of the vortex (at the point where the superfluid density reaches zero). In order to derive the vortex structure, a set of boundary conditions is required. In the radial direction, the boundary conditions are then given by[5]:

$$a(r \to 0) = 0 \quad \text{and} \quad a(r \to \infty) = 1, \tag{74}$$

meaning that the superfluid density relaxes to the bulk value away from the vortex.

We factorize the amplitude function in a radial and an angular part[6]:

$$a(r,\phi) = f(r)\Phi(\phi). \tag{75}$$

Since the structure is periodic, the general solution for $\Phi(\phi)$ is thus given by:

$$\Phi(\phi) = \sum_{n=-\infty}^{\infty} a_n e^{in\phi}, \tag{76}$$

leading to a basis of angular modes for the vortex structure. In order to find the lowest energy state, one usually restricts the problem to one of the many possible modes:

$$\Phi(\phi) = e^{in\phi} \quad \text{with} \quad n \in \mathbb{Z}, \tag{77}$$

which results in the velocity field and circulation (using (70) and (72)) for a single mode given by:

---

[5] Note that the condition at $r \to \infty$ could be replaced by $\partial_r a_{r\to\infty} = 0$. This could however lead to numerical difficulties in the center of the vortex.

[6] This product decomposition is not generally valid in all coordinate systems [31].

$$\mathbf{v}(r) = n\frac{\hbar}{mr}\mathbf{e}_\phi \Rightarrow \kappa = n\frac{h}{m}, \tag{78}$$

where the velocity field diverges in the point where the superfluid vanishes. It was noted before that for our case, the most energetic vortex states are those with the least circulation quanta. Since the object of interest is the vortex structure with a minimal free energy, the value of n will be restricted to $n = \pm 1$. The state with $n = 1$ is known as the "vortex," where the state with $n = -1$ is known as the "anti-vortex." This means that the vortex velocity field is given by[7]:

$$\mathbf{v}(r) = \pm\frac{\hbar}{mr}\mathbf{e}_\phi, \tag{79}$$

where the "+" sign is for vortices and the "-" sign for anti-vortices.

Currently, there is no analytical solution available for the full vortex structure $f(r)$. Calculations including vortices are therefore either done numerically (for the exact structure) or variationally. One way to numerically find the minimal structure is by writing down the equations of motion (the Euler-Lagrange equations for the free energy (71)), which is analogous to what was done for the soliton in the previous section. Directly solving the equations of motion, however, is a numerical challenge due to the divergence of the velocity field in the center of the vortex. A second numerical method is briefly discussed further on. The disadvantage of the full numerical approach is that it takes time. As an alternative, it is possible to work with a variational model. By working with a variational model, it is possible to retain a fair amount of accuracy while gaining several orders of magnitude in computational speed. The usage of variational models is discussed in the next subsection. A disadvantage of using variational models is however that a certain structure is proposed, meaning the variational guess can be wrong in certain situations. When using variational models, one should consequently always check the validity of the model and the range of application.

6.3. A variational model for the vortex core

In order to speed up the vortex calculations, a variational model can be used to describe the vortex structure. First of all, the variational model should meet the required boundary conditions (74). Second, the variational model should contain the necessary information to describe the vortex physics. For example, in liquid helium, the vortex core sizes are of the order of nanometers [33], meaning that the vortex core structure will not play a prominent role in the vortex physics; in this case, a simple hollow cylinder is already a good variational model for the vortex core. For vortices in ultracold gases on the other hand, the vortex core size is of the order of micrometers [34], meaning that its structure becomes important[8]; a simple cylindric hole will no longer capture the entire vortex physics. In order to provide a more detailed description, different variational models are available [9, 30].

---

[7] Note that this velocity field is the same as the elementary vortex flow known in classical hydrodynamics [32].

[8] The condensate size to vortex core size is typically in the range 10–50.

The variational model that will be discussed here is the hyperbolic tangent model:

$$f(r) = \tanh\left(\frac{r}{\sqrt{2}\xi}\right), \tag{80}$$

where the quantity ξ is defined as the healing length. The hyperbolic tangent (80) is the exact solution of the Gross-Pitaevskii equation in 1D for a condensate with a hard wall boundary [9, 35]. Since the variational model describes the healing from a hole in the condensate, it is expected that this model will also sufficiently describe the vortex physics. The merit of the presented effective field theory in Section 4 is that an analytical solution can be derived for the vortex healing length ξ; this will be done in the remainder of this subsection. Using the definitions (71), the free energy of the variational vortex structure is given by:

$$F = \int_0^\infty r\mathrm{d}r \left[X(a) + \frac{A}{2r^2}\tanh^2\left(\frac{r}{\sqrt{2}\xi}\right) + \frac{\rho_{\mathrm{qp}}\left(\tanh\left(\frac{r}{\sqrt{2}\xi}\right)\right)}{4\xi^2\cosh^4\left(\frac{r}{\sqrt{2}\xi}\right)} \right], \tag{81}$$

where the value of the constant A is defined as:

$$A = 2C|\Delta_\infty|^2. \tag{82}$$

The second term in the integrand of (81) causes a divergence, since

$$\lim_{R\to\infty} \frac{A}{2}\int_0^R \frac{1}{r}\tanh^2\left(\frac{r}{\sqrt{2}\xi}\right)\mathrm{d}r \propto \log(R) \tag{83}$$

diverges logarithmically with increasing radius of the integration domain. The physical reason is clear: the velocity profile of a vortex decays as $1/r$, so that the kinetic energy of the superflow will grow as the logarithm of the container size. However, the derivative with respect to ξ of this kinetic energy of the superflow does not diverge. This can be seen by first switching to a dimensionless variable $x = r/\xi$:

$$F = \xi^2\int_0^\infty xX(a)\mathrm{d}x + \frac{A}{2}\lim_{R\to\infty}\left(\int_0^{R/\xi} \tanh^2\left(\frac{x}{\sqrt{2}}\right)\frac{\mathrm{d}x}{x}\right) + \int_0^\infty \frac{\rho_{qp}\left(\tanh(x/\sqrt{2})\right)}{4\cosh^4(x/\sqrt{2})}\mathrm{d}x. \tag{84}$$

The last term no longer contains a dependency on ξ, so its derivative with respect to ξ vanishes. We obtain

$$\frac{\mathrm{d}F}{\mathrm{d}\xi} = 2\xi\int_0^\infty xX(a)\mathrm{d}x + \frac{A}{2}\lim_{R\to\infty}\frac{\mathrm{d}}{\mathrm{d}\xi}\left[\int_0^{R/\xi} \tanh^2\left(\frac{x}{\sqrt{2}}\right)\frac{\mathrm{d}x}{x}\right] \tag{85}$$

The remaining derivative now acts on the boundary of the integration domain. Applying

$$\begin{aligned}\frac{\mathrm{d}}{\mathrm{d}\xi}\int_0^{R/\xi} g(x)\mathrm{d}x &= \lim_{\Delta\xi\to 0}\frac{1}{\Delta\xi}\left(\int_0^{R/(\xi+\Delta\xi)} g(x)\mathrm{d}x - \int_0^{R/\xi} g(x)\mathrm{d}x\right)\\ &= \lim_{\Delta\xi\to 0}\frac{1}{\Delta\xi}\left(\frac{R}{\xi+\Delta\xi}-\frac{R}{\xi}\right)g\left(\frac{R}{\xi}\right) = -\frac{R}{\xi^2}g\left(\frac{R}{\xi}\right)\end{aligned} \tag{86}$$

to (85) we get

$$\frac{\mathrm{d}F}{\mathrm{d}\xi} = 2\xi\int_0^\infty xX(a)\mathrm{d}x - \frac{A}{2\xi}\lim_{R\to\infty}\left[\tanh^2\left(\frac{R}{\sqrt{2}\xi}\right)\right], \tag{87}$$

so that

$$\frac{\mathrm{d}F}{\mathrm{d}\xi} = 0 \Leftrightarrow 2\xi\int_0^\infty xX(a)\mathrm{d}x = \frac{A}{2\xi}. \tag{88}$$

With $A = 2C|\Delta_\infty|^2$ as above, and

$$B = \int_0^\infty xX(a)\mathrm{d}x \tag{89}$$

we find a closed form result

$$\xi = \frac{1}{2}\sqrt{\frac{A}{B}}. \tag{90}$$

The formula for the healing length (90) can also be plotted, this is done in **Figure 6**. In both limits, the healing length shows to be in a good agreement with the exact limits.

6.4. Comparison to the exact (numerical) solution

In order to check the validity of the variational model (80) (and thus the results it produces) is, the variational structure should be compared with the exact vortex structure. This exact vortex structure is easily obtained by a direct minimization of the free energy functional (71). As mentioned before, the direct minimization of the free energy is more suitable for the calculation of the vortex structures; the reason why this method is preferential lies in the fact that the velocity field diverges for $r \to 0$. The divergence of the velocity field in the origin will be strongly pronounced when solving the equations of motion. While in the case of a direct minimization, the same divergence will have less impact on the solution.

The numerical method that was used in order to determine the exact vortex structure for a given set of parameters (β, a_s, ζ) is discussed in full detail in [38]. In a nutshell, this method

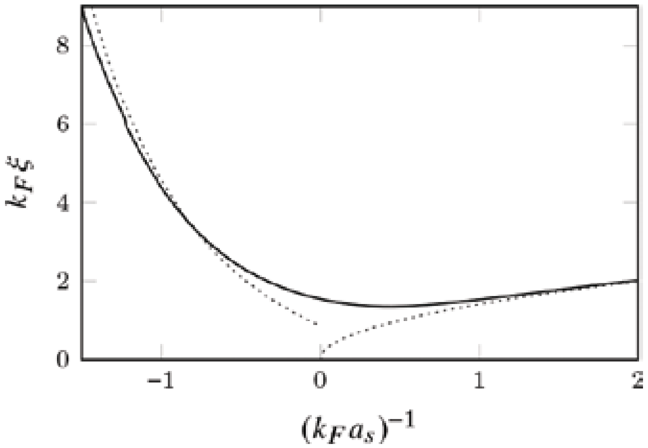

Figure 6. The vortex variational healing length (90) throughout the BEC-BCS crossover for the case $\beta = 100$ and $\zeta = 0$. The dotted lines yield the exact solutions in the deep BEC [36] and BCS [37] limits. This plot made using the same data as in [38].

comes down to making a discretized version of the vortex structure: $\{f_1, f_2, \ldots, f_N\}$, where $f_1 = 0$ and $f_N = 1$ due to the boundary conditions. During the minimization procedure, a program runs through the list of points $\{f_n | n \in \{2, 3, \ldots, N-1\}\}$, where it suggests a (random) new value; if the new value results in a lower energy, it is accepted as the new value of the vortex structure. The minimization program continues to run until a certain tolerance is reached and the structure is not changing any more.

Once the exact structure is obtained, it can be analyzed and compared to the variational vortex structure. As an example, we can look at the relative difference in the free energy throughout the BEC-BCS crossover for different temperatures and polarizations. From the plots shown in **Figure 7**, it can be seen that the difference in free energy is around the order of 1%; this seems

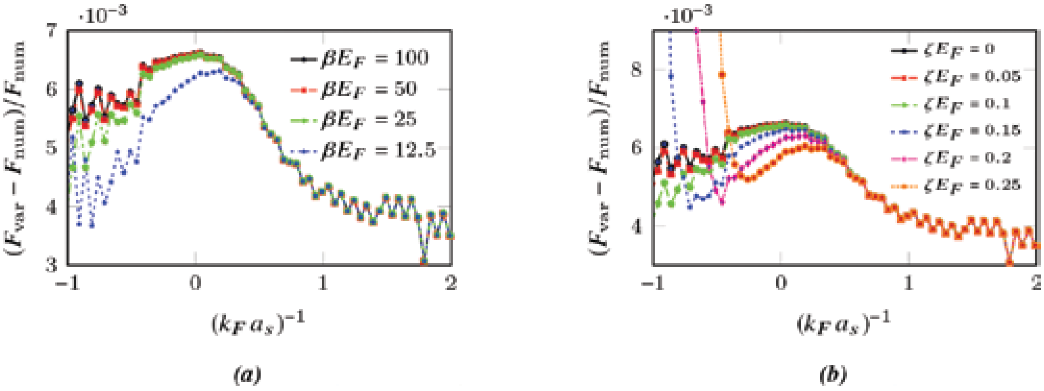

Figure 7. The relative energy difference between the exact and variational solutions throughout the BEC-BCS crossover for different values of the temperature β and polarization ζ. These results were also shown and discussed in [38].

to suggest that the variational guess is a good guess.[9] Moreover, the results in **Figure 7** allow to provide an error bar on energy calculations using the variational structure. This error bar on the energy is useful for example when making phase diagrams including vortex structures. In order to be sure whether the variational model is indeed a good description of the vortex hole, other parameters were also tested and discussed in [38]. The conclusion from the numerical analysis was that the variational model is indeed a good fit for describing the vortex structure.

7. Concluding section

In this chapter, an effective field theory for the description of dilute fermionic superfluids was derived. The main advantages of an effective field theory are the gain in computational speed and the fact that it allows analytic solutions for dark solitons and the variational healing length of the vortex structure. Both the gain in computational speed and the availability of an analytic starting point contribute to the possibility to study several soliton/vortex phenomena throughout the entire BEC-BCS crossover at finite temperatures β for a given polarization ζ within a reasonable computational time span.

On the subject of soliton dynamics, we specifically looked at 1D dark solitons, for which an exact analytical solution was derived. Using this solution, the effect of spin-imbalance on the soliton properties was studied, revealing that the unpaired particles of the excess component mainly reside inside the soliton core. Additionally, the EFT has also been employed in the study of the snake instability of dark solitons [25] and the dynamics of dark soliton collisions [27] in imbalanced superfluid Fermi gases.

For vortices, the structure of a vortex was studied, for which unfortunately no analytical solution is available at the moment. Using a variational model, an analytical solution for the vortex healing length was derived. The variational model was compared with the exact solution. From this analysis, the variational model was found to be a good fit for the exact vortex structure. Other EFT research on vortices includes the behavior of vortices in multiband systems [39] and the study of the "vortex charge" [40].

Acknowledgements

The authors gratefully acknowledge the financial support provided by the Fund for Scientific Research Flanders (FWO), through the FWO project: G042915 N (Superfluidity and superconductivity in multi-component quantum condensates). One of us (N.V.) acknowledges a Ph.D. fellowship of the University of Antwerp (2014BAPDOCPROEX167). One of us (W.V.A.) acknowledges a Ph.D. fellowship from the FWO (1123317 N). We also acknowledge financial support from the Research Fund (BOF-GOA) of the University of Antwerp.

---

[9] In **Figure 7b**, the energy difference seems to blow up towards the BCS limit. This divergence is due to the fact that at that point superfluidity is lost due to polarization (Clogston limit); at this point superfluidity disappears.

Author details

Wout Van Alphen[1], Nick Verhelst[1]*, Giovanni Lombardi[1], Serghei Klimin[1,2] and Jacques Tempere[1,3]

*Address all correspondence to: nick.verhelst@uantwerpen.be

1 TQC, University of Antwerp, Antwerpen, Belgium

2 Department of Theoretical Physics, State University of Moldova, Chisinau, Moldova

3 Lyman Laboratory of Physics, Harvard University, Cambridge, USA

References

[1] Giorgini S, Pitaevskii LP, Stringari S. Theory of ultracold atomic Fermi gases. Reviews of Modern Physics. 2008;**80**:1215-1274

[2] Ketterle W, Zwierlein MW. Making, probing and understanding ultracold Fermi gases. In: Ignuscio M, Ketterle W, Salomon C, editors. Ultracold Fermi Gases, Proceedings of the International School of Physics "Enrico Fermi", course CLXIV; 20–30 June 2006, Varenna. Amsterdam: IOS Press; 2008

[3] Tempere J, Devreese JPA. Path-integral description of cooper pairing. In: Gabovich A, editor. Superconductors: Materials, Properties and Applications. InTech; 2012. pp. 383-414 (ISBN: 978-953-51-0794-1). Open access online publication

[4] Zee A. Quantum Field Theory in a Nutshell. Princeton: Princeton University Press; 2010

[5] Feynman RP, Hibbs AR. Quantum Mechanics and Path Integrals. New York: Dover Publications Inc.; 2010

[6] Schulman LS. Techniques and Applications of Path Integration. New York: Dover Publications Inc.; 1981

[7] Kleinert H. Path Integrals in Quantum Mechanics, Statistics, Polymer Physics, and Financial Markets. Singapore: World Scientific; 2009

[8] Berezin FA. The Method of Second Quantization. New York: Academic Press; 1966

[9] Pethick CJ, Smith H. Bose-Einstein Condensation in Dilute Gases. Cambridge, UK: Cambridge University Press; 2008

[10] Stoof HTC, Gubbels KB, Dickerscheid DBM. Ultracold Quantum Fields. New York: Springer-Verlag; 2009

[11] Stratonovich RL. On a method of calculating quantum distribution functions. Soviet Physics Doklady. 1957;**2**:416

[12] Hubbard J. Calculation of partition functions. Physical Review Letters. 1959;**3**:77

[13] Nagaosa N. Quantum Field Theory in Condensed Matter Physics. Berlin: Springer; 1999

[14] Altland A, Simons B. Condensed Matter Field Theory. Cambridge: Cambridge University Press; 2006

[15] Kleinert H. Hubbard-Stratonovich transformation: Successes, failure, and cure. Electronic Journal of Theoretical Physics. 2011;**8**:57

[16] Clogston AM. Upper limit for the critical field in hard superconductors. Physical Review Letters. 1962;**9**:266

[17] Lombardi G. Effective field theory for superfluid Fermi gases [PhD thesis]. Universiteit Antwerpen, Belgium; 2017

[18] Lombardi G, Van Alphen W, Klimin SN, Tempere J. Soliton-core filling in superfluid Fermi gases with spin imbalance. Physical Review A. 2016;**93**:013614

[19] Denschlag J, Simsarian JE, Feder DL, Clark CW, Collins LA, Cubizolles J, Deng L, Hagley EW, Helmerson K, Reinhardt WP, Rolston SL, Schneider BI, Phillips WD. Generating solitons by phase engineering of a Bose-Einstein condensate. Science. 2000;**287**:97

[20] Burger S, Bongs K, Dettmer S, Ertmer W, Sengstock K, Sanpera A, Shlyapnikov GV, Lewenstein M. Dark solitons in Bose-Einstein condensates. Physical Review Letters. 1999;**83**:5198

[21] Anderson BP, Haljan PC, Regal CA, Feder DL, Collins LA, Clark CW, Cornell EA. Watching dark solitons decay into vortex rings in a Bose-Einstein condensate. Physical Review Letters. 2001;**86**:2926

[22] Becker C, Stellmer S, Soltan-Panahi P, Dörscher S, Baumert M, Richter E-M, Kronjger J, Bongs K, Sengstock K. Oscillations and interactions of dark and dark-bright solitons in Bose-Einstein condensates. Nature Physics. 2008;**4**:496

[23] Ku MJH, Mukherjee B, Yefsah T, Zwierlein MW. Cascade of solitonic excitations in a superfluid Fermi gas: From planar solitons to vortex rings and lines. Physical Review Letters. 2016;**116**:045304

[24] Klimin SN, Tempere J, Devreese JT. Finite-temperature effective field theory for dark solitons in superfluid Fermi gases. Physical Review A. 2014;**90**:053613

[25] Lombardi G, Van Alphen W, Klimin SN, Tempere J. Snake instability of dark solitons across the BEC-BCS crossover: An effective-field-theory perspective. Physical Review A. 2017;**96**:033609

[26] Donadello S, Serafni S, Tylutki M, Pitaevskii LP, Dalfovo F, Lamporesi G, Ferrari G. Observation of solitonic vortices in Bose-Einstein condensates. Physical Review Letters. 2014;**113**:065302

[27] Van Alphen W, Lombardi G, Klimin SN, Tempere J. arXiv:1709.00862 [cond-mat.quant-gas] (2017) URL: https://arxiv.org/abs/1709.00862

[28] Zwierlein MW, Schirotzek A, Schunck CH, Ketterle W. Fermionic superfluidity with imbalanced spin populations. Science. 2006;**311**:492

[29] Partridge GB, Li W, Kamar RI, Liao Y-a, Hulet RG. Pairing and phase separation in a polarized Fermi gas. Science. 2006;**311**:503

[30] Verhelst N, Tempere J. Vortex structures in ultracold atomic gases. In: Perez-de-Tejada H, editor. Vortex Dynamics. Intech; 2017. pp. 1-55. Open access online publication

[31] Yerly WE. An Elementary Treatise on Fourier's Series, and Spherical, Cylindrical, and Ellipsoidal Harmonics, with Applications to Problems in Mathematical Physics. New York: Dover; 1959

[32] Anderson JD. Fundamentals of Aerodynamics. London: McGraw-Hill Education; 2011

[33] Donnelly RJ. Quantized Vortices in Helium II. Cambridge: Cambridge University Press; 1991

[34] Cooper NR. Rapidly rotating atomic gases. Advances Physics. 2008;**57**:539

[35] Pitaevskii L, Stringari S. Bose-Einstein Condensation in Dilute Gases. Cambridge: Cambridge University Press; 2001

[36] Pitaevskii LP. Vortex lines in an imperfect Bose gas. Soviet Physics—JETP. 1961;**13**:451

[37] Marini M, Pistolesi F, Strinati GC. Evolution from BCS superconductivity to Bose condensation: Analytic results for the crossover in three dimensions. The European Physical Journal B. 1998;**1**:151

[38] Verhelst N, Klimin SN, Tempere J. Verification of an analytic fit for the vortex core profile in superfluid Fermi gases. Physica C. 2017;**533**:96-100

[39] Klimin SN, Tempere J, Lombardi G, Devreese JT. Finite temperature effective field theory and two-band superfluidity in Fermi gases. European Physical Journal B. 2015;**88**:122

[40] Klimin SN, Tempere J, Verhelst N, Miloševic MV. Finite-temperature vortices in a rotating Fermi gas. Physical Review A. 2016;**94**:023620

Topological Interplay between Knots and Entangled Vortex-Membranes

Su-Peng Kou

Additional information is available at the end of the chapter

http://dx.doi.org/10.5772/intechopen.72809

Abstract

In this paper, the Kelvin wave and knot dynamics are studied on three dimensional smoothly deformed entangled vortex-membranes in five dimensional space. Owing to the existence of local Lorentz invariance and diffeomorphism invariance, in continuum limit gravity becomes an emergent phenomenon on 3 + 1 dimensional zero-lattice (a lattice of projected zeroes): on the one hand, the deformed zero-lattice can be denoted by curved space-time for knots; on the other hand, the knots as topological defect of 3 + 1 dimensional zero-lattice indicates matter may curve space-time. This work would help researchers to understand the mystery in gravity.

Keywords: vortex-membrane, knot, gravity

1. Introduction

A vortex (point-vortex, vortex-line, vortex-membrane) consists of the rotating motion of fluid around a common centerline. It is defined by the vorticity in the fluid, which measures the rate of local fluid rotation. In three dimensional (3D) superfluid (SF), the quantization of the vorticity manifests itself in the quantized circulation $\oint \mathbf{v} \cdot d\mathbf{l} = \frac{h}{m}$ where h is Planck constant and m is atom mass of SF. Vortex-lines can twist around its equilibrium position (common centerline) forming a transverse and circularly polarized wave (Kelvin wave) [1, 2]. Because Kelvin waves are relevant to Kolmogorov-like turbulence [3, 4], a variety of approaches have been used to study this phenomenon. For two vortex-lines, owing to the interaction, the leapfrogging motion has been predicted in classical fluids from the works of Helmholtz and Kelvin [5–10]. Another interesting issue is entanglement between two vortex-lines. In mathematics, vortex-line-entanglement can be characterized by knots with different linking numbers. The study of knotted vortex-lines and their dynamics has attracted scientists from diverse settings, including classical fluid dynamics and superfluid dynamics [11, 12].

In the paper [13], the Kelvin wave and knot dynamics in high dimensional vortex-membranes were studied, including the leapfrogging motion and the entanglement between two vortex-membranes. A new theory—*knot physics* is developed to characterize the entanglement evolution of 3D leapfrogging vortex-membranes in five-dimensional (5D) inviscid incompressible fluid [13, 14]. According to knot physics, it is the 3D quantum Dirac model that describes the knot dynamics of leapfrogging vortex-membranes (we have called it knot-crystal, that is really plane Kelvin-waves with fixed wave-length). The knot physics may give a complete interpretation on quantum mechanics.

In this paper, we will study the Kelvin wave and knot dynamics on 3D deformed knot-crystal, particularly the topological interplay between knots and the lattice of projected zeroes (we call it zero-lattice). Owing to the existence of local Lorentz invariance and diffeomorphism invariance, the gravitational interaction emerges: on the one hand, the deformed zero-lattice can be denoted by curved space-time; on the other hand, the knots deform the zero-lattice that indicates matter may curve space-time (see below discussion).

The paper is organized as below. In Section 2, we introduce the concept of "zero-lattice" from projecting a knot-crystal. In addition, to characterize the entangled vortex-membranes, we introduce geometric space and winding space. In Section 3, we derive the massive Dirac model in the vortex-representation of knot states on geometric space and that on winding space. In Section 4, we consider the deformed knot-crystal as a background and map the problem onto Dirac fermions on a curved space-time. In Section 5, the gravity in knot physics emerges as a topological interplay between zero-lattice and knots and the knot dynamics on deformed knot-crystal is described by Einstein's general relativity. Finally, the conclusions are drawn in Section 6.

2. Knot-crystal and the corresponding zero-lattice

2.1. Knot-crystal

Knot-crystal is a system of two periodically entangled vortex-membranes that is described by a special pure state of Kelvin waves with fixed wave length $\mathbf{Z}_{\text{knot-crystal}}\left(\vec{x}, t\right)$ [13, 14]. In emergent quantum mechanics, we consider knot-crystal as a ground state for excited knot states, i.e.,

$$\mathbf{Z}_{\text{knot-crystal}}\left(\vec{x}, t\right) = \begin{pmatrix} z_{\mathrm{A}}\left(\vec{x}, t\right) \\ z_{\mathrm{B}}\left(\vec{x}, t\right) \end{pmatrix} \to |\text{vacuum}\rangle. \tag{1}$$

On the one hand, a knot is a piece of knot-crystal and becomes a topological excitation on it; on the other hand, a knot-crystal can be regarded as a composite system with multi-knot, each of which is described by same tensor state.

Because a knot-crystal is a plane Kelvin wave with fixed wave vector k_0, we can use the tensor representation to characterize knot-crystals [13],

$$\tilde{\mathbf{\Gamma}}^I_{\text{knot-crystal}} = \left(\vec{n}^I_\sigma \sigma^I\right) \otimes \left(\vec{n}_\tau \tau + \vec{1}\,\tau_0\right) \tag{2}$$

where $\vec{1} = \begin{pmatrix} 1 & 0 \\ 0 & 1 \end{pmatrix}$ and σ^I, τ^I are 2 × 2 Pauli matrices for helical and vortex degrees of freedom, respectively. For example, a particular knot-crystal is called SOC knot-crystal $\mathbf{Z}_{\text{knot-crystal}}\left(\vec{x}\right)$ [13], of which the tensor state is given by

$$\left\langle \sigma^X \otimes \vec{1} \right\rangle = \vec{n}^X_\sigma = (1,0,0), \left\langle \sigma^Y \otimes \vec{1} \right\rangle = \vec{n}^Y_\sigma = (0,1,0), \left\langle \sigma^Z \otimes \vec{1} \right\rangle = \vec{n}^Z_\sigma = (0,0,1). \tag{3}$$

For the SOC knot-crystal, along x-direction, the plane Kelvin wave becomes $\mathrm{z}(x) = \sqrt{2} r_0 \cos\left(k_0 \cdot x\right)$; along y-direction, the plane Kelvin wave becomes $\mathrm{z}(y) = \frac{1}{\sqrt{2}} r_0 \left(e^{ik\cdot y} + ie^{-ik\cdot y}\right)$; along z-direction, the plane Kelvin wave becomes $\mathrm{z}(z) = r_0 e^{ik\cdot z}$.

For a knot-crystal, another important property is generalized spatial translation symmetry that is defined by the translation operation $\mathcal{T}\left(\Delta x^I\right) = e^{i\cdot\left(\widehat{k^I_0}\cdot\Delta x^I\right)\cdot\tilde{\mathbf{\Gamma}}^I_{\text{knot-crystal}}}$

$$\begin{aligned} \mathbf{Z}\left(x^I, t\right) &\to \mathcal{T}\left(\Delta x^I\right)\mathbf{Z}\left(x^i, t\right) \\ &= e^{i\cdot\left(\widehat{k^I_0}\cdot\Delta x^i\right)\cdot\tilde{\mathbf{\Gamma}}^I_{\text{knot-crystal}}}\mathbf{Z}\left(x^i, t\right). \end{aligned} \tag{4}$$

Here $\widehat{k}^I$ is $-i\frac{d}{dx^I}$ $(I = x, y, z)$. For example, for the knot states on 3D SOC knot-crystal, the translation operation along x^I-direction becomes

$$\mathcal{T}\left(\Delta x^I\right) = e^{i\left(\widehat{\tilde{k}}^I\cdot\Delta x^I\right)\cdot\left(\sigma^I \otimes \vec{1}\right).} \tag{5}$$

2.2. Winding space and geometric space

For a knot-crystal, we can study it properties on a 3D space (x, y, z). In the following part, we call the space of (x, y, z) *geometric space*. According to the generalized spatial translation symmetry, each spatial point (x, y, z) in geometric space corresponds to a point denoted by three winding angles $\left(\Phi_x(x), \Phi_y(y), \Phi_z(z)\right)$ where $\Phi_{x^I}\left(x^I\right)$ is the winding angle along x^I-direction. As a result, we may use the winding angles along different directions to denote a given point $\vec{\Phi}\left(\vec{x}\right) = \left(\Phi_x(x), \Phi_y(y), \Phi_z(z)\right)$. We call the space of winding angles $\left(\Phi_x(x), \Phi_y(y), \Phi_z(z)\right)$ *winding space*. See the illustration in **Figure 1(d)**.

For a 1D leapfrogging knot-crystal that describes two entangled vortex-lines with leapfrogging motion, the function is given by

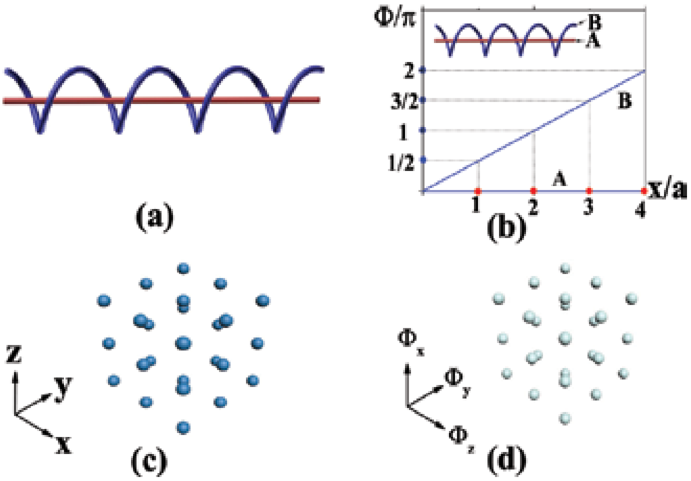

Figure 1. (a) An illustration of a 1D knot-crystal; (b) the relationship between winding angle Φ and coordinate position x. The red dots consist of a 1D zero-lattice in geometric space and the blue dots consist of a zero-lattice in winding space; (c) an illustration of a 3D uniform zero-lattice in geometric space; and (d) an illustration of a 3D uniform zero-lattice in winding space.

$$\mathbf{Z}\left(\vec{x},t\right) = r_0 \begin{pmatrix} \cos\left(\dfrac{\omega^* t}{2}\right) \\ -i\sin\left(\dfrac{\omega^* t}{2}\right) \end{pmatrix} e^{i\frac{\pi}{a}x} e^{-i\omega_0 t + i\omega^* t/2}, \tag{6}$$

where ω^* is angular frequency of leapfrogging motion. For the 1D σ_z-knot-crystal, the coordinate on winding space is $\Phi(x) = \frac{\pi}{a}x$. Another example is 3D SOC knot-crystal [10], of which the function is given by

$$\begin{aligned} \mathbf{Z}_{\mathrm{KC}}\left(\vec{x},t\right) = \begin{pmatrix} z_{\mathrm{KC,A}}\left(\vec{x},t\right) \\ z_{\mathrm{KC,B}}\left(\vec{x},t\right) \end{pmatrix} = r_0 \begin{pmatrix} \cos\left(\dfrac{\omega^* t}{2}\right) \\ -i\sin\left(\dfrac{\omega^* t}{2}\right) \end{pmatrix} e^{-i\omega_0 t + i\omega^* t/2} \\ \cdot\sqrt{2}r_0 \cos\left(\Phi_x(x)\right) \cdot \left(\frac{1}{\sqrt{2}} r_0 \left(e^{i\Phi_y(y)} + ie^{-i\Phi_y(y)}\right)\right) e^{i\Phi_z(z)}, \end{aligned} \tag{7}$$

where the coordinates on winding space are $\Phi_x(x) = \frac{\pi}{a}x$, $\Phi_y(y) = \frac{\pi}{a}y$, $\Phi_z(z) = \frac{\pi}{a}z$, respectively.

In addition, there exists generalized spatial translation symmetry on winding space. On winding space, the translation operation $\mathcal{T}\left(\Delta\Phi^I\right)$ becomes

$$\mathcal{T}\left(\Delta\Phi^I\right) = e^{i\cdot\sum_i \Delta\Phi^I \cdot \tilde{\Gamma}^I_{\text{knot-crystal}}} \tag{8}$$

where $\Delta\Phi^I$ denotes the distance on winding space.

2.3. Zero-lattice

Before introduce zero-lattice, we firstly review the projection between two entangled vortex-membranes $z_{A/B}\left(\vec{x},t\right)=\xi_{A/B}\left(\vec{x},t\right)+i\eta_{A/B}\left(\vec{x},t\right)$ along a given direction θ in 5D space by

$$\widehat{P}_{\theta}\begin{pmatrix}\xi_{A/B}\left(\vec{x},t\right)\\ \eta_{A/B}\left(\vec{x},t\right)\end{pmatrix}=\begin{pmatrix}\xi_{A/B,\theta}\left(\vec{x},t\right)\\ \left[\eta_{A/B,\theta}\left(\vec{x},t\right)\right]_{0}\end{pmatrix}\tag{9}$$

where $\xi_{A/B,\theta}\left(\vec{x},t\right)=\xi_{A/B}\left(\vec{x},t\right)\cos\theta+\eta_{A/B}\left(\vec{x},t\right)\sin\theta$ is variable and $\left[\eta_{A/B,\theta}\left(\vec{x},t\right)\right]_{0}=\xi_{A/B}\left(\vec{x},t\right)\sin\theta-\eta_{A/B}\left(\vec{x},t\right)\cos\theta$ is constant. So the projected vortex-membrane is described by the function $\xi_{A/B,\theta}\left(\vec{x},t\right)$. For two projected vortex-membranes described by $\xi_{A,\theta}\left(\vec{x},t\right)$ and $\xi_{B,\theta}\left(\vec{x},t\right)$, a zero is solution of the equation

$$\widehat{P}_{\theta}\left[z_{A}\left(\vec{x},t\right)\right]\equiv\xi_{A,\theta}\left(\vec{x},t\right)=\widehat{P}_{\theta}\left[z_{B}\left(\vec{x},t\right)\right]\equiv\xi_{B,\theta}\left(\vec{x},t\right).\tag{10}$$

After projection, the knot-crystal becomes a zero lattice. For example, a 1D leapfrogging knot-crystal is described by

$$\mathbf{Z}_{KC}\left(\vec{x},t\right)=r_{0}\begin{pmatrix}\cos\left(\dfrac{\omega^{*}t}{2}\right)\\ -i\sin\left(\dfrac{\omega^{*}t}{2}\right)\end{pmatrix}e^{i\frac{\pi}{a}x}e^{-i\omega_{0}t+i\omega^{*}t/2}.\tag{11}$$

According to the knot-equation $\widehat{P}_{\theta}[z_{KC,A}(x)]=\widehat{P}_{\theta}[z_{KC,B}(x)]$, we have

$$\overline{x}_{0}=a\cdot X+\frac{a}{\pi}\omega_{0}t\tag{12}$$

where $\theta=-\frac{\pi}{2}$ and $\overline{x}_{0}$ is the position of zero. As a result, we have a periodic distribution of zeroes (knots).

For a 3D leapfrogging SOC knot-crystal described by $\mathbf{Z}_{KC}\left(\vec{x},t\right)=\begin{pmatrix}z_{KC,A}\left(\vec{x},t\right)\\ z_{KC,B}\left(\vec{x},t\right)\end{pmatrix}$, we have similar situation—the solution of zeroes does not change when the tensor order changes, i.e., $\left\langle\sigma\otimes\vec{1}\right\rangle=\vec{n}_{\sigma}=(0,0,1)\rightarrow\vec{n}_{\sigma}=\left(n_{x},n_{y},n_{x}\right)$ with $\left|\vec{n}_{\sigma}\right|=1$ [13]. We call the periodic distribution of zeroes to be *zero-lattice*. See the illustration of a 1D zero-lattice in **Figure 1(b)** and 3D zero-lattice in **Figure 1(c)**.

Along a given direction $\vec{e}$, after shifting the distance a, the phase angle of vortex-membranes in knot-crystal changes π, i.e.,

$$\vec{\Phi}\left(\vec{x},t\right)\rightarrow\vec{\Phi}\left(\vec{x}+a\cdot\vec{e},t\right)=\vec{\Phi}\left(\vec{x},t\right)+\pi. \tag{13}$$

Thus, on the winding space, we have a corresponding "zero-lattice" of discrete lattice sites described by the three integer numbers

$$\vec{X}=(X,Y,Z)=\frac{1}{\pi}\vec{\Phi}-\frac{1}{\pi}\vec{\Phi}\ \mathrm{mod}\ \pi. \tag{14}$$

See the illustration of a 1D zero-lattice in **Figure 1(b)** and 3D zero-lattice in **Figure 1(d)**.

3. Dirac model for knot on zero-lattice

3.1. Dirac model on geometric space

3.1.1. Dirac model in sublattice-representation on geometric space

It was known that in emergent quantum mechanics, a 3D SOC knot-crystal becomes multi-knot system, of which the effective theory becomes a Dirac model in quantum field theory. In emergent quantum mechanics, the Hamiltonian for a 3D SOC knot-crystal has two terms—the kinetic term from global winding and the mass term from leapfrogging motion. Based on a representation of projected state, a 3D SOC knot-crystal is reduced into a "two-sublattice" model with discrete spatial translation symmetry, of which the knot states are described by $|\mathrm{L}\rangle$ and $|\mathrm{R}\rangle$ (or the Wannier states $c_{\mathrm{L},i}^{\dagger}|\mathrm{vacuum}\rangle$ and $c_{\mathrm{R},j}^{\dagger}|\mathrm{vacuum}\rangle$). We call it the Dirac model in *sublattice-representation*.

In sublattice-representation on geometric space, the equation of motion of knots is determined by the Schrödinger equation with the Hamiltonian

$$\begin{aligned}\mathcal{H}_{\mathrm{knot}}&=\int\left(\psi^{\dagger}\widehat{\mathrm{H}}_{\mathrm{knot}}\psi\right)d^{3}x,\\ \widehat{\mathrm{H}}_{\mathrm{knot}}&=-c_{\mathrm{eff}}\vec{\Gamma}\cdot\vec{p}_{\mathrm{knot}}+m_{\mathrm{knot}}c_{\mathrm{eff}}^{2}\Gamma^{5},\end{aligned} \tag{15}$$

where $\psi^{\dagger}\left(t,\vec{x}\right)$ is an four-component fermion field as $\psi^{\dagger}\left(t,\vec{x}\right)=\left(\psi_{\uparrow L}^{\dagger}\left(t,\vec{x}\right)\ \psi_{\uparrow R}^{\dagger}\left(t,\vec{x}\right)\ \psi_{\downarrow L}^{\dagger}\left(t,\vec{x}\right)\ \psi_{\downarrow R}^{\dagger}\left(t,\vec{x}\right)\right)$. Here, L,R label two chiral-degrees of freedom that denote the two possible sub-lattices, $\uparrow,\downarrow$ label two spin degrees of freedom that denote the two possible winding directions. We have

$$\Gamma^{5}=\vec{1}\otimes\iota_{x}, \tag{16}$$

and

$$\begin{aligned}\Gamma^{1}&=\sigma^{x}\otimes\iota_{y},\\ \Gamma^{2}&=\sigma^{y}\otimes\iota_{y},\\ \Gamma^{3}&=\sigma^{z}\otimes\iota_{y}.\end{aligned} \tag{17}$$

$\vec{p}_{\mathrm{knot}} = \hbar_{\mathrm{knot}}\vec{k}$ is the momentum operator. $m_{\mathrm{knot}}c_{\mathrm{eff}}^2 = 2\hbar_{\mathrm{knot}}\omega^*$ plays role of the mass of knots and $c_{\mathrm{eff}} = \frac{a \cdot J}{\hbar_{\mathrm{knot}}} = 2a\omega_0$ play the role of light speed where a is a fixed length that denotes the half pitch of the windings on the knot-crystal.

In addition, the low energy effective Lagrangian of knots on 3D SOC knot-crystal is obtained as

$$\mathcal{L}_{3\mathrm{D}} = \overline{\psi}\left(i\gamma^{\mu}\widehat{\partial}_{\mu} - m_{\mathrm{knot}}\right)\psi \tag{18}$$

where $\overline{\psi} = \psi^{\dagger}\gamma^0$, γ^{μ} are the reduced Gamma matrices,

$$\gamma^1 = \gamma^0\Gamma^1, \gamma^2 = \gamma^0\Gamma^2, \gamma^3 = \gamma^0\Gamma^3, \tag{19}$$

and

$$\gamma^0 = \Gamma^5, \gamma^5 = i\gamma^0\gamma^1\gamma^2\gamma^3. \tag{20}$$

3.1.2. Dirac model in vortex-representation on geometric space

In this paper, we derive the effective Dirac model for a knot-crystal based on a representation of vortex degrees of freedom. We call it *vortex-representation*.

In Ref. [13], it was known that a knot has four degrees of freedom, two spin degrees of freedom ↑ or ↓ from the helicity degrees of freedom, the other two vortex degrees of freedom from the vortex degrees of freedom that characterize the vortex-membranes, A or B. The basis to define the microscopic structure of a knot is given by $|\uparrow, \mathrm{A}\rangle$, $|\uparrow, \mathrm{B}\rangle$, $|\downarrow, \mathrm{A}\rangle$, $|\downarrow, \mathrm{B}\rangle$.

We define operator of knot states by the region of the phase angle of a knot: for the case of $\phi_0 \operatorname{mod}(2\pi) \in (-\pi, 0]$, we have $c^{\dagger}|0\rangle$; for the case of $\phi_0 \operatorname{mod}(2\pi) \in (0, \pi]$, we have $\left(c^{\dagger}|0\rangle\right)^{\dagger}$. As shown in **Figure 2**, we label the knots by Wannier state $|i, \mathrm{A}, \uparrow\rangle$, $|i+1, \mathrm{A}, \uparrow\rangle^*$, $|i+2, \mathrm{A}, \uparrow\rangle$, $|i+3, \mathrm{A}, \uparrow\rangle^* \ldots$.

To characterize the energy cost from global winding, we use an effective Hamiltonian to describe the coupling between two-knot states along x^I-direction on 3D SOC knot-crystal

$$Jc^{\dagger}_{\mathrm{A/B}i}T^I_{\mathrm{A/B,\,A/B}}c_{\mathrm{A/B},\,i+e^I} \tag{21}$$

with the annihilation operator of knots at the site i, $c_{\mathrm{A/B},\,i} = \begin{pmatrix} c_{\mathrm{A/B},\uparrow,i} \\ c_{\mathrm{A/B},\downarrow,i} \end{pmatrix}$. J is the coupling constant between two nearest-neighbor knots. According to the generalized translation symmetry, the transfer matrices $T^I_{\mathrm{A/B,\,A/B}}$ along x^I-direction are defined by

$$T^I_{\mathrm{A,A}} = T^I_{\mathrm{B,B}} = e^{ia\left(\widehat{k}^I \cdot \sigma^I\right)} \tag{22}$$

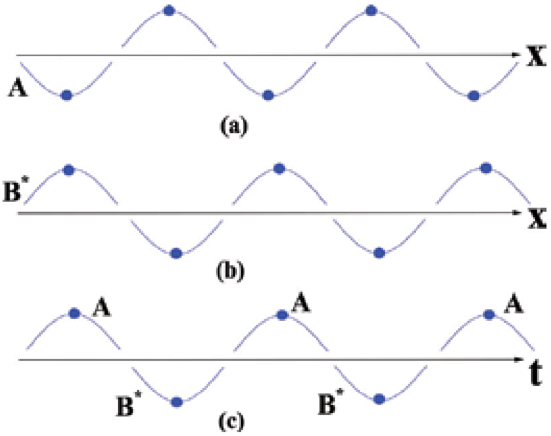

Figure 2. An illustration of knot states in vortex-representation: A and B denote two 1D vortex-lines. Here B* denotes conjugate representation of vortex-line-B. The curves with blue dots denote knots on the knot-crystal—the curves with blue dot above the line are denoted by $c_i^\dagger|0\rangle$ and the curves with blue dot below the line are denoted by $\left(c_i^\dagger|0\rangle\right)^\dagger$.

and

$$T^I_{\mathrm{A,B}} = T^I_{\mathrm{B,A}} = 0. \tag{23}$$

After considering the spin rotation symmetry and the symmetry of vortex-membrane-A and vortex-membrane-B, the effective Hamiltonian from global winding energy can be described by a familiar formulation

$$\mathcal{H}_{\text{coupling}} = \widehat{\mathcal{H}}_{\text{coupling, B}} + \widehat{\mathcal{H}}_{\text{coupling, A}} \tag{24}$$

where

$$\widehat{\mathcal{H}}_{\text{coupling, A}} = J\sum_{i,I} c^\dagger_{\mathrm{A},i} e^{ia\left(\widehat{k}^I \cdot \sigma^I\right)} c_{\mathrm{A},i+e^I} + h.c. \tag{25}$$

and

$$\widehat{\mathcal{H}}_{\text{coupling, B}} = J\sum_{i,I} c^\dagger_{\mathrm{B},i} e^{ia\left(\widehat{k}^I \cdot \sigma^I\right)} c_{\mathrm{B},i+e^I} + h.c. \tag{26}$$

We then use path-integral formulation to characterize the effective Hamiltonian for a knot-crystal as

$$\int \mathcal{D}\psi^\dagger\left(t, \vec{x}\right)\mathcal{D}\psi(t) e^{i\mathcal{S}/\hbar} \tag{27}$$

where $\mathcal{S} = \int \mathcal{L}dt$ and $\mathcal{L} = i\sum_i \psi_i^\dagger \partial_t \psi_i - \mathcal{H}_{\text{coupling}}$. To describe the knot states on 3D knot-crystal, we have introduced a four-component fermion field to be

$$\psi(\mathbf{x}) = \begin{pmatrix} \psi_{\mathrm{A},\uparrow}\left(t, \vec{x}\right) \\ \psi_{\mathrm{B},\uparrow}\left(t, \vec{x}\right) \\ \psi_{\mathrm{A},\downarrow}\left(t, \vec{x}\right) \\ \psi_{\mathrm{B},\downarrow}\left(t, \vec{x}\right) \end{pmatrix} \tag{28}$$

where A, B label vortex degrees of freedom and ↑, ↓ label two spin degrees of freedom that denote the two possible winding directions along a given direction $\vec{e}$.

In continuum limit, we have

$$\begin{aligned} \mathcal{H}_{\text{coupling}} &= \widehat{\mathcal{H}}_{\text{coupling, B}} + \widehat{\mathcal{H}}_{\text{coupling, A}} \\ &= 2aJ \sum_{k} \psi^{\dagger}_{\mathrm{A},k} \left[\sigma_x \cos k_x + \sigma_y \cos k_y + \sigma_z \cos k_z\right] \psi_{\mathrm{A},k} \\ &+ 2aJ \sum_{k} \psi^{\dagger}_{\mathrm{B},k} \left[\sigma_x \cos k_x + \sigma_y \cos k_y + \sigma_z \cos k_z\right] \psi_{\mathrm{B},k} \end{aligned} \tag{29}$$

where the dispersion of knots is

$$E_{\mathrm{A/B},k} \simeq c_{\text{eff}} \left[\left(\vec{k} - \vec{k}_0\right) \cdot \vec{\sigma}\right], \tag{30}$$

where $\vec{k}_0 = \left(\frac{\pi}{2}, \frac{\pi}{2}, \frac{\pi}{2}\right)$ and $c_{\text{eff}} = 2aJ$ is the velocity. In the following part we ignore $\vec{k}_0$.

Next, we consider the mass term from leapfrogging motion, of which the angular frequency ω^*. For leapfrogging motion obtained by [10], the function of the two entangled vortex-membranes at a given point in geometric space is simplified by

$$\begin{pmatrix} z_{\mathrm{A}}\left(\vec{x} = 0, t\right) \\ z_{\mathrm{B}}\left(\vec{x} = 0, t\right) \end{pmatrix} = \frac{r_0}{2} \begin{pmatrix} 1 + e^{i\omega^* t} \\ 1 - e^{i\omega^* t} \end{pmatrix}. \tag{31}$$

At $t = 0$, we have $\begin{pmatrix} z_{\mathrm{A}}\left(\vec{x}, t\right) \\ z_{\mathrm{B}}\left(\vec{x}, t\right) \end{pmatrix} = \begin{pmatrix} 1 \\ 0 \end{pmatrix}$; at $t = \frac{\pi}{\omega^*}$, we have $\begin{pmatrix} z_{\mathrm{A}}\left(\vec{x}, t\right) \\ z_{\mathrm{B}}\left(\vec{x}, t\right) \end{pmatrix} = \begin{pmatrix} 0 \\ 1 \end{pmatrix}$. The leapfrogging knot-crystal leads to periodic varied knot states, i.e., at $t = 0$ we have a knot on vortex-membrane-A that is denoted by $|\sigma, \mathrm{A}\rangle$; at $t = \frac{\pi}{\omega^*}$ we have a knot on vortex-membrane-B denoted by $|\sigma, \mathrm{B}\rangle$. As a result, the leapfrogging motion becomes a global winding along time direction, $|t, \mathrm{A}\rangle$, $\left|t + \frac{\pi}{\omega^*}, \mathrm{B}\right\rangle$, $\left|t + \frac{2\pi}{\omega^*}, \mathrm{A}\right\rangle$, $\left|t + \frac{3\pi}{\omega^*}, \mathrm{B}\right\rangle$, … See the illustration of vortex-representation of knot states for knot-crystal in **Figure 2(c)**. After a time period $t = \frac{\pi}{\omega^*}$, a knot state $\phi_{\mathrm{A}} \mathrm{mod}(2\pi) \in (-\pi, 0]$ turns into a knot state $\phi_{\mathrm{B}} \mathrm{mod}(2\pi) \in (-\pi, 0]$. Thus, we use the following formulation to characterize the leapfrogging process,

$$\psi_{\mathrm{A}}^{\dagger}\psi_{\mathrm{B}}^{\dagger}. \tag{32}$$

After considering the energy from the leapfrogging process, a corresponding term is given by

$$2\hbar_{\mathrm{knot}}\omega^{*}\psi_{\mathrm{A}}^{\dagger}\psi_{\mathrm{B}}^{\dagger}+h.c. \tag{33}$$

From the global rotating motion denoted $e^{-i\omega_0 t}$, the winding states also change periodically. Because the contribution from global rotating motion $e^{-i\omega_0 t}$ is always canceled by shifting the chemical potential, we do not consider its effect.

From above equation, in the limit $\left|\vec{k}\right| \rightarrow 0$ we derive low energy effective Hamiltonian as

$$\begin{aligned}\mathcal{H}_{\mathrm{3D}} \simeq 2aJ\sum_{k}\psi_{\mathrm{A},k}^{\dagger}\left(\vec{\sigma}\cdot\vec{k}\right)\psi_{\mathrm{A},k}\\ +2aJ\sum_{k}\psi_{\mathrm{B},k}^{\dagger}\left(\vec{\sigma}\cdot\vec{k}\right)\psi_{\mathrm{B},k}\\ +2\hbar_{\mathrm{knot}}\omega^{*}\textstyle\sum_{k,\sigma}\psi_{\mathrm{A},\sigma,k}^{\dagger}\psi_{\mathrm{B},\sigma,k}^{\dagger}\end{aligned} \tag{34}$$

$$\begin{aligned}= c_{\mathrm{eff}}\int\Psi^{\dagger}\left[\mathcal{T}_{z}\otimes\left(\vec{\sigma}\cdot\hat{k}\right)\right]\Psi d^{3}x\\ +m_{\mathrm{knot}}c_{\mathrm{eff}}^{2}\int\Psi^{\dagger}\left(\tau_{x}\otimes\vec{1}\right)\Psi d^{3}x.\end{aligned} \tag{35}$$

where

$$\Psi(\mathbf{x})=\begin{pmatrix}\psi_{\mathrm{A},\uparrow}\left(t,\vec{x}\right)\\ \psi_{\mathrm{B},\uparrow}^{*}\left(t,\vec{x}\right)\\ \psi_{\mathrm{A},\downarrow}\left(t,\vec{x}\right)\\ \psi_{\mathrm{B},\downarrow}^{*}\left(t,\vec{x}\right)\end{pmatrix}. \tag{36}$$

We then re-write the effective Hamiltonian to be

$$\mathcal{H}_{\mathrm{3D}}=\int\left(\Psi^{\dagger}\hat{H}_{\mathrm{3D}}\Psi\right)d^{3}x \tag{37}$$

and

$$\hat{H}_{\mathrm{3D}}=c_{\mathrm{eff}}\,\vec{\Gamma}\cdot\vec{p}_{\mathrm{knot}}+m_{\mathrm{knot}}c_{\mathrm{eff}}^{2}\Gamma^{5} \tag{38}$$

where

$$\begin{aligned}\Gamma^{5}=\tau^{x}\otimes\vec{1},\Gamma^{1}=\tau^{z}\otimes\sigma^{x},\\ \Gamma^{2}=\tau^{z}\otimes\sigma^{y},\Gamma^{3}=\tau^{z}\otimes\sigma^{z}.\end{aligned} \tag{39}$$

$\overrightarrow{p} = \hbar_{\text{knot}} \overrightarrow{k}$ is the momentum operator. $\Psi^{\dagger} = \left(\psi^{*}_{\text{A},\uparrow}, \psi_{\text{B},\uparrow}, \psi^{*}_{\text{A},\downarrow}, \psi_{\text{B},\downarrow}\right)$ is the annihilation operator of four-component fermions. $m_{\text{knot}} c^{2}_{\text{eff}} = 2\hbar_{\text{knot}} \omega^{*}$ plays role of the mass of knots and $c_{\text{eff}} = \frac{2a \cdot J}{\hbar_{\text{knot}}}$ play the role of light speed where a is a fixed length that denotes the half pitch of the windings on the knot-crystal. In the following parts, we set $\hbar_{\text{knot}} = 1$ and $c_{\text{eff}} = 1$.

Due to Lorentz invariance (see below discussion), the geometric space becomes geometric space-time, i.e., $(x, y, z) \to (x, y, z, t)$. Here, we may consider $\overrightarrow{\Gamma}$ and Γ^{5} to be *entanglement matrices* along spatial and tempo direction in winding space-time, respectively. A complete set of entanglement matrices $\left(\overrightarrow{\Gamma}, \Gamma^{5}\right)$ is called *entanglement pattern*. The coordinate transformation along $x/y/z/t$-direction is characterize by $e^{i\overrightarrow{\Gamma} \cdot \widehat{k}} \cdot \overrightarrow{x}$ and $e^{i\Gamma^{5} \cdot \widehat{\omega}} t$, respectively. Now, the knot becomes topological defect of 3 + 1D entanglement—a knot is not only anti-phase changing along arbitrary spatial direction $\overrightarrow{e}$ but also becomes anti-phase changing along tempo direction (along tempo direction, a knot switches a knot state $|\text{A/B}\rangle$ to another knot state $|\text{B/A}\rangle$).

Finally, the low energy effective Lagrangian of 3D SOC knot-crystal is obtained as

$$\begin{aligned} \mathcal{L}_{3\text{D}} &= i\Psi^{\dagger}\partial_{t}\Psi - \mathcal{H}_{3\text{D}} \\ &= \overline{\Psi}\left(i\gamma^{\mu}\widehat{\partial}_{\mu} - m_{\text{knot}}\right)\Psi \end{aligned} \tag{40}$$

where $\overline{\Psi} = \Psi^{\dagger}\gamma^{0}$, γ^{μ} are the reduced Gamma matrices,

$$\gamma^{1} = \gamma^{0}\Gamma^{1}, \gamma^{2} = \gamma^{0}\Gamma^{2}, \gamma^{3} = \gamma^{0}\Gamma^{3}, \tag{41}$$

and

$$\gamma^{0} = \Gamma^{5} = \tau_{x} \otimes 1, \gamma^{5} = \overrightarrow{i\gamma}^{0}\gamma^{1}\gamma^{2}\gamma^{3}. \tag{42}$$

In addition, we point out that there exists intrinsic relationship between the knot states of sublattice-representation and the knot states of vortex-representation

$$\begin{pmatrix} |\text{A}\rangle \\ |\text{B}\rangle \end{pmatrix} = \mathcal{U}\begin{pmatrix} |\text{L}\rangle \\ |\text{R}\rangle \end{pmatrix} \tag{43}$$

where $\mathcal{U} = \exp\left[i\pi\begin{pmatrix} 0 & -i \\ i & 0 \end{pmatrix}\right]$. From the sublattice-representation of knot states, the knot-crystal becomes an object with staggered R/L zeroes along $x/y/z$ spatial directions and time direction; From the vortex-representation of knot states, the knot-crystal becomes an object with global winding along $x/y/z$ spatial directions and time direction. See the illustration of knot states of vortex-representation on a knot-crystal in **Figure 2**.

3.1.3. Emergent Lorentz-invariance

We discuss the emergent Lorentz-invariance for knot states on a knot-crystal.

Since the Fermi-velocity c_{eff} only depends on the microscopic parameter J and a, we may regard c_{eff} to be "light-velocity" and the invariance of light-velocity becomes an fundamental principle for the knot physics. The Lagrangian for massive Dirac fermions indicates emergent SO(3,1) Lorentz-invariance. The SO(3,1) Lorentz transformations S_{Lor} is defined by

$$S_{\text{Lor}}\gamma^{\mu}S_{\text{Lor}}^{-1} = \gamma'^{\mu} \tag{44}$$

$(\mu = 0, 1, 2, 3)$ and

$$S_{\text{Lor}}\gamma^{5}S_{\text{Lor}}^{-1} = \gamma^{5}. \tag{45}$$

For a knot state with a global velocity $\vec{v}$, due to SO(3,1) Lorentz-invariance, we can do Lorentz boosting on $\left(\vec{x}, t\right)$ by considering the velocity of a knot,

$$\begin{aligned} t \to t' &= \frac{t - \vec{x} \cdot \vec{v}}{\sqrt{1 - \vec{v}^{2}}}, \\ \vec{x} \to \vec{x}' &= \frac{\vec{x} - \vec{v} \cdot t}{\sqrt{1 - \vec{v}^{2}}}. \end{aligned} \tag{46}$$

We can do non-uniform Lorentz transformation $S_{\text{Lor}}\left(\vec{x}, t\right)$ on knot states $\Psi\left(\vec{x}, t\right)$. The *inertial reference-frame* for quantum states of the knot is defined under Lorentz boost, i.e.,

$$\Psi\left(\vec{x}, t\right) \to \Psi'\left(\vec{x}', t'\right) = S_{\text{Lor}} \cdot \Psi\left(\vec{x}', t'\right). \tag{47}$$

For a particle-like knot, a uniform wave-function of knot states $\psi(t)$ is

$$\psi(t) = \frac{1}{\sqrt{V}}e^{-i2\omega^{*}t}. \tag{48}$$

Under Lorentz transformation with small velocity $\left|\vec{v}\right|$, this wave-function $\psi(t)$ is transformed into

$$\begin{aligned} \psi(t) &= \frac{1}{\sqrt{V}}e^{-i2\omega^{*}t} \\ &\to \psi' = \frac{1}{\sqrt{V}}e^{-i2\omega^{*}t'} \\ &\simeq \frac{1}{\sqrt{V}}e^{-i2\omega^{*}t}\exp\left(-i\left(E_{\text{knot}}t - \vec{p}_{\text{knot}} \cdot \vec{x}\right)\right) \end{aligned} \tag{49}$$

where $E_{\mathrm{knot}} \simeq \frac{\vec{p}^{\,2}_{\mathrm{knot}}}{2m_{\mathrm{knot}}}$, $\vec{p}_{\mathrm{knot}} \simeq \omega\, \vec{v}$ and $m_{\mathrm{knot}}c^2 = 2\omega^*$. As a result, we derive a new distribution of knot-pieces by doing Lorentz transformation, that are described by the plane-wave wave-function $\frac{1}{\sqrt{V}} e^{-i2\omega^* t} \exp\left(-i\left(E_{\mathrm{knot}} t - \vec{p}_{\mathrm{knot}} \cdot \vec{x}\right)\right)$. The new wave-function $\frac{1}{\sqrt{V}} \exp(-i(E_{\mathrm{knot}} t - \vec{p}_{\mathrm{knot}} \cdot \vec{x}))$ comes from the Lorentz boosting S_{Lor}.

Noninertial system can be obtained by considering non-uniformly velocities, i.e., $\vec{v} \to \Delta \vec{v}\left(\vec{x}, t\right)$. According to the linear dispersion for knots, we can do local Lorentz transformation on $\left(\vec{x}, t\right)$ i.e.,

$$\begin{aligned} t \to t'\left(\vec{x}, t\right) &= \frac{t - \vec{x} \cdot \Delta \vec{v}}{\sqrt{1 - \left(\Delta \vec{v}\right)^2}}, \\ \vec{x} \to \vec{x}'\left(\vec{x}, t\right) &= \frac{\vec{x} - \Delta \vec{v} \cdot t}{\sqrt{1 - \left(\Delta \vec{v}\right)^2}}. \end{aligned} \tag{50}$$

We can also do non-uniform Lorentz transformation $S_{\mathrm{Lor}}\left(\vec{x}, t\right)$ on knot states $\Psi\left(\vec{x}, t\right)$, i.e.,

$$\begin{aligned} \Psi\left(\vec{x}, t\right) &\to \Psi'\left(\vec{x}'\left(\vec{x}, t\right), t'\left(\vec{x}, t\right)\right) \\ &= S_{\mathrm{Lor}}\left(\vec{x}, t\right) \cdot \Psi\left(\vec{x}, t\right) \end{aligned} \tag{51}$$

where the new wave-functions of all quantum states change following the non-uniform Lorentz transformation $S_{\mathrm{Lor}}\left(\vec{x}, t\right)$. It is obvious that there exists intrinsic relationship between noninertial system and curved space-time.

3.2. Dirac model on winding space

In this part, we show the effective Dirac model of knot states on winding space.

The coordinate measurement of zero-lattice on winding space is the winding angles, $\vec{\Phi}$. Along a given direction $\vec{e}$, after shifting the distance a, the winding angle changes π. The position is determined by two kinds of values: $\vec{X}$ are integer numbers

$$\vec{X} = (X, Y, Z) = \frac{1}{\pi} \vec{\Phi} - \frac{1}{\pi} \vec{\Phi} \bmod \pi \tag{52}$$

and $\vec{\phi}$ denote internal winding angles

$$\vec{\phi} = \left(\phi_x, \phi_y, \phi_z\right) = \vec{\Phi} \bmod \pi \tag{53}$$

with $\phi_x, \phi_y, \phi_z \in (0, \pi]$.

Therefore, on winding space, the effective Hamiltonian turns into

$$\widehat{H}_{3\mathrm{D}} = \vec{\Gamma} \cdot \vec{p}_{\mathrm{knot}} + m_{\mathrm{knot}}\Gamma^5 = \vec{\Gamma} \cdot \vec{p}_{X,\,\mathrm{knot}} + \vec{\Gamma} \cdot \vec{p}_{\phi,\,\mathrm{knot}} + m_{\mathrm{knot}}\Gamma^5 \tag{54}$$

where $\vec{p}_X = \frac{1}{a} i \frac{d}{d\vec{X}}$ and $\vec{p}_\phi = \frac{1}{a} i \frac{d}{d\vec{\phi}}$. Because of $\phi_j \in (0, \pi]$, quantum number of $\vec{p}_\phi$ is angular momentum $\vec{L}_\phi$ and the energy spectra are $\frac{1}{a}\left|\vec{L}_\phi\right|$. If we focus on the low energy physics $E \ll \frac{1}{a}$ (or $\vec{L}_\phi = 0$), we may get the low energy effective Hamiltonian as

$$\widehat{H}_{3\mathrm{D}} \simeq \vec{\Gamma} \cdot \vec{p}_{X,\,\mathrm{knot}} + m_{\mathrm{knot}}\Gamma^5. \tag{55}$$

We introduce *3 + 1D winding space-time* by defining four coordinates on winding space, $\Phi = \left(\vec{\Phi}, \Phi_t\right)$ where Φ_t is phase changing under time evolution. For a fixed entanglement pattern $\left(\vec{\Gamma}, \Gamma^5\right)$, the coordinate transformation along $x/y/z/t$-direction on winding space-time is given by $e^{i\vec{\Gamma}\cdot\widehat{\Phi}}$ and $e_t^{i\Gamma^5\cdot\widehat{\Phi}}$, respectively.

For low energy physics, the position in 3 + 1D winding space-time is 3 + 1D zero-lattice of winding space-time labeled by four integer numbers, $\mathbf{X} = \left(\vec{X}, X_0\right)$ where

$$\begin{aligned} \vec{X} &= \frac{1}{\pi}\vec{\Phi} - \frac{1}{\pi}\vec{\Phi} \bmod \pi, \\ X_0 &= \frac{1}{\pi}\Phi_t - \frac{1}{\pi}\Phi_t \bmod \pi. \end{aligned} \tag{56}$$

The lattice constant of the winding space-time is always π that will never be changed. As a result, the winding space-time becomes an effective *quantized* space-time. Because of $x_\mu = a \cdot X_\mu$, the effective action on 3 + 1D winding space-time becomes

$$\mathcal{S}_{3\mathrm{D}} \simeq (a)^4 \sum_{X,\,Y,\,Z,\,X_0} \mathcal{L}_{3\mathrm{D}} \tag{57}$$

where

$$\mathcal{L}_{3\mathrm{D}} = \overline{\Psi}\left[i\frac{1}{a}(\gamma^\mu)\widehat{\partial}_\mu - m_{\mathrm{knot}}\right]\Psi. \tag{58}$$

4. Deformed zero-lattice as curved space-time

In this section, we discuss the knot dynamics on smoothly deformed knot-crystal (or deformed zero-lattice). We point out that to characterize the entanglement evolution, the corresponding Biot-Savart mechanics for a knot on smoothly deformed zero-lattice is mapped to that in quantum mechanics on a curved space-time.

4.1. Entanglement transformation

Firstly, based on a uniform 3D knot-crystal (uniform entangled vortex-membranes), we introduce the concept of "*entanglement transformation* (*ET*)".

Under global entanglement transformation, we have

$$\Psi\left(\vec{x},t\right) \to \Psi'\left(\vec{x},t\right) = \widehat{U}_{\mathrm{ET}}\left(\vec{x},t\right) \cdot \Psi\left(\vec{x},t\right) \tag{59}$$

where

$$\widehat{U}_{\mathrm{ET}}\left(\vec{x},t\right) = e^{i\delta\vec{\Phi}\cdot\vec{\Gamma}} \cdot e^{i\delta\Phi_t\cdot\Gamma^5}. \tag{60}$$

Here, $\delta\vec{\Phi}$ and $\delta\Phi_t$ are constant winding angles along spatial $\vec{\Phi}$-direction and that along tempo direction on geometric space-time, respectively. The dispersion of the excitation changes under global entanglement transformation.

In general, we may define (local) entanglement transformation, i.e.,

$$\widehat{U}_{\mathrm{ET}}\left(\vec{x},t\right) = e^{i\delta\vec{\Phi}\left(\vec{x}.t\right)\cdot\vec{\Gamma}} \cdot e^{i\delta\Phi_t\left(\vec{x}.t\right)\cdot\Gamma^5} \tag{61}$$

where $\delta\vec{\Phi}\left(\vec{x},t\right)$ and $\delta\Phi_t\left(\vec{x},t\right)$ are not constant. We call a system with smoothly varied-($\delta\vec{\Phi}\left(\vec{x},t\right)$, $\delta\Phi_t\left(\vec{x},t\right)$) *deformed knot-crystal* and its projected zero-lattice *deformed (3 + 1D) zero-lattice*.

4.2. Geometric description for deformed zero-lattice: curved space-time

For knots on a deformed zero-lattice, there exists an intrinsic correspondence between an entanglement transformation $\widehat{U}_{\mathrm{ET}}\left(\vec{x},t\right)$ and a local coordinate transformation that becomes a fundamental principle for emergent gravity theory in knot physics.

For zero-lattice, $\widehat{U}_{\mathrm{ET}}\left(\vec{x},t\right)$ changes the winding degrees of freedom that is denoted by the local coordination transformation, i.e.,

$$\begin{aligned} \vec{\Phi}\left(\vec{x},t\right) &\Rightarrow \vec{\Phi}'\left(\vec{x},t\right) = \vec{\Phi}\left(\vec{x},t\right) + \delta\vec{\Phi}\left(\vec{x},t\right), \\ \Phi_t\left(\vec{x},t\right) &\Rightarrow \Phi_t'\left(\vec{x},t\right) = \Phi_t\left(\vec{x},t\right) + \delta\Phi_t\left(\vec{x},t\right). \end{aligned} \tag{62}$$

These equations also imply a curved space-time: the lattice constants of the 3 + 1D zero-lattice (the size of a lattice constant with 2π angle changing) are not fixed to be $2a$, i.e.,

$$2a \to 2a_{\mathrm{eff}}\left(\vec{x},t\right) \tag{63}$$

The distance between two nearest-neighbor "lattice sites" on the spatial/tempo coordinate changes, i.e.,

$$\begin{aligned}\Delta \vec{x} &= \left(\vec{x} + \vec{e}_x\right) - \vec{x} = \vec{e}_x, \\ \Delta \vec{x}' &= \left(\vec{x}' + \vec{e}'_x\right) - \vec{x}' = \vec{e}'_x\left(\vec{x}, t\right)\end{aligned} \tag{64}$$

and

$$\begin{aligned}\Delta t &= (t + e_0) - t = e_0, \\ \Delta t' &= (t' + e'_0) - t' = e'_0\left(\vec{x}, t\right)\end{aligned} \tag{65}$$

where $e_a (a = 0, 1, 2, 3)$ and $e'_a\left(\vec{x}, t\right)$ are the unit-vectors of the original frame and the deformed frame, respectively. See the illustration of a 1 + 1D deformed zero-lattice on winding space-time with a non-uniform distribution of zeroes in **Figure 3(d)**.

However, for deformed zero-lattice, the information of knots in projected space is invariant: when the lattice-distance of zero-lattice changes $a \to a_{\text{eff}}\left(\vec{x}, t\right)$, the size of the knots correspondingly changes $a \to a_{\text{eff}}\left(\vec{x}, t\right)$. Therefore, due to the invariance of a knot, the deformation of zero-lattice does not change the formula of the low energy effective model for knots on

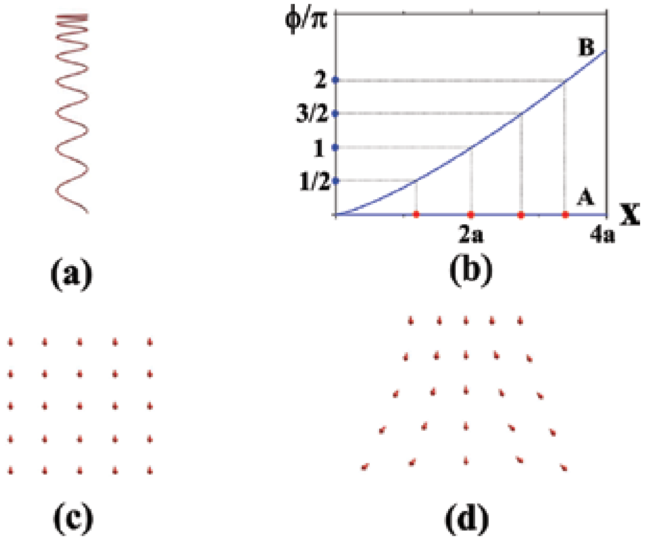

Figure 3. (a) An illustration of deformed knot-crystal; (b) an illustration of smoothly deformed relationship between winding angle Φ and spatial coordinate x. The zero-lattice in winding space is still uniform; while the zero-lattice in geometric space is deformed; (c) an illustration of a uniform 1 + 1D zero-lattice in geometric space-time; and (d) an illustration of a deformed 1 + 1D zero-lattice in geometric space-time.

winding space-time. Because one may smoothly deform the zero-lattice and get the same low energy effective model for knots on winding space-time, there exists *diffeomorphism invariance*, i.e.,

$$\begin{aligned}&\text{Knot–invariance on winding space–time}\\&\Rightarrow \text{Diffeomorphism invariance.}\end{aligned} \tag{66}$$

Therefore, from the view of mathematics, the physics on winding space-time is never changed! The invariance of the effective model for knots on winding space-time indicates the diffeomorphism invariance

$$\mathcal{S}_{\text{zero}-\text{lattice}} \equiv (a)^4 \sum_{X,\, Y,\, Z,\, X_0} \overline{\Psi}\left[i\frac{1}{a}\gamma^{\mu}\overset{X}{\underset{\mu}{\widehat{\partial}}} - m_{\text{knot}}\right]\Psi. \tag{67}$$

On the other hand, the condition of very smoothly entanglement transformation guarantees a (*local*) *Lorentz invariance* in long wave-length limit. Under local Lorentz invariance, the knot-pieces of a given knot are determined by local Lorentz transformations.

According to the local coordinate transformation, the deformed zero-lattice becomes a curved space-time for the knots. In continuum limit $\Delta k \ll (a)^{-1}$ and $\Delta\omega \ll \omega_0$, the diffeomorphism invariance and (local) Lorentz invariance emerge together. E. Witten had made a strong claim about emergent gravity, "*whatever we do, we are not going to start with a conventional theory of non-gravitational fields in Minkowski space-time and generate Einstein gravity as an emergent phenomenon.*" He pointed out that gravity could be emergent only if the notion on the space-time on which diffeomorphism invariance is simultaneously emergent. For the emergent quantum gravity in knot physics, diffeomorphism invariance and Lorentz invariance are simultaneously emergent. In particular, the diffeomorphism invariance comes from information invariance of knots on winding space-time—when the lattice-distance of zero-lattice changes, the size of the knots correspondingly changes.

To characterize the deformed 3 + 1D zero-lattice $\left(\vec{x}'\left(\vec{x},t\right), t'\left(\vec{x},t\right)\right)$, we introduce a geometric description. In addition to the existence of a set of vierbein fields e^a, the space metric is defined by $\eta_{ab}e^a_\alpha e^b_\beta = g_{\alpha\beta}$ where η is the internal space metric tensor. The geometry fields (vierbein fields $e^a\left(\vec{x},t\right)$ and spin connections $\omega^{ab}\left(\vec{x},t\right)$) are determined by the non-uniform local coordinates $\left(\vec{x}'\left(\vec{x},t\right), t'\left(\vec{x},t\right)\right)$. Furthermore, one needs to introduce spin connections $\omega^{ab}\left(\vec{x},t\right)$ and the Riemann curvature two-form as

$$\begin{aligned}R^a_b &= d\omega^a_b + \omega^a_c \wedge \omega^c_b\\&= \frac{1}{2}R^a_{b\mu\nu}dx^\mu \wedge dx^\nu,\end{aligned} \tag{68}$$

where $R^a_{b\mu\nu} \equiv e^a_\alpha e^\beta_b R^\alpha_{\beta\mu\nu}$ are the components of the usual Riemann tensor projection on the tangent space. The deformation of the zero-lattice is characterized by

$$R^{ab} = d\omega^{ab} + \omega^{ac} \wedge \omega^{cb}. \tag{69}$$

So the low energy physics for knots on the deformed zero-lattice turns into that for Dirac fermions on curved space-time

$$\mathcal{S}_{\text{curved}-\text{ST}} = \int \sqrt{-g}\,\overline{\Psi}\left(e_a^\mu \gamma^a \left(i\widehat{\partial}_\mu + i\omega_\mu\right) - m_{\text{knot}}\right)\Psi d^4x \tag{70}$$

where $\omega_\mu = \left(\omega_\mu^{0i}\gamma^{0i}/2, \omega_\mu^{ij}\gamma^{ij}/2\right)$ $(i,j = 1,2,3)$ and $\gamma^{ab} = -\frac{1}{4}\left[\gamma^a,,\gamma^b\right]$ $(a,b = 0,1,2,3)$ [15]. This model described by $\mathcal{S}_{\text{curved}-\text{ST}}$ is invariant under local (non-compact) SO(3,1) Lorentz transformation $S\left(\vec{x},t\right) = e^{\theta_{ab}\left(\vec{x},t\right)\gamma^{ab}}$ as

$$\begin{aligned}
\Psi\left(\vec{x},t\right) \to \Psi'\left(\vec{x},t\right) &= S\left(\vec{x},t\right)\Psi\left(\vec{x},t\right), \\
\gamma^\mu \to \left(\gamma^\mu\left(\vec{x},t\right)\right)' &= S\left(\vec{x},t\right)\gamma^\mu\left(S\left(\vec{x},t\right)\right)^{-1}, \\
\omega_\mu \to \omega'_\mu\left(\vec{x},t\right) &= S\left(\vec{x},t\right)\omega_\mu\left(\vec{x},t\right)\left(S\left(\vec{x},t\right)\right)^{-1} \\
&+ S\left(\vec{x},t\right)\partial_\mu\left(S\left(\vec{x},t\right)\right)^{-1}.
\end{aligned} \tag{71}$$

γ^5 is invariant under local SO(3,1) Lorentz symmetry as

$$\begin{aligned}
\gamma^5 \to (\gamma^5)' &= S\left(\vec{x},t\right)\gamma^5\left(S\left(\vec{x},t\right)\right)^{-1} \\
&= \gamma^5.
\end{aligned} \tag{72}$$

In general, an SO(3,1) Lorentz transformation $S\left(\vec{x},t\right)$ is a combination of spin rotation transformation $\widehat{R}\left(\vec{x},t\right) = \widehat{R}_{\text{spin}}\left(\vec{x},t\right) \cdot \widehat{R}_{\text{space}}\left(\vec{x},t\right)$ and Lorentz boosting $S_{\text{Lor}}\left(\vec{x},t\right)$.

In physics, under a Lorentz transformation, a distribution of knot-pieces changes into another distribution of knot-pieces. For this reason, the velocity c_{eff} and the total number of zeroes N_{knot} are invariant,

$$c_{\text{eff}} \to c'_{\text{eff}} \equiv c_{\text{eff}} \tag{73}$$

and

$$N_{\text{knot}} \to N'_{\text{knot}} \equiv N_{\text{knot}}. \tag{74}$$

4.3. Gauge description for deformed zero-lattice

4.3.1. Deformed entanglement matrices and deformed entanglement pattern

The deformation of the zero-lattice leads to deformation of entanglement pattern, i.e.,

$$\left(\vec{\Gamma}, \Gamma^5\right) \to \left(\vec{\Gamma}'(\mathbf{x}), (\Gamma^5)'(\mathbf{x})\right) \tag{75}$$

where

$$\vec{\Gamma}'(\mathbf{x}) = \widehat{U}_{\mathrm{ET}}(\mathbf{x})\, \vec{\Gamma}\, \widehat{U}_{\mathrm{ET}}(\mathbf{x})^{-1}, \; (\Gamma^5)'(\mathbf{x}) = \widehat{U}_{\mathrm{ET}}\left(\vec{x}, t\right)\Gamma^5 \widehat{U}_{\mathrm{ET}}(\mathbf{x})^{-1}. \tag{76}$$

$\mathbf{x}$ denotes the space-time position of a site of zero-lattice, $\left(\vec{x}, t\right)$. Each entanglement matrix becomes a unit SO(4) vector-field on each lattice site. The deformed zero-lattice induced by local entanglement transformation $\widehat{U}_{\mathrm{ET}}(\mathbf{x})$ is characterized by four SO(4) vector-fields (four entanglement matrices) $\left(\vec{\Gamma}'(\mathbf{x}), (\Gamma^5)'(\mathbf{x})\right)$. See the illustration of a 2D deformed zero-lattice in **Figure 4(d)**, in which the arrows denote deformed entanglement matrix $(\Gamma^5)'(\mathbf{x})$.

4.3.2. Gauge description for deformed tempo entanglement matrix

Firstly, we study the unit SO(4) vector-field of deformed tempo entanglement matrix $(\Gamma^5)'(\mathbf{x})$. To characterize $(\Gamma^5)'(\mathbf{x})$, the reduced Gamma matrices γ^μ is defined as

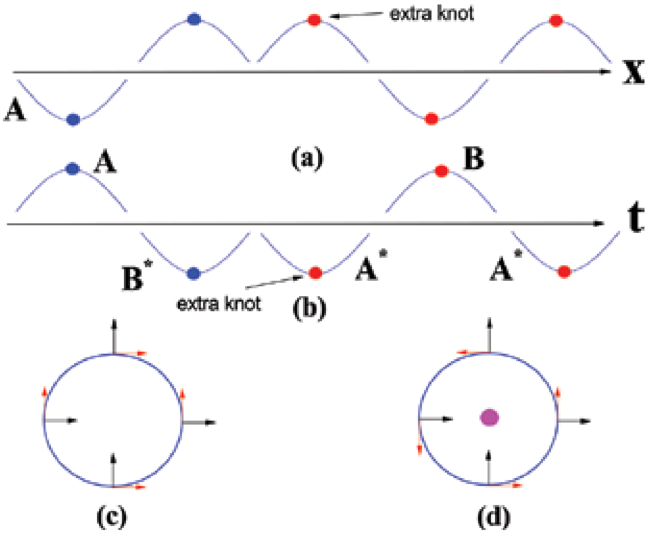

Figure 4. (a) An illustration of the effect of an extra knot on a 1D knot-crystal along spatial direction; (b) an illustration of the effect of an extra knot on a 1D knot-crystal along tempo direction. Here A*/B* denotes conjugate representation of vortex-line-A/B; (c) the entanglement pattern for a uniform knot-crystal. The arrows denote the directions of entanglement matrices; and (d) the entanglement pattern for a knot-crystal with an extra knot at center. The purple spot denotes the knot. The red arrows that denote local tangential entanglement matrices have vortex-like configuration on 2D projected space.

$$\gamma^1 = \gamma^0\Gamma^1, \gamma^2 = \gamma^0\Gamma^2, \gamma^3 = \gamma^0\Gamma^3, \tag{77}$$

and

$$\gamma^0 = \Gamma^5 = \tau^x \otimes 1, \gamma^5 = \overrightarrow{i\gamma}^0\gamma^1\gamma^2\gamma^3. \tag{78}$$

Under this definition ($\gamma^0 = \Gamma^5$), the effect of deformed zero-lattice from spatial entanglement transformation $e^{i\Gamma^1\cdot\Delta\Phi x}$, $e^{i\Gamma^2\cdot\Delta\Phi_y}$, $e^{i\Gamma^3\cdot\Delta\Phi_z}$ can be studied due to

$$\Gamma^5 \to \left(\Gamma^5\right)'(\mathbf{x}) = \widehat{U}_{\mathrm{ET}}^{x/y/z}\left(\vec{x}, t\right)\Gamma^5\widehat{U}_{\mathrm{ET}}^{x/y/z}(\mathbf{x})^{-1} \neq \Gamma^5. \tag{79}$$

However, the effect of deformed zero-lattice from tempo entanglement transformation $e^{i\delta\Phi_t\cdot\Gamma^5}$ cannot be well defined due to

$$\Gamma^5 \to \left(\Gamma^5\right)'(\mathbf{x}) = \widehat{U}_{\mathrm{ET}}^{t}\left(\vec{x}, t\right)\Gamma^5\widehat{U}_{\mathrm{ET}}^{t}(\mathbf{x})^{-1} = \Gamma^5. \tag{80}$$

We introduce an SO(4) transformation $\widehat{U}\left(\vec{x}, t\right)$ that is a combination of spin rotation transformation $\widehat{R}(\mathbf{x})$ and spatial entanglement transformation (entanglement transformation along $x/y/z$-direction) $\widehat{U}_{\mathrm{ET}}^{x/y/z}(\mathbf{x}) = e^{i\delta\vec{\Phi}(\mathbf{x})\cdot\vec{\Gamma}}$, i.e.,

$$\widehat{U}(\mathbf{x}) = \widehat{R}(\mathbf{x}) \oplus \widehat{U}_{\mathrm{ET}}^{x/y/z}(\mathbf{x}). \tag{81}$$

Here, $\oplus$ denotes operation combination. Under a non-uniform SO(4) transformation $\widehat{U}(\mathbf{x})$, we have

$$\gamma^0 \to \widehat{U}\,(\mathbf{x})\gamma^0\left(\widehat{U}(\mathbf{x})\right)^{-1} = \left(\gamma^0(\mathbf{x})\right)' = \sum\nolimits_a \gamma^a n^a(\mathbf{x}) \tag{82}$$

where $\mathbf{n} = \left(n^1, n^2, n^3\phi_0^0\right) = \left(\vec{n}, \phi_0^0\right)$ is a unit SO(4) vector-field. For the deformed zero-lattice, according to $\left(\gamma^0(\mathbf{x})\right)' \neq \gamma^0$, the entanglement matrix $\Gamma^5 = \gamma^0$ along tempo direction is varied, $\Gamma^5 \to \left(\Gamma^5\right)'(\mathbf{x}) \neq \Gamma^5$.

In general, the SO(4) transformation is defined by $\widehat{U}(\mathbf{x}) = e^{\Phi_{ab}(\mathbf{x})\gamma^{ab}}$ $\left(\gamma^{ab} = -\frac{1}{4}\left[\gamma^a, \gamma^b\right]\right)$. Under the SO(4) transformation, we have

$$\begin{aligned} \gamma^\mu \to \left(\gamma^\mu(\mathbf{x})\right)' &= \widehat{U}(\mathbf{x})\gamma^\mu\left(\widehat{U}(\mathbf{x})\right)^{-1}, \\ A_\mu \to A_\mu'\left(\vec{x}, t\right) &= \widehat{U}\left(\vec{x}, t\right)A_\mu(\mathbf{x})\left(\widehat{U}(\mathbf{x})\right)^{-1} \\ &\quad + \widehat{U}(\mathbf{x})\partial_\mu\left(\widehat{U}(\mathbf{x})\right)^{-1}. \end{aligned} \tag{83}$$

In particular, γ^5 is invariant under the SO(4) transformation as

$$\gamma^5 \to \left(\gamma^5\right)' = \widehat{U}\,(\mathbf{x})\gamma^5\left(\widehat{U}(\mathbf{x})\right)^{-1} = \gamma^5. \tag{84}$$

The correspondence between index of γ^a and index of space-time x^a is

$$\begin{aligned} &\gamma^1 \Leftrightarrow x, \gamma^2 \Leftrightarrow y, \\ &\gamma^3 \Leftrightarrow z, \gamma^0 \Leftrightarrow t. \end{aligned} \tag{85}$$

We denote this correspondence to be

$$(1,2,3,0)_{\mathrm{ET}} \Leftrightarrow (1,2,3,0)_{\mathrm{ST}} \tag{86}$$

where $(1,2,3,0)_{\mathrm{ET}}$ denotes the index order of γ^a and $(1,2,3,0)_{\mathrm{ST}}$ denotes the index order of space-time x^a.

As a result, we can introduce an auxiliary gauge field $A_\mu^{ab}(\mathbf{x})$ and use a gauge description to characterize the deformation of the zero-lattice. The auxiliary gauge field $A_\mu^{ab}(\mathbf{x})$ is written into two parts [15]: SO(3) parts

$$A^{ij}(\mathbf{x}) = \mathrm{tr}\left(\gamma^{ij}\left(\widehat{U}(\mathbf{x})\right)d\left(\widehat{U}(\mathbf{x})\right)^{-1}\right) \tag{87}$$

and SO(4)/SO(3) parts

$$\begin{aligned} A^{i0}(\mathbf{x}) &= \mathrm{tr}\left(\gamma^{i0}\widehat{U}(\mathbf{x})\right)d\left(\widehat{U}(\mathbf{x})\right)^{-1}) \\ &= \gamma^0 d\left(\gamma^i(\mathbf{x})\right)' = -\gamma^i d\left(\gamma^0(\mathbf{x})\right)'. \end{aligned} \tag{88}$$

The total field strength $\mathcal{F}^{ij}(\mathbf{x})$ of $i,j = 1,2,3$ components can be divided into two parts

$$\mathcal{F}^{ij}(\mathbf{x}) = F^{ij} + A^{i0} \wedge A^{j0}. \tag{89}$$

According to pure gauge condition, we have Maurer-Cartan equation,

$$\mathcal{F}^{ij}(\mathbf{x}) = F^{ij} + A^{i0} \wedge A^{j0} \equiv 0 \tag{90}$$

or

$$\begin{aligned} F^{ij} &= dA^{ij} + A^{ik} \wedge A^{kj} \\ &\equiv -A^{i0} \wedge A^{j0}. \end{aligned} \tag{91}$$

Finally, we emphasize the equivalence between γ^{0i} and Γ^i, i.e., $\gamma^{0i} \Leftrightarrow \Gamma^i$.

4.3.3. Gauge description for deformed spatial entanglement matrix

Next, we study the unit SO(4) vector-field of deformed spatial entanglement matrix $\left(\Gamma^i\right)'(\mathbf{x})$. To characterize $\left(\Gamma^i\right)'(\mathbf{x})$, the reduced Gamma matrices γ^μ is defined as

$$\gamma^1 = \gamma^0\Gamma^j, \gamma^2 = \gamma^0\Gamma^k, \gamma^3 = \gamma^0\Gamma^5, \tag{92}$$

and

$$\begin{aligned} \gamma^0 &= \Gamma^i = \tau^z \otimes \sigma^i, \\ \gamma^5 &= i\gamma^0\gamma^1\gamma^2\gamma^3. \end{aligned} \tag{93}$$

Here, Γ^i, Γ^j, and Γ^k are three orthotropic spatial entanglement matrices. Under this definition ($\gamma^0 = \Gamma^i$), the effect of deformed zero-lattice from partial spatial/tempo entanglement transformation $e^{i\Gamma^j \cdot \Delta\Phi_j}$, $e^{i\Gamma^k \cdot \Delta\Phi_k}$, $e^{i\Gamma^5 \cdot \Delta\Phi_t}$ can be studied due to

$$\Gamma^i \to \left(\Gamma^i\right)'(\mathbf{x}) = \widehat{U}_{\mathrm{ET}}^{x_j/x_k/t}\left(\vec{x}, t\right)\Gamma^i \widehat{U}_{\mathrm{ET}}^{x_j/x_k/t}(\mathbf{x})^{-1} \neq \Gamma^i. \tag{94}$$

However, the effect of deformed zero-lattice from spatial entanglement transformation $e^{i\delta\Phi_t \cdot \Gamma^5}$ cannot be well defined due to

$$\Gamma^i \to \left(\Gamma^i\right)'(\mathbf{x}) = \widehat{U}_{\mathrm{ET}}^{x_i}\left(\vec{x}, t\right)\Gamma^i \widehat{U}_{\mathrm{ET}}^{x_i}(\mathbf{x})^{-1} = \Gamma^i. \tag{95}$$

We use similar approach to introduce the gauge description. We can also define the reduced Gamma matrices $\tilde{\gamma}^\mu$ as

$$\tilde{\gamma}^1 = \tilde{\gamma}^0\Gamma^2, \tilde{\gamma}^2 = \tilde{\gamma}^0\Gamma^3, \tilde{\gamma}^3 = \tilde{\gamma}^0\Gamma^5, \tag{96}$$

and

$$\begin{aligned} \tilde{\gamma}^0 &= \Gamma^i = \tau^z \otimes \sigma^x, \\ \tilde{\gamma}^5 &= i\tilde{\gamma}^0\tilde{\gamma}^1\tilde{\gamma}^2\tilde{\gamma}^3. \end{aligned} \tag{97}$$

The correspondence between index of $\tilde{\gamma}^a$ and index of space-time x^a is

$$\begin{aligned} &\tilde{\gamma}^1 \Leftrightarrow y, \tilde{\gamma}^2 \Leftrightarrow z, \\ &\tilde{\gamma}^3 \Leftrightarrow t, \tilde{\gamma}^0 \Leftrightarrow x. \end{aligned} \tag{98}$$

We denote this correspondence to be

$$(1, 2, 3, 0)_{\mathrm{ET}} \Leftrightarrow (2, 3, 0, 1)_{\mathrm{ST}}. \tag{99}$$

Now, the SO(4) transformation $\tilde{U}\left(\vec{x}, t\right) = e^{\Phi_{ab}\left(\vec{x}, t\right)\tilde{\gamma}^{ab}}$ $\left(\tilde{\gamma}^{ab} = -\frac{1}{4}\left[\tilde{\gamma}^a, , \tilde{\gamma}^b\right]\right)$ is not a combination of spin rotation symmetry and entanglement transformation along *x*/*y*/*z*-direction. However, for the case of a or b to be 0, $\tilde{U}\left(\vec{x}, t\right) = e^{\Phi_{a0}\left(\vec{x}, t\right)\tilde{\gamma}^{a0}}$ denotes the entanglement transformation along *y*/*z*/*t*-direction. The unit SO(4) vector-field on each lattice site becomes

$$\tilde{U}(\mathbf{x})\tilde{\gamma}^0\left(\tilde{U}(\mathbf{x})\right)^{-1} = \left(\tilde{\gamma}^0(\mathbf{x})\right)' = \sum\nolimits_a \tilde{\gamma}^a \tilde{n}^a(\mathbf{x}) \tag{100}$$

where $\tilde{\mathbf{n}} = \left(\tilde{n}^1, , \tilde{n}^2, , \tilde{n}^3, \tilde{\phi}_0^0\right)$ is a unit vector-field. The auxiliary gauge field $\tilde{A}^{ab}(\mathbf{x})$ are defined by

$$\tilde{A}^{ab}(\mathbf{x}) = \mathrm{tr}\left(\tilde{\gamma}^{ij}\left(\tilde{U}(\mathbf{x})\right)d\left(\tilde{U}(\mathbf{x})\right)^{-1}\right). \tag{101}$$

According to pure gauge condition, we also have the following Maurer-Cartan equation,

$$\tilde{F}^{ij} = d\tilde{A}^{ij} + \tilde{A}^{ik} \wedge \tilde{A}^{kj} \equiv -\tilde{A}^{i0} \wedge \tilde{A}^{j0}. \tag{102}$$

Finally, we emphasize the equivalence between $\tilde{\gamma}^{0i}$ and Γ^a, i.e., $\tilde{\gamma}^{01} \Leftrightarrow \Gamma^2$, $\tilde{\gamma}^{02} \Leftrightarrow \Gamma^3$, $\tilde{\gamma}^{03} \Leftrightarrow \Gamma^5$.

4.3.4. Hidden SO(4) invariant for gauge description

In addition, there exists a hidden global SO(4) invariant for entanglement matrices along different directions in 3 + 1D (winding) space-time $\left(\vec{\Gamma}, \Gamma^5\right) \to \left(\vec{\Gamma}', (\Gamma^5)'\right)$. To show the hidden SO(4) invariant, we define the reduced Gamma matrices $\tilde{\gamma}^\mu$ as

$$\begin{aligned}
\tilde{\gamma}^1 &= \tilde{\gamma}^0\Gamma^2, \tilde{\gamma}^2 = \tilde{\gamma}^0\Gamma^3, \tilde{\gamma}^3 = \tilde{\gamma}^0\Gamma^5, \\
\tilde{\gamma}^0 &= \alpha\Gamma^1 + \beta\Gamma^2 + \gamma\Gamma^3 + \delta\Gamma^5, \\
\tilde{\gamma}^5 &= i\tilde{\gamma}^0\tilde{\gamma}^1\tilde{\gamma}^2\tilde{\gamma}^3
\end{aligned} \tag{103}$$

with $\alpha^2 + \beta^2 + \gamma^2 + \delta^2 = 1$. Here, α, β, γ, δ are constant.

Under this description, we can study the entanglement deformation along orthotropic spatial/tempo directions to $x' = \alpha x + \beta y + \gamma z + \delta t$.

4.4. Relationship between geometric description and gauge description for deformed zero-lattice

Due to the generalized spatial translation symmetry there exists an *intrinsic relationship* between gauge description for entanglement deformation between two vortex-membranes and geometric description for global coordinate transformation of the same deformed zero-lattice.

On the one hand, to characterize the changes of the positions of zeroes, we must consider a curved space-time by using geometric description, $\mathbf{x} = \left(\vec{x}, t\right) \to \mathbf{x}' = \left(\vec{x}', t'\right)$. On the other hand, we need to consider a varied vector-field

$$\left(\gamma^{0}(\mathbf{x})\right)' = \widehat{U}(\mathbf{x})\gamma^{0}\left(\widehat{U}(\mathbf{x})\right)^{-1} = \sum\nolimits_{a}\gamma^{a}n^{a}(\mathbf{x}) \tag{104}$$

by using gauge description. There exists intrinsic relationship between the geometry fields $e^{a}(\mathbf{x})$ $(a = 1, 2, 3, 0)$ and the auxiliary gauge fields $A^{a0}(\mathbf{x})$.

For a non-uniform zero-lattice, we have

$$\begin{aligned} \vec{\Phi}\left(\vec{x}, t\right) &\Rightarrow \vec{\Phi}'\left(\vec{x}, t\right) = \vec{\Phi}\left(\vec{x}, t\right) + \delta\vec{\Phi}\left(\vec{x}, t\right), \\ \Phi_{t}\left(\vec{x}, t\right) &\Rightarrow \Phi'_{t}\left(\vec{x}, t\right) = \Phi_{t}\left(\vec{x}, t\right) + \delta\Phi_{t}\left(\vec{x}, t\right). \end{aligned} \tag{105}$$

On deformed zero-lattice, the "lattice distances" become dynamic vector fields. We define the vierbein fields $e^{a}(\mathbf{x})$ that are supposed to transform homogeneously under the local symmetry, and to behave as ordinary vectors under local entanglement transformation along x^{a}-direction,

$$e^{a}(\mathbf{x}) = dx^{a}(\mathbf{x}) = \frac{a}{\pi}d\Phi^{a}(\mathbf{x}). \tag{106}$$

For the smoothly deformed vector-fields $n^{i}(\mathbf{x}) \ll 1$, within the representation of $\Gamma^{5} = \gamma^{0}$ we have

$$\begin{aligned} \frac{d\Phi^{i}(\mathbf{x})}{2\pi} &= n^{i}(\mathbf{x}) = \mathrm{tr}\left[\gamma^{0}d\gamma^{i}(\mathbf{x})\right] \\ &= A^{i0}(\mathbf{x}), i = 1, 2, 3. \end{aligned} \tag{107}$$

Thus, the relationship between $e^{i}(\mathbf{x})$ and $A^{i0}(\mathbf{x})$ is obtained as

$$e^{i}(\mathbf{x}) \equiv (2a)A^{i0}(\mathbf{x}). \tag{108}$$

According to this relationship, the changing of entanglement of the vortex-membranes curves the 3D space.

On the other hand, within the representation of $\Gamma^{i} = \tilde{\gamma}^{0}$ we have

$$\begin{aligned} \frac{d\Phi^{a}(\mathbf{x})}{2\pi} &= \tilde{n}^{a}(\mathbf{x}) = \mathrm{tr}\left[\tilde{\gamma}^{0}d\tilde{\gamma}^{a}(\mathbf{x})\right] \\ &= \tilde{A}^{i0}(\mathbf{x}), i = j, k, 0, \end{aligned} \tag{109}$$

and

$$e^{0}(\mathbf{x}) = dt(\mathbf{x}) = \frac{a}{\pi}d\Phi_{t}(\mathbf{x}) = (2a)\tilde{A}^{30}(\mathbf{x}). \tag{110}$$

According to this relationship, the changing of entanglement of the vortex-membranes curves the 4D space-time.

In addition, we point out that for different representation of reduced Gamma matrix, there exists intrinsic relationships between the gauge fields $A(\mathbf{x})$ and $\tilde{A}(\mathbf{x})$. After considering these relationships, we have a complete description of the deformed zero-lattice on the geometric space-time,

5. Emergent gravity

Gravity is a natural phenomenon by which all objects attract one another including galaxies, stars, human-being and even elementary particles. Hundreds of years ago, Newton discovered the inverse-square law of universal gravitation, $F = \frac{GMm}{r^2}$ where G is the Newton constant, r is the distance, and M and m are the masses for two objects. One hundred years ago, the establishment of general relativity by Einstein is a milestone to learn the underlying physics of gravity that provides a unified description of gravity as a geometric property of space-time. From Einstein's equations $R_{\mu\nu} - \frac{1}{2} R g_{\mu\nu} = 8\pi G T_{\mu\nu}$, the gravitational force is really an effect of curved space-time. Here $R_{\mu\nu}$ is the 2nd rank Ricci tensor, R is the curvature scalar, $g_{\mu\nu}$ is the metric tensor, and $T_{\mu\nu}$ is the energy-momentum tensor of matter.

In this section, we point out that there exists emergent gravity for knots on zero-lattice.

5.1. Knots as topological defects

5.1.1. Knot as SO(4)/SO(3) topological defect in 3 + 1D space-time

A knot corresponds to an elementary object of a knot-crystal; a knot-crystal can be regarded as composite system of multi-knot. For example, for 1D knot, people divide the knot-crystal into N identical pieces, each of which is just a knot.

From point view of *information*, each knot corresponds to a zero between two vortex-membranes along the given direction. For a knot, there must exist a zero point, at which $\xi_{\mathrm{A}}(x)$ is equal to $\xi_{\mathrm{B}}(x)$. The position of the zero is determined by a local solution of the zero-equation, $F_\theta(x) = 0$ or $\xi_{\mathrm{A},\theta}(x) = \xi_{\mathrm{B},\theta}(x)$.

From point view of *geometry*, a knot (an anti-knot) removes (or adds) a projected zero of zero-lattice that corresponds to removes (or adds) half of "lattice unit" on the zero-lattice according to

$$\Delta x_i = \pm a_{\mathrm{eff}}\left(\vec{x}, t\right) \simeq \pm a. \tag{111}$$

As a result, a knot looks like a special type of edge dislocation on 3 + 1D zero-lattice. The zero-lattice is deformed and becomes mismatch with an additional knot.

From point view of *entanglement*, a knot becomes topological defect of 3 + 1D winding space-time: along x-direction, knot is anti-phase changing denoted by $e^{i\Gamma^1 \cdot \Delta \Phi x}$, $\Delta \Phi x = \pi;$ along y-direction, knot is anti-phase changing denoted by $e^{i\Gamma^2 \cdot \Delta \Phi_y}$, $\Delta \Phi_y = \pi$; along z-direction, knot is anti-phase changing denoted by $e^{i\Gamma^3\cdot\Delta\Phi_z}$, $\Delta\Phi_z = \pi$; along t-direction, knot is anti-phase changing denoted by $e^{i\Gamma^5\cdot\Delta\Phi_t}$, $\Delta\Phi_t = \pi$. **Figure 4(a)** and **(b)** shows an illustration a 1D knot.

In mathematics, to generate a knot at (x_0, y_0, z_0, t_0), we do global topological operation on the knot-crystal, i.e.,

$$e^{i\Gamma^1\cdot\Delta\Phi x}(\mathbf{x})|0\rangle \tag{112}$$

with $\Delta\Phi x = 0, x < x_0$ and $\Delta\Phi x = \pi, x \geq x_0$;

$$e^{i\Gamma^2\cdot\Delta\Phi_y(\mathbf{x})}|0\rangle \tag{113}$$

with $\Delta\Phi_y = 0, y < y_0$ and $\Delta\Phi_y = \pi, y \geq y_0$;

$$e^{i\Gamma^3\cdot\Delta\Phi_z(\mathbf{x})}|0\rangle \tag{114}$$

with $\Delta\Phi_z = 0, z < z_0$ and $\Delta\Phi_z = \pi, z \geq x_0$;

$$e^{i\Gamma^5\cdot\Delta\Phi_t(\mathbf{x})}|0\rangle \tag{115}$$

with $\Delta\Phi_t = 0, t < t_0$ and $\Delta\Phi_t = \pi, t \geq t_0$. As a result, due to the rotation symmetry in 3 + 1D space-time, a knot becomes SO(4)/SO(3) topological defect. Along arbitrary direction, the local entanglement matrices around a knot at center are switched on the tangential sub-space-time.

5.1.2. Knot as SO(3)/SO(2) magnetic monopole in 3D space

To characterize the topological property of a knot on the 3 + 1D zero-lattice, we use gauge description. We firstly study the tempo entanglement deformation and define $\Gamma^5 = \gamma_0$. Under this gauge description, we can only study the effect of a knot on three spatial zero-lattice.

When there exists a knot, the periodic boundary condition of knot states along arbitrary direction is changed into anti-periodic boundary condition,

$$\Delta\Phi x = \pi, \Delta\Phi_y = \pi, \Delta\Phi_z = \pi. \tag{116}$$

Consequently, along given direction (for example x-direction), the local entanglement matrices on the tangential sub-space are switched by $e^{i\Gamma^1\cdot\Delta\Phi x}$ $(\Delta\Phi x = \pi)$. Along x-direction, in the limit of $x \to -\infty$, we have the local entanglement matrices on the tangential sub-space as Γ^2 and Γ^3; in the limit of $x \to \infty$, we have the local entanglement matrices on the tangential sub-space as $e^{i\Gamma^1\cdot\Delta\Phi x}(\Gamma^2)e^{-i\Gamma^1\cdot\Delta\Phi x} = -\Gamma^2$ and $e^{i\Gamma^1\cdot\Delta\Phi x}(\Gamma^3)e^{-i\Gamma^1\cdot\Delta\Phi x} = -\Gamma^3$.

Because we have similar result along x^i-direction for the system with an extra knot, the system has generalized spatial rotation symmetry. Due to the generalized spatial rotation symmetry, when moving around the knot, the local tangential entanglement matrices (we may use indices j, k to denote the sub space) must rotate synchronously. See the red arrows that denote local tangential entanglement matrices in **Figure 4(c)** and **(d)**. In **Figure 4(d)**, local tangential entanglement matrices induced by an extra (unified) knot shows vortex-like topological configuration in projected 2D space (for example, x-y plane). As a result, local tangential entanglement matrices induced by an extra knot can be exactly mapped onto that of an orientable sphere with fixed chirality.

To characterize the topological property of 3 + 1D zero-lattice with an extra (unified) knot, we apply gauge description and write down the following constraint

$$\iiint \rho_F dV = \frac{1}{4\pi}\iint \epsilon_{jk}\epsilon_{ijk}F_{jk}^{jk}\cdot dS_i \tag{117}$$

where

$$\begin{aligned} F^{ij} &= dA^{ij} + A^{ik}\wedge A^{kj} \\ &\equiv -A^{i0}\wedge A^{j0} \end{aligned} \tag{118}$$

and $\rho_F = \sqrt{-g}\psi^{\dagger}\psi$. The upper indices of F_{jk}^{jk} label the local entanglement matrices on the tangential sub-space and the lower indices of F_{jk}^{jk} denote the spatial direction. The non-zero Gaussian integrate $\frac{1}{4\pi}\iint \epsilon_{jk}\epsilon_{ijk}F_{jk}^{jk}\cdot dS_i$ just indicates the local entanglement matrices on the tangential sub-space $A^{i0}\wedge A^{j0}$ to be the local frame of an orientable sphere with fixed chirality.

As a result, the entanglement pattern with an extra 3D knot is topologically deformed and the 3D knot becomes SO(3)/SO(2) *magnetic monopole.* From the point view of gauge description, a knot traps a "magnetic charge" of the auxiliary gauge field, i.e.,

$$N_F = \int \sqrt{-g}\Psi^{\dagger}\Psi d^3x = q_m \tag{119}$$

where $q_m = \frac{1}{4\pi}\iint \epsilon_{jk}\epsilon_{ijk}F_{jk}^{jk}\cdot dS_i$ is the "magnetic" charge of auxiliary gauge field A^{jk}. For single knot $N_F = 1$, the "magnetic" charge is $q_m = 1$.

5.1.3. *Knot as SO(3)/SO(2) magnetic monopole in 2 + 1D space-time*

Next, we study the spatial entanglement deformation and define $\Gamma^i = \tilde{\gamma}_0$. Under this gauge description, we can only study the effect of a knot on 2D spatial zero-lattice and 1D tempo zero-lattice.

In the 2 + 1D space-time, a knot also leads to π-phase changing,

$$\Delta\Phi i = \pi, \Delta\Phi_j = \pi, \Delta\Phi_t = \pi. \tag{120}$$

Due to the spatial-tempo rotation symmetry, the knot also becomes SO(3)/SO(2) magnetic monopole and traps a "magnetic charge" of the auxiliary gauge field $\tilde{A}^{jk}$, i.e.,

$$N_F = \int \sqrt{-g}\Psi^{\dagger}\Psi d^3x = \tilde{q}_m \tag{121}$$

where $\tilde{q}_m$ is the "magnetic" charge of auxiliary gauge field $\tilde{A}^{ij}$. Remember that the correspondence between index of $\tilde{\gamma}^i$ and index of space-time x^i is $\tilde{\gamma}^1 \Leftrightarrow y$, $\tilde{\gamma}^2 \Leftrightarrow z$, $\tilde{\gamma}^3 \Leftrightarrow t$.

To characterize the induced magnetic charge, we write down another constraint

$$\iiint \rho_F dV = \frac{1}{4\pi}\iint \epsilon_{ij}\epsilon_{ijk}\tilde{F}^{ij}_{jk} \cdot dS_i \tag{122}$$

where

$$\begin{aligned}\tilde{F}^{ij} &= d\tilde{A}^{ij} + \tilde{A}^{ij} \wedge \tilde{A}^{ij} \\ &\equiv -\tilde{A}^{i0} \wedge \tilde{A}^{j0}.\end{aligned} \tag{123}$$

The upper indices of $\tilde{F}^{ij} = d\tilde{F}^{ij} + \tilde{F}^{ik} \wedge \tilde{F}^{kj}$ denote the local entanglement matrices on the tangential sub-space-time and the lower indices of $\tilde{F}^{ij}_{jk}$ denote the spatial direction. Therefore, according to above equation, the 2 + 1D zero-lattice is globally deformed by an extra knot.

In general, due to the hidden SO(4) invariant, for other gauge descriptions $\tilde{\gamma}^0 = \alpha\Gamma^1 + \beta\Gamma^2 + \gamma\Gamma^3 + \delta\Gamma^5$, a knot also play the role of SO(3)/SO(2) magnetic monopole and traps a "magnetic charge" of the corresponding auxiliary gauge field.

5.2. Einstein-Hilbert action as topological mutual BF term for knots

It is known that for a given gauge description, a knot is an SO(3)/SO(2) magnetic monopole and traps a "magnetic charge" of the corresponding auxiliary gauge field. For a complete basis of entanglement pattern, we must use four orthotropic SO(4) rotors $\left((\Gamma^1)'(\mathbf{x}), (\Gamma^2)'(\mathbf{x}), (\Gamma^3)'(\mathbf{x}),\right.$ $\left.(\Gamma^5)'(\mathbf{x})\right)$ and four different gauge descriptions to characterize the deformation of a knot (an SO(4)/SO(3) topological defect) on a 3 + 1D zero-lattice.

Firstly, we use Lagrangian approach to characterize the deformation of a knot (an SO(3)/SO(2) topological defect) on a 3D spatial zero-lattice, $N_F = q_m$. The topological constraint in Eq. (117) can be re-written into

$$\frac{i}{4}\mathrm{tr}\sqrt{-g}\overline{\Psi}\gamma^i(\gamma^{0i}/2)\Psi = \epsilon_{jk}\epsilon_{ijk}\frac{1}{4\pi}\widehat{D}_i F^{jk}_{jk} \tag{124}$$

or

$$\frac{i}{4}\mathrm{tr}\sqrt{-g}\overline{\Psi}\varpi^{0i}_0\gamma^i(\gamma^{0i}/2)\Psi = i\epsilon_{0ijk}\epsilon_{0ijk}\varpi^{0i}_0\frac{1}{4\pi}\widehat{D}_i F^{jk}_{jk} \tag{125}$$

where $\widehat{D}_i = i\widehat{\partial}_i + i\omega_i$ is covariant derivative in 3 + 1D space-time. ϖ^{0i} is a field that plays the role of Lagrangian multiplier. The upper index i of ϖ^{0i} denotes the local radial entanglement matrix around a knot, along which the entanglement matrix does not change. Thus, we use the dual field ϖ^{0i} to enforce the topological constraint in Eq. (117). That is, to denote the upper index of F^{jk} that is the local tangential entanglement matrices, we set antisymmetric property of upper index of ϖ^{0i} and that of F^{jk}. Because ϖ^{0i} and ω^{0i} have the same SO(3,1) generator $\left(\gamma^{0i}/2\right)$, due to SO(3,1) Lorentz invariance we can do Lorentz transformation and absorb the dual field ϖ^{0i} into ω^{0i}, i.e., $\omega^{0i} \to \left(\omega^{0i}\right)' = \omega^{0i} + \varpi^{0i}$. As a result, the dual field ϖ^{0i} is replaced by ω^{0i}.

In the path-integral formulation, to enforce such topological constraint, we may add a topological mutual BF term S_{MBF} in the action that is

$$\begin{aligned} S_{\mathrm{MBF1}} &= -\frac{1}{4\pi}\int \epsilon_{0ijk}\epsilon_{0\nu\lambda\kappa} R^{0i}_{0\nu} F^{jk}_{\lambda\kappa} d^4x \\ &= -\frac{1}{4\pi}\int \epsilon_{0ijk} R^{0i} \wedge F^{jk} \end{aligned} \tag{126}$$

where

$$R^{0i} = d\omega^{0i} + \omega^{0j} \wedge \omega^{ji}. \tag{127}$$

From $F^{jk} \equiv -A^{j0} \wedge A^{k0}$ and $e^i \wedge e^j = (2a)^2 A^{j0} \wedge A^{k0}$. The induced topological mutual BF term S_{MBF1} is linear in the conventional strength in R^{0i} and F^{jk}. This term is becomes

$$S_{\mathrm{MBF1}} = \frac{1}{4\pi(2a)^2}\int \epsilon_{0ijk} R^{0i} \wedge e^j \wedge e^k. \tag{128}$$

Next, we use Lagrangian approach to characterize the deformation of a knot (an SO(3)/SO(2) topological defect) on 2 + 1D space-time, $N_F = \tilde{q}_m$. Using the similar approach, we derive another topological mutual BF term S_{MBF2} in the action that is

$$S_{\mathrm{MBF2}} = -\frac{1}{4\pi}\int \epsilon_{0ijk}\epsilon_{0\nu\lambda\kappa} \tilde{R}^{0i}_{0\nu} \tilde{F}^{jk}_{\lambda\kappa} d^4x = -\frac{1}{4\pi}\int \epsilon_{0ijk} \tilde{R}^{0i} \wedge \tilde{F}^{jk} \tag{129}$$

where $\tilde{R}^{0i} = d\tilde{\omega}^{0i} + \tilde{\omega}^{0j} \wedge \tilde{\omega}^{ji}$. From $\tilde{F}^{k0} \equiv -\tilde{A}^{kj} \wedge \tilde{A}^{j0}$ and $\tilde{e}^i \wedge \tilde{e}^j = (2a)^2 \tilde{A}^{j0} \wedge \tilde{A}^{k0}$, this term becomes

$$S_{\mathrm{MBF2}} = \frac{1}{4\pi(2a)^2}\int \epsilon_{ijk0} \tilde{R}^{0i} \wedge \tilde{e}^j \wedge \tilde{e}^k. \tag{130}$$

The upper index of $\tilde{R}^{0i}$ denotes entanglement transformation along given direction in winding space-time. We unify the index order of space-time into $(1,2,3,0)_{\mathrm{ST}}$ and reorganize the upper index. The topological mutual BF term becomes $\frac{1}{4\pi(2a)^2}\int \epsilon_{ijk0} R^{ij} \wedge e^k \wedge e^0$. In Ref. [16–19], a topological description of Einstein-Hilbert action is proposed by S. W. MacDowell and F. Mansouri. The topological mutual BF term proposed in this paper is quite different from the MacDowell-Mansouri action.

According to the diffeomorphism invariance of winding space-time, there exists symmetry between the entanglement transformation along different directions. Therefore, with the help of a complete set of definition of reduced Gamma matrices γ^{μ}, there exist other topological mutual BF terms $S_{\mathrm{MBF},i}$. For the total topological mutual BF term $S_{\mathrm{MBF}} = \sum_i S_{\mathrm{MBF},i}$ that characterizes the deformation of a knot (an SO(4)/SO(3) topological defect) on a 3 + 1D zero-lattice, the upper index of the topological mutual BF term $R^{ij} \wedge e^k \wedge e^l$ must be symmetric, i.e., $i, j, k, l = 1, 2, 3, 0$.

By considering the SO(3,1) Lorentz invariance, the topological mutual BF term S_{MBF} turns into the Einstein-Hilbert action S_{EH} as

$$\begin{aligned} S_{\mathrm{MBF}} = S_{\mathrm{EH}} &= \frac{1}{16\pi(a)^2}\int \epsilon_{ijkl} R^{ij} \wedge e^k \wedge e^l \\ &= \frac{1}{16\pi G}\int \sqrt{-g} R d^4 x \end{aligned} \tag{131}$$

where G is the induced Newton constant which is $G = a^2$. The role of the Planck length is played by $l_p = a$, that is the "lattice" constant on the 3 + 1D zero-lattice.

Finally, from above discussion, we derived an effective theory of knots on deformed zero-lattice in continuum limit as

$$\begin{aligned} S &= \mathcal{S}_{\mathrm{zero-lattice}} + S_{\mathrm{EH}} \\ &= \int \sqrt{-g(x)}\,\overline{\Psi}\left(e_a^{\mu}\gamma^a \widehat{D}_{\mu} - m_{\mathrm{knot}}\right)\Psi d^4 x. \\ &+ \frac{1}{16\pi G}\int \sqrt{-g} R d^4 x \end{aligned} \tag{132}$$

where $\widehat{D}_{\mu} = i\widehat{\partial}_{\mu} + i\omega_{\mu}$. The variation of the action S via the metric $\delta g_{\mu\nu}$ gives the Einstein's equations

$$R_{\mu\nu} - \frac{1}{2} R g_{\mu\nu} = 8\pi G T_{\mu\nu}. \tag{133}$$

As a result, in continuum limit a knot-crystal becomes a space-time background like smooth manifold with emergent Lorentz invariance, of which the effective gravity theory turns into *topological* field theory.

For emergent gravity in knot physics, an important property is topological interplay between zero-lattice and knots. From the Einstein-Hilbert action, we found that the key property is duality between Riemann curvature R^{ij} and strength of auxiliary gauge field F^{kl}: *the deformation of entanglement pattern leads to the deformation of space-time*.

In addition, there exist a natural energy cutoff $\hbar\omega_0$ and a natural length cutoff a. In high energy limit ($\Delta\omega \sim \omega_0$) or in short range limit ($\Delta x \sim a$), without well-defined 3 + 1D zero-lattice, there does not exist emergent gravity at all.

6. Discussion and conclusion

In this paper, we pointed out that owing to the existence of local Lorentz invariance and diffeomorphism invariance there exists emergent gravity for knots on 3 + 1D zero-lattice. In knot physics, the emergent gravity theory is really a topological theory of entanglement deformation. For emergent gravity theory in knot physics, a topological interplay between 3 + 1D zero-lattice and the knots appears: on the one hand, the deformation of the 3 + 1D zero-lattice leads to the changes of knot-motions that can be denoted by curved space-time; on the other hand, the knots trapping topological defects deform the 3 + 1D zero-lattice that indicates matter may curve space-time. The Einstein-Hilbert action S_{EH} becomes a topological mutual BF term S_{MBF} that exactly reproduces the low energy physics of the general relativity. In **Table 1**, we emphasize the relationship between modern physics and knot physics.

In addition, this work would help researchers to understand the mystery in gravity. In modern physics, matter and space-time are two *different* fundamental objects and matter may move in (flat or curved) space-time. In knot physics, the most important physics idea for gravity is the unification of matter and space-time, i.e.,

$$\text{Matter (knots)} \Leftrightarrow \text{Space–time(zero–lattice)}. \tag{134}$$

One can see that matter (knots) and space-time (zero-lattice) together with motion of matter are *unified* into a simple phenomenon—entangled vortex-membranes and matter (knots) curves space-time (3 + 1D zero-lattice) via a *topological* way.

In the end of the paper, we address the possible physical realization of a 1D knot-crystal based on quantized vortex-lines in ^{4}He superfluid. Because the emergent gravity in knot physics is topological interplay between zero-lattice and knots, there is no Einstein gravity on a 1D knot-crystal based on entangled vortex-lines in ^{4}He superfluid. However, the curved space-time could be simulated.

Firstly, we consider two straight vortex-lines in ^{4}He superfluid between opposite points on the system. Then, we rotate one vortex line around another by a rotating velocity ω_0. Now, the

Modern physics	Knot physics
Matter	Knot: a topological defect of 3 + 1 D zero-lattice
Motion	Changing of the distribution of knot-pieces
Mass	Angular frequency for leapfrogging motion
Inertial reference system	A knot under Lorentz boosting
Coordinate translation	Entanglement transformation
Space-time	3 + 1D zero-lattice of projected entangled vortex-membranes
Curved space-time	Deformed 3 + 1D zero-lattice
Gravity	Topological interplay between 3 + 1D zero-lattice and knots

Table 1. The relationship between modern physics and knot physics.

winding vortex-line becomes a helical one described by $r_0 e^{ik_0 \cdot x - i\omega_0 t + i\phi_0}$ with $\omega_0 \simeq \left(\frac{\kappa}{4\pi} \ln \frac{1}{k_0 a_0}\right) k_0^2$. As a result, a knot-crystal is realized. For ^{4}He superfluid, $\kappa = h/m$ is the discreteness of the circulation owing to its quantum nature [2]. h is Planck constant and m is atom mass of SF. So $\kappa = h/m$ is about 10^{-3} cm^2/s. The length of the half pitch of the windings $a = \frac{\pi}{k_0}$ is set to be 10^{-5} cm, and the distance between two vortex lines r_0 is set to be 10^{-6} cm. We then estimate the effective light speed c_{eff} that is defined by $c_{\text{eff}} = \frac{\kappa k_0}{2\pi} \left(\ln \frac{1}{k_0 a_0} - \frac{1}{2}\right)$ (a_0 denotes the vortex filament radius which is much smaller than any other characteristic size in the system). The effective light speed c_{eff} is about 4 m/s. A non-uniform winding length leads to an effective curved 1 + 1D space-time.

However, at finite temperature, there exist mutual friction and phonon radiation for Kelvin waves on quantized vortex-lines in ^{4}He superfluid. After considering these dissipation effects, the Kelvin waves are subject to Kolmogorov-like turbulence (even in quantum fluid [3, 4]).

Acknowledgements

This work is supported by NSFC Grant No. 11674026.

Author details

Su-Peng Kou

Address all correspondence to: spkou@bnu.edu.cn

Department of Physics, Beijing Normal University, Beijing, P.R. China

References

[1] Thomson W. XXIV. Vibrations of a columnar vortex. Philosophical Magazine. 1880;**10**:155

[2] Donnelly RJ. Quantized Vortices in Helium II. Cambridge: Cambridge University Press; 1991

[3] Svistunov BV. Superfluid turbulence in the low-temperature limit. Physical Review B. 1995;**52**:3647

[4] Vinen WF. Classical character of turbulence in a quantum liquid. Physical Review B. 2000; **61**:1410

[5] Dyson FW. The potential of an anchor ring. Philosophical Transactions of the Royal Society A. 1893;**184**:1041

[6] Hicks WM. On the mutual threading of vortex rings. Proceedings of the Royal Society of London A. 1922;**102**:111

[7] Borisov AV, Kilin AA, Mamaev IS. The dynamics of vortex rings: Leapfrogging, choreographies and the stability problem. Regular and Chaotic Dynamics. 2013;**18**:33

[8] Wacks DH, Baggaley AW, Barenghi CF. Coherent laminar and turbulent motion of toroidal vortex bundles. Physics of Fluids. 2014;**26**:027102

[9] Caplan RM, Talley JD, Carretero-González R, Kevrekidis PG. Scattering and leapfrogging of vortex rings in a superfluid. Leapfrogging Kelvin waves, Physics of Fluids. 2014;**26**: 097101

[10] Hietala N, Hänninen R, Salman H, Barenghi CF. Leapfrogging Kelvin waves. arXiv: 1603.06403

[11] Kleckner D, Irvine WTM. Creation and dynamics of knotted vortices. Nature Physics. 2013;**9**:253

[12] Hall DS, Ray MW, Tiurev K, Ruokokoski E, Gheorghe AH, Möttönen M. Tying quantum knots. Nature Physics. 2016;**12**:478

[13] Kou SP. Kelvin wave and knot dynamics on entangled vortices. International Journal of Modern Physics B. 2017;**31**:1750241

[14] Kou SP. Knot physics on entangled vortex-membranes: Classification, dynamics and effective theory. International Journal of Modern Physics B. 2018;**32**:1850090

[15] In this paper, we use $I = x, y, z, i, j = 1, 2, 3$ and, $a, b = 1, 2, 3, 0$

[16] MacDowell SW, Mansouri F. Unified geometric theory of gravity and supergravity. Physical Review Letters. 1977;**38**:739

[17] Mansouri F. Superunified theories based on the geometry of local (super-) gauge invariance. Physical Review D. 1977;**16**:2456

[18] Van Nieuwenhuizen P. Supergravity. Physics Reports. 1981;**68**:189

[19] Chamseddine A, West P. Supergravity as a gauge theory of supersymmetry. Nuclear Physics B. 1977;**129**:39

Chapter 4

“Clean” Liquid Helium

Miguel Gabal, Javier Sesé, Conrado Rillo and
Stefano Spagna

Additional information is available at the end of the chapter

http://dx.doi.org/10.5772/intechopen.74907

Abstract

Liquid helium is the coldest fluid that exists in nature. By virtue of this fact, any unwanted substance present in liquid helium, that is, any impurity, will be “frozen” and will be in solid form. In practice, these solid impurities can be easily eliminated to obtain “optically clean” liquid. However, even “optically clean” filtered liquid helium may contain a non-negligible quantity of molecular hydrogen. These minute traces of molecular hydrogen are the causes of a known problem worldwide: the blockage of capillary tubes in helium evaporation cryostats. This problem seriously affects a wide range of cryogenic equipment used in low-temperature physics research at a considerable operational cost increase. In this chapter, we propose an underlying mechanism for this effect and provide a definitive solution by means of production of hydrogen-free liquid helium, that is, not only “optically clean” liquid helium but completely “clean” liquid helium. Moreover, basic superfluidity research studies could benefit from the availability of “clean” liquid helium.

Keywords: helium liquefaction, helium cryogenics, small-scale helium liquefiers, hydrogen contamination, impedance blockage, helium purification

1. Introduction

It is well known that the performance of continuously operating ^{4}He evaporation cryostats is often degraded as a result of the blocking of fine capillary tubes used as flow impedances to achieve temperatures below 4.2 K. This effect has been generally attributed to nitrogen or air impurities entering the capillary tubes from the main bath. However, even the most thorough laboratory best practices adopted to maintain the helium bath clean and prevent impurities from entering the capillary tubes fail. The blocking problem often recurs with no apparent cause.

Many low-temperature research laboratories around the world have experienced this nuisance at a considerable financial cost because helium is boiled off when the equipment has to be warmed up to room temperature in order to unblock the capillary tube and thus, recover the low-temperature operation performance.

This chapter summarizes the work performed during the last 3 years to obtain "Clean" liquid helium and to solve the flow impedance blocking issue definitely. On the other hand, the availability of clean liquid helium opens the door for the preparation of finite H_2 concentrations in superfluid ^4He. These ^4He-H_2 liquid mixtures with known H_2 concentrations will be the key to experimentally study very interesting phenomena like the possible existence of a supercooled stable liquid phase of molecular hydrogen that could exhibit superfluidity [1].

After a detailed description of low-temperature production in ^4He evaporation cryostats (Section 2), we describe the underlying physical mechanism responsible for the blockages (Section 3). This is based upon the freezing of molecular H_2 traces present in the liquid helium bath. Solid H_2 is accumulated at the impedance low-pressure side and, after some time, it produces a total impedance blockage.

Section 4 shows that the presence of H_2 traces in helium is unavoidable due to its occurrence in the natural gas wells where this fossil gas is harvested, forcing helium gas suppliers to specify a lower bound for impurity levels at about 100 ppb even in high-grade helium.

Finally, Section 5 describes a (small-scale) helium recovery plant capable of producing gas and liquid helium with ultra-high purity (H_2 molecular concentration $y_{H2} < 10^{-14}$) named by us as "Clean helium." Apart from other possible applications in which extreme pure rare gases may be needed, "Clean helium" reliably avoids the low-temperature flow impedance blocking issue.

Details, other than those given here, can be found in Gabal's Ph.D. thesis [2].

2. Low-temperature production in ^4He evaporation cryostats

The simplest way to reduce the temperature in a liquid helium bath is by pumping on it following the liquid–vapor coexistence curve of the ^4He phase diagram. However, this method is very uneconomical since about 40% of the liquid must be evaporated to cool the remaining liquid from, for example, 4.2 to 1.3 K, due to the large change of its specific heat in this temperature range [3]. In practice, it is more efficient to leave the main bath at 4.2 K and 100 kPa (1 bar) and to cool only a small fraction of the fluid in a separate container to reach the lower temperature using a ^4He evaporation cryostat design [4, 5]. Other advantages are the smaller vacuum required to achieve the lowest temperature and the absence of interruptions in the operation of the refrigerator: having the main bath at atmospheric pressure, the liquid helium refills can be done easily while the ^4He main bath is pumped through the impedance.

Figure 1 shows a simple diagram of a continuously operating ^4He evaporation cryostat. In such a refrigerator, a small fraction of the liquid from the main 4.2 K bath flows through a suitable flow impedance into a small vessel of several cubic centimeters often referred to as the

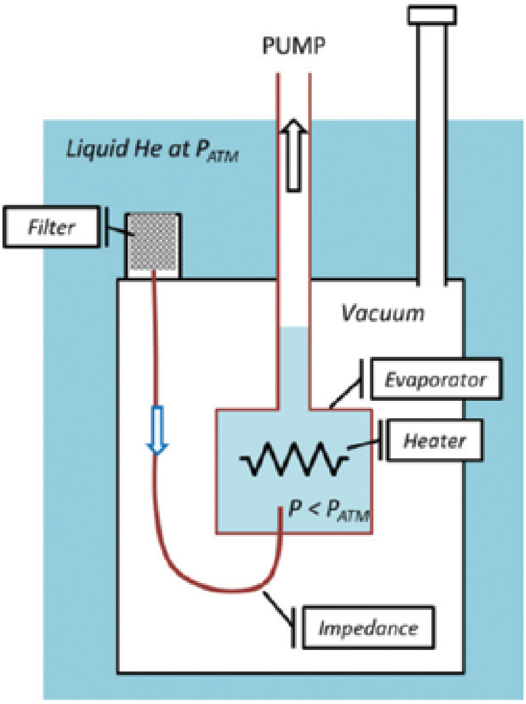

Figure 1. Schematic drawing of continuously operating ^{4}He refrigerator.

"pot" located inside the cryostat [3]. The vacuum space allows to thermally isolate the small cold vessel from the main 4.2 K bath.

Thanks to the pumping action, the liquid from the main bath at atmospheric pressure, P_{ATM}, is isenthalpically expanded through the impedance and reaches the pot at a lower temperature. Almost half of the heat of evaporation is used to cool the liquid, and thus, the other half can be used to cool the experiment.

In general, the impedance Z is given in terms of the flow through the capillary $\dot{V}$ and the pressure drop across it, ΔP, (typically from 100 kPa to 100 Pa) by:

$$\dot{V} = \frac{\Delta P}{(\eta Z)} \tag{1}$$

where η is the viscosity of the liquid helium. Impedances in the range of 10^{10}–10^{11} cm^{-3} are typically used in most cryogenic applications. Cooling power of the order of 5 mW or more is easily achievable at the impedance outlet once we consider the heat of evaporation of ^{4}He (≈ 83 J/mol) and a typical flow rate of $\dot{V}$=10^{-4} mol/s = 0.13 sL/mn that can be obtained with a mid-sized mechanical pump. In practice, the impedance is usually built with an appropriate length of fine CuNi capillary tube, usually with a short length of wire inside it to increase the impedance value.

If the impedance value (Z) is too large, there will be insufficient refrigeration and no liquid will accumulate in the evaporation vessel. If the impedance is too small, more liquid than required will flow, with the level rising higher at the vessel. This will not prevent the device from working but will result in higher helium consumption and a higher minimum temperature [5].

Historically, the appearance of a blockage in the capillary has been attributed to nitrogen or air impurities, for example, from [3]: "*During cooldown the refrigerator should be connected to a volume with pressurized very pure* ^{4}*He gas in order to prevent* N_2 *or air from entering and blocking the fill capillary. Sometimes problems arise because impurities in the main liquid helium bath (e.g. frozen air) block the fine capillary used for the impedance. One therefore has to put a filter in front of the capillary and keep the main* ^{4}*He clean.*"

During an initial cooldown of a cryostat, if the liquid helium transfer is not carefully carried out (e.g., forgetting to purge the Dewar with helium gas prior to transferring liquid helium), any residual air inside the cryostat can enter, freeze and block the impedance during the precool process. But, if the system has been cooled very carefully with high-purity liquid helium, and, the correct flow through the impedance has been verified, there is only a substance capable to pass through the filter and to block the impedance. This is molecular hydrogen, as we demonstrate in the following section.

Other authors [4] recommended the impedance construction: "*Problems with plugged capillaries sometimes occurred when the impedance was increased using a fine wire, hence, longer capillaries without wires are favored. The filters, which were necessary to prevent plugging of the impedance by frozen air or other particulate matter, were disks of sintered copper felt compression fitted at both ends of the capillary.*".

As we see, the impedance geometry can affect the time necessary to produce the solid that blocks the impedance, but if the helium bath contains molecular hydrogen traces, sooner or later, the problem will occur.

3. Flow impedance blocking issue

3.1. Liquid helium purity

With a boiling point of 4.2 K at 100 KPa, liquid helium is the coldest fluid that exists in nature. Below its critical temperature (Tc = 5.2 K), any unwanted substance present in the liquid phase, that is, any impurity, will be in solid form, resulting in mist, snow, suspensions or particulates [6]. The vapor pressure of these solid impurities will be, in general, negligibly small ($\ll 10^{-9}$ Pa), except for the case of the hydrogen isotopes and their molecular combinations [7] for which this is of the order of 10^{-2} Pa and 10^{-5} Pa, at 5.2 and 4.2 K, respectively. The solid impurities are usually charged and can be easily eliminated by electrostatic precipitation using Petryanov filters to obtain "optically clean" liquid, as demonstrated by Abrikosova and Shal'nikov [7]. But, even "optically clean" filtered liquid helium may contain a relevant quantity of non-solid hydrogen, that is, molecular hydrogen traces.

The He-H_2 gas mixture has attracted much interest in the scientific community because it is the simplest system for the study of intermolecular potentials [8–10]. The interaction potential of hydrogen and helium has been extensively studied by Silvera [11]. The Lennard-Jones wells for the weakly interacting He-He, He-H_2 and H_2-H_2 pairs are 10.8, 13.34 and 34.3 K, respectively. According to this study, H_2 molecules may have a bound state with He atoms, reside in liquid He surface states and penetrate the liquid helium. Thus, in addition to the possible presence of hydrogen molecules in the helium vapor, due to the non-negligible vapor pressure of solid hydrogen at 4.2 K, there may also exist a non-negligible amount of these hydrogen molecules "dissolved" in the liquid He phase.

In general, liquid helium in research laboratories is either delivered by a distributor of specialty gases or produced by liquefaction of both commercial grade and recovered gas. Liquid helium is subsequently stored and transferred to the application's cryostat requiring cryogenic cooling at atmospheric pressure and temperatures around 4.2 K. Since the triple point of H_2 is at 13.84 K and 7.04 kPa, the equilibrium vapor pressure of solid H_2 at those temperatures (≈ 4.2 K) is very small, of the order of $\approx 10^{-5}$ Pa. Therefore, if there is enough H_2 in the He gas being liquefied to produce a partial pressure higher than the equilibrium vapor pressure at 4.2 K, the H_2 molecules will directly nucleate into solid clusters. At atmospheric pressure (10^5 Pa), those solid clusters will be in equilibrium with a H_2 molar fraction in the vapor phase of the order 10^{-10} ($y_{H2} = (10^{-5}\ \text{Pa}/10^5\ \text{Pa}) = 10^{-10}$).

Even though there are no experimental reports about solubility of H_2 in liquid helium, theoretical calculations from classical solubility theory [12] indicate that the limiting solubility of solid hydrogen in liquid helium at 4.2 K would yield to molar fractions in the liquid phase, x_{H_2}, of the order of $\approx 10^{-10}$, that is, the same order of magnitude than the H_2 molar fraction in the vapor phase, y_{H_2}.

Furthermore, the solid hydrogen vapor pressure and the theoretical limiting solubility of solid hydrogen in liquid helium decrease exponentially with temperature, both becoming very small ($\approx 10^{-9}$ Pa and $\approx 10^{-14}$, respectively) below 3 K. Thus, the maximum concentration of H_2 molecules present in liquid helium will be determined by the exact temperature and pressure conditions of the helium bath. For this chapter, the H_2 molar fractions in the vapor, y_{H_2}, and in the liquid, x_{H_2}, below 3 K, both being of the order of $\approx 10^{-14}$, will be considered negligible. Furthermore, at temperatures near or below 1 K, hydrogen may be regarded as being totally insoluble in He [12].

Thus, unless H_2 impurities are completely eliminated prior to He liquefaction, that is, its molar fraction is reduced from its typical values in the range $y_{H_2} = 10^{-6}$–10^{-5} down to $\approx 10^{-14}$, the liquid He, as produced, will have traces of H_2, up to a maximum concentration level determined by the temperature (e.g., $x_{H_2} \approx 10^{-10}$ at 4.2 K). If the temperature of liquid helium is further reduced, as it is the case in small capillary impedances, for attaining very low temperatures, $T < 3$ K, the excess H_2 will condense and accumulate at the impedance low-pressure side and, after some time, it will produce a total impedance blockage.

Many applications requiring liquid helium cooling are not sensitive to contaminants of any kind and consequently, do not require special provisions for helium cleanness and precautions to avoid contamination during liquid helium refills. On the other hand, there are a considerable number of low-temperature applications that require achieving temperatures below 4 K [5], which are very sensitive to impurities present in the liquid and, therefore, those applications need extreme pure liquid helium for proper operation [13].

3.2. The impedance blocking problem

The impedance-blocking problem arises when liquid helium, containing traces of H_2, is transferred to a cryostat in which the liquid is pumped through a very small capillary or impedance tube, to produce temperatures below 4.2 K using evaporation cooling.

To reduce any impedance blocking, a widespread and generally accepted "low-temperature best practice" is to stop any solid impurity at strategic locations along the helium supply chain with submicron metal-sintered filters. The first opportunity to stop solid impurities in a typical laboratory workflow is while transferring helium from a storage Dewar to the application cryostat for the first time, i.e. during initial cooldown. To this end, many laboratories incorporate a metal filter at the outlet "tip" of the helium transfer line so that the solid impurities are trapped in the line and not transferred into the application cryostat. Once the helium transfer is complete, the line is warmed up, the impurities are flushed away and the tip is ultrasonically cleaned. If any impurities should make it past the first filter, and, furthermore, to filter any other solid impurities already present in the application apparatus, a second "best practice" employed by cryostat designers is to incorporate a similar type of filter at the inlet of the impedance tube at the cold end of the apparatus cryostat.

It is important to appreciate, however, that mechanical filtering of this type is limited in its effectiveness and cannot selectively discriminate and separate H_2 molecules from their helium carrier flow (a two-phase liquid and vapor helium flow), neither during liquid transfer nor during pumping. This is because despite the relatively high binding energies reported for hydrogen with the surface of some solids [14, 15], which involve potentials of the order of several hundred K, the specific surface area per unit volume of the metal-sintered filters commonly used in this application is below 0.5 m^2/g. This is about three-to-four orders of magnitude smaller than the area per unit volume exhibited by state-of-the-art solid H_2 storage devices. Moreover, the porous size of media grade selected (0.5 microns) is also more than three orders of magnitude larger than the H_2 molecular radius. Based on these considerations, the contribution of H_2 physical sorption on the walls of the mechanical filter is estimated to be very small and, furthermore, limited by the very small vapor pressure of solid hydrogen at the temperature of liquid He.

Thus, in light of these considerations, we postulate that despite the adoption of these simple "best practices," H_2 molecules will inevitably first enter the application cryostat during helium refills and then, the impedance fine capillary tubes during continuous operation below 4.2 K. As a result, part of the H_2 molecules, carried by the helium flow, will freeze (or precipitate) inside the capillary. This is a consequence of the reduction in temperature and total pressure of helium, which is accompanied by a sizable reduction in solid hydrogen vapor pressure and in the hydrogen limited solubility in liquid helium. So that, sooner or later, depending on the specific dimensions and helium flow rate pumped through the capillary, a blockage will appear. When this occurs, the whole set up has to be warmed up, at least up to about 14 K (hydrogen melting point) but more often to room temperature, with a dramatic loss of time and liquid helium.

Figure 2 illustrates molecular H_2, present in the liquid helium bath, flowing through a submicron-sized metallic-sintered filter (e.g., 500 nm as average pore size) placed to stop solid impurities entering the fine capillary impedance tube. When the temperature in the capillary is reduced below 3 K by evaporation cooling, the H_2 vapor pressure, as well as the limiting solubility of H_2 in helium, becomes negligibly small ($x_{H_2} < 10^{-14}$). Therefore, all the H_2 present in the liquid helium heterogeneously nucleates along the walls of the impedance tube. A similar mechanism in a completely different working fluid and temperature range, for the freezing of water molecule impurities in nitrogen gas, has been proposed to explain blocking in micromachined Joule-Thomson coolers operating approximately at 100 K [16, 17].

As an example, a typical two-phase He flow of only 1 sL/min, having x_{H_2} =0.35 ppb ($3.5 \cdot 10^{-10}$) of H_2 molecules [i.e., corresponding to the vapor pressure of solid hydrogen in liquid helium under typical laboratory conditions (4.2 K and 100 kPa)], pumped through a cylindrical tube impedance of 66-μm effective diameter [e.g., the low temperature impedance of a Quantum Design, Physical Properties Measurement System (PPMS)] [18], may produce a solid hydrogen cylinder block of 66-μm diameter that, in about 24 h, will have 132 μm of height. The exact time for the blocking to occur will depend on the exact solid hydrogen distribution in the impedance. Instead, several years would be necessary to produce the same effect when pumping helium with a lower concentration of H_2 molecules similar to the vapor pressure of solid hydrogen at 3 K, x_{H_2} =0.0075 ppt ($7.5 \cdot 10^{-15}$). This is the reason why we consider the vapor pressure of solid hydrogen at 3 K negligibly small regarding impedance blockage.

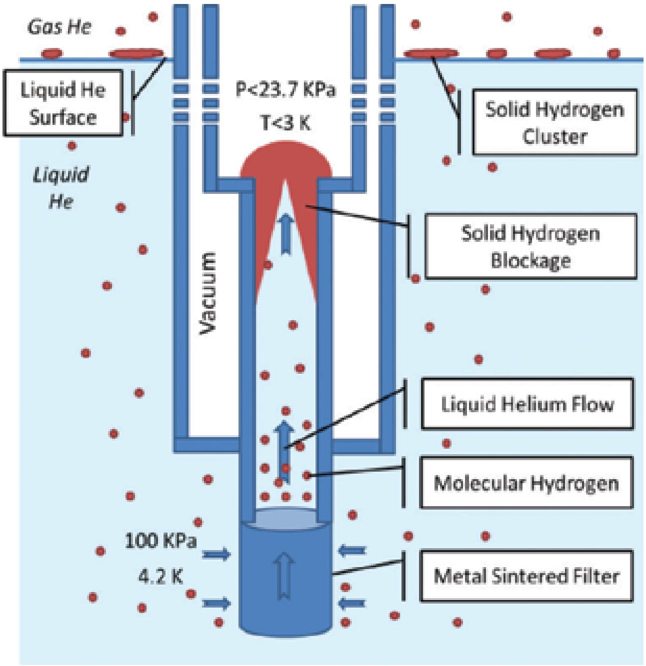

Figure 2. Schematic description of low-temperature impedance blockage by molecular H_2 present in liquid He.

3.3. Pumping two-phase liquid: vapor helium through a capillary impedance tube

When two-phase liquid–vapor He is pumped from a bath at 4.2 K and 100 kPa (10^5 Pa), through a capillary impedance tube, the He stream cools down through its P–T vapor–liquid equilibrium saturation line, $\pi_{H_2}(T)$. Thus, if there is enough hydrogen to form solid clusters, the saturation molar fraction of molecular H_2 in the vapor phase will be the starting concentration, $y_{H_2}(T)\big|_{eq}$. This can be calculated from cryocondensation theory (see Section 5.1), in this case, the vapor pressure saturation line of hydrogen, $\pi_{H_2}(T)$:

$$y_{H_2}(T)\Big|_{eq} = \frac{\pi_{H_2}(T)}{\pi_{He}(T)}, \quad T \le 4.2K \tag{2}$$

On the other hand, at the very low concentration levels under discussion, solid hydrogen may dissolve in the liquid [12]. In that case, the molar fraction of solid H_2 dissolved in the liquid phase, $x_{H_2}(T)$, may be estimated from classical solubility theory.

Figure 3 shows the saturation molar fraction of H_2 in the vapor phase, $y_{H_2}(T)\big|_{eq}$, calculated using expression [Eq. (2)] in the interval 3–4.2 K (solid line). Similarly, the molar fraction of H_2 obtained from its theoretical limiting solubility in the liquid phase, $x_{H_2}(T)\big|_{eq}$, obtained from expression (1) in the work of Jewel and McClintock [12] (dashed line), is also shown. Both are very similar.

Thus, a well-defined lower limit for H_2 concentration as a function of temperature in helium vapor phase is obtained from the vapor pressure of solid hydrogen. Since solid hydrogen can be considered as a volatile solute (i.e., the solute vapor pressure is not negligible) for T > 3 K, there is a well-defined minimum solubility in the liquid phase for each temperature. This minimum solubility is also obtained from the vapor pressure. Furthermore, to know whether the actual value of the solubility of H_2 in the liquid phase is higher than the minimum value is not relevant because this already justifies the experimentally observed blockage times. In fact, if it is higher, it will just reduce the blockage time of the impedance.

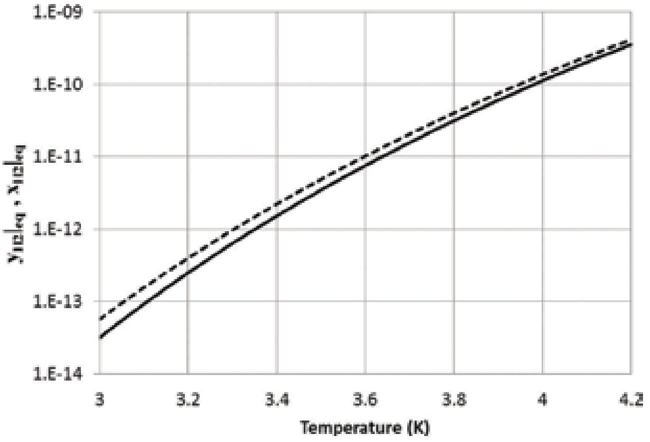

Figure 3. Low-temperature H_2 saturation molar fraction in helium, obtained from the limiting solubility of H_2 in He (dashed line, $x_{H2}(T)\big|_{eq}$ [12]), and, from the H_2 equilibrium-saturation vapor pressure (solid line, $y_{H2}(T)\big|_{eq}$ [19]), as a function of T in the range 3–4.2 K, at π_{He}(T).

Thus, when the pumped helium stream expands and cools down inside the capillary impedance, from 4.2 to 3 K, the H_2 molar fraction in the two-phase liquid–vapor helium flowing through the impedance decreases by four orders of magnitude (from $\approx 10^{-10}$ to $\approx 10^{-14}$), and, consequently, the excess H_2 freezes or precipitates and blocks the capillary.

4. Sources of hydrogen in helium

Helium is a nonrenewable and scarce resource on Earth. It is formed by natural radioactive decay from some thorium and uranium minerals. Today, commercial helium is predominantly extracted from natural gas sources. Alternative sources of helium production have been investigated over the years such as the ability of extracting helium from non-hydrocarbon sources. In 2016, scientists from the United Kingdom reported the discovery of a large helium reserve, 54 BCN (1.53×10^{12} sL, i.e., 2.7×10^5 Tm) in Tanzania, trapped in ancient rocks and not intermixed with natural gas [20]. Additionally, the possibilities of helium extraction from the atmosphere [21] or from CO_2 stream [22] are being studied. Despite these future opportunities, helium is still a nonrenewable resource that must be used responsibly by mankind. This implies recycling helium when it is possible.

The present commercial helium production is extracted from a few natural gas fields around the world (located in Canada, the USA, Algeria, Poland, Qatar, China, Russia, Australia and Indonesia). These sources have a considerable amount of helium-rich gas (around 1%) to make extraction economically feasible.

Let us consider the Linde Group helium extraction facility in Darwin, Australia [23]. In this facility, the raw feed gas flow is 20,730 Nm^3/h with up to 3 mol% helium. The purification process of the feed gas consists of partial condensation of nitrogen in two stages, cryogenic adsorption and finally, catalytic oxidation of hydrogen followed by a dryer system.

After the purification, the refined helium is liquefied using a Bryton process and stored for further distribution. The raw gas has 0.1 mol% of hydrogen (1000 ppm), and the final processed 99.999% helium has up to 1 ppm.

Therefore, molecular H_2 is naturally present in helium gas as obtained from natural gas sources [24], and, in general, different methods are used to eliminate it, prior to large-scale helium liquefaction, for worldwide distribution [23, 25]. However, despite the effort to eliminate it completely, very precise analytical methods indicate that even ultra-high pure commercial grade He gas, 99.9999% pure, thus, containing less than 1000 ppb in volume of total impurities, may contain up to 500 ppb in volume of H_2 (i.e., a hydrogen molar fraction $y_{H_2} = 5 \cdot 10^{-7}$ in He gas) [21, 26–28].

If the purified helium gas has a molar fraction of y_{H_2} =500 ppb ($5 \cdot 10^{-7}$), after the liquefaction of this gas, the liquid helium will contain solid hydrogen in equilibrium with a molar fraction of H_2 molecules given by x_{H_2} =0.35 ppb ($3.5 \cdot 10^{-10}$) (i.e., corresponding to the vapor pressure of solid hydrogen in liquid helium under typical laboratory conditions [4.2 K and 100 kPa)], and, as we have seen in the previous section, this small amount of hydrogen may produce blockages in thin impedances in only a few hours.

Apart from natural gas sources, there are other possibilities to introduce small amounts of hydrogen in the helium recovery system. These include oil degradation in high-pressure compressors or pumps, outgassing of metallic pipes or diffusion of naturally present atmospheric H_2 [29] through plastic pipes and gas bags [30]. Thus, the presence of traces of H_2 in laboratory Helium Recovery Plants: Large Scale (LS-HRP) or Small Scale (SS-HRP), up to the ppm range ($y_{H_2}=10^{-6}$), seems to be unavoidable.

5. Clean helium recovery plant

Up to this point, we have described the impedance blocking problem, and we have shown how a small amount of H_2 ($y_{H_2}<10^{-10}$) is enough to produce the blocking of fine capillary tubes used to achieve temperatures below 4.2 K in helium-pumped cryostats. We have seen that hydrogen is naturally present in raw helium sources. Therefore, the production of hydrogen-free "Clean" helium is necessary to reliably operate cryostats with small impedances for long periods without interruptions. In the following paragraphs, we present a helium recovery plant capable of producing "Clean" helium.

We propose a helium purification and liquefaction system layout using small-scale helium liquefiers based on closed-cycle refrigerators (cryocoolers). The commercial Advanced technology liquefiers (ATLs) [31, 32] have a liquefaction rate of 30 L/Day with a performance of 0.16 (L/h)/kW, close to the performance of industrial size Collins liquefiers (0.5–1.2 (L/h)/kW) [33]. This technology adapts the liquefaction rate to the consumption, it is modular and scalable and it covers needs of consumption from a few liters per day up to liquefaction rates of the Collins industrial technology >240 L/Day.

The purification stage of the "Clean helium" recovery plant proposed is based on a combination of two purification techniques:

- the cryocondensation, performed with an advanced technology purifier (ATP) [34], for the elimination of all the impurities present in the recovered helium, except hydrogen and
- the chemisorption of hydrogen by a non-evaporable getter alloy.

5.1. Cryocondensation by advanced technology purifier

Purification by cryocondensation [35] is a method to separate undesired components (impurities) from a given mixture, by freezing them. The effectiveness of this method depends on the working temperature of the purifier; it must be low enough to ensure that the vapor pressure of the impurities is negligible. The cryocondensation method can provide high levels of purification at low temperatures, even at high-input gas flows and without the need of consumable items.

For this first stage, we use the advanced technology purifiers (ATPs) [34]. These purifiers are equipped with a 10 K class cryocooler (Sumitomo CH-208R) as the refrigerator element.

The gas input flows into the Dewar neck at room temperature, and it is cooled in direct contact with the cold head and the output heat exchanger while it descends through the neck down to the Dewar bottom.

When the gas reaches the condensation temperature for the component "j" (see **Figure 4**), at some point, near the cold head first stage, the component "j" will start to solidify by impingement on the metallic cold surfaces of the cold head cylinder and heat exchanger walls. Below the cold head, the gas temperature decreases further, and the molar fraction in the vapor phase of the component "j" will decrease rapidly with T, as πj (T):

$$y_j(T) = \frac{\pi_j(T)}{p_T}, \quad T \leq T_j \tag{3}$$

When a region of temperature of ≈15 K is reached, the helium can be considered pure from all impurities except for hydrogen and neon. At this point, the gas passes through a mechanical filter with a passage in the micron range, which will avoid the possible dragging of solid particle impurities toward the output.

After the filter, to be energy efficient, the clean and cold helium is forced to exchange the enthalpy from 15 to 300 K with the warm and dirty helium that enters the purifier. To do that, the helium output path consists of a heat exchanger in the form of a thin-walled stainless-steel tube coiled with the form of a solenoid around the cold head.

Thanks to the heat exchange, the cold outgoing gas cools the warm incoming gas, and therefore, the required power of the cold head is minimized. So, the system can manage high flows. In addition, the coldhead excess power during purification will counteract the growing inefficiencies caused by the solid impurities' coating around the cold surfaces.

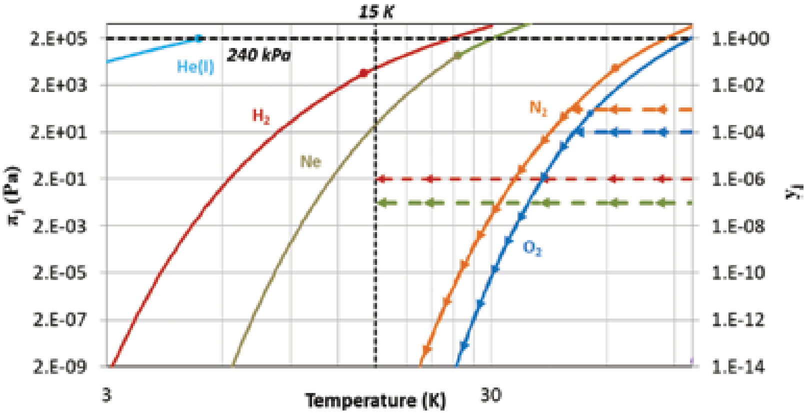

Figure 4. Partial pressures π_j(T) and molar fractions $y_j(T)$ of H_2, Ne, N_2 and O_2 in a gas mixture at 240 kPa [19]. The arrow lines indicate examples of impurities cooldown paths [e.g., initial impurities concentration in the mixture: H_2 (1 ppm), Ne (0.1 ppm), O_2 (100 ppm) and (N_2 1000 ppm)]. Starting from the high temperature side, the molar fraction of each impurity is constant until its vapor pressure line is reached, after which it decreases exponentially. Black dashed lines indicate the working point of the purifier filter, at 240 kPa and 15 K.

This system can purify gas flows up to 30 sL/min with 10,000 ppm of impurities. The output flow quality is about six orders of magnitude better for the main contaminants (i.e., air in the case of recovered helium).

The purifier can operate without interruptions during, at least, 1 month, and can purify more than 1 million sL of recovered helium (with a typical average impurity volume concentration of 300 ppms in total). The regeneration procedure is totally automated and it takes 7 h. Thus, the operational down-time ratio is only 1.25%.

Once the main contaminants have been removed, the second purification stage needs only to eliminate the remaining hydrogen via chemisorption by the non-evaporable getter (NEG) material.

5.2. Chemisorption by non-evaporable getter materials

Getters are solid materials, usually metallic alloys, which can chemisorb gas molecules in its surface; they can be considered as chemical pumps. They are widely used for a variety of applications such as vacuum systems, electronic devices, sensors and MEMS, energy devices, gas purification, and so on. [36]

For a proper absorption of gas molecules, the surface of the getter material must be clean. The surface cleaning process, also called getter activation, is done in two different ways, depending on the type of getter:

- For evaporable getters, the active surface is obtained by sublimation under vacuum of a fresh metallic film.
- For non-evaporable getters (NEGs), the active surface is produced by thermal diffusion of the surface contaminants into the bulk of the NEG material itself. After air exposure, the main contaminant is oxygen present in the passivating oxide layer.

For gas purification systems, NEGs are generally used, and from now on, we focus on them.

NEGs are typically based on zirconium alloys. Examples of these alloys are Zr(84%)-Al(16%) and Zr(70%)-V(24.6%)-Fe(5,4%). Zirconium-based systems are very reactive for a wide variety of gas molecules such as H_2, H_2O, O_2, N_2, CO, CO_2, and so on.

For active gases such as N_2, O_2, CO, CO_2, and so on, the reactions proceed by dissociative chemisorption followed by a reaction to form oxides, carbides or nitrides [37]. If the concentration of these gases is high, the getter surface is quickly passivated. To maintain active state of the getter surface, the material can be maintained at high temperature (e.g., 400°C), thus avoiding the formation of a passivation layer. In this way, the surface contaminants diffuse into the bulk of the NEG material.

Hydrogen sorption is governed by a different reaction. Hydrogen easily diffuses into a getter because it dissociates on the getter surface into atomic hydrogen. The hydrogen atoms easily slip into the atomic lattice of the metal grains [37]. As Rameshan explains, hydrogen in the interior of a NEG forms a solid solution that exhibits an equilibrium pressure, which depends on the concentration of the hydrogen and the temperature of the material. Sieverts' law describes this relationship:

$$\log P = A + 2\log Q - B/T \tag{4}$$

where P is the H_2 equilibrium pressure in torr, Q is the H_2 concentration in the NEG alloy in torr·L/g, T is the temperature of the getter in K and A and B are constants for different NEG alloys (e.g., A = 4.8, B = 6116 for Zr(70%)-V(24.6%)-Fe(5,4%), commercialized under the name St707 [38]). When the hydrogen concentration exceeds 20 torr·L/g, a phenomenon called "hydrogen embrittlement" occurs due to the change of the lattice parameters [37]. With enough time under these conditions, the getter alloy becomes a fine powder that can cause problems in the getter application.

An NEG material working at ambient temperature is an ideal candidate for the elimination of the remaining molecular hydrogen in helium that has been purified by cryosorption in the ATP. **Figure 5** shows that the hydrogen concentration in helium after passing through the getter will be better than grade 14 ($y_{H_2} \ll 10^{-14}$), that is, several orders of magnitude lower than at 400°C. Even more, the hydrogen capacity of the getter is higher, and the sorption speed is still reasonably high [38].

5.3. Clean helium recovery plant configuration

Our "Clean helium" (extreme pure helium free of molecular H_2) low-pressure ($P < Pc$) SS-HRP concept is depicted in **Figure 6**. The plant is initially fed with commercial grade 5 (99.999% pure) helium gas that may contain up to a H_2 molar fraction of 10^{-6} [25]. The gas is further purified by cryocondensation by one or more cryo-refrigerator-based purifiers (ATPs), each with a total effective volume to store solid impurities of several liters and a maximum purification flow rate of around 30 sL/min at 20 K.

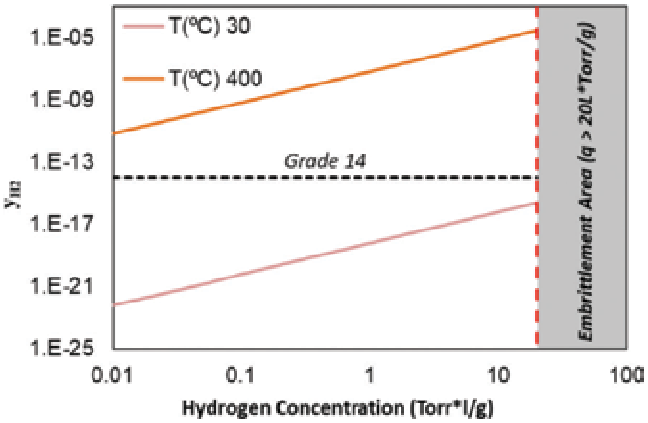

Figure 5. Hydrogen molar fraction, y_{H_2}, calculated from equilibrium isotherms of the St 707 getter alloy obtained from Sievert's law. y_{H_2} increases accordingly when the material captures hydrogen molecules until it reaches the embrittlement area.

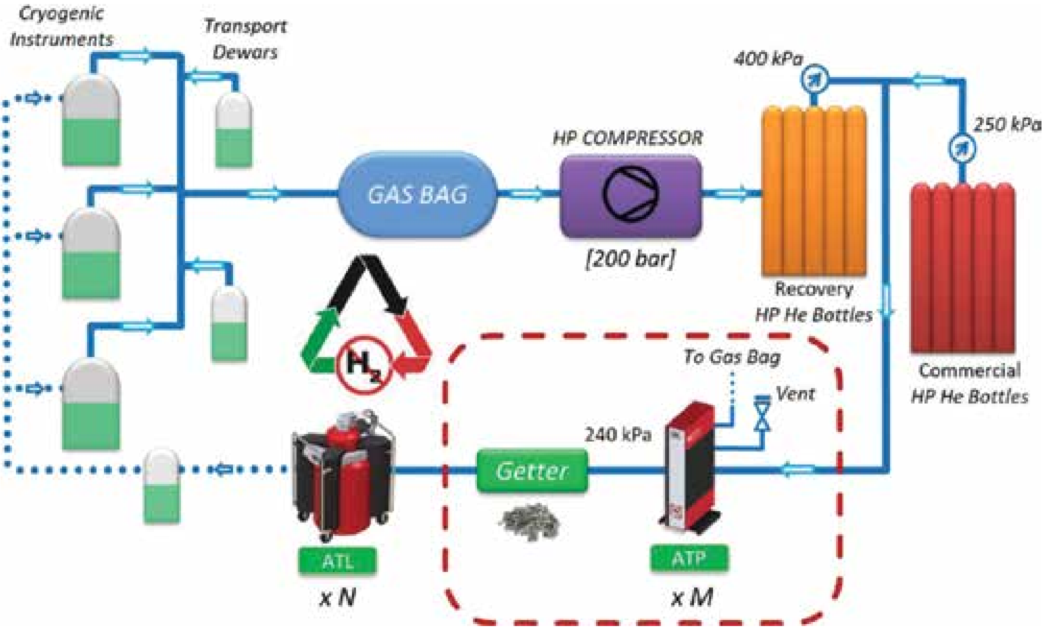

Figure 6. Schematic configuration of a small-scale "Clean Helium" recovery plant (free of hydrogen). Gas bag, compressor and recovery helium bottles are not completely free of H_2 (orange). The commercial He bottles are the main source of contamination (red). The bypass is closed when the ATP operation temperature is T > 3 K.

The purification temperature in the coldest zone of the ATP Dewar will be in the range between 10 and 30 K, and this does not guarantee a negligible vapor pressure of solid H_2 nor a negligible solubility in liquid He. Thus, the purified gas will contain H_2 molecules that need to be eliminated before liquefaction. A solution tested in our plant consists of the chemisorption of the remaining H_2 molecules in the ATP output gas by a getter material at room temperature (**Figure 6**). The non-evaporable getter (NEG) materials used in this study are:

- thermally activated media-based [Zr(70%)-V(24.6%)-Fe(5.4%)] St707 [38] and
- Ni(31%)-NiO(32%)-SiO_2(24%)-MgO(13%)-based oxides working at room temperature.

This solution is extremely efficient since there are no helium losses at all. On the other hand, in this configuration, the St707 getter only traps hydrogen, and it does in a reversible way. Therefore, once it is near saturation, typically, every two years, it can be regenerated by heating it up to a specific H_2 desorption temperature (typically >500°C).

The H_2-free He from the double purification stage (cryocondensation + chemisorption) is then fed a parallel network of advanced technology liquefiers (ATLs) [31] that produce H_2-free ultra-pure liquid helium (named by us as "Clean Helium"). The instruments are always filled with ATL "Clean Liquid Helium." Obviously, commercial liquid helium should never be transferred to hydrogen-sensitive instruments because the absence of H_2 is not guaranteed. In this small-scale HP-HRP, helium boil-off from the cryogenic instruments is collected in a gas bag and compressed in the recovery bottles at 2 × 10^4 kPa (200 bar). A H_2O dryer, plumbed in the series after the compressor, not shown in the scheme of **Figure 6**, should always be used.

When a pressure drop develops between the input and the output of one of the ATPs, due to the accumulation of solid impurities (H_2, N_2, O_2), an ATP regeneration process is automatically initiated. The input and the output gas ports of the given ATP are closed, so that this ATP is now isolated and the entire ATP Dewar volume is heated up to around 130 K so that all the low-vapor pressure impurities, collected in solid form, for example, H_2, N_2 and O_2, are sublimated and released to the atmosphere through a vent valve. Before restarting a new purification cycle, the ATP cools down again to the temperature of normal operation at 10 K.

Nevertheless, as we have seen in Section 5.2, some getter materials are capable of eliminating other impurities besides hydrogen; the chemical reactions are competitive. Therefore, if the input gas contains other impurities (e.g., some ppms of O_2, N_2, H_2O, etc.), the getter duration until the saturation is reduced significantly.

In the first version of the "Clean Helium" plant, we used a getter placed after the commercial pure helium (99.999%, less than $y_j < 10^{-5}$ in total) bottles (**Figure 7**). With this configuration, we were able to produce hydrogen-free liquid helium in 3 months. From that moment, impedance blockages start to appear due to the saturation of the NEG produced by the presence of different impurities (N_2, O_2, CO, CO_2, etc).

The purified helium at the ATP output, with a working temperature < 20 K, has a negligible concentration of molecular content ($y_j < 10^{-14}$) of all impurity constituents (i.e., N_2, O_2, H_2O,

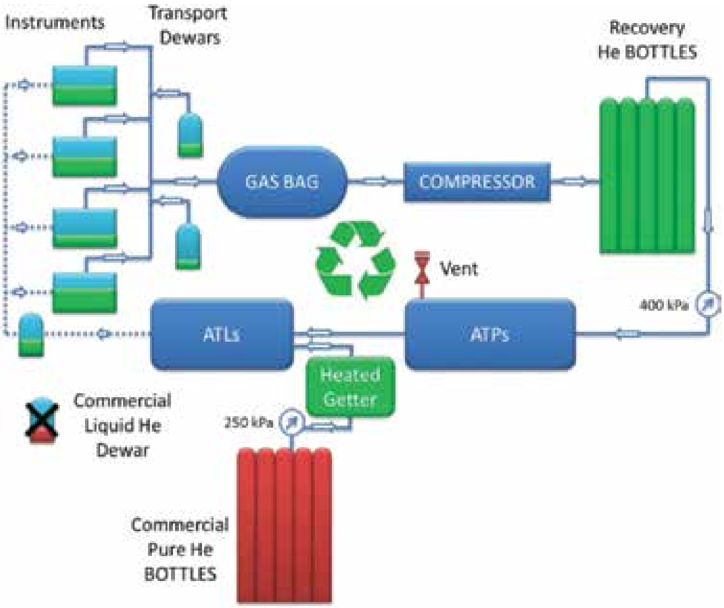

Figure 7. Schematic configuration of a first-generation small-scale helium recovery plant . The commercial He bottles are the main source of H_2 contamination (red), and it is purified with a heated getter before helium enters in the recovery plant.

CO_2, etc.) except for the neon and hydrogen case (see **Figure 4**). The neon is not a problematic substance for the impedance clogging issue, since at liquid helium temperature (4.2 K at P_{atm}), the vapor pressure is negligible; besides, if there exists a molecular concentration at higher temperatures, it is not affected by the getter material because it is a noble gas like helium. Therefore, the best place to put the hydrogen grabber is at the ATP output (**Figure 6**), when the helium is extremely pure. In fact $y_j < 10^{-14}$ for all the substances except for the $H_{2;}$ thus, the unique function of the getter is to capture H_2. In this way, the process is optimized and the life of the getter material extends.

The "Clean helium" gas produced by the Clean Helium Recovery Plant (**Figure 6**) is ultimately liquefied in a commercial ATL and transferred directly or by intermediate transport Dewars into the application instruments. The evaporated gas from non-H_2 sensitive instruments, that could be initially filled with commercial non-"Clean" liquid (e.g., NMRs, MEGs, high field magnet cryostats, etc.), and can have a hydrogen quantity equal or below that corresponding to the vapor pressure of the hydrogen at 4.2 K and 100 kPa (i.e., $y_{H_2} = 3.5 \cdot 10^{-10}$), is also collected in the gas bag, compressed and injected again in the ATPs for purification and complete elimination of the H_2 impurities.

The validity of the "Clean helium" plant concept is demonstrated by the fact that impedance blockages have been completely eliminated for more than 3 years, when the plant configuration was implemented in the Cryogenic Liquids Service at the University of Zaragoza [39]. Furthermore, the efficiency of the double purification method presented in this chapter was verified by extra-sensitive H_2 detection techniques presented in [2], for both gas and liquid phases.

6. Conclusions

We have proposed a plausible mechanism for explaining the capillary blocking issue that occurs in many laboratories using helium evaporation cryostats. The unavoidable presence of traces of molecular hydrogen is at the heart of the problem. Molecular hydrogen condenses in the low-pressure side of the fine capillary tubes when helium is pumped to obtain temperatures below 4.2 K. Finally, we have found a solution to produce hydrogen-free liquid helium in two steps: (1) cryocondensation of the air components and (2) chemical adsorption of hydrogen molecular traces that are not solidified in step (1). We have already demonstrated the validity of this solution for more than 3 years.

Acknowledgements

The authors are greatly appreciative and acknowledge the financial support from the Spanish Ministry of Economy and Competitiveness through the Project No. MAT2015- 64083-R and through the *Personal Técnico de Apoyo (PTA) 2016* program for personal funding. They would also like to acknowledge the use of Servicio General de Apoyo a la Investigación-SAI, Universidad de Zaragoza

Thanks

We want to acknowledge the collaboration and support of the technical team of the Servicio General de Apoyo a la Investigación-SAI, specifically to Mrs. M. Castrillo, Mr. D. Finol, Mr. F. Gómez, Dr. A. Arauzo, Mr. E. Guerrero and Mr. P. Tellez for their technical support. We thank Dr. Christoph Haberstroh from TU Dresden for additional discussion and very useful information.

Author details

Miguel Gabal[1,2], Javier Sesé[1,3], Conrado Rillo[1,4]* and Stefano Spagna[5]

*Address all correspondence to: crillo@unizar.es

1 Departamento de Física de la Materia Condensada, Universidad de Zaragoza,
Zaragoza, Spain

2 Servicio General de Apoyo a la Investigación-SAI, Universidad de Zaragoza,
Zaragoza, Spain

3 Instituto de Nanociencia de Aragón (INA), Universidad de Zaragoza, Zaragoza, Spain

4 Instituto de Ciencia de Materiales de Aragón (ICMA), Universidad de Zaragoza-CSIC,
Zaragoza, Spain

5 Quantum Design Inc., San Diego, California, USA

References

[1] Marin JM, Boronat J, Casulleras J. Finite H_2 concentrations in superfluid 4He. Physica B. Jul. 2000;**284-288**:95-96

[2] Gabal M. New Cryocooler-Based Helium Liquefaction and Purification Techniques. From Recovered Gas to Ultra-Pure Liquid [thesis]. Colección de Estudios de Física. University of Zaragoza; 2016

[3] Pobell F. Matter and Methods at Low Temperatures. Berlin, Heidelberg: Springer Berlin Heidelberg; 2007

[4] Engel BN, Ihas GG, Adams ED, Fombarlet C. Insert for rapidly producing temperatures between 300 and 1 K in a helium storage Dewar. The Review of Scientific Instruments. Sep. 1984;**55**(9):1489

[5] DeLong LE, Symko OG, Wheatley JC. Continuously operating ^{4}He evaporation refrigerator. The Review of Scientific Instruments. Nov. 1971;**42**(1):147

[6] Gabal M, Arauzo A, Camón A, Castrillo M, Guerrero E, Lozano MP, Pina MP, Sesé J, Spagna S, Diederichs J, Rayner G, Sloan J, Galli F, van der Geest W, Haberstroh C, Dittmar N, Oca A, Grau F, Fernandes A, Rillo C. Hydrogen-free liquid-helium recovery plants: The solution for low-temperature flow impedance blocking. Physical Review Applied. Aug. 2016;**6**(2):24017

[7] Abrikosova II, Shal′nikov AI. The purity of liquid helium. Cryogenics (Guildf). 1971; **11**(2):137-138

[8] Riehl JW, Kinsey JL, Waugh JS, Rugheimer JH. Spin–lattice relaxation and the anisotropic part of the he-H2 intermolecular potential. The Journal of Chemical Physics. Sep. 1968;**49**(12):5276

[9] Riehl JW, Fisher CJ, Baloga JD, Kinsey JL. Spin-lattice relaxation and the anisotropic part of the H_2-He and H_2-Ne intermolecular potential. The Journal of Chemical Physics. Aug. 1973;**58**(10):4571

[10] Gordon MD, Secrest D. Helium-atom–hydrogen-molecule potential surface employing the LCAO–MO–SCF and CI methods. The Journal of Chemical Physics. Sep. 1970;**52**(1):120

[11] Silvera IF. Ultimate fate of a gas of atomic hydrogen in a liquid-helium chamber: Recombination and burial. Physical Review B. Apr. 1984;**29**(7):3899-3904

[12] Jewell C, McClintock PVE. A note on the purity of liquid helium-4. Cryogenics (Guildf). Nov. 1979;**19**(11):682-683

[13] Dittmar N, Welker D, Haberstroh C, Hesse U, Krzyzowski M. Operating parameters of liquid helium transfer lines used with continuous flow cryostats at low sample temperatures. IOP Conf. Ser. Mater. Sci. Eng. vol. 101. no. 1. p. 12097, Dec. 2015

[14] Züttel A. Hydrogen storage methods. Naturwissenschaften. 2004;**91**(4):157-172

[15] Bénard P, Chahine R. Storage of hydrogen by physisorption on carbon and nanostructured materials. Scripta Materialia. 2007;**56**(10):803-808

[16] Lerou PPPM, ter Brake HJM, Holland HJ, Burger JF, Rogalla H. Insight into clogging of micromachined cryogenic coolers. Applied Physics Letters. Feb. 2007;**90**(6):64102

[17] Cao HS, Vanapalli S, Holland HJ, Vermeer CH, ter Brake HJM. Clogging in micromachined Joule-Thomson coolers: Mechanism and preventive measures. Applied Physics Letters. 2013;**103**(3):34107

[18] Model PPMS 9T (Physical Properties Measurement System). San Diego, CA, USA: manufactured by Quantum Design Inc

[19] Lemmon EW, Huber ML, McLinden MO. NIST Standard Reference Database 23: Reference Fluid Thermodynamic and Transport Properties, version 9.1. Natl. Inst. Stand. Technol. Gaithersbg. 2013

[20] Danabalan D, Gluyas JG, Macpherson CG, Abraham-James TH, Bluett JJ, Barry PH, Ballentine CJ. New high-grade helium discoveries in Tanzania. In: Goldschmidt Conference, 2016, vol. 47, no. 2002, p. 2497

[21] Nuttall WJ, Clarke RH, Glowacki BA, editors. The Future of Helium as a Natural Resource. Routledge; 2012

[22] Cockerill R. Air Products to obtain helium from CO_2. 2013. [Online]. Available: http://www.gasworld.com/news/helium-air-products-to-obtain-helium-from-co2/2002951.article

[23] Lindemann U, Boeck S, Blum L, Kurtcuoglu K. Turnkey Helium Purification and Liquefaction Plant for Darwin, Australia. AIP Conf. Proc., vol. 1218, no. 1, pp. 271-274, 2010

[24] McFarland DF. Composition of gas from a well at Dexter, Kan. Transactions of Kansas Academy of Science. 1903;**19**:60-62

[25] Froehlich P, Clausen JJ. Large Scale Helium Liquefaction and Considerations for Site Services foe a Plant Located in Algeria. In: AIP Conference Proceedings, 2008, vol. 985, pp. 549-556

[26] Linde Helium Catalog, Linde Gases Division, USA. 2016

[27] Air Liquide Specialty Gases catalog, Air Liquide Group, France. 2016

[28] Praxair Helium Catalog. Danbury, USA: Praxair Technology, Inc; 2016

[29] Novelli PC, Lang PM, Masarie K a, Hurst DF, Myers R, Elkins JW. Molecular hydrogen in the troposphere: Global distribution and budget. Journal of Geophysical Research. 1999;**104**(D23):30427

[30] Gabal M, Lozano MP, Oca A, Pina MP, Sesé J, Rillo C. Helium contamination through polymeric walls. Physics Procedia. 2015;**67**:141-146

[31] Model ATL 160 (Advanced Technology Liquefier). San Diego, CA, USA: manufactured by Quantum Design Inc. Available at: http://www.qdusa.com/products/helium-liquefiers.html

[32] Rillo C et al. Enhancement of the liquefaction rate in small-scale helium liquefiers working near and above the critical point. Physical Review Applied. 2015;**3**(5):51001

[33] Chialvo C et al. Smart energy compressors for helium liquefiers. In S. D. Miller & R. G. Ross Jr, eds. Cryocoolers 18. International Cryocooler Conference, Inc., Boulder, CO.; 2014. pp. 551-556

[34] Model ATP 30 (Advanced Technology Purifier). San Diego, CA, USA: manufactured by Quantum Design Inc. Available at: http://www.qdusa.com/products/helium-liquefiers.html

[35] Barron RF. Separation and purification systems. In: Cryogenic Systems. Clarendon Press; 1985. pp. 223-226

[36] SAES, "Getter Applications." [Online]. Available: https://www.saesgetters.com/applications

[37] Rameshan R. Getters for reliable hermetic packages. Jet Propulsion. 1999;**100336**:1-89

[38] St707 Non Evaporable Getters Activatable at Low Temperature, manufactured by SAES Pure Gas Inc., CA, USA

[39] Servicio de Líquidos Criogénicos. Servicio General de Apoyo a la Investigación - SAI. Zaragoza. Spain: Universidad de Zaragoza

Section 3

Superconductivity: Modelling and Experiment

Chapter 5

Intermediate State in Type-I Superconductors

Vladimir Kozhevnikov

Additional information is available at the end of the chapter

http://dx.doi.org/10.5772/intechopen.75742

Abstract

Intermediate state in type-I superconductors is one of the oldest challenges of superconductivity put forward by Gorter and Casimir, Pearls, F. London, and Landau back in the 1930s. In this chapter, we review the main properties of this state and principal theoretical approaches to interpret them. Recent experimental and theoretical achievements in this field are discussed in more details.

Keywords: type-I superconductors, intermediate state, thermodynamic properties, magnetization

1. Introduction

Intermediate state (IS) is defined as a thermodynamically equilibrium state in which a type-I superconductor is split for domains of superconducting (S) and normal (N) phases [1–3]. For completeness of description, we begin with a brief overview of properties of the Meissner state, which will be necessary for discussion of the IS properties.

1.1. Meissner state in cylindrical specimens

Consider a specimen of a type-I superconductor at temperature $T < T_c$ in a free space (vacuum) subjected to a uniform magnetic field $H < H_{cr}(T)$, where T_c is critical temperature at zero field and $H_{cr}(T)$ is critical field of the S/N transition at given T. (We use notation H_{cr} instead of commonly used H_c because the latter is reserved for thermodynamic critical field, which can be different from H_{cr}). Assume that the specimen is a long cylinder with a circular base of radius $R \gg \lambda$ (λ is the penetration depth) and H is parallel to the cylinder as shown in **Figure 1a**. A demagnetizing factor η [2, 4] of such a specimen is zero, which means that outside it $B = H_i = H$ (we use CGS units) all the way down to the sample surface.

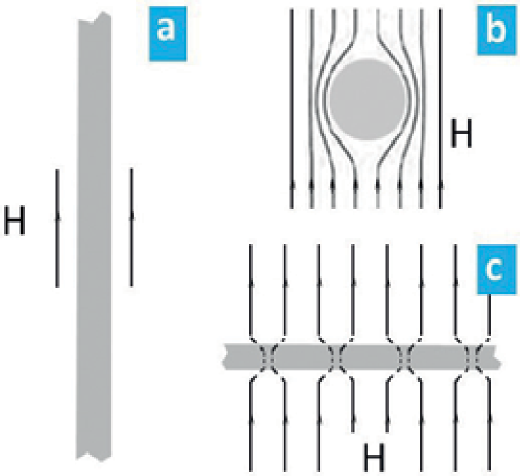

Figure 1. Cross-sectional view of specimens (shown in gray) with demagnetizing factor $\eta = 0$ (a), $\eta = 1/2$ (b), and $\eta = 1$ (c) in a weak magnetic field H. In (a) and (b) the specimen (a cylinder) is in the Meissner state; in (c) the specimen (an infinite slab) is in the intermediate state starting from any H exceeding zero.

Here B is magnetic induction or magnetic flux density [5] or merely B-field [6]. B is an average microscopic magnetic field available for measurements [2]. H_i is magnetic field strength, also referred as magnetic and magnetizing force [4], Maxwell field [7], thermodynamic field [8], magnetic field [5], H-field [6], and others. And H is applied field set by a magnet power supply (for simplicity we will ignore a small contribution of Earth magnetism); it is the field away from the specimen or the field which would be in a space occupied by the specimen if the latter is absent. Away from the specimen, H_i is identical to H, but it can be not so near and inside the specimen. Everywhere outside the specimen, $B = H_i$ because magnetic permeability of the free space, as well as permeability of the N phase in superconductors, $\mu \equiv B/H_i$ is unity by definition.

Our cylindrical specimen is in the Meissner state, implying that inside it $B = 0$ and $H_i = H$ due to continuity of the tangential component of this field [9]. A jump of induction at the specimen surface $\Delta B = H$ means that there is a surface current I, in which linear density $g \equiv I/l = \Delta Bc/4\pi = cH/4\pi$, where l is length of the specimen and c is speed of light. This surface current is regarded as a screening current protecting the specimen interior from the external field. Taking into account direction of $\mathbf{g}$ ($= \mathbf{n} \times \mathbf{H}c/4\pi$, where $\mathbf{n}$ is the unit vector normal to the surface and directed outward), we arrive at a well-familiar formula for the specimen magnetic moment M:

$$M = -gl\frac{A}{c} = \left(\frac{cH}{4\pi}l\right)\frac{A}{c} = -\frac{H}{4\pi}V, \tag{1}$$

where A and V are the base area and volume of the specimen, respectively.

The same result follows from definition of the field strength:

$$H_i \equiv B - 4\pi m, \tag{2}$$

where m is magnetization, which in superconductors is a *macroscopic* average of the magnetic moment per unit volume $m = M/V$ and, as it was mentioned above, $H_i = H$ due to geometry of our specimen.

Thermodynamics of our and any other singly connected superconductor can be described using total free energy $\tilde{F}_M(T, V, H)$, which differential $d\tilde{F}_M(T, V, H)$ is [2].

$$d\tilde{F}_M = -SVdT - \mathbf{M} \cdot d\mathbf{H}, \tag{3}$$

where S is entropy per unit volume and a small variation of V due to changing magnetic field is neglected.

Integrating Eq. (3) at constant temperature, we arrive at another well-known and very important formula for the total free energy of the singly connected superconductors in magnetic field [1, 2]:

$$\left(\tilde{F}_M\right)_{sH} = \left(\tilde{F}_M\right)_{s0} - \int_0^H \mathbf{M} \cdot d\mathbf{H} = \left(\tilde{F}_M\right)_n - \frac{H_c^2}{8\pi} V - \int_0^H \mathbf{M} \cdot d\mathbf{H}, \tag{4}$$

where $\left(\tilde{F}_M\right)_{s0}$ is the total free energy of the S state in zero field, $\left(\tilde{F}_M\right)_n$ is the total free energy of the N state, and $\left(H_c^2/8\pi\right)V$ is the condensation energy, where H_c is thermodynamic critical field. Note that, since M in the N state is zero (because μ of the N phase is unity), the total free energy for this state does not depend on the field. This means that $\left(\tilde{F}_M\right)_n = F_{n0}$ and $\left(\tilde{F}_M\right)_{s0} = F_{s0}$, where F_{n0} and F_{s0} are Helmholtz free energies $F(T, V, B)$ in the normal and superconducting states at zero field, respectively.

Importance of Eq. (4) is associated, firstly, with the fact that neither $\left(\tilde{F}_M\right)_n$ nor the condensation energy $\left(H_c^2/8\pi\right)V$ depends on the specimen shape, and therefore Eq. (4) is valid for singly connected specimens of *any* shape. Secondly, Eq. (4) explicitly shows that the extra total free energy (above the free energy of the ground state $\left(\tilde{F}_M\right)_{s0}$) is the specimen magnetic energy $E_M = -\int_0^H \mathbf{M} \cdot d\mathbf{H}$, representing energy of interaction of the external field H with the specimen magnetic moment M induced by this field. More specifically, E_M is kinetic energy of electrons (Cooper pares) carrying the induced currents [1]. And thirdly, Eq. (4) shows that the source of E_M is condensation energy. Finiteness of the later makes transition to the N state a mandatory property of any superconductor [2]. At the S/N transition, the magnetic energy of any specimen equals to its condensation energy, or area under $M(H)$ curve plotted as $4\pi M/VH_c$ vs. H/H_c, when $\mathbf{M}$ is aligned to $\mathbf{H}$, is 1/2.

This as-called rule of 1/2 (or in general case Eq. (4)), represents the energy balance or the first law of thermodynamics for singly connected superconductors at constant temperature; compliance with this rule/equation is a necessary condition for discussion of equilibrium properties of superconductors [1].

Using Eq. (1) for M of our cylindrical sample, we rewrite Eq. (4) as

$$\tilde{F}_M(H) = F_n - \frac{H_c^2}{8\pi}V + \frac{H^2}{8\pi}V. \tag{5}$$

Now a question arises; up to what fields Eq. (1) is valid? Vast majority of superconductors are of type II, for which Eq. (1) holds up to a low critical field $H_{c1} < H_{cr}$ and $H_{cr} = H_{c2}$, which is an upper critical field. However there is a relatively small group of mostly pure elementary materials, for which Eq. (1) (or the Meissner condition $B = 0$) holds in the entire field range of the superconducting state, i.e., up to H_{cr}. Those are type-I superconductors. An example of $M(H)$ dependences for a typical type-I superconductor with $\eta = 0$ is shown in **Figure 2**.

S/N transition takes place when free energies of the S and N states are equal, i.e., $\tilde{F}_M(H_{cr}) = \left(\tilde{F}_M\right)_n$. For our type-I cylindrical sample, as seen from Eq. (5), this implies that $H_{cr} = H_c$ and therefore the S/N transition in specimens with $\eta = 0$ must be discontinuous, i.e., thermodynamic phase transition of the first order, in full agreement with experimental results, e.g., with those shown in **Figure 2**.

1.2. Intermediate state

Now, we turn our cylinder perpendicular to the applied field. In a weak field, the specimen is in the Meissner state (inside it $B = 0$), but the pattern of field lines looks now as shown in **Figure 1b**. The external field near the specimen is tangential to its surface, which follows from always valid conditions of continuity of the normal component of B and of tangential component

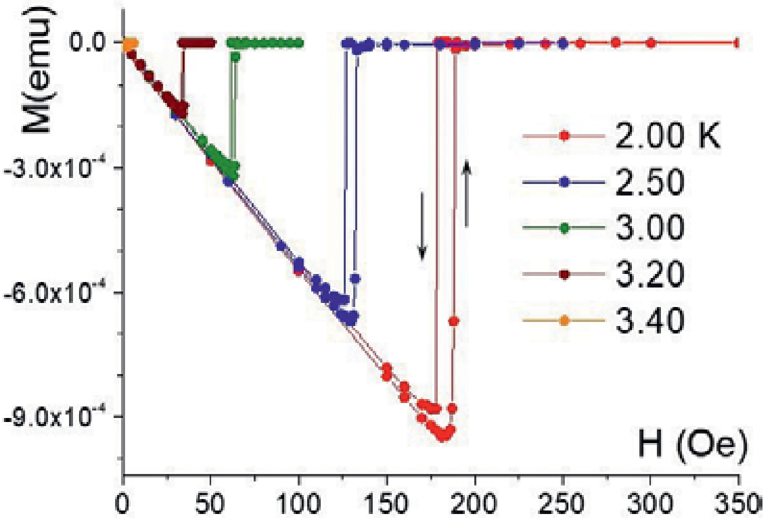

Figure 2. Experimental data for magnetic moment of a pure indium film 2.79 μ m thick measured in parallel applied field H at indicated temperatures. Errors up and down indicate that the measurements were conducted at increasing and decreasing field, respectively.

of H_i [2, 4]. Indeed, our cylindrical specimen in perpendicular field in the Meissner state represents a uniformly magnetized ($B = const = 0$) prolate ellipsoid with $\eta = 1/2$ [2, 4]. Inside of any uniform ellipsoid, H_i is also uniform, and when **H** is parallel to an axis of ellipsoid with respect to which the demagnetizing factor is η, the fields H_i, B, and H are connected with each other as.[1]

$$(1-\eta)H_i + \eta B = H. \tag{6}$$

Hence, the field H_i inside our specimen in the Meissner state is $H/(1-\eta)$, and therefore H_i on the external side of the specimen surface (the external field) is

$$H_i = Hsin\theta/(1-\eta), \tag{7}$$

where θ is the angle between the normal and the applied field **H**.

Therefore near the "poles" of our specimen the field is zero, whereas near "equator" it is twice as big as the applied field. This implies that the external field near "equator" reaches the critical value H_c at $H = H_c(1-\eta) = H_c/2$. When H is increased beyond this value, the field must enter the specimen destroying superconductivity. However, contrarily to the previous (parallel) case, superconductivity cannot be destroyed completely because there is still plenty of condensation energy left in the specimen.

Indeed, the specimen magnetic moment $M \equiv (B - H_i)V/4\pi = -HV/4\pi(1-\eta) = -HV/2\pi$; therefore magnetic energy E_M at $H = H_c/2$ is

$$E_M = -\int_0^{0.5H_c} \mathbf{M} \cdot d\mathbf{H} = \frac{VH_c^2}{16\pi} < \frac{VH_c^2}{8\pi}. \tag{8}$$

Hence, as seen from Eq. (4), $\tilde{F}_M < \left(\tilde{F}_M\right)_n$, and therefore the specimen must remain superconducting.

At the first sight, one might expect that at $H > H_c(1-\eta)$, the field will gradually enter the specimen, thus destroying superconductivity over the field range from $H_c(1-\eta)$ to H_c. The superconducting cylinder in such case would stay resistanceless with gradually changing volume of the S core as shown in **Figure 3**. However, this scenario is problematic because as soon as the field enters the specimen, the density of the field lines near the "equator" decreases and hence the field inside the convex blue region in **Figure 3** becomes smaller than H_c. Then this region should go back to the S state.[2] This means that when $H > H_c(1-\eta)$, the ellipsoidal specimen splits into S and N regions, as it was suggested for the first time by Gorter and Casimir [10].

---

[1] Derivation of Eq. (6) can be found in [2]; Maxwell using it in [4] refers to Poisson.

[2] Historically impossibility of configuration like that shown in **Figure 3** was explained basing on a paradigm of instability of the N phase against transforming to the S phase at $H_i < H_c$ (see, e.g. [8]). However, this (the N phase at $H_i < H$) *does take place* in specimens in the IS, but only at H_i in the upper part of the IS field range. At the lower edge of this range (at $H = (1-\eta)H_c$) B in the first N domain and therefore H_i throughout the specimen is always H_c.

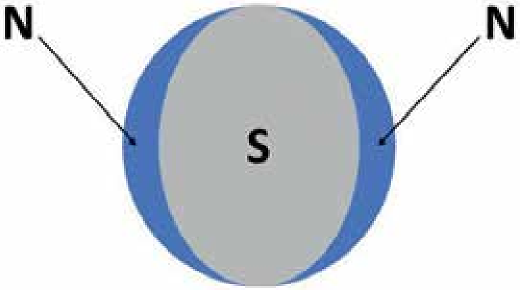

Figure 3. Cross section of the cylindrical sample in case if superconducting phase (S, colored in gray) is gradually replaced by the normal (N, colored in blue) phase filled by the field.

After Peierls [11] this inhomogeneous state in type-I superconductors is named the intermediate state. Properties of the IS were (and in some extent still are) one of the longest-standing challenges of physics of superconductivity. Below we will expose the main theoretical ideas and key experimental achievements addressing these properties. Comprehensive reviews of the experimental and theoretical works on the IS published before 1970 are available in [1, 12, 13]; for references to more recent publications, we recommend papers by Brandt and Das [14] and Clem et al. [15].

2. Model of Peierls and London

The first successful theoretical model of the IS magnetic properties was developed in 1936 independently by Peierls [11] and London [16]. In this model properties of ellipsoidal samples are considered in an averaged limit, in which the nonuniform induction B is replaced by average $\overline{B}$. This allowed to use Eq. (6) with demagnetizing factor η calculated for uniform ellipsoid. However Eq. (6) has two unknowns, B and H_i, both of which are needed to calculate the specimen magnetic moment. Basing on a paradigm that the N phase is unstable at $H_i < H_c$, Peierls and London *postulated* that inside the specimen in the IS (i.e., at $(1-\eta)H_c < H < H_c$),

$$H_i = H_c. \tag{9}$$

Eqs. (2), (6), and (9) constitute a complete system of equations. Solving it one finds B, H_i, and M:

$$H \le H_c(1-\eta)\begin{cases} B = 0 \\ H_i = H/(1-\eta) \\ M = HV/4\pi(1-\eta) \end{cases} \tag{10}$$

$$H_c(1-\eta) \le H \le H_c\begin{cases} \overline{B} = (H - H_c(1-\eta))/\eta \\ H_i = H_c \\ M = V(H-H_c)/4\pi\eta \end{cases}. \tag{11}$$

Graphs of these functions for $\overline{B}$ and M are shown in **Figure 4** in reduced coordinates. It is important that area under the graphs for $4\pi M(H)/VH_c$ vs. H/H_c is the same 1/2. Therefore this model meets the necessary thermodynamic condition of Eq. (4). The PL model fits well experimental data obtained for thick specimens, i.e., when the field inhomogeneities near the surfaces through which the flux enters and leaves the specimen are negligible. Overall, the PL model represents a global description of the IS in zero-order approximation [8]. Similar model for the mixed state in type-II superconductors is available in [17]. For type-I superconductors this new model converts to the model of Peierls and London.

3. Landau laminar models

Magnetic flux structure of the IS was for the first time considered by Landau [18] for an infinite parallel-plane plate (slab) in perpendicular field, i.e., for the sample-field configuration shown in **Figure 1c**. In such a specimen the surface current (and hence the Meissner state) is absent because $\overline{B} = H$, and therefore $g = \left(H - \overline{B}\right)c/4\pi = 0$ at any H from zero to H_{cr}. Due to that the IS starts at H right above zero, no matter how small is this field. Magnetic moment of this specimen (Landau considered thick plate) is $M(H) = (-H_c + H)V/4\pi$; graphs for $\overline{B}$ and M are shown by the green lines in **Figure 4a** and **b**.

Assuming that (i) the plate is split for regularly structured S and N laminae and (ii) the boundary of a cross section of the S laminae is the line of induction B with magnitude H_c at the S/N interface, Landau calculated shape of rounded corners of the S laminae near the sample surface. Landau's scenario for cross section of the S-lamina near the surface is shown in **Figure 5a**. To meet the second assumption, Landau splits a central field line for two branches (*oba* and *ocd* in **Figure 5a**) making a sharp (90°) turn at the splitting point (*o*). Hence, in this scenario the field fills *all* space outside the specimen, as it is supposed to be the case in magnetostatics. On the other hand, splitting the field line challenges the magnetostatics rules [4], and the sharp turn of the line may cost the system too much energy [2, 19].

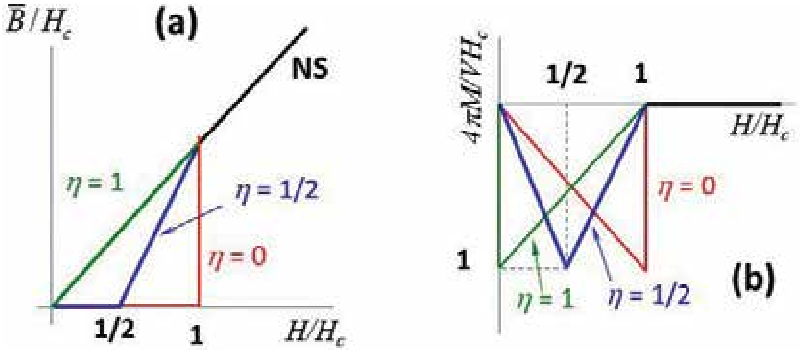

Figure 4. Peierls and London model. Average magnetic induction (a) and magnetic moment (b) for specimens with demagnetizing factor $\eta = 1$ (infinite slab in perpendicular field, green line), $\eta = 1/2$ (long cylinder in perpendicular field, blue line) and $\eta = 0$ (long cylinder in parallel field, red line). NS designates the normal state (black line).

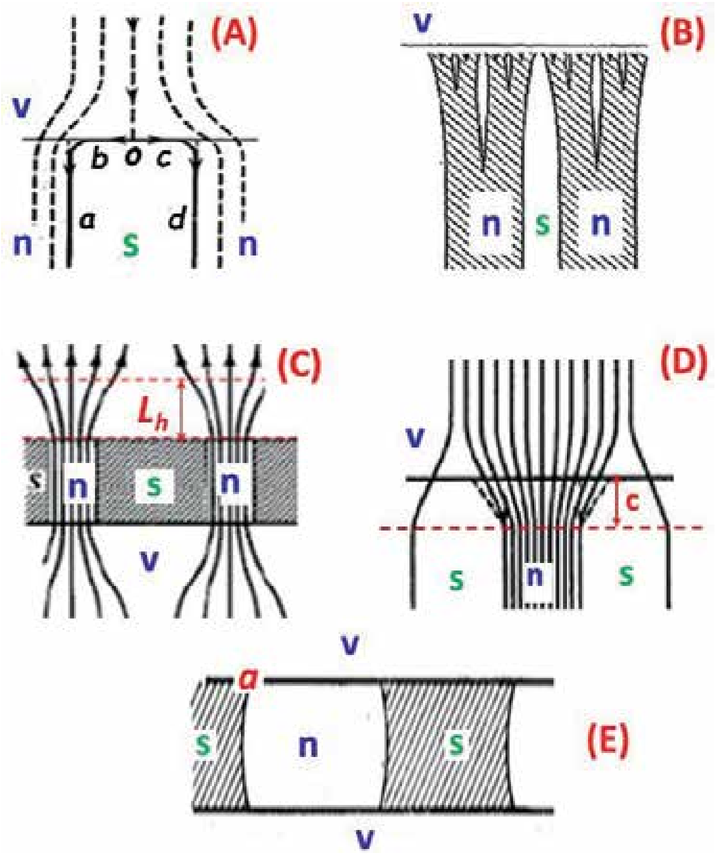

Figure 5. Cross-sectional views of the S and N laminae and of the field distribution (in A, C, and D) near the surface(s) of a type-I plane-parallel slab in perpendicular magnetic field. (A) Landau [18], (B) Landau [19], (C) Tinkham [3], (D) Abrikosov [7], and (E) Marchenko [20]. Letters *s* and *n* designate superconducting and normal phases, respectively; *v* designates the free space. In (C) *v* also designates a void in the static field outside the sample. See text for other notations.

The rounded corners and the field inhomogeneity near the surface yield an excess energy of the system favoring to a fine laminar structure (directly proportional to a period D of the one-dimensional laminar lattice). On the other hand, there is an excess energy associated with the surface tension at the S/N interface in the bulk, which favors to a coarse structure (reversely proportional to D). Optimizing sum of these two energy contributions in the specimen free energy, Landau calculated the period:

$$D^2 = \frac{\delta d}{f_L(h)}, \tag{12}$$

where δ is a wall-energy parameter characterizing the S/N surface tension and associated with the coherence length [2, 3] and $f_L(h)$ is the Landau spacing function determined by the shape of the corners and the near-surface field inhomogeneity and $h = H/H_c$. $f_L(h)$ was calculated numerically in [21], and an analytical form of this function was obtained in [22] (see also [2]).

Soon thereafter Landau abandoned this model, admitting that the proposed flux structure does not correspond to a minimum of the free energy [23]. So, he suggested another so-called branching model [19, 23] (see also [1, 8]), in which N laminae near the surface split for many thin branches as shown in **Figure 5B**, so that the flux emerges from the sample uniformly over the whole surface. However, this branching model was disproved by Meshkovskii and Shalnikov when they for the first time directly measured flux structure of the IS [24].

4. Other versions of near-surface properties

One of the important consequences of the Landau models is demonstration of significance of the near-surface field distribution and domain shape (FDDS) for forming and stabilizing the flux structure of the IS. On that reason it is worth to briefly overview other available scenarios for FDDS.

There are two simplified modifications of the original (non-branching) Landau's version of FDDS.

Tinkham [3] proposed that the dominant contribution in the surface-related properties comes from field inhomogeneities outside the sample extending over a "healing length" L_h as shown in **Figure 5C**. $L_h = \left(D_n^{-1} + D_s^{-1}\right)^{-1}$, where D_n and D_s are the widths of the normal and superconducting laminae, respectively. Correspondingly, Tinkham neglects the roundness of the laminae corners (b and c in **Figure 5A**). This version meets the limiting cases—$D \to 0$ when either $D_s \to 0$ or $D_n \to 0$—and is consistent with images of the IS flux structure (see, e.g., [13, 24, 25]). Tinkham's FDDS works surprisingly well for the IS [25, 26]; it was also successfully validated for the mixed state in type-II superconductors [27]. Note that all of these are in spite of apparent contradiction of the Tinkham's scenario with basics of magnetostatics, since it allows for existence of voids in the static magnetic field near the sample (e.g., in a region designated by v in **Figure 5C**).

Abrikosov [7] proposed another simplified version of Landau's FDDS. He assumed that major role is played by the round corners and therefore neglected the field inhomogeneity outside the specimen. However, the latter means that the field near the surface is uniform, and therefore this scenario is inconsistent with images of the IS flux structure. Abrikosov's version of FDDS is shown in **Figure 5D**, where size of the corners c is the same as L_h in the Tinkham's scenario.

An interesting result for a possible domain shapes was obtained by Marchenko [20]. Like Landau [18], Marchenko used conformal mapping to calculate the domain shape in infinite slab but in a tilted field. He found that in a *strongly tilted* field width of the S-domains can increase as shown in **Figure 5E**. We note that in such case, the field lines should leave the N domains converging instead of diverging as in **Figure 5A–D**, because bending of the lines over sharp corners (marked a in **Figure 5E**) would take enormous energy [2]. Therefore this scenario also allows for existence of the voids in the field outside the specimen; and moreover, it may lead to appearance of a maximum in the field magnitude in the free space above the N laminae.

To conclude this section on theoretically predicted scenarios for the near-surface properties of the IS, we note that neither of them is consistent simultaneously with the classical magnetostatics and with experimental images of the flux structure. So far no experimental results on

FDDS in the IS have been reported. Hence measurements of these properties are open and important (see, e.g., Landau's papers [18, 19, 23]) problem of fundamental superconductivity[3].

5. Key experiments

Although we began this chapter from theoretical models, a real story of the IS has started from experiment. Measuring electrical resistance R of tin wires, De Haas with collaborators revealed a strong dependence of $R(H)$ on direction of the applied field H: instead of a sharp S/N transition at a threshold field (H_c) in the parallel field, R returns to its full value gradually at the field range from about $H_c/2$ to H_c when the field is perpendicular [29, 30]. Later it was shown that reproducible $R(H)$ in the perpendicular field is liner [28]; one of the graphs for $R(H)$ from [28] is reproduced in **Figure 6**. The linear $R(H)$ is consistent with the Peierls-London model; however, it was revealed that transition from the Meissner state to the IS takes place at H_I, which is somewhat greater than $(1-\eta)H_c$ =0.5H_c.

The first observation of the IS magnetic structure was achieved by Meshkovsky and Shalnikov, who mapped the field in a gap between two tin hemispheres with radius 2 cm using a resistive probe made of a tiny bismuth wire [24]. Originally this experiment was designed to verify the

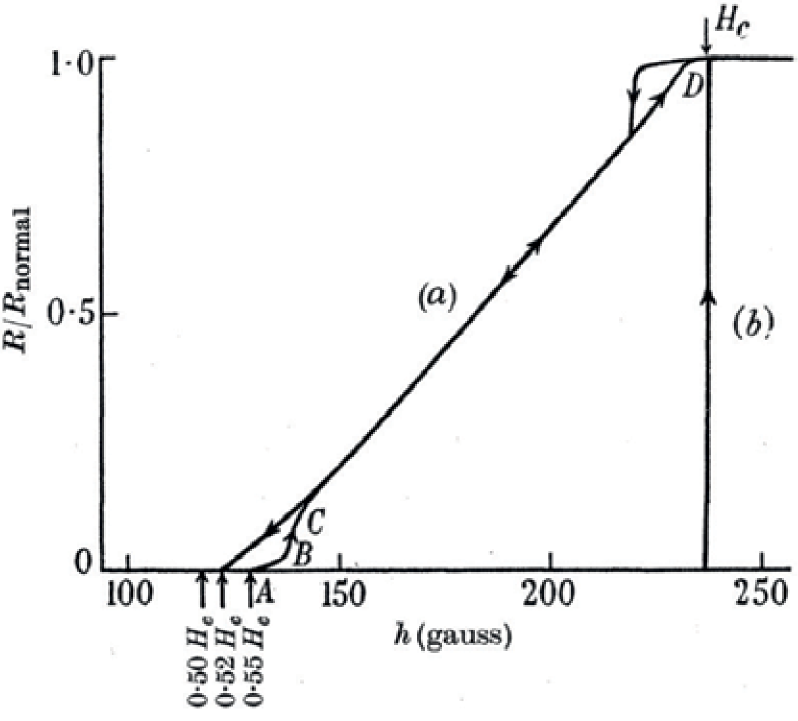

Figure 6. Relative resistance of a high-purity tin cylindrical wire of 0.4 mm in diameter and 5 cm in length at temperature 1.666 K (a) in increasing and in decreasing transverse field and (b) in increasing longitudinal field. After Andrew [28].

---

[3] First results of direct measurements of FDDS were recently presented in V. Kozhevnikov, A. Suter, T. Prokscha, C. Van Haesendonck arXiv:1802.08299v1 [cond-mat.supr-con] (2018).

Landau branching model, according to which the field near the surface is uniform and the flux structure can be observed only in a narrow gap inside the specimen provided the gap width is less than some critical value estimated by Landau [19]. It turned out that there is no critical gap and the field is inhomogeneous both inside (in the gap) and outside the specimen. These results unambiguously turned down the branching model. Typical images and diagrams for the field distribution obtained by Meshkovsky and Shalnikov are available in [1].

Further progress in imaging the IS structure was reached using Bitter or powder technique and magneto-optics [13]. It was established that the flux pattern in flat plates in perpendicular field consists of irregular corrugated laminae transforming into N (S) fractional laminae and tubes near the low (high) end of the IS field range. A numerous variety of different flux patterns were reported when samples are in nonequilibrium state [12].

A detailed study of the IS flux pattern was conducted by Faber with tin and high-purity aluminum parallel-plane plate specimens [31]. It was found that at high reduced temperature ($\approx 0.9T_c$) in a broad field range, the structure is pass-independent (i.e., reproducible at increasing at decreasing fields) and consists of corrugated laminae. Therefore Faber concluded that the laminar flux structure is equilibrium structure of the IS. Typical images of the pass-independent flux pattern in perpendicular field from the Faber's work are shown in **Figure 7**.

A breakthrough in forming *regular and controllable* IS flux structure was achieved by Sharvin [32]. Applying the field tilted with respect to a single-crystal Sn specimen, Sharvin obtained a regular linear laminar structure as shown in **Figure 8**. Measuring period of the structure and using Landau's formula, Eq. (12), corrected to account the field inclination, Sharvin calculated the wall-energy parameter δ. Similar experiments and calculations Sharvin performed for In [32].

The aforementioned difference between the critical field H_I observed in resistive measurements and theoretically expected value for this field $(1-\eta)H_c$ was investigated by Desirant and Shoenberg in a detailed study of magnetization of long cylindrical specimens of different radii in transverse field [33]. Apart from confirmation of the resistive results, Desirant and

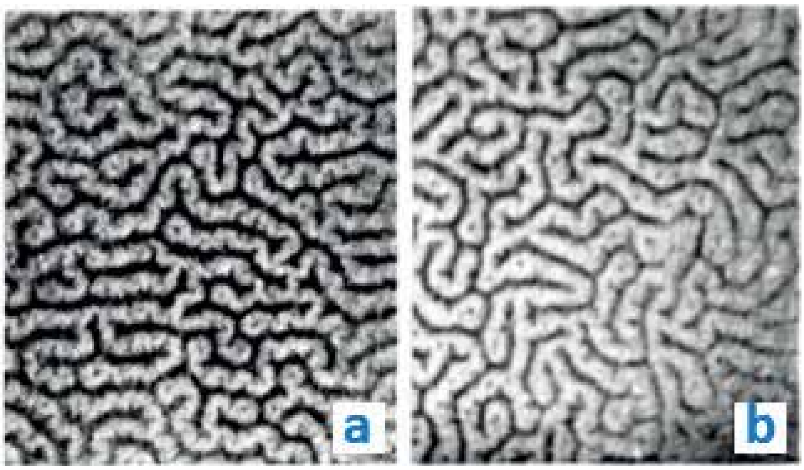

Figure 7. Typical images of pass-independent flux structures of the IS obtained with aluminum parallel-plane plate specimen in perpendicular field at temperature $0.92T_c$ and the field $0.38H_c$ (a) and $0.53H_c$ (b). Dark areas are superconducting. After Faber [31].

Shoenberg revealed that the critical field of the IS/NS transition H_{cr} is appreciably smaller than the thermodynamic critical field H_c measured in parallel field. It was also found that the differences $\Delta H_I = H_I - (1-\eta)H_c$ and $\Delta H_{cr} = H_c - H_{cr}$ depend on the specimen radius: the smaller the radius, the greater the differences. One of magnetization curves reported in [34] is reproduced in **Figure 9**.

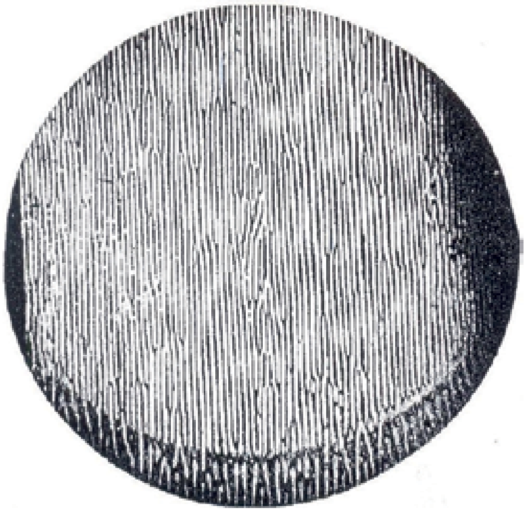

Figure 8. Photograph of the IS flux structures taken with a single-crystal tin disc-shaped specimen (∅ 50 × 2 mm^2) in the field tilted for 15° with respect to the specimen at temperature $0.58T_c$ and field $0.95H_c$. Light areas are normal. After Sharvin [32].

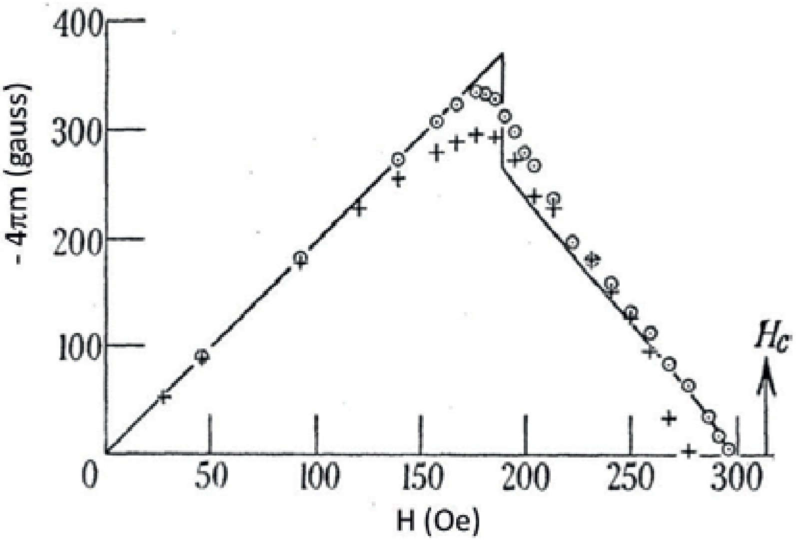

Figure 9. Magnetization curve ($m = M/V$) of cylindrical mercury specimen with radius 23 μm in transverse field at temperature 2.12 K measured at increasing (⊙) and decreasing (+) fields. H_c is thermodynamic critical field measured in parallel field. Solid line based on landau branching model [19] with wall-energy parameter adjusted for best fit. After Desirant and Shoenberg [34].

The differences of ΔH_I and ΔH_{cr} are usually interpreted as a price paid by the specimen for the extra energy needed to create the S/N interfaces in assumption that ΔH_I and ΔH_{cr} are small [3, 8]. We note that this explanation is not full because significant part of the extra free energy is associated with the field inhomogeneity near the specimen surface. On the other hand, the observed extension of the Meissner state (up to $H_I > (1-\eta)H_c$) means that $4\pi M/V$ at H_I is greater than H_c, the value following from the PL model. This "excess magnetic moment" is consistent with the rule of 1/2, and it is indeed seen in **Figure 9** and in other data reported by Desirant and Shoenberg. However this feature can hardly be attributed to the S/N surface tension.

Egorov et al. [35] measured induction B in the bulk of N domains of a high-purity single-crystal tin slab ($18 \times 12 \times 0.56$ mm^3) in perpendicular field using μSR spectroscopy. Reported results are shown in **Figure 10**. H_t in this graph corresponds to H_{cr} in our notations. The tubular phase mentioned in the caption most probably corresponds to the filament state discussed in [36].

Results of Egorov et al. show that B in N domains is H_c at low applied field and decreases with increasing field down to H_{cr} at the IS/N transition. But induction B in N domains equals to the field strength H_i. Therefore the original postulate used in the PL and Landau models ($H_i = H_c$) is correct for the low reduced fields, but it can be not so at higher fields.

Recently the IS problem was revisited by Kozhevnikov et al. [25, 26] via magneto-optics and measurements of electrical resistivity and magnetization in high-purity indium films of different thickness in the fields of different orientations. An immediate motivation for this research was discrepancy in values of the coherence length for Sn and In following from Sharvin's results for the IS structure [32, 33] and those obtained from the measured magnetic field profile in the

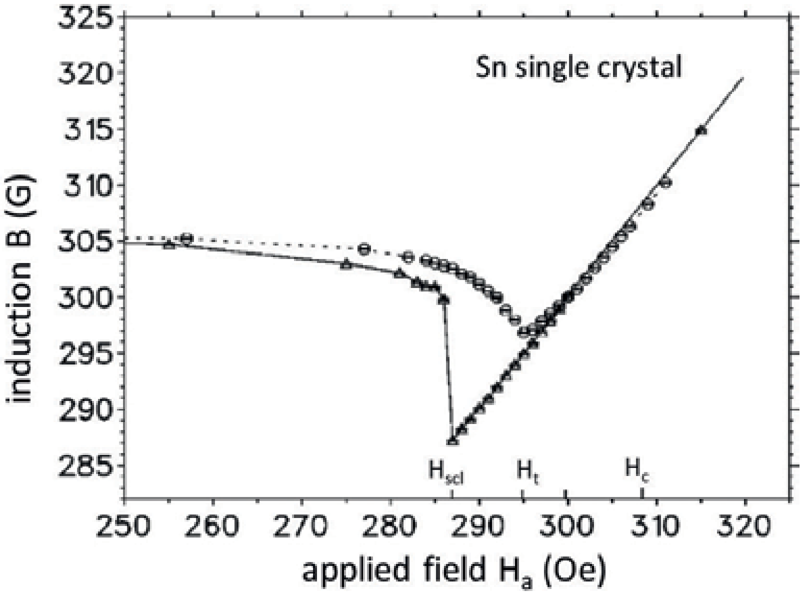

Figure 10. Induction in N domains of the Sn single-crystal plate at temperature 0.08 K measured at increasing (circles, solid line) and decreasing (triangles, dashed line) applied field. For decreasing field the N state is field supercooled down to H_{scl}. At increasing field the laminar structure transforms to one with tubular S regions at H_t. After Egorov et al. [35].

Meissner state [37]. In **Figure 11** we reproduce typical magneto-optical images obtained for a 2.5-μm-thick film. The most unexpected result revealed with this specimen is that in perpendicular field the critical field $H_{cr} \approx 0.4 H_c$ at $T \to 0$. A typical magnetization curve obtained with another (3.86-μm-thick) film is shown in **Figure 12**. H_{cr} for this specimen at 2.5 K is $0.65 H_c$ and

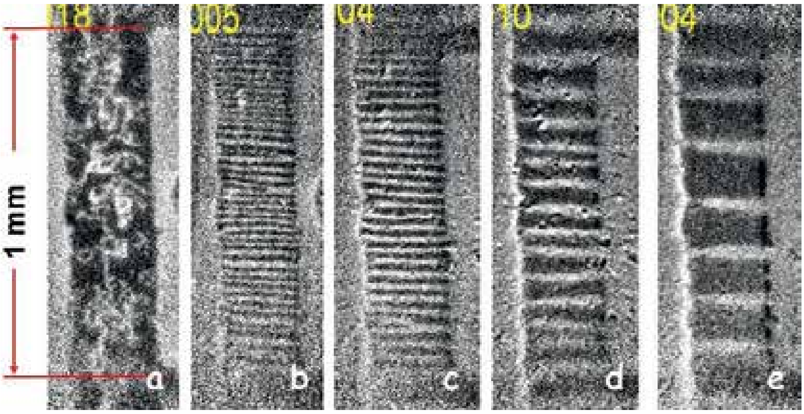

Figure 11. Magneto-optical images taken with 2.5-μm-thick in film at 2.5 K. [$H_{\|}$, $H_{\perp}$ in Oe]: (a) [0, 1], (b) [60, 8], (c) [100, 6], (d) [110, 3], and (e) [115, 1.3]. Superconducting regions are black. After Kozhevnikov et al. [25].

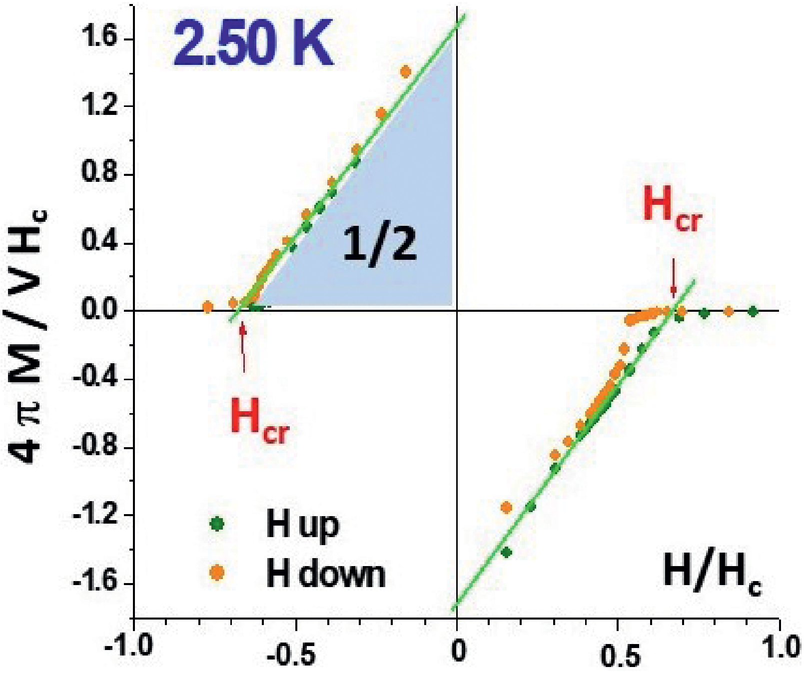

Figure 12. Magnetization curve of 3.86-μm-thick indium film measured in perpendicular field at 2.5 K. Green (orange) circles represent the data measured at increasing (decreasing) field. Shadowed area represents the specimen condensation energy (1/2 in the reduced coordinates of this graph). H_c was determined from magnetization curve in parallel field, and the specimen volume was determined from the slope of that curve. After Kozhevnikov et al. [25].

$4\pi M(0)/V = 1.6H_c$. All data were well reproducible, and the area under magnetization curves plotted in reduced coordinate is close to 1/2, meaning that the obtained experimental results reflect the equilibrium properties of the IS. However these results conflict with available theoretical models. A new model, consistently addressing outcomes of this work and explaining earlier revealed "anomalies," is presented in [25, 26]. We discuss it in the following section.

6. Laminar model for flat slab in tilted field

The simplest of experientially observed equilibrium domain structures of the IS is one-dimensional laminar lattice in slab-like specimens placed in a tilted field. Therefore such a specimen/field configuration is the most convenient for modeling. A laminar model for tilted field (LMTF) was developed in [25, 26]. Schematics of the specimen in the LMFT is shown in **Figure 13**.

Setting of the model is:

(I) Specimen is in the free space (vacuum).

(II) Specimen thickness $d \gg \lambda$. This means that negative surface tension of S/V (V stands for vacuum) interfaces due to nonzero $H_{\|}$ is neglected.

(III) Longitudinal sizes of the specimen (along x and y axes) are much greater than thickness d, i.e., the slab is considered infinite. This means that flux of the perpendicular component of the applied field $H_{\perp}$ is conserved, and therefore $H_{\perp} = \overline{B}_{\perp} = B_{\perp}\rho_n$, where $\overline{B}_{\perp}$ is average perpendicular component of the induction over the specimen, $B_{\perp}$ is perpendicular component of the induction in N domains (considered uniform), and ρ_n is volume fraction of the N phase: $\rho_n = D_n/D = V_n/V$ with D_n and V_n designating the width of the N laminae and a total volume of the N phase, respectively.

(IV) $B_{\|} = (H_i)_{\|} = H_{\|}$ due to the absence of the demagnetizing field along y-axis or along the parallel component of the applied field $H_{\|}$.

(V) Tinkham's version of the FDDS (see **Figure 5C**) is adopted due to its simplicity and consistency with the experimental images.

We start from construction of a thermodynamic potential $\tilde{F}(T, V, H_i)$, which is the Legendre transform of the Helmholtz free energy $F(T, V, B)$ to the variables (T, V, H_i). It is often referred to as the Gibbs free energy[4]:

$$\tilde{F} = F - \frac{\mathbf{B} \cdot \mathbf{H}_i}{4\pi} V = F - \frac{B_{\|} H_{i\|}}{4\pi} V - \frac{B_{\perp} H_{i\perp}}{4\pi} V = F - \frac{B_{\|} H_{i\|}}{4\pi} V = F - \frac{H_{\|}^2}{4\pi} V, \tag{13}$$

where $F(T, V, B)$ is Helmoltz free energy. The term $(\mathbf{B} \cdot \mathbf{H}_i/4\pi)V$ reflects work done by the magnet power supply to keep the set field H when the flux in the system changes [2]. In our case the flux of the perpendicular component is fixed, and therefore the term $(B_{\perp} H_{i\perp}/4\pi)V$

---

[4] It should be remembered that canonical Gibbs free energy is function of pressure, but not volume, as in this case.

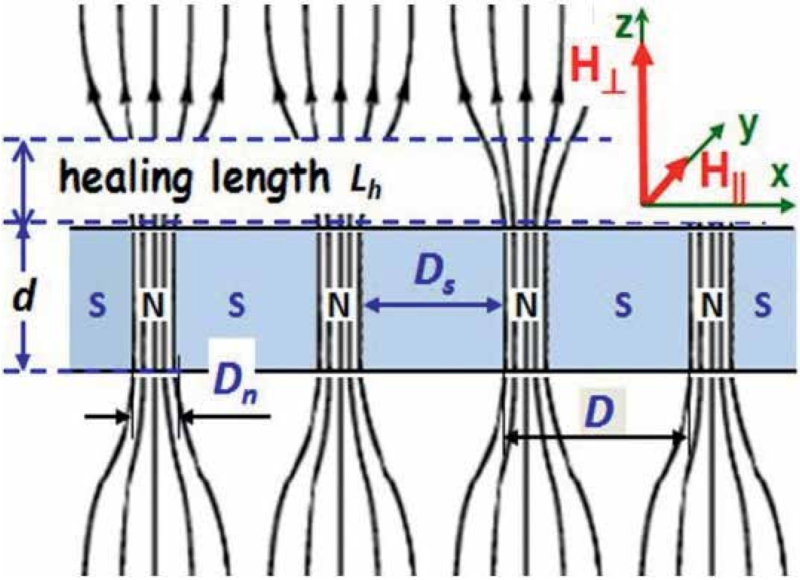

Figure 13. Cross-sectional view of the specimen/field configuration in the laminar model for tilted field. $H_\parallel$ and $H_\perp$ are parallel and perpendicular components of the applied field, respectively. Domains are rectangular parallelepipeds extended along $H_\parallel$ (y-axis). The healing length L_h is the characteristic distance over which the disturbed field relaxes to the uniformly distributed state. In N domains the parallel component of the induction $B_\parallel = H_\parallel$, while the perpendicular component $B_\perp = H_\perp/\rho_n$, where $\rho_n = D_n/D = V_n/V$ is volume fraction of the N phase and V_n is the total volume of the N phase. After Kozhevnikov et al. [26].

drops out. On that reason in pure perpendicular field, $\tilde{F} = F$ [2, 3, 8]. On the other hand, $H_{i\parallel} = H_\parallel$, due to the specimen geometry (see setting (iv) above).

To transform $\tilde{F}(T, V, H_i)$ to the total free energy $\tilde{F}(T, V, H)_M$, we need to add terms associated with energy of interaction of the applied field H with the specimen. In pure parallel case, this term is $+\left(H^2/8\pi\right)V$ [2]. In pure perpendicular case, it is $-\left(H^2/8\pi\right)V$ (see appendix in [26] and/or [2]). Therefore in our case the total free energy of the specimen is

$$\tilde{F}_M = \tilde{F} + \left[\frac{H_\parallel^2}{8\pi} - \frac{H_\perp^2}{8\pi}\right]V. \tag{14}$$

Now, summing:

- **a.** Free energy at zero field $V\left[f_{n0} - H_c^2(1-\rho_n)/8\pi\right)]$, where $f_{n0} = F_{n0}/V$ is free energy density of the N state in zero field.
- **b.** Energy of the field B in the N domains $V\rho_n\left(B_\perp^2 + B_\parallel^2\right)/8\pi$.
- **c.** Energy of the S/N interfaces $2VH_c^2\delta/8\pi D$.
- **d.** Excess energy of the field over the healing length $2VL_h\left(\rho_n B_\perp^2 - H_\perp^2\right)/8\pi d$, and plugging all in Eq. (14), one obtains for $\tilde{f}_M = \tilde{F}_M/V$:

$$\tilde{f}_M = f_{n0} - (1-\rho_n)\frac{H_c^2}{8\pi} + \frac{H_\perp^2}{8\pi\rho_n} - \rho_n\frac{H_\parallel^2}{8\pi} + 2\frac{H_c^2}{8\pi}\frac{\delta}{D} + 2\frac{H_\perp^2}{8\pi}\frac{D}{d}(1-\rho_n)^2 + \frac{H_\parallel^2}{8\pi} - \frac{H_\perp^2}{8\pi}. \tag{15}$$

Then, minimizing $\tilde{f}_M$ with respect to D, one finds equilibrium period of the structure

$$D^2 = \frac{d\delta}{\rho_n^2(1-\rho_n)^2}\frac{H_c^2}{B_\perp^2} = \frac{d\delta}{(1-\rho_n)^2}\frac{H_c^2}{H_\perp^2}. \tag{16}$$

After plugging this optimal D into Eq. (15), the latter takes form:

$$\tilde{f}_M = f_{n0} - \frac{H_c^2}{8\pi}(1-\rho_n)\left[1 - h_\parallel^2 - \frac{h_\perp^2}{\rho_n} - 4h_\perp\sqrt{\frac{\delta}{d}}\right], \tag{17}$$

where $h_\perp$ and $h_\parallel$ are reduced components of the applied field $H_\perp/H_c$ and $H_\parallel/H_c$, respectively. Important to note that with the optimal D the terms related to the S/N interfaces and to the field inhomogeneity near the surface are equal. This means that "responsibility" for deviation of the properties of real specimens from those in the PL model is equally shared between these two contributions in the specimen free energy.

Minimizing $\tilde{f}_M$ with respect to ρ_n, one finds equilibrium volume fraction of the N component:

$$\rho_n^2 = h_\perp^2/\left(1 - 4h_\perp\sqrt{\delta/d} - h_\parallel^2\right). \tag{18}$$

At the IS/N transition ρ_n=1, hence

$$h_{cr\perp} = \sqrt{4(\delta/d) + 1 - h_\parallel^2} - 2\sqrt{\delta/d}. \tag{19}$$

And magnitude of the reduced induction $b = B/H_c$ in the N domains is

$$b^2 = b_\perp^2 + b_\parallel^2 = h_\perp^2/\rho_n^2 + h_\parallel^2 = 1 - 4h_\perp\sqrt{\delta/d}. \tag{20}$$

Before calculating the magnetic moment, we transform Eq. (17) substituting ρ_n from Eq. (18) and using $b_\perp$ from Eq. (20): $b_\perp^2 = 1 - 4h_\perp\sqrt{\delta/d} - h_\parallel^2$. Then Eq. (17) becomes very compact:

$$\tilde{f}_M = f_{n0} - \frac{H_c^2}{8\pi}(b_\perp - h_\perp)^2 = f_{n0} - \frac{B_\perp^2}{8\pi}(1-\rho_n)^2. \tag{21}$$

Now one can calculate the specimen magnetic moment from the definitive relationship Eq. (3):

$$\mathbf{M} \equiv -\nabla_H\left(\tilde{F}_M\right) = -\left(\frac{\partial\tilde{F}_M}{\partial H_\parallel}y + \frac{\partial\tilde{F}_M}{\partial H_\perp}z\right), \tag{22}$$

where y and z are unit vectors along the y and z axes, respectively.

The first term in Eq. (22) is

$$\frac{\partial \tilde{F}_M}{\partial H_\parallel} = \frac{V}{H_c} \cdot \frac{\partial \tilde{f}_M}{\partial h_\parallel} = \frac{V}{H_c} \cdot \frac{H_c^2}{8\pi}\, 2(b_\perp - h_\perp)\,\frac{\partial b_\perp}{\partial h_\parallel}. \tag{23}$$

Since $\partial b_\perp / \partial h_\parallel = h_\parallel / b_\perp$ (see Eq. (20)), the final form of the parallel component of the specimen magnetic moment is

$$-M_\parallel = \frac{\partial \tilde{F}_M}{\partial H_\parallel} = \frac{V}{H_c}\frac{H_c^2}{8\pi}\, 2(b_\perp - h_\perp)\,\frac{h_\parallel}{b_\perp} = \frac{VH_c}{4\pi}\left(1 - \frac{h_\perp}{b_\perp}\right) h_\parallel = \frac{V}{4\pi}(1 - \rho_n) H_\parallel. \tag{24}$$

And the perpendicular component of the moment is

$$-M_\perp = \frac{\partial \tilde{F}_M}{\partial H_\perp} = \frac{V}{H_c}\frac{\partial \tilde{f}_M}{\partial h_\perp} = -\frac{V}{H_c}\frac{2H_c^2}{8\pi}(b_\perp - h_\perp)\left(\frac{\partial b_\perp}{\partial h_\perp} - 1\right) = \frac{V}{4\pi}(1 - \rho_n)\left(1 - \frac{\partial B_\perp}{\partial H_\perp}\right) B_\perp. \tag{25}$$

All obtained formulas are analyzed in detail in [25, 26], where it is shown that the model correctly describes experimental data. In particular, the coherence length calculated from measured D using Eq. (16) agrees well with that obtained from the magnetic field profile measured in [36]. Here we confine our discussion by limiting cases.

In *parallel field* ($H_\perp = 0$) the model (Eq. (18)) yields $\rho_n = 0$, meaning that the specimen is in the Meissner state where the N phase is absent. Then $\tilde{f}_M$ (Eq. (17)) converts to Eq. (5):

$$\tilde{f}_M = f_n - \frac{H_c^2}{8\pi}(1 - h^2) = f_n - \frac{H_c^2}{8\pi} + \frac{H^2}{8\pi}, \tag{26}$$

and $M = M_\parallel$ (Eq. (24)) converts to Eq. (1):

$$M_\parallel = M = -\frac{V}{4\pi} H. \tag{27}$$

In *perpendicular field* ($H_\parallel = 0$) one can see that $h_{cr} (= h_{cr\perp})$ decreases with decreasing thickness d (Eq. (19)) in accord with the experimental data [25, 26, 33], and the induction $B (= b \cdot H_c)$ in N domains equals to H_c at $H = H_I = 0$ and decreases with increasing H (Eq. (20)), as it was found experimentally in [34]. For magnetization $4\pi M/V$ at $H \to 0$, when $\rho_n = 0$, the model (Eq. (25)) yields

$$\frac{4\pi M(0)}{V} = \frac{V}{4\pi}\left(1 - \frac{\partial B_\perp}{\partial H_\perp}\right) H_c. \tag{28}$$

Since B decreases with increasing H, $(\partial B_\perp / \partial H_\perp) < 0$, and therefore the expression in parentheses is greater than unity. This makes $4\pi M(0)/V$ greater than H_c, thus explaining appearance of the excess magnetization at H_I as it is seen, e.g., in **Figures 9** and **12**.

The infinite slab in perpendicular field represents ellipsoid with $\eta = 1$. If the slab is thick (i.e., $d \gg \delta$), the LMTF model converts to the PL model for specimens with unity demagnetization.

Specifically, in the thick slabs $\rho_n = H/H_c$ (Eq. (18)), and therefore (a) $B = (h/\rho_n)H_c = H_c$ and $H_i = B/\mu = H_c$, and (b) $4\pi M/V = -H_c + H$, meaning that $4\pi M(0)/V = -H_c$ and $H_{cr} = H_c$, exactly as it takes place in the PL model (**Figure 4b**). The third condition of Eq. (11) $\overline{B} = H$ follows from the law of the flux conservation always valid for infinite slabs. Thus the LMTF model explains why the PL model works the best for thick specimens: because in such case combined contributions due to near-surface field inhomogeneity and due to the S/N interfaces (both are characterized by the ratio δ/d) are negligible compared to the bulk terms in Eqs. (15) and (17).

Now, when we are convinced in correctness of the formulas for magnetization (see more in [25, 26]), we can rewrite Eq. (17) in its canonical form coinciding with the mandatory form for the total free energy Eq. (4):

$$\tilde{F}_M = \tilde{F}_M(H=0) - \int_0^H \mathbf{M} \cdot d\mathbf{H} = F_{s0} - \int_0^H \mathbf{M} \cdot d\mathbf{H} = F_{n0} - \frac{H_c^2}{8\pi} V - \int_0^H \mathbf{M} \cdot d\mathbf{H} \tag{29}$$

where the components of **M** are given by Eqs. (24 and 25).

7. Concluding remarks

More than three decades starting from the 1930s, the problem of the IS was in the main focus of experimental and theoretical researches on superconductivity. This resulted in significant progress reached in understanding properties of the IS as well as properties of superconducting state as a whole. Excellent reviews of these researches are available in [1, 12]. However some puzzles in the IS properties remained open until their possible explanations emerged in studies of recent years. In this chapter we mostly focused at results of these studies.

In particular, we discussed a recently developed phenomenological model of the IS composed for infinite slabs in arbitrary tilted magnetic field. Naturally, this model is not and cannot be free of disadvantages. One of them can be associated with the use of an oversimplified Tinkham approximation for the field distribution and domain shape near the surface through which the flux enters and leaves the specimen. We believe that modern experimental capabilities associated, e.g., with muon spectroscopy and noninvasive scanning magnetic microscopy, can help to resolve this important and very interesting issue, which we discussed in the Section IV. The new model discussed in Section VI is restricted by the slab-like specimens. Its extension to all ellipsoidal shapes covered in the model of Peierls and London is another possible avenue of research on the IS.

Finally, it is important to remind that the IS is one of two inhomogeneous superconducting states. The second state is the mixed state in type-II superconductors, taking place in vast majority of superconducting materials, including those used in practical applications. Therefore understanding of properties of the IS can help to understand properties of the mixed state. As an example, the field distribution and shape of the normal domains (vortices in type-II materials) near the specimen surface should be similar in both these inhomogeneous states.

Author details

Vladimir Kozhevnikov

Address all correspondence to: vladimir@itf.fys.kuleuven.be

Tulsa Community College, Tulsa, Oklahoma, USA

References

[1] Shoenberg D. Superconductivity. 2nd. ed. Cambridge: Cambridge University Press; 1952

[2] Landau LD, Lifshitz EM, Pitaevskii LP. Electrodynamics of Continuous Media. 2nd ed. Amsterdam: Elsevier; 1984

[3] Tinkham M. Introduction to Superconductivity. Mineola: Dover Publication; 1996

[4] Maxwell JC. A Treatise on Electricity and Magnetism. 2nd ed. Vol. II. Oxford: Clarendon Press; 1881

[5] Jackson JD. Classical Electrodynamics. 3d ed. Hoboken NJ: JohnWiley and Sons; 1999

[6] Purcell EM. Electricity and Magnetism. Boston MA: McGraw-Hill; 1985

[7] Abrikosov AA. Fundamentals of the Theory of Metals. Amsterdam: Elsevier Science Pub. Co.; 1988

[8] De Gennes PG. Superconductivity of Metals and Alloys. Boulder, CO: Westview; 1966

[9] Tamm IE. Fundamentals of the Theory of Electricity. Moscow: Mir; 1979

[10] Gorter CJ, Casimir H. Physica. 1934;**1**:306

[11] Peierls R. Proceedings of the Royal Society of London. Series A. 1936;**155**:613

[12] Livingston JD, DeSorbo W. In: Parks RD, editor. Superconductivity II. N.Y.: Marcel Dekker; 1969. p. 1235

[13] Huebener RP. Magnetic Flux Structures in Superconductors. 2nd ed. N.Y.3: Springler-Verlag; 2010

[14] Brandt EH, Das MP. Journal of Superconductivity and Novel Magnetism. 2001;**24**:57

[15] Clem JR, Prozorov R, Wijngaarden RJ. Physical Review B. 2013;**88**:104504

[16] London F. Physica. 1936;**3**:450

[17] Kozhevnikov V, Valente-Feliciano A-M, Curran PJ, Richter G, Volodin A, Suter A, Bending S J, Van Haesendonck C. Journal of Superconductivity and Novel Magnetism. 2018. https://doi.org/10.1007/s10948-018-4622-y

[18] Landau LD. ZhETF. 1937;**7**:371

[19] Landau LD. ZhETF. 1943;**13**:377

[20] Marchenko VI. ZhETF. 1976;**71**:2194

[21] Lifshitz EM, Sharvin YV. Doklady Akademii Nauk SSSR. 1951;**79**:783

[22] Fortini A, Paumier E. Physical Review B. 1972;**5**:1850

[23] Landau LD. Nature. 1938;**141**:688

[24] Meshkovsky AG, Shalnikov AI. ZhETF. 1947;**17**:851

[25] Kozhevnikov V, Wijngaarden RJ, de Wit J, Van Haesendonck C. Physical Review B. 2014; **89**(R):100503

[26] Kozhevnikov V, Van Haesendonck C. Physical Review B. 2014;**90**:104519

[27] Neidermayer C, Forgan EM, Gluckler H, Hofer A, Morenzoni E, Pleines M, Prokscha T, Riseman TM, Brike M, Jackson TJ, Litterst J, Long MW, Luetkens H, Schatz A, Schatz G. Physical Review Letters. 1999;**83**:3932

[28] Andrew ER. Proceedings of the Royal Society of London A. 1948;**194**:80

[29] de HaasWJ, Voogd J. Communications from the Laboratory of Physics of the University of Leiden, 1931:214d

[30] de HaasWJ, Voogd J, Jonker JM. Physica.1934;**1**:281

[31] Faber IT. Proceedings of the Royal Society of London. Series A. 1958;**248**:460

[32] Sharvin YV. ZhETF. 1957;**33**:1341

[33] Sharvin YV. ZhETF. 1960;**38**:298

[34] Desirant M, Shoenberg D. Proceedings of the Royal Society of London A. 1948;**194**:63

[35] Egorov VS, Solt G, Baines C, Herlach D, Zimmermann U. Physical Review B. 2001;**64**: 024524

[36] Kozhevnikov V, Valente-Feliciano A-M, Curran PJ, Suter A, Liu AH, Richter G, Morenzoni E, Bending SJ, Van Haesendonck C. Physical Review B. 2017;**95**:174509

[37] Kozhevnikov V, Suter A, Fritzsche H, Gladilin V, Volodin A, Moorkens T, Trekels M, Cuppens J, Wojek BM, Prokscha T, Morenzoni E, Nieuwenhuys GJ, Van Bael MJ, Temst K, Van Haesendonck C, Indekeu JO. Physical Review B. 2013;**87**:104508

Emerging Superconductivity and Topological States in Bismuth Chalcogenides

Jifeng Shao and Wenka Zhu

Additional information is available at the end of the chapter

http://dx.doi.org/10.5772/intechopen.73057

Abstract

In this chapter, we review the recent experimental work in emerging superconductors, i.e., bismuth chalcogenides, including the newly discovered $BiS(e)_2$-based layered superconductors and some topological superconductor candidates. Their crystal structure and various physical properties are reviewed in detail, with the correlation between structure and superconductivity as the main clue throughout this chapter. Bi_2OS_2 is the simplest structure in Bi—O—S compounds and probably the parent compound of this series. Superconductivity emerges when carriers are introduced by intercalation or chemical substitution. The superconducting layer is extended to $BiSe_2$ layer in $LaO_{1-x}F_xBiSe_2$, which has an improved superconductivity. Moreover, the topological insulator Bi_2Se_3 can be turned into superconductors by intercalating metal atoms into van der Waals space, e.g., $Sr_xBi_2Se_3$, a potential topological superconductor, whose quantum oscillations reveal a possible topological surface state. The intermediate external pressure can efficiently suppress superconductivity, which reemerges when pressure is further increased, while T_c is nearly invariant in high-pressure region, indicating an unconventional pairing state.

Keywords: bismuth chalcogenides, $BiS(e)_2$-based superconductors, crystal structure, intercalation, topological superconductors, high pressure

1. Introduction

Superconductivity was first discovered in the resistivity measurement of mercury by Kamerlingh Onnes in 1911. Its resistance abruptly vanishes at 4.1 K. Zero resistance means no energy loss in electric transport, which could greatly solve the energy crisis in the future. Since then, superconductivity has been a long-lasting hot topic in condensed matter physics. Exploring room temperature superconductors is one of the ultimate dreams.

However, so far, only two kinds of unconventional superconducting systems have exceeded the Macmillan limit at ambient pressure, i.e., the cuprate and iron-based superconductors. In general, the correlation of structure and typical properties is always a useful guideline for effectively searching for special functional materials. In fact, the structure of both cuprate and iron-based superconductors can be characterized as a sandwiched "hamburger" model. It consists of superconducting layers (CuO_2 plane, Fe_2M_2 (M = As, P, S, Se, and Te) layer) and spacer layers, which stack alternatively along the c-axis [1, 2]. Superconductivity occurs when the charged carriers are generated by the defects or substitution in superconducting layers or more commonly provided by the space layers; namely, a new superconducting layer probably means a new superconducting system. The spacer layer can be easily tuned by doping, substitution, intercalation, and pressure, which could affect superconductivity [3]. Therefore, materials with layered structure have been regarded as the most promising playground for exploring new high-T_c superconductors.

In 2010, superconductivity arising from the topological insulator Bi_2Se_3 by Cu intercalation was first reported [4]. It has drawn much attention since $Cu_xBi_2Se_3$ is proposed as a topological superconductor candidate, as evidenced by the zero-bias conductance peak and quantum oscillation experiment [5, 6]. Very recently, superconductivity with topological states was also reported in its isostructural compounds, $Sr_xBi_2Se_3$ and $Nb_xBi_2Se_3$ [7, 8]. In 2012, an exotic superconductivity was discovered in a new layered structure $Bi_4O_4S_3$ with zero-resistance superconducting temperature at about 4.5 K [9]. Soon, another new BiS_2-based superconductor $LaO_{0.5}F_{0.5}BiS_2$ was reported, whose structure is more definite and the zero-resistance superconducting temperature is about 8 K for the samples annealed under high pressure [10]. As its structure is very similar to the iron-based superconductor LaOFeAs, this system has been intensively researched, and lots of isostructural superconductors have been synthesized, including $ReO_{1-x}F_xBiS_2$ (Re: Ce, Pr, Nd, Yb), $Sr_{1-x}Re_xFBiS_2$ (Re: La, Ce), $EuBiS_2F$, and $Eu_3Bi_3S_4F_4$ [11–15]. These researches are focused on tuning the spacer layers. The attempts to explore new superconducting layers only succeed in $LaO_xF_xBiSe_2$ and $Sr_{0.5}La_{0.5}FBiSe_2$ [16–18]. So far, the superconducting layer of this system has been extended to $BiCh_2$ (Ch: S, Se). In this chapter, the crystal structure and superconducting properties of Bi—O—S superconductors, $LaO_{1-x}F_xBiSe_2$ single crystals, and $Sr_xBi_2Se_3$ single crystals are briefly reviewed.

2. Crystal structure and superconducting properties

2.1. Bi—O—S superconductors

The element composition of $Bi_4O_4S_3$ is the same as $Bi_4O_4(SO_4)_xBi_2S_4$ (x = 0.5), and its parent $Bi_6O_8S_5$ is an oxide insulator composed of alternatively stacked BiS_2 and $Bi_2O_2 + SO_4 + Bi_2O_2$ layers along the c-axis. It has a tetragonal structure with I4/mmm space group and its schematic crystal structure is shown in **Figure 1(c)**. Band calculations demonstrate that the half vacancy of SO_4 layer generates electron carriers into BiS_2 layer. The normal state of $Bi_4O_4S_3$ is metallic and the superconductivity mainly originates from the Bi $6p_x$ and $6p_y$ orbitals in BiS_2 layers. Therefore, the BiS_2 layer is called the superconducting layer in this family.

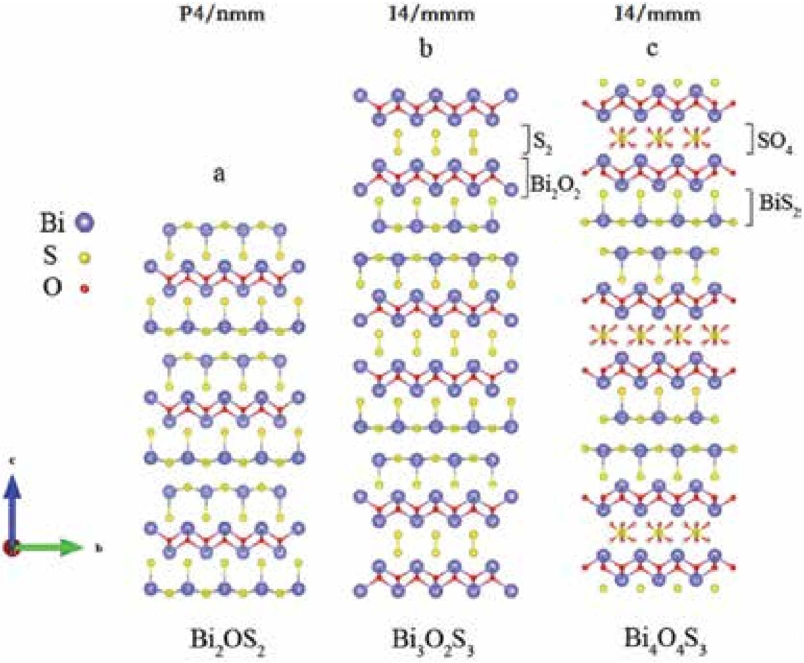

Figure 1. Crystal structures of (a) Bi_2OS_2, (b) $Bi_3O_2S_3$, and (c) $Bi_4O_4S_3$ [21].

However, the chemical composition studies show that it probably contains two new Bi—O—S phases, i.e., Bi_2OS_2 and $Bi_3O_2S_3$. Their schematic structures can be seen in **Figure 1(a)** and **(b)**. Bi_2OS_2 is an insulating phase and its content is less than 10%. $Bi_3O_2S_3$ is the main phase and likely accounts for the 4.5 K superconductivity in $Bi_4O_4S_3$. And the superconductivity can be suppressed by the amount of Bi_2OS_2-like stacking faults [19]. Once the quality of $Bi_3O_2S_3$ sample is improved, the superconducting volume fraction will be enhanced with its zero-resistance superconducting temperature increased up to 4.9 K [20].

The crystal structure of $Bi_3O_2S_3$ is similar to $Bi_4O_4S_3$ with the same I4/mmm space group, a = 3.9674 Å and b = 41.2825 Å. The electron carriers are believed to be generated from S_2^{2-} layers replacing the vacancy of SO_4^{2-} layers in $Bi_4O_4S_3$. The chemical composition of Bi_2OS_2 can also be expressed as $BiOBiS_2$. Then we can see it is isostructural with $LaOBiS_2$ with P4/nmm space group, a = b = 3.9744 Å and c = 13.7497 Å. $BiOBiS_2$ has the simplest structure and composition, then it is probably the parent compound of this BiS_2-based family. Besides, superconductivity is likely to be induced by introducing carriers into spacer layer. In fact, F-doped Bi_2OS_2 has been reported to exhibit bulk superconductivity below 5 K [21, 22].

Figure 2 shows the powder XRD patterns of $Bi_3O_2S_3$, $BiO_{1-x}F_xBiS_2$, and Bi_2OS_2 samples. We can see that samples of Bi—O—S compounds tend to contain impurities such as Bi_2O_3, Bi, and Bi_2S_3, because their synthesis temperature is relatively low (520°C for $Bi_4O_4S_3$ and $Bi_3O_2S_3$, and 400°C for $Bi_2(O,F)S_2$) [9, 19–21]. Besides, these samples can only be synthesized in a narrow temperature region. Another difficulty in detecting their actual composition and structure is that several strong diffraction peaks in the powder XRD patterns are very close to each other.

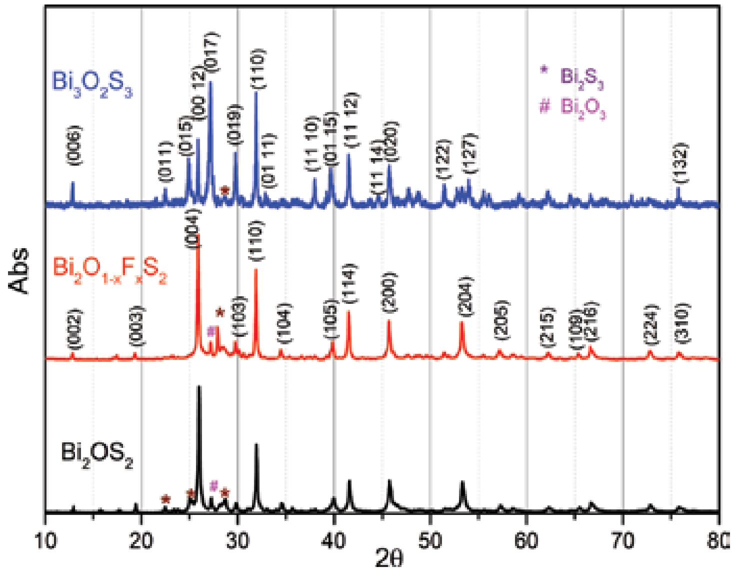

Figure 2. Powder XRD patterns of $Bi_3O_2S_3$, Bi_2OS_2, and $Bi_2O_{1-x}F_xS_2$ polycrystalline samples. The special characters (*, #) represent the impurity phases.

Hence, bulk superconductivity is very important in this system. Up to now, high-quality samples, especially single crystals, are still needed to investigate the relationship of structure and properties, in view of the multiple competing low-energy crystal structures in this system.

The physical properties of Bi—O—S superconductors are introduced, taking $Bi_3O_2S_3$ and F-doped Bi_2OS_2 for instance [20, 21]. **Figure 3(a)** shows the temperature dependence of resistivity and magnetoresistivity under different applied magnetic fields for $Bi_3O_2S_3$. Its normal state is metallic-like and a sharp drop in resistivity appears at 5.8 K and quickly down to zero at 4.9 K. The upper critical field is estimated from resistivity versus temperature curves under different applied magnetic fields perpendicular to the sample surface, as seen in the insets of **Figure 3(a)**. According to the Werthamer-Helfand-Hohenberg (WHH) formula, the upper critical field $\mu_0H_{c2}(0)$ is evaluated to be about 4.84 T.

The shielding volume fraction is about 100%, revealing bulk superconductivity, as seen in **Figure 3(b)**. The divergence in temperature dependence of magnetic susceptibility and the M-H curves characterize $Bi_3O_2S_3$ as a type-II superconductor. The Hall effect shows a remarkable nonlinear magnetic field dependence of transverse resistivity, which means it is likely a multiband superconductor [23]. However, the Hall resistivity at different temperatures is all negative, indicating that the dominant charge carriers are electron-type. The evaluated charge carrier density is about 1.5×10^{19} cm^{-3}. It is much lower than those of cuprate and iron-based superconductors, implying a low superfluid density. Chemical substitution effects seem to increase the charge carrier density, but ultimately inhibit the superconductivity [24–26].

A clear specific heat anomaly appears around the superconducting transition temperature, as seen in **Figure 3(d)**, confirming the bulk superconductivity in $Bi_3O_2S_3$. The electronic specific

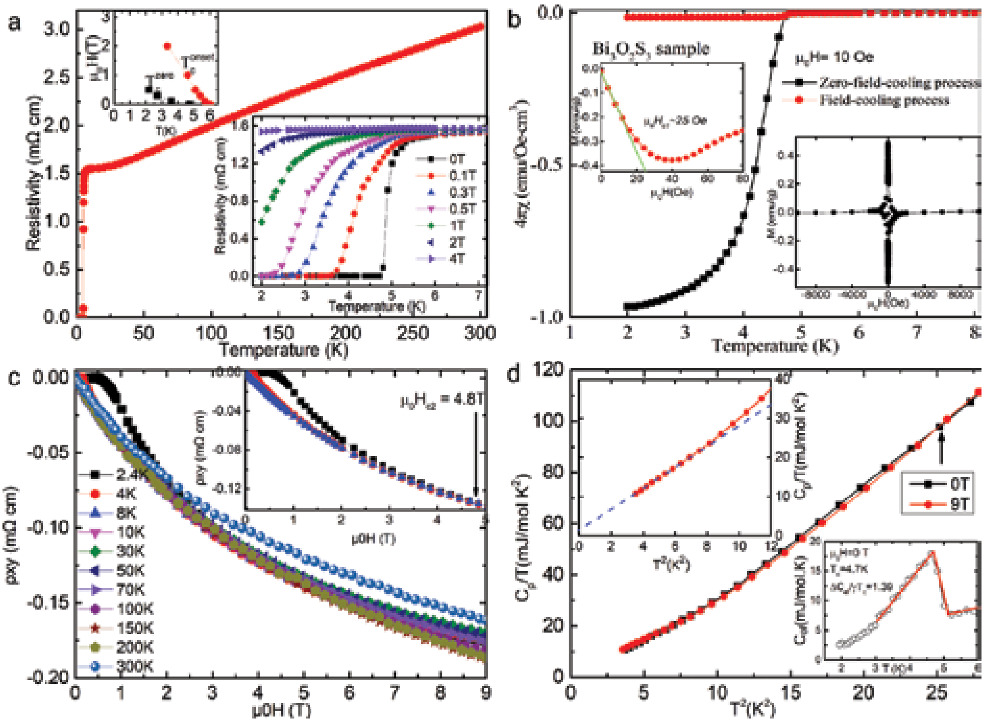

Figure 3. (a) Temperature dependence of resistivity for $Bi_3O_2S_3$. The lower inset shows the curves of resistivity versus temperature under different applied magnetic fields and the upper inset shows the field dependence of T_c^{onset} and T_c^{zero}. (b) Temperature dependence of magnetic susceptibility for $Bi_3O_2S_3$ and the insets show the magnetic field dependence of magnetic susceptibility at 2 K. (c) Hall resistivity versus magnetic field at different temperatures. (d) Curves of C/T versus T^2 in superconducting state (0 T) and normal state (9 T). The upper inset shows the data of normal state at low temperature region. The lower inset shows the temperature dependence of calculated electron specific heat in superconducting state [20].

heat coefficient γ and phonon specific heat coefficient β for the normal state under 9 T are obtained as 1.65 mJ/(mol K^2) and 2.6 mJ/(mol K^4), respectively, using linear fitting of C/T versus T^2. As the phononic contribution to the heat capacity is generally independent of the external magnetic field, the electronic specific heat of superconducting state can be expressed by the equation

$$C_e(T) = C(T, H = 0) - C(T, H = 9T) + \gamma T. \tag{1}$$

The estimated value of $\Delta C_e/\gamma T_c$ is comparable to the BCS weak-coupling limit 1.43.

Undoped Bi_2OS_2 was predicted to be an insulating oxide by the band structure calculations. However, we can see it is almost metallic from 300 K to 30 K, and a weak semiconductor behavior emerges below 30 K, which may be originating from the impurities. The F-doping can significantly decrease the normal state resistivity and increase the shielding volume fraction, as shown in **Figure 4**. The best doping ratio is about 0.24. From the temperature dependence of magnetic susceptibility, the best doped sample has a bulk type-II-like

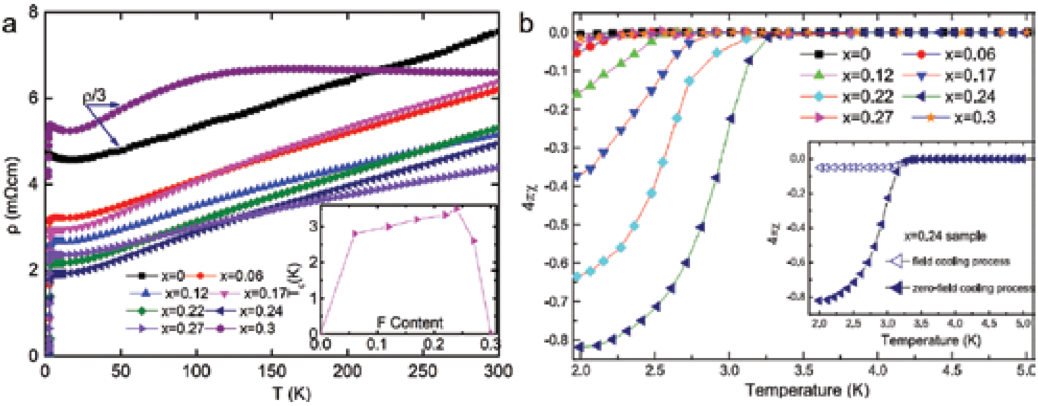

Figure 4. (a) Temperature dependence of resistivity for $BiO_{1-x}F_xBiS_2$. The inset shows the variation of T_c with different F-doping content. (b) Temperature dependence of magnetic susceptibility for $BiO_{1-x}F_xBiS_2$ under ZFC process. The inset presents the FC and ZFC data for x = 0.24 sample [21].

superconductivity. When doping content exceeds 0.27, superconductivity disappears and the resistivity increases quickly. Besides, the quality of samples (x > 0.27) synthesized by conventional solid state reaction method begins to deteriorate with increasing doping content [21]. In fact, the $Bi_2(O,F)S_2$ samples synthesized by topotactic fluorination using XeF_2 also contain bismuth impurity [22]. It is difficult to get pure samples because the optimal synthesis temperature is only around 400°C.

2.2. Re(O,F)BiCh$_2$ (Ch: S, Se) superconductors

Re(O,F)BiS$_2$ (Re: La, Ce, Pr, Nd, Yb) superconductors have been intensively studied since the report of $LaO_{0.5}F_{0.5}BiS_2$. Their structure is more definite and similar to "1111" phase of iron-based superconductors. Single crystals of this structure have been successfully synthesized [27]. Structure tuning is mainly concentrated on the spacer layers rather than the superconducting layer. And only the electron-doping into the insulating parent can induce superconductivity [28]. Here, we introduce the crystal structure and various physical properties of $LaO_{1-x}F_xBiSe_2$ single crystals, which also firstly extend the superconducting layer to $BiSe_2$ layer.

The powder XRD pattern and crystal structure of $LaO_{0.59}F_{0.41}BiSe_2$ superconducting single crystal are presented in **Figure 5**. No impurity phase is found and each peak is indexed. It has a P4/nmm tetragonal lattice with the refined lattice constants a = b = 4.1377 Å and c = 14.1566 Å, which are larger than those of $LaO_{0.5}F_{0.5}BiS_2$ for the larger ionic radius of Se^{2-}. **Figure 6** shows a comparison of the temperature dependence of resistivity for La(O,F)BiS$_2$ and La(O,F)BiSe$_2$ samples. $LaOBiS_2$ can be described as an insulator while $LaOBiSe_2$ is metallic. For $LaO_{0.5}F_{0.5}BiS_2$, it exhibits a semiconducting behavior before the superconducting transition begins. The transport property of $LaO_{0.5}F_{0.5}BiSe_2$ is similar to $Bi_3O_2S_3$ but with a lower residual resistivity. Other isostructural compounds such as $LaO_{0.5}F_{0.5}BiTe_2$ and $LaO_{0.5}F_{0.5}SbS_2$ are also reported, but no superconductivity can be observed down to 1.7 K [16].

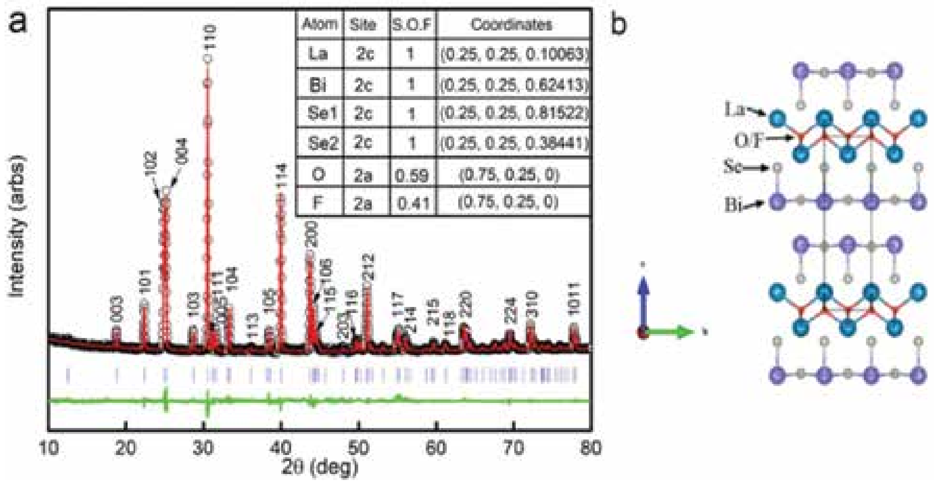

Atom	Site	S.O.F	Coordinates
La	2c	1	(0.25, 0.25, 0.10063)
Bi	2c	1	(0.25, 0.25, 0.62413)
Se1	2c	1	(0.25, 0.25, 0.81522)
Se2	2c	1	(0.25, 0.25, 0.38441)
O	2a	0.59	(0.75, 0.25, 0)
F	2a	0.41	(0.75, 0.25, 0)

Figure 5. (a) Powder XRD pattern (black circles) with the Rietveld refinement (red curve) and Miller indices for $LaO_{0.59}F_{0.41}BiSe_2$. The inset table summarizes the structural parameters. (b) Crystal structure of $LaO_{0.59}F_{0.41}BiSe_2$. The rectangle indicates the unit cell [17].

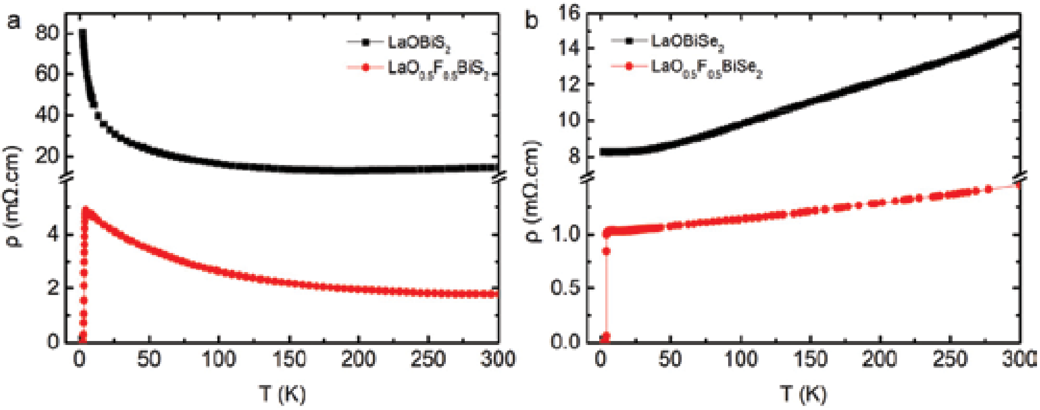

Figure 6. A comparison of the temperature dependence of resistivity between (a) $La(O,F)BiS_2$ and (b) $La(O,F)BiSe_2$.

Fluorine doping effect on the superconductivity of $LaO_{1-x}F_xBiSe_2$ single crystals is shown in **Figure 7(a)** and **(b)**. F-doping can significantly decrease the resistivity of normal state and increase the superconducting transition temperature and shielding volume fraction. Unfortunately, the flux method can only grow single crystals with the largest F content of about 0.5. For example, the sample with F-doping amount of 0.52 was grown by a nominal component of 0.9. The magnetic susceptibility measurement shows $LaO_{1-x}F_xBiSe_2$ has a bulk superconductivity and belongs to the type-II superconductors. Upper critical magnetic field can be evaluated from the resistivity versus temperature under various magnetic fields. As seen in **Figure 7(c)** and **(d)**, the upper critical fields at zero temperature are estimated to be 29 T and 1 T for H||ab and H⊥ab, respectively, which indicate large anisotropy.

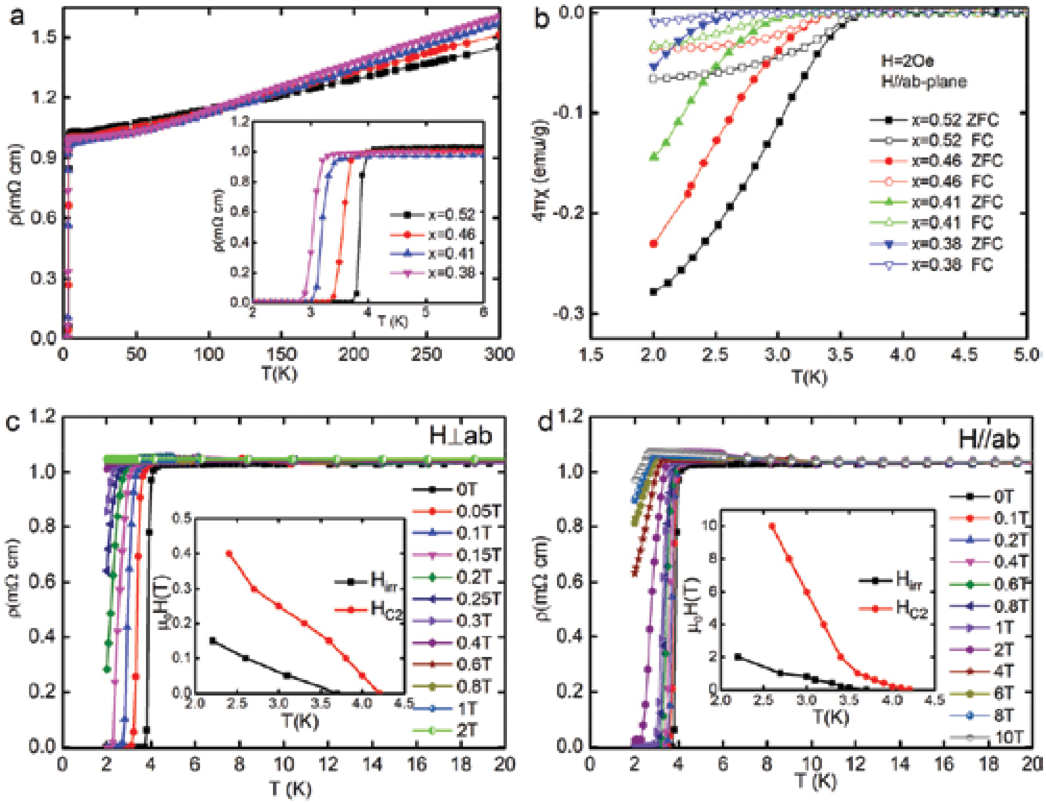

Figure 7. Superconducting properties of $LaO_{1-x}F_xBiSe_2$ single crystals with different F-doping contents. (a) Temperature dependence of resistivity and an enlarged view near the superconducting transition temperature for all samples. (b) ZFC and FC magnetic susceptibility versus temperature with magnetic field applied parallel to ab-plane for all samples. (c) and (d) Resistivity versus temperature with magnetic field applied perpendicular to and parallel to ab-plane, respectively, for the x = 0.52 sample [17].

The anisotropy parameter γ_s of the $LaO_{1-x}F_xBiSe_2$ superconducting single crystal is investigated by measuring the angular dependence of resistivity under various magnetic fields at 3 K (see **Figure 8**). Note that the angle θ describes the deviation of magnetic field with respect to the ab-plane of single crystal. Only the data with magnetic field below 1 T are selected for the reduced magnetic field, because the $H_{C2}(0)$ for H⊥ab is about 1 T. The reduced magnetic field is calculated by the equation

$$H_{red} = H\sqrt{\sin^2\theta + \gamma_s^{-2}\cos^2\theta}. \tag{2}$$

According to the Ginzburg-Landau theory [29], the curves of resistivity versus reduced magnetic field under different magnetic fields should merge into one. The resultant anisotropy parameter at 3 K is about 30 (see **Figure 8(b)**), which is close to the result of upper critical field within the ab-plane.

Considering that the T_c of $LaO_{0.5}F_{0.5}BiS_2$ is increased from 2.7 K to 10.6 K under a hydrostatic pressure of 1.68 GPa [30], the highest T_c among the BiS_2-based superconductors, higher T_c, above 10.6 K

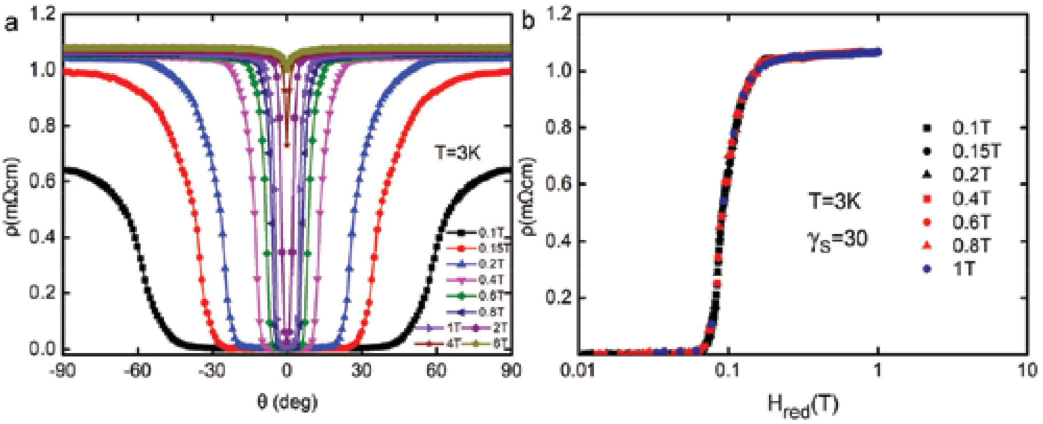

Figure 8. Anisotropy of $LaO_{1-x}F_xBiSe_2$ superconducting single crystal. (a) Angular dependence of resistivity taken under magnetic fields from 0.1 T to 6 T at 3 K for $LaO_{0.48}F_{0.52}BiSe_{1.93}$ single crystal. (b) Scaling of the resistivity vs. the reduced magnetic field H_{red} [17].

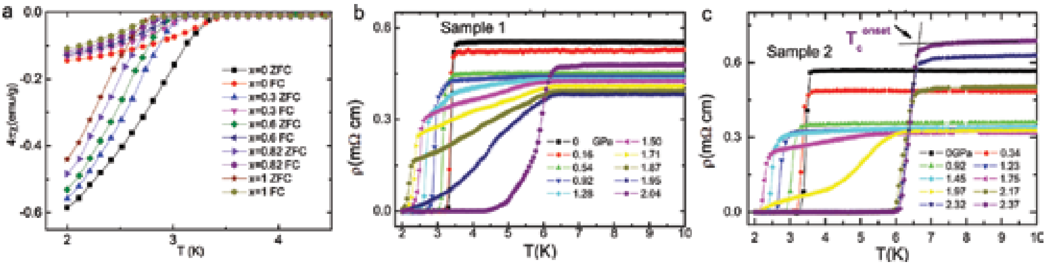

Figure 9. High-pressure effect on the superconductivity of $LaO_{0.5}F_{0.5}BiSe_2$ single crystal. (a) High-pressure effect on the temperature dependence of magnetic susceptibility. (b) and (c) High-pressure effect on the transport properties of two single crystal samples of $LaO_{0.5}F_{0.5}BiSe_2$ [31].

is expected for $LaO_{0.5}F_{0.5}BiSe_2$ under external pressure since its zero-resistance temperature is about 3.5 K. However, we find that its superconductivity and shielding volume fraction decrease unexpectedly with increasing pressure below 1 GPa hydrostatic pressure, as seen in **Figure 9(a)**. Another experiment with higher pressure shows that a new superconducting phase emerges at about 1.2 GPa and T_c reaches about 6.5 K at 2.17 GPa [31]. Accompanied by this crossover, the normal state is switched from that with a low temperature resistivity upturning to a metallic one. Accordingly, the normal state resistivity also shows a nonmonotonic change with the external pressure. These facts suggest that the $BiSe_2$-based system is very different from the BiS_2-based system.

2.3. $M_xBi_2Ch_2$ (Ch: Se, Te) superconductors

Topological insulator has linearly dispersive band structures and its topological surface state exhibits metallic properties while the bulk state is insulating. If its spin-momentum locking effect combines with superconductivity, Majorana fermion may exist, which is useful for quantum computing. At first, the topological superconductors were mostly focused on the proximity-induced superconductivity. The discovery of $Cu_xBi_2Se_3$ superconductor opens a new gate to topological superconductors, i.e., superconductors induced by doping into topological insulators, which are expected to be the candidate of three-dimensional topological superconductors. Recently, a series of superconductors based on the topological insulators have been reported, such as $Cu_x(PbSe)_5(Bi_2Se_3)_6$ [32], $Sr_xBi_2Se_3$ [7], $Nb_xBi_2Se_3$ [8], and $Tl_xBi_2Te_3$ [33]. Here, we put emphasis on the crystal structure and physical properties of $Sr_xBi_2Se_3$ single crystals.

The structure of $Sr_xBi_2Se_3$ is similar to that of $Cu_xBi_2Se_3$ and isomorphic to the parent Bi_2Se_3. Sr atoms may act as a bipolar dopant that can be embedded in the van der Waals space or randomly substitute for Bi. The actual Sr doping content of $Sr_xBi_2Se_3$ is very little so that it is hard to define its precise position. Nevertheless, the lattice constants of $Sr_xBi_2Se_3$ are a little larger than those of Bi_2Se_3, while the lattice constants of $Bi_{2-x}Sr_xSe_3$ are smaller. The c-axis lattice constant of $Bi_{2-x}Sr_xSe_3$ decreases slightly with increasing doping content (see **Figure 10(b)**). In addition, all samples grown in $Bi_{2-x}Sr_xSe_3$ ratio show no signs of superconductivity at 1.8 K, as seen in **Figure 11(a)**. Therefore, we could use **Figure 10(a)** as the schematic structure diagram.

The linear curves of Hall resistivity versus magnetic field indicate that $Sr_xBi_2Se_3$ has only one electron-like bulk carrier. The carrier density increases slightly with decreasing temperature. Its average is around 2.3×10^{19} cm^{-3}, about 1–2 orders of magnitude lower than $Cu_xBi_2Se_3$. **Figure 11(d)** and **(e)** shows that the T_c of superconducting samples changes little with different Sr contents, but the shielding volume fraction is very different. Only those samples with Sr content above 0.06 have a large shielding volume fraction. Moreover, the superconductivity is very stable in air, as evidenced by the almost unchanged shielding volume fraction for the sample placed in air even for a month. This provides great convenience for experimental research.

The topological surface state of $Sr_xBi_2Se_3$ single crystal has been investigated through Shubnikov-de Haas oscillation measurements. Clear oscillations in resistivity and Hall resistivity can be observed under high magnetic field at different temperatures, as shown in **Figure 12(a)** and **(c)**. The oscillation amplitudes become more pronounced for higher magnetic field and lower temperature. However, the oscillatory periods measured at different temperatures remain constant, so only the data at 0.35 K with the most noticeable oscillations are selected to deduce the Landau level

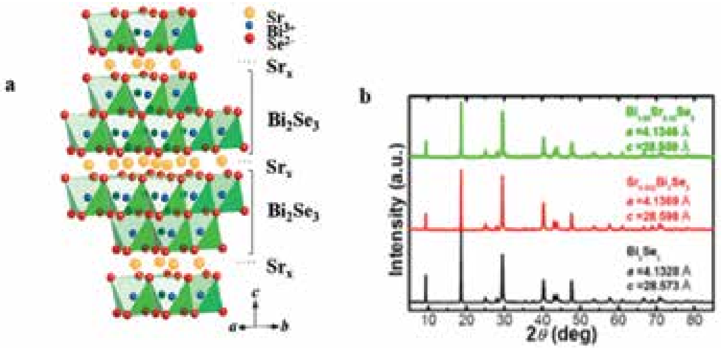

Figure 10. Crystal structure of $Sr_xBi_2Se_3$ superconductors. (a) Schematic diagram of $Sr_xBi_2Se_3$ crystal structure. (b) Powder XRD patterns of $Sr_xBi_2Se_3$, Bi_2Se_3, and $Bi_{2-x}Sr_xSe_3$ [7].

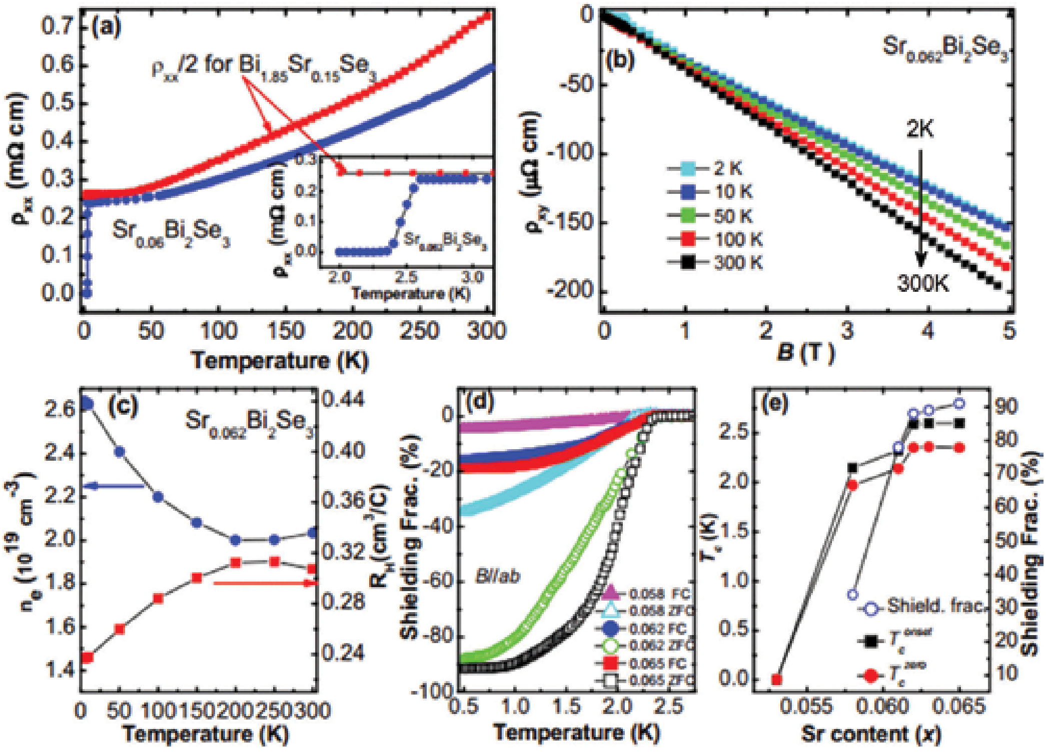

Figure 11. Superconducting properties of $Sr_xBi_2Se_3$. (a) Temperature dependence of resistivity for $Sr_xBi_2Se_3$ and $Bi_{2-x}Sr_xSe_3$. (b) Hall resistivity versus magnetic field curves measured at different temperatures. (c) Temperature dependence of estimated Hall coefficient and charge carrier density. (d) Temperature dependence of susceptibility for samples with different Sr contents. (e) Plot of T_c^{onset}, T_c^{zero}, and shielding volume fraction as a function of Sr content [7].

indices. In fact, the measured resistivity and Hall resistivity actually contain contributions from both the surface and bulk conductance when a large parallel bulk conduction channel is present. Therefore, the least confusing method is to convert resistivity into conductance to determine the Landau index because its components are additive [34]. The following equations are used to calculate conductance

$$G_{xx} = \frac{R_{xx}}{R_{xx}^2 + R_{xy}^2}, \quad G_{xy} = \frac{R_{xy}}{R_{xx}^2 + R_{xy}^2}. \tag{3}$$

After removing the nonoscillatory background, the oscillatory components are obtained and plotted as a function of 1/B. The frequencies are 146 T for longitudinal conductance and 144.8 T for Hall conductance, which are comparable to those of Bi_2Se_3 but smaller than $Cu_xBi_2Se_3$. The integer Landau index n corresponds to the valleys in ΔG_{xx}, while the valleys in ΔG_{xy} are assigned to n + 1/4 [see **Figure 13(a)** and **(c)**]. The 1/4 shift arises to match the valleys in $d\Delta G_{xy}/dB$ with the valleys in ΔG_{xx} [34]. The obtained intercepts of the linear fittings for n versus 1/B are both close to the value for an ideal Dirac system, i.e., −0.5 rather than 0 or 1 (see **Figure 13(b)** and **(d)**). Thus, it provides transport evidence for the existence of Dirac fermions in $Sr_xBi_2Se_3$ superconductor.

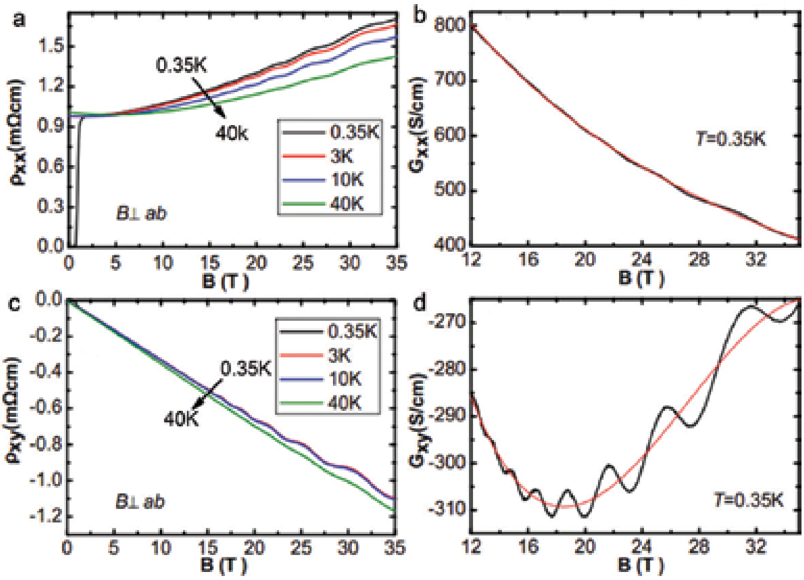

Figure 12. SdH oscillations under high magnetic field for $Sr_xBi_2Se_3$ single crystal. (a) and (c) Magnetic field dependence of resistivity and Hall resistivity at different temperatures. (b) and (d) Magnetic field dependence of the fitted longitudinal and Hall conductivity at 0.35 K [7].

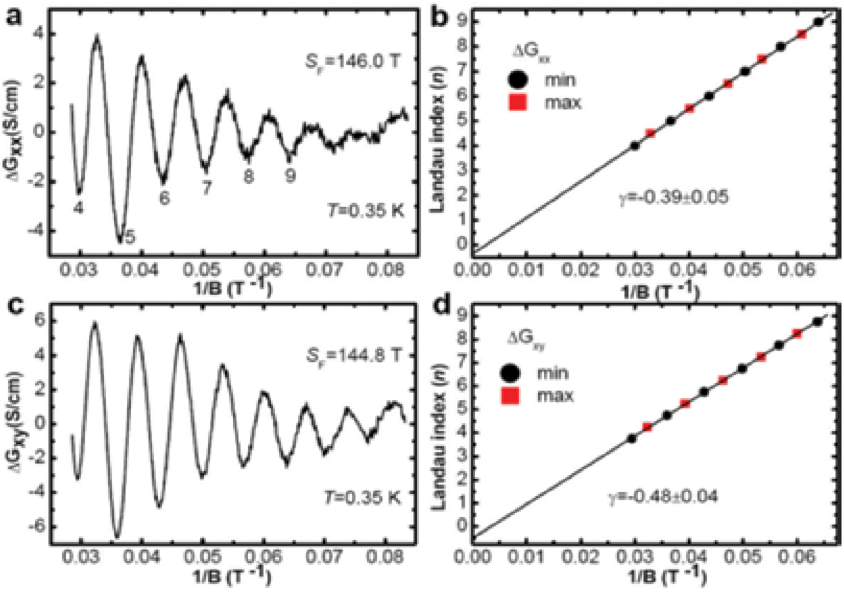

Figure 13. (a) and (c) Oscillatory component of the longitudinal and Hall conductivity at 0.35 K plotted against 1/B. (b) The Landau index n versus 1/B, where n and n + 1/2 correspond to the valleys and peaks of ΔG_{xx}. (d) n versus 1/B derived from (c), where n + 1/4 corresponds to the valleys of ΔG_{xy} [7].

The superconductivity of $Sr_xBi_2Se_3$ is very sensitive to external pressure below 1 GPa, as seen in **Figure 14(a)** and **(b)**. With the increasing applied pressure, the T_c and shielding volume fraction decrease but the normal state resistivity increases. This depression of superconductivity can be

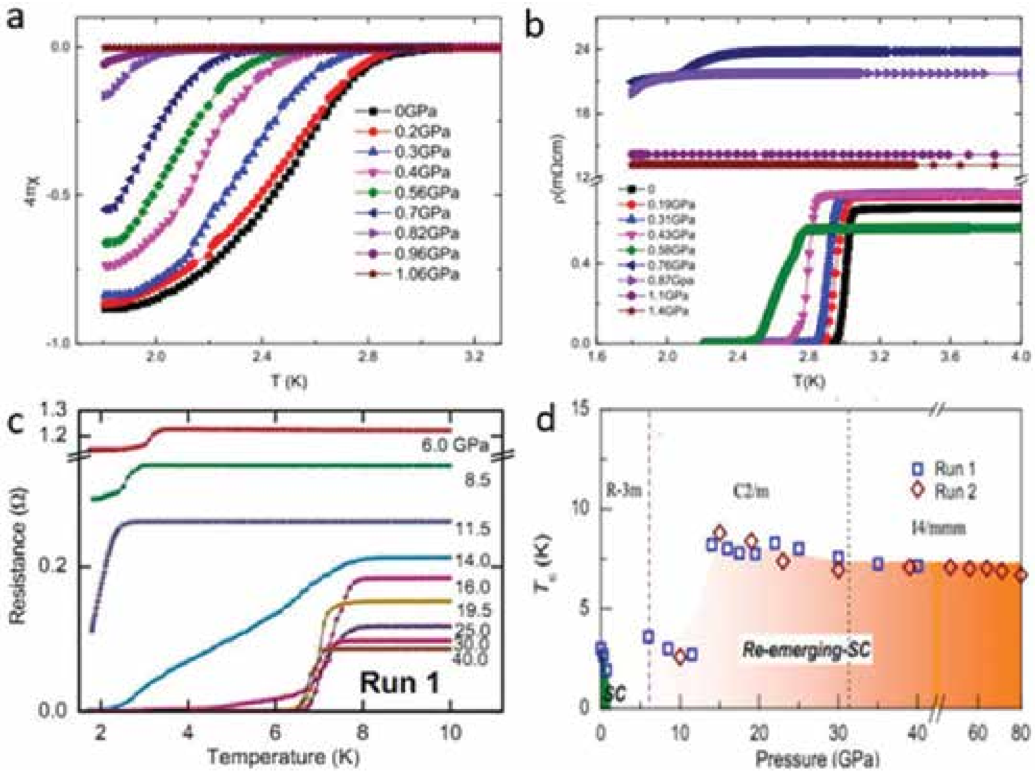

Figure 14. (a) Temperature dependence of magnetic susceptibility under different pressures. (b) and (c) Temperature dependence of resistance under high pressure. (d) The structural phase diagram on pressure for $Sr_xBi_2Se_3$ [35].

attributed to the reduction of charge carrier density, which is apparent from the normal state resistivity. However, if the pressure continues to increase, the normal state resistivity begins to decrease and a sign of superconducting transition occurs at 6 GPa. Then, the T_c^{onset} and the charge carrier density estimated from the normal state resistivity gradually increase with the increasing pressure, and T_c^{onset} reaches around 8 K when $P > 14$ GPa. But unfortunately, the T_c^{onset} remains almost constant for the pressure up to 40 GPa, although the normal state resistivity keeps decreasing. The reemerging superconductivity is very robust and the T_c^{onset} still changes little under 80 GPa [35]. In fact, the whole process contains three structural phases, i.e., R-3 m, C2/m, and I4/mmm, as seen in **Figure 14(d)**. The structural transitions and pressure-invariant T_c are very similar to the parent compound Bi_2Se_3, which needs further investigations.

3. Conclusions

The discovery of superconductivity in layered compound $Bi_4O_4S_3$ brings in a new BiS_2-based superconducting family, including the Bi─O─S compounds, Re(O,F)BiS_2, and MFBiS_2 superconductors. The superconducting layer is extended to $BiSe_2$ layer in $LaO_{1-x}F_xBiSe_2$ and $Sr_{1-x}La_xFBiSe_2$. The crystal structure and various superconducting properties are reviewed for selective systems. Hall effect and specific heat suggest that they are probably multiband superconductors and can be described by BCS weak-coupling theory. Moreover, bismuth chalcogenide topological insulators can be turned into superconductors by doping, which are potential candidates for 3D topological superconductors. For example, the topological surface state of $Sr_xBi_2Se_3$ is well supported by SdH oscillations under high magnetic field. The intermediate external pressure can efficiently suppress the superconductivity, which reemerges when pressure is further increased, while Tc is nearly invariant in high-pressure region, indicating an unconventional pairing state.

Acknowledgements

We acknowledge the support from the National Natural Science Foundation of China (Grant nos. 51603207, U1532267, and 11574288).

J.S. would like to dedicate his best love to his dear wife, Lv Youyou, who always encourages and supports his research and life. Best wishes for their love and coming baby. W.Z. would like to express his special thanks to his dearest daughters, Lily and Amy.

Conflict of interest

The authors declare no competing financial interests.

Author details

Jifeng Shao[1,2] and Wenka Zhu[2*]

*Address all correspondence to: wkzhu@hmfl.ac.cn

1 TianQin Research Center for Gravitational Physics, School of Physics and Astronomy,
Sun Yat-sen University, Zhuhai, China

2 High Magnetic Field Laboratory, Chinese Academy of Sciences, Hefei, China

References

[1] Yang J, Liang J, Jin D, Ying S, Tang W, Rao G. The influence of fluorine on the structures and properties of $Pr_{2-x}Sr_xCuO_{4-y}$ (x = 0.0, 0.4, 1.0). Journal of Physics: Condensed Matter. 1997;**9**:1249-1259. DOI: 10.1088/s0953-8984(97)75992-7

[2] Stewart GR. Superconductivity in iron compounds. Reviews of Modern Physics. 2011;**83**: 1589-1652. DOI: 10.1103./RevModPhys.83.1589

[3] Burrard-Lucas M, Free DG, Sedlmaier SJ, Wright JD, Cassidy SJ, Hara Y, Corkett AJ, Lancaster T, Baker PJ, Blundell SJ, Clarke SJ. Enhancement of the superconducting

transition temperature of FeSe by intercalation of a molecular spacer layer. Nature Materials. 2013;**12**:15-19. DOI: 10.1038/NMAT3464

[4] Hor YS, Williams AJ, Checkelsky JG, Roushan P, Seo J, Xu Q, Zandbergen HW, Yazdani A, Ong NP, Cava RJ. Superconductivity in $Cu_xBi_2Se_3$ and its implications for pairing in the undoped topological insulator. Physical Review Letters. 2010;**104**:057001. DOI: 10.1103/PhysRevLett.104.057001

[5] Sasaki S, Kriener M, Segawa K, Yada K, Tanaka Y, Sato M, Ando Y. Topological superconductivity in $Cu_xBi_2Se_3$. Physical Review Letters. 2011;**107**:217001. DOI: 10.1103/PhysRevLett.107.217001

[6] Lawson BJ, Hor YS, Li L. Quantum oscillations in the topological superconductor candidate $Cu_{0.25}Bi_2Se_3$. Physical Review Letters. 2012;**109**:226406. DOI: 10.1103/PhysRevLett.109.226406

[7] Liu Z, Yao X, Shao J, Zuo M, Li P, Tan S, Zhang C, Zhang Y. Superconductivity with topological surface state in SrxBi2Se3. Journal of the American Chemical Society. 2015;**137**:10512. DOI: 10.1021/jacs.5b06815

[8] Smylie MP, Claus H, Welp U, Kwok W-K, Qiu Y, Hor YS, Snezhko A. Evidence of nodes in the order parameter of the superconducting doped topological insulator $Nb_xBi_2Se_3$ via penetration depth measurements. Physical Review B. 2016;**94**:180510(R). DOI: 10.1103/PhysRevB.94.180510

[9] Mizuguchi Y, Fujihisa H, Gotoh Y, Suzuki K, Usui H, Kuroki K, Demura S, Takano Y, Izawa H, Miura O. BiS_2-based layered superconductor $Bi_4O_4S_3$. Physical Review B. 2012;**86**:220510. DOI: 10.1103/PhysRevB.86.220510

[10] Mizuguchi Y, Demura S, Deguchi K, Takano Y, Fujihisa H, Gotoh Y, Izawa H, Miura O. Superconductivity in novel BiS_2-based layered superconductor $LaO_{1-x}F_xBiS_2$. Journal of the Physical Society of Japan. 2012;**81**:114725. DOI: 10.1143/jpsj.81.114725

[11] Yazici D, Huang K, White BD, Chang AH, Friedman AJ, Maple MB. Superconductivity of F-substituted $LnOBiS_2$ (Ln=La, Ce, Pr, Nd, Yb) compounds. Philosophical Magazine. 2013;**93**:673-680. DOI: 10.1080/14786435.2012.724185

[12] Lin X, Ni X, Chen B, Xu X, Yang X, Dai J, Li Y, Yang X, Luo Y, Tao Q, Cao G, Xu Z. Superconductivity induced by La doping in $Sr_{1-x}La_xFBiS_2$. Physical Review B. 2013;**87**:020504(R). DOI: 10.1103/PhysRevB.87.020504

[13] Lin L, Li Y, Jin Y, Huang H, Chen B, Xu X, Dai J, Zhang L, Yang X, Zhai H, Cao G, Xu Z. Coexistence of superconductivity and ferromagnetism in $Sr_{0.5}Ce_{0.5}FBiS_2$. Physical Review B. 2015;**91**:014508. DOI: 10.1103/PhysRevB.91.014508

[14] Zhai H-F, Tang Z-t, Jiang H, Xu K, Zhang K, Pan Z, Bao J-K, Sun Y-L, Wen-He J, Nowik I, Felner I, Li Y-K, Xu X-F, Tao Q, Feng C-M, Xu Z-A, Cao G-H. Possible charge-density wave, superconductivity, and f-electron valence instability in $EuBiS_2F$. Physical Review B. 2014;**90**:064518. DOI: 10.1103/PhysRevB.90.064581

[15] Zhai H-F, Zhang P, Si-Qi W, He C-Y, Tang Z-T, Jiang H, Sun Y-L, Bao JI-K, Nowik I, Felner I, Zeng Y-W, Li Y-K, Xiao-Feng X, Tao Q, Zhu-An X, Cao G-H. Anomalous Eu

valence state and superconductivity in Undoped $Eu_3Bi_3S_4F_4$. Journal of the American Chemical Society. 2014;**136**:15386-15393. DOI: 10.1021/ja508564s

[16] Krzton-Maziopa A, Guguchia Z, Pomjakushina E, Pomjakushin V, Khasanov R, Luetkens H, Biswas PK, Amato A, Keller H, Conder K. Superconductivity in a new layered bismuth oxyselenide: $LaO_{0.5}F_{0.5}BiSe_2$. Journal of Physics: Condensed Matter. 2014;**26**:215702. DOI: 10.1088/0953-8984/26/21/215702

[17] Shao J, Liu Z, Yao X, Zhang L, Li P, Tan S, Zhang C, Zhang Y. Superconducting properties of $BiSe_2$-based $LaO_{1-x}F_xBiSe_2$ single crystals. EPL. 2014;**107**:37006. DOI: 10.1209/0295-5075/107/37006

[18] Li L, Xiang Y, Chen Y, Jiao W, Zhang C, Li Z, Dai J, Li Y. Superconductivity and abnormal pressure effect in $Sr_{0.5}La_{0.5}FBiSe_2$ superconductor. Superconductor Science and Technology. 2016;**29**:04LT03. DOI: 10.1088/0953-2048/29/4/04LT03

[19] Adam Phelan W, Wallace DC, Arpino KE, Neilson JR, Livi KJ, Seabourne CR, Scott AJ, McQueen TM. Stacking variants and superconductivity in the Bi—O—S system. Journal of the American Chemical Society. 2013;**135**:5372. DOI: 10.1021/ja4011767

[20] Shao J, Yao X, Liu Z, Li P, Tan S, Zhang C, Zhang Y. Bulk superconductivity in single-phase $Bi_3O_2S_3$. Physica Status Solidi RRL: Rapid Research Letters. 2014;**8**:845-848. DOI: 10.1002/pssr.201409254

[21] Shao J, Yao X, Liu Z, Li P, Tan S, Zhang C, Zhang Y. Superconductivity in $BiO_{1-x}F_x$-BiS_2 and possible parent phase of $Bi_4O_4S_3$ superconductor. Superconductor Science and Technology. 2015;**28**:015008. DOI: 10.1088/0953-2048/28/1/015008

[22] Okada T, Ogino H, Shimoyama J-i, Kishio K. Topotactic synthesis of a new BiS_2-based superconductor $Bi_2(O,F)S_2$. Applied Physics Express. 2015;**8**:023102. DOI: 10.7567/apex.8.023102

[23] Biswas PK, Amato A, Baines C, Khasanov R, Luetkens H, Lei H, Petrovic C, Morenzoni E. Low superfluid density and possible multigap superconductivity in the BiS_2-based layered superconductor $Bi_4O_4S_3$. Physical Review B. 2013;**88**:224515. DOI: 10.1103/PhysRevB.88.224515

[24] Yao X, Shao J, Liu Z, Zhang L, Tan S, Zhang C, Zhang Y. A comparison of the effects of Sm and Pb doping in $Bi_4O_4S_3$ superconductors. Journal of Superconductivity and Novel Magnetism. 2014;**27**:2555-2562. DOI: 10.1007/s10948-014-2624-y

[25] Liu Y, Tong P, Tan SG, Lu WJ, Li LJ, Zhao BC, Zhang SB, Sun YP. The effects of Cu doping on the physical properties of the new layered superconductor $Bi_{4-x}Cu_xO_4S_3$. Physica B. 2013;**412**:119-121. DOI: 10.1016/j.physb.2012.12.028

[26] Jha R, Awana VPS. Effect of Se doping in recently discovered layered $Bi_4O_4S_3$ superconductor. Physica C. 2014;**498**:45-49. DOI: 10.1016/j.physc.2014.01.003

[27] Nagao M, Miura A, Demura S, Deguchi K, Watauchi S, Takei T, Takano Y, Kumada N, Tanaka I. Growth and superconducting properties of F-substituted $ROBiS_2$ (R = La, Ce, Nd) single crystals. Solid State Communications. 2014;**178**:33-36. DOI: 10.1016/j.ssc.2013.10.019

[28] Yazici D, Huang K, White BD, Jeon I, Burnett VW, Friedman AJ, Lum IK, Nallaiyan M, Spagna S, Maple MB. Superconductivity induced by electron doping in $La_xM_xOBiS_2$ (M= Ti, Zr, Hf, Th). Physical Review B. 2013;**87**:174512. DOI: 10.1103/PhysRevB.87.174512

[29] Blatter G, Geshkenbein VB, Larkin AI. From isotropic to anisotropic superconductors: A scaling approach. Physical Review Letters. 1992;**68**:875. DOI: 10.1103/PhysRevLett.68.875

[30] Jha R, Kishan H, Awana VPS. Effect of hydrostatic pressures on the superconductivity of new BS_2 based $REO_{0.5}F_{0.5}BiS_2$ (RE = La, Pr and Nd) superconductors. Journal of Physics and Chemistry of Solids. 2015;**84**:17-23. DOI: 10.1016/j.jpcs.2014.12.005

[31] Liu J, Li S, Li Y, Zhu X, Wen H-H. Pressure-tuned enhancement of superconductivity and change of ground state properties in $LaO_{0.5}F_{0.5}BiSe_2$ single crystal. Physical Review B. 2014;**90**:094507. DOI: 10.1103/PhysRevB.90.094507

[32] Sasaki S, Segawa K, Ando Y. Superconductor derived from a topological insulator heterostructure. Physical Review B. 2014;**90**:220504(R). DOI: 10.1103/PhysRevB.90.220504

[33] Wang Z, Taskin AA, Frolich T, Braden M, Ando Y. Superconductivity in $Tl_{0.6}Bi_2Te_3$ derived from a topological insulator. Chemistry of Materials. 2016;**28**:779-784. DOI: 10.1021/acs.Chemmater. 5b03727

[34] Xiong J, Luo Y, Khoo YH, Jia S, Cava RJ, Ong NP. High-field Shubnikov-de Haas oscillations in the topological insulator Bi_2T_2Se. Physical Review B. 2012;**86**:045314. DOI: 10.1103/PhysRevB.86.045314

[35] Zhou Y, Chen X, Zhang R, Shao J, Wang X, An C, Zhou Y, Park C, Tong W, Pi L, Yang Z, Zhang C, Zhang Y. Pressure-induced reemergence of superconductivity in topological insulator Sr0.065Bi2Se3. Physical Review B. 2016;**93**:144514. DOI: 10.1103/PhysRevB.93.144514

Chapter 7

Effects of Isovalent Substitutions and Heat Treatments on T_c, Orthorhombicity, Resistivity, AC Magnetic Shielding and Irreversibility Line in High-T_c Superconductors

Abdelhakim Nafidi

Additional information is available at the end of the chapter

http://dx.doi.org/10.5772/intechopen.74354

Abstract

We report here the preparation, X-ray diffraction with Rietveld refinement, AC magnetic susceptibility ($\chi_{ac} = \chi' + i\chi''$), resistivity, iodometric measurements and effect of heat treatments in $(Y_{1-x}Sm_x)SrBaCu_3O_{6+z}$. Each sample has undergone two types of heat treatment: oxygen annealing [O] and argon annealing followed by oxygen annealing [AO]. For each x, the [AO] heat treatment increases the orthorhombicity $\varepsilon = (b - a)/(b + a)$ (for $0 \le x \le 1$), T_c (for $x \ge 0.4$) and reduced the linear resistivity parameters with a diminution of the interaction of holes with phonons. At all $T < T_c$ and for any applied field H_{dc}, we observed an enhancement of AC magnetic shielding and the irreversibility line in the samples [AO] for $x > 0.5$, revealing an improvement in the pinning properties. Remarkable correlations were found. In the [AO] samples, the measured data are explained by the increase in phase purity, in cationic and chain oxygen ordering, p_{sh} and the decrease in d[Cu(1)─(Sr/Ba)].

Keywords: chain oxygen order-disorder, heat treatments control of T_c, Rietveld refinement structure, phase transition, irreversibility line, AC magnetic shielding, resistivity, $(Y_{1-x}Sm_x)(SrBa)Cu_3O_{6+z}$ type-II superconductors

1. Introduction

$YBa_2Cu_3O_{6.95}$ is superconducting below 92 K and characterized by double $Cu(2)O_2$ layers (oriented along the a-b plane) responsible for carrying the supercurrent and Cu(1)O chains (along the b direction) that provide a charge reservoir for these planes [1, 2].

IntechOpen

The four distinct crystallographic sites Y, Ba, Cu plane, and Cu chain can be substituted with different elements. Single-phase $LnBa_2Cu_3O_{6+z}$ (Ln = rare earth) can be synthesized with $T_c = 92$ K. All these compounds show an orthorhombically distorted oxygen-deficient triple-perovskite structure and both the orthorhombic distortion and T_c depend sensitively on the oxygen content (6 + z) [3]. Wada et al. [4], Izumi et al. [5] studied the structural and superconducting properties of $La_{1+x}Ba_{2-x}Cu_3O_y$ (with $0 \leq x \leq 0.5$). They concluded that in order to have T_c maximal, this structure must have an ordered arrangement of La and Ba along c axis with an occupation factor of 0 and 1 for the oxygen at (1/2, 0, 0) and (0, 1/2, 0), respectively.

We want to see if an isovalent substitution of Ba^{+2} by Sr^{+2} with smaller ionic radius can modify the results discussed above when Y^{+3} is replaced by the rare earth Sm^{+3} with bigger ionic radius. Understanding the effect of the Y and Ba atomic plans on the superconductivity in these compounds, we have studied the structural, superconducting and magnetic properties of $(Y_{1-x}Sm_x)SrBaCu_3O_{6+z}$. We found that the effect of heat treatments on these properties depended on the content of Sm.

2. Experimental techniques

We prepared the polycrystalline samples by solid-state sintering of oxides (Y_2O_3, Sm_2O_3, CuO) with a purity of 99.999% and carbonates ($SrCO_3$ 99.999% pure, $BaCO_3$ with a purity of 99.99%). All these chemicals were thoroughly mixed in desired proportions and calcined at 950°C in air for 12–18 h. The obtained ceramic was ground, mixed, pelletized and heated in air at 980°C for 16–24 h. This was repeated twice. For each sample, the circular pellets were subjected to heat treatment in oxygen at 450°C for 60–72 h and furnace cooled. This was denoted as sample [O].

X-ray diffraction spectra of the samples were measured with Philips diffractometer fitted with a secondary beam graphite monochromator and using Cu Kα (40 kV/20 mA) radiation. The angle 2θ was varied from 20° to 120° in steps of 0.025°and the counting time per step was 10 s. The XRD spectra were resolved with Rietveld refinement.

A detailed description of the basic arrangement of the experiment of the AC magnetic susceptibility can be found in [6]. The sample in the form of a slab is placed in the magnetic field $H_{ext} = H_{dc} + H_{ac}\cos(\omega t)$ with the static component H_{dc} and the AC component with the amplitude H_{ac} and the frequency $f = \omega/2\pi$. The sample's magnetic response was detected by a pick-up coil surrounding the sample. Superconducting transitions were determined by the measure of the real (χ') and the imaginary (χ'') parts of the AC magnetic susceptibility as a function of temperature in $H_{ac} = 0.11$ Oe and at f = 1500 Hz. Also, χ' and χ'' were measured in $0 < H_{dc} < 150$ Oe with applied H_{ac}.

We used the Van Der Pauw method [7] for measuring resistivity $\rho(T)$. The sample was attached to a cane in a cryostat with closed helium circuit with a cryogenic pump, a regulator of temperature (1 μA–10 mA) and 1 μV resolution digital voltmeter controlled with a computer. T_c was determined by both the measured $\chi'(T)$ and $\rho(T)$.

For each x, the same sample [O] was then heated in argon at 850°C for about 12 h, cooled to 20°C and oxygen was allowed to flow instead of argon and the sample was annealed at 450°C for about 72 h. This sample is denoted as [AO]. XRD, resistivity and AC susceptibility measurements were done on a part of this sample. We measured $6 + z$ by iodometry technique on a part of each sample.

3. Results

3.1. Crystalline structure

The X-ray diffraction spectra of all the samples are shown in **Figure 1** [8]. After the [AO] heat treatment, the reflections were sharper so the samples were well crystallized. The [AO] heat treatment increases the orthorhombic cleaving. For example, the (123) and (213) peaks at $2\theta \approx 58.5°$ (and (200) and (006) reflections at $2\theta \approx 47°$) which were ill-resolved for the [O] samples were clearly identified after the [AO] heat treatment, as shown in **Figure 1**. Some weak unidentified impurity peaks (marked by crosses in **Figure 1(a)** were seen in the [O] samples and their amplitudes increase with x. They disappeared after the [AO] treatment shown in **Figure 1(b)**. This indicates an improvement of crystallographic quality of the samples [AO].

In **Figure 2** we show, respectively, the variation of the parameters a, b, c and the volume V of the unit cell obtained with Rietveld refinement [9] as a function of x and heat treatment. When x increases, the lattice parameter a (c and the volume V of the unit cell) increased but b is constant leading to a decrease of the orthorhombicity ($\varepsilon = (b - a)/(b + a)$) ε [O] in **Figure 3**. The substitution of Y^{+3} (0.893 Å) by the rare earth Sm^{+3} (0.965 Å), with a superior ionic radius, leads to a linear increase of c and V.

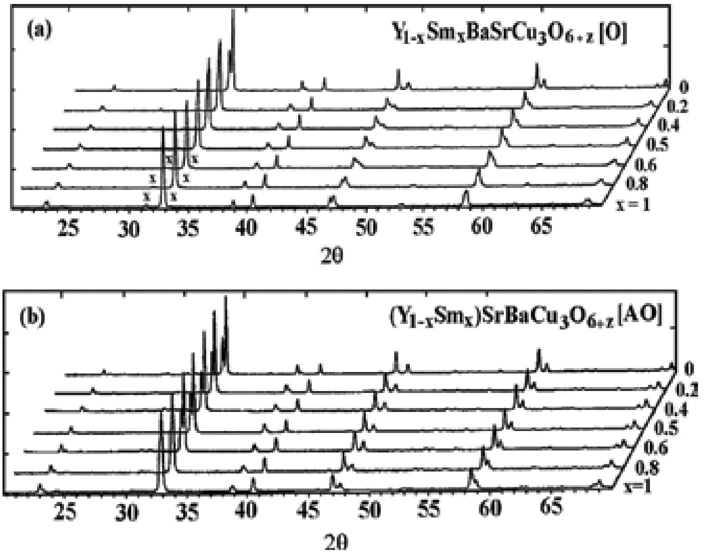

Figure 1. XRD (Cu Kα) patterns of $(Y_{1-x}Sm_x)SrBaCu_3O_{6+z}$ as a function of x. (a) Samples [O] annealed in oxygen at 450°C, (b) samples [AO] heated in argon at 850°C followed by annealing in oxygen at 450°C (x = impurity peaks).

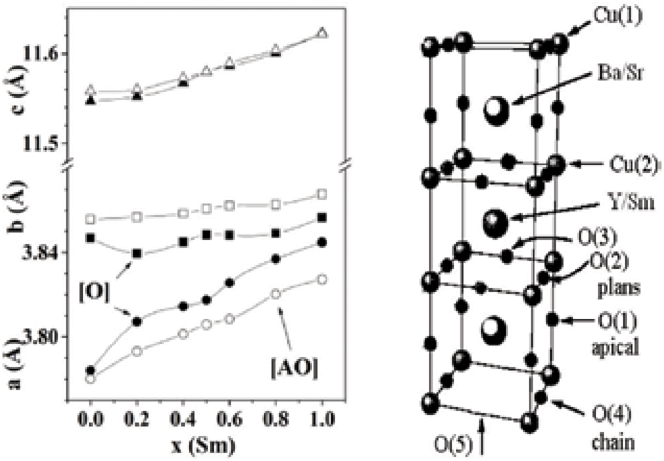

Figure 2. Variation of the parameters a, b and c of $(Y_{1-x}Sm_x)SrBaCu_3O_{6+z}$ as a function of x and heat treatment in the left. The unit cell of $(Y_{1-x}Sm_x)SrBaCu_3O_{6+z}$ in the right.

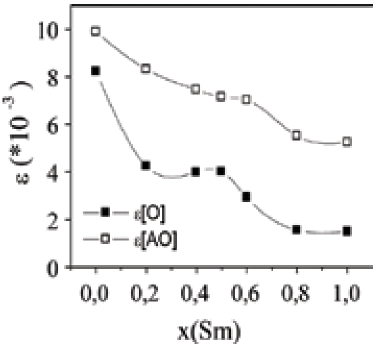

Figure 3. Variation of the orthorhombicity of $(Y_{1-x}Sm_x)SrBaCu_3O_{6+z}$ as a function of x and heat treatment.

The orthorhombicity depends strongly on the Sm content x. When x increases from 0 to 1, ε decreases quickly from 8.24×10^{-3} to 1.5×10^{-3} in the samples [O] in **Figure 3**. This indicated a structural phase transition from orthorhombic to tetragonal. ε decreases slowly from 9.9×10^{-3} to 5.24×10^{-3} with an orthorhombic symmetry in the samples [AO]. We found also that the orthorhombicity depends strongly on the heat treatment [AO]. For each x, the latter increased the orthorhombicity (for $0 \leq x \leq 1$). The increase was maximum, from 1.5×10^{-3} to 5.24×10^{-3} for x = 1 in [12].

3.2. Real part of the AC magnetic susceptibility and T_c

The critical temperature T_c of the transition from the superconductor to the normal state depends strongly on the effect of [AO] heat treatment as seen in the real part of AC susceptibility $\chi'(T)$ in **Figure 4**. The imaginary part of AC susceptibility $\chi''(T)$ in **Figure 4** shows a single peak T_p. This defined clearly the value of T_c for all the samples. We can see in **Figure 5** that when x was increased from 0 to 1, $T_c[O]$ decreased from 83 K to 79.3 K. $T_c[AO]$ first decreases

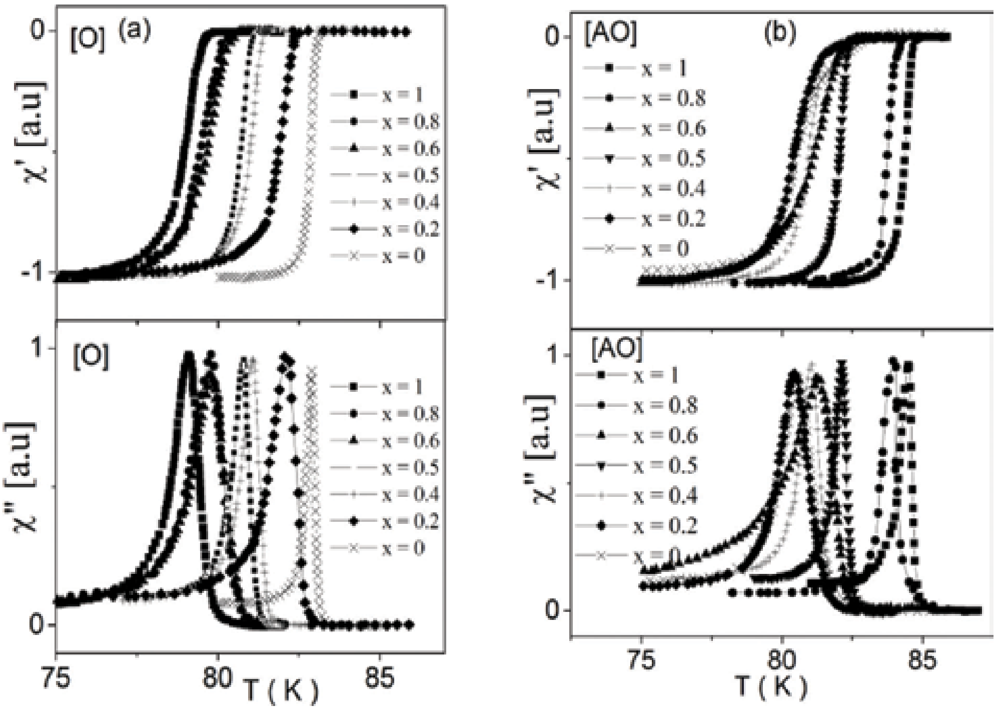

Figure 4. χ′ and χ″ of $(Y_{1-x}Sm_x)SrBaCu_3O_{6+z}$ as a function of temperature. (a) Heat treatment [O], (b) heat treatment [AO].

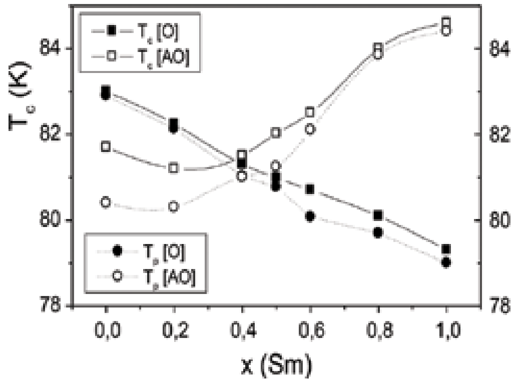

Figure 5. T_c and T_p of $(Y_{1-x}Sm_x)SrBaCu_3O_{6+z}$ as a function of x(Sm) following the [O] and [AO] heat treatments.

from 81.7 K (for x = 0) to 81.2 K (for x = 0.2) (like in the samples [O]) and then increases to 85 K for $SmSrBaCu_3O_{6+z}$. For each x, the [AO] heat treatment increases T_c for x ≥ 0.4 and decreases it for x < 0.4. A maximum of increase in T_c of 6 K was observed in $SmSrBaCu_3O_{6+z}$ [AO] [8].

For each x, the [AO] heat treatment increases ε (for 0 ≤ x ≤ 1) in **Figure 3** and T_c (for x ≥ 0.4) in **Figure 5**. The [AO] heat treatment makes the coupling of the superconducting grains by Josephson junctions took place at higher temperature. This effect is revealed by the net displacement of T_p to higher temperature for x ≥ 0.4.

x	**0**		**0.2**		**0.4**		**0.5**		**0.6**		**0.8**		**1**	
Heat treatment	**[O]**	**[AO]**	**[O]**	**[AO]**	**[O]**	**[AO]**	**[O]**	**[AO]**	**[O]**	**[AO]**	**[O]**	**[AO]**	**[O]**	**[AO]**
a (Å)	3.846	3.855	3.839	3.856	3.845	3.858	3.848	3.860	3.848	3.862	3.849	3.862	3.856	3.867
b (Å)	3.784	3.780	3.807	3.793	3.814	3.801	3.817	3.805	3.825	3.808	3.837	3.820	3.844	3.827
c (Å)	11.55	11.56	11.55	11.56	11.57	11.57	11.58	11.58	11.59	11.59	11.60	11.60	11.62	11.62
V (Å)	168.0	168.4	168.8	169.0	169.6	169.7	170.1	170.1	170.5	170.4	171.3	171.1	172.3	172.0
ε (10^{-3})	8.24	9.90	4.24	8.32	3.99	7.46	4.02	7.16	2.93	7.02	1.56	5.52	1.50	5.24
T_c (K)	83	81.7	82.24	81.2	81.3	81.5	81	82.02	80.7	82.5	80.1	84	79.3	84.6
T_p (K)	82.9	80.4	82.13	80.3	81.02	81	80.77	81.24	80.07	82.1	79.7	83.86	79	84.4
ΔT_c	0.4	0.41	1.42	2	1.1	1	0.92	0.8	1.7	2.9	1.58	0.72	1.5	0.8
ΔT_p	0.3	1.2	0.89	1.3	0.7	0.9	0.65	0.56	1.2	2.2	1.05	0.56	0.96	0.51
K′ (Oe)	—	—	2068	3390	1679	3848	1447	5177	1057	5910	936	8165	1677	11,741
n	—	—	1.41	1.50	1.33	1.53	1.13	1.88	1.14	1.63	0.91	1.54	1.31	1.33

Table 1. Structural, superconducting and magnetic parameters of $(Y_{1-x}Sm_x)SrBaCu_3O_{6+z}$.

Table 1 shows the exact measured values of the structural parameters a, b, c, V and ε of each sample as a function of the heat treatment.

3.3. Real part of the AC magnetic susceptibility and the shielding effect

The effect of [AO] heat treatment on T_c was remarkable. The temperature at which the diamagnetism sets in is taken as T_c and it was found to be dependent on both x and the heat treatment employed. Since the same sample was used for both heat treatments, one can compare the diamagnetic response and note that screening current of the [AO] sample increased considerably compared to that of the [O] sample for each x (see, for example, the case x = 0.8 in **Figure 6(a)**). **Table 1** shows the exact measured values of the superconducting parameters T_c, T_p, ΔT_c and ΔT_p of each sample as a function of the heat treatment.

We can see in **Figure 7** the shielding effect S which is the amplitude of the real part of the AC susceptibility [10–12]. S represents the exclusion of the magnetic flux by the sample in alternative dynamic mode. S was set arbitrarily equal to 0.89, 0.97 and 1, respectively, for x = 0.5, 0.8, and 1, for the sample [AO] at 55 K and for H_{dc} = 0 Oe.

For each x > 0.5, the [AO] heat treatment increases the shielding effect at all $T < T_c$ and for any applied H_{dc}. For example, in SmSrBaCu3O$_{6+z}$ (x = 1), S[AO] = 2 S[O] at T = 65 K and H_{dc} = 126.5 Oe [13]. When H_{dc} increases, S[AO] decreases slowly than S[O]. For example, at T = 55 K, S[AO] decreases by 10% whereas S[O] decreases by 70%. This indicated an improvement of the quality of the grains and intergranular coupling in the samples [AO].

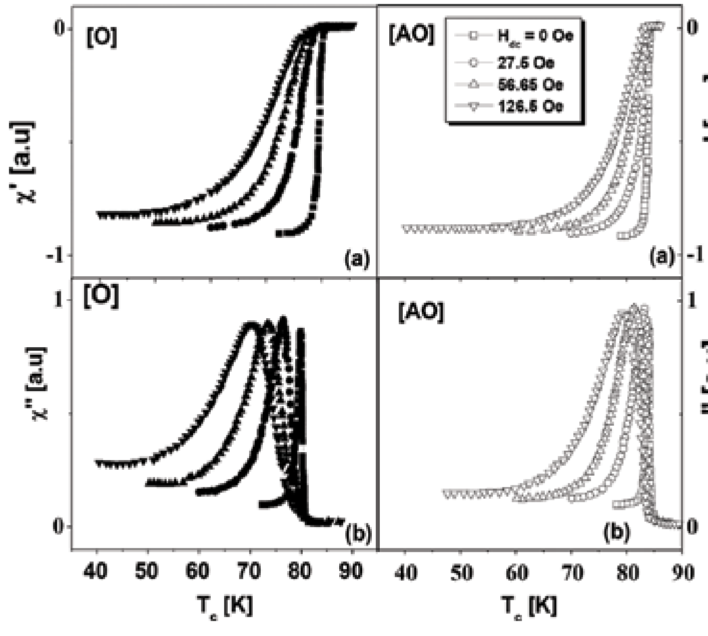

Figure 6. (a) χ′ and (b) χ″ of (Y$_{0.2}$Sm$_{0.8}$)SrBaCu$_3$O$_{6+z}$ as a function of the temperature and heat treatment at four fields H_{dc} ($0 < H_{dc} < 126.5$ Oe).

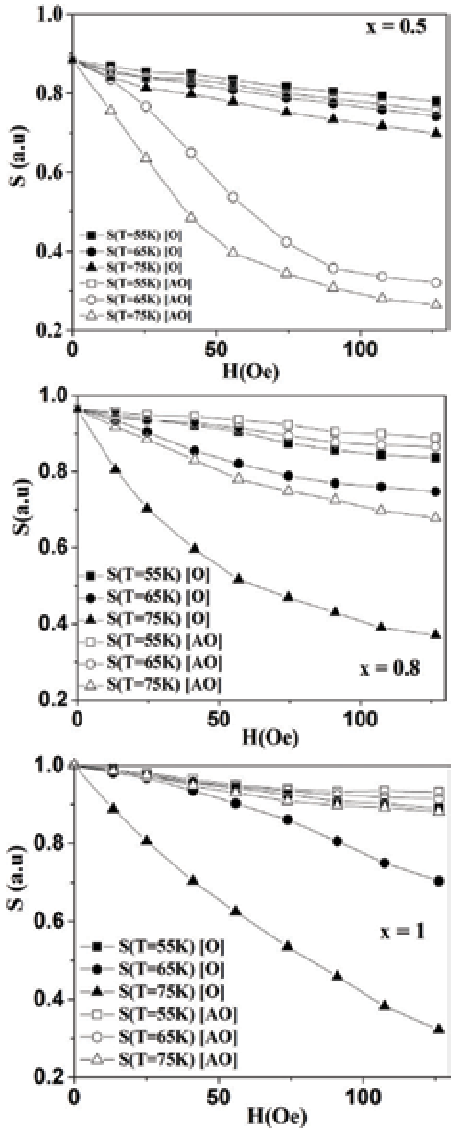

Figure 7. Shielding effect S of $(Y_{1-x}Sm_x)SrBaCu_3O_{6+z}$ as a function of the field H_{dc} and heat treatment at three different temperatures (55, 65 and 75 K).

3.4. Imaginary part of the AC magnetic susceptibility and irreversibility line

Looking to the imaginary part of the AC susceptibility χ'', of the sample $Y_{0.2}Sm_{0.8}SrBaCu_3O_{6+z}$ in **Figure 6(b)** for example, we can see that the width ΔT_p at half maximum of the transition in $\chi''(T)$ (see **Table 1**) was smaller in the samples [AO] at all H_{dc} and the peak T_p shifted less than in the sample [O]. **Figure 8** shows the field H_{dc} as a function of $t = T_p/T_c$ with an enhancement of the irreversibility line due to argon treatment for $x \geq 0.5$ [14]. The data can be analyzed with the help of following relation $H = K' (1 - t)^n$ [15]. Straight line plots were obtained when ln(H) was plotted against ln(1 – t) in **Figure 9**. For example, the value of K′ was estimated to be 1677

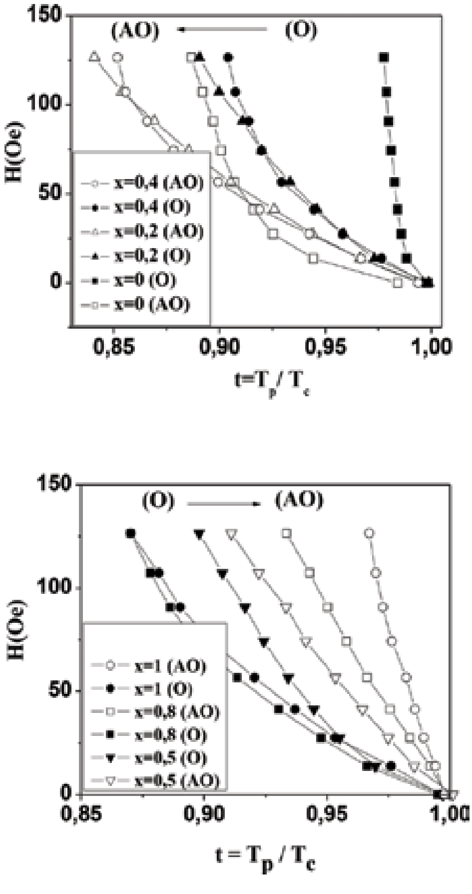

Figure 8. H as a function of t = T_p/T_c and heat treatment of $(Y_{1-x}Sm_x)SrBaCu_3O_{6+z}$.

and 11,741 Oe, respectively, for the samples [O] and [AO] in $SmSrBaCu_3O_{6+z}$ (x = 1). K′ may be interpreted as the field necessary to reduce the intergranular critical current to zero in the limit of T_p = 0 K. We note that the argon treatment considerably increases the value of K′ and n, in **Table 1** and **Figure 10**, indicating an improvement in the pinning properties. The dashed line indicates the value n = 1.5 for the cuprites given by Miller et al. [15].

3.5. Resistivity

Figure 11 shows that the resistivity ρ(T) of the sample $SmSrBaCu3O_{6+z}$ increases with the temperature. For each temperature, ρ[AO] is superior to ρ[O]. For each x, T_c (ρ = 0) ≈ T_c (χ′) and for each heat treatment T_c (χ′) is superior to T_c (ρ = 0) by 2–3 K with T_p (χ″) ≈ T_c (ρ = 0). The linear part of ρ(T), in the normal state, follows the relationship $\rho = \rho_0 + \alpha T$, where ρ_0 is the residual resistivity extrapolated to T = 0 K and α is the slope dρ/dT. For example, the sample $SmBaSrCu_3O_{6+z}$ [O] has α = 1.8 (μΩ cm/K), ρ_0 = 242 (μΩ cm) and ρ297 K = 785 (μΩ cm). The treatment [AO] reduced considerably these parameters; in particular α[AO] = 0.9 (μΩ cm/K). This indicates a reduction of the interaction of carrier charges with phonons.

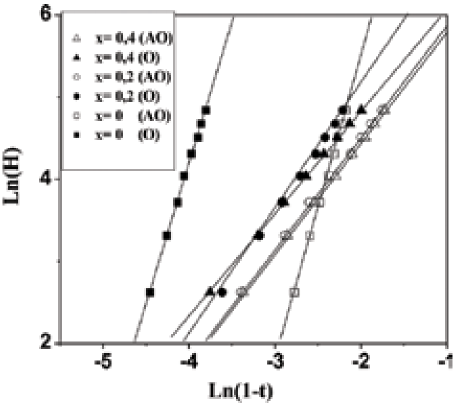

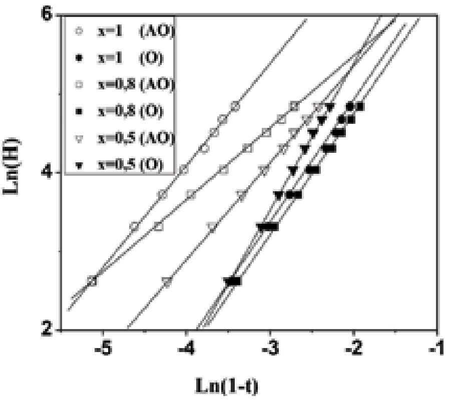

Figure 9. Ln(H) as a function of ln(1 − t) and heat treatment of $(Y_{1-x}Sm_x)SrBaCu_3O_{6+z}$.

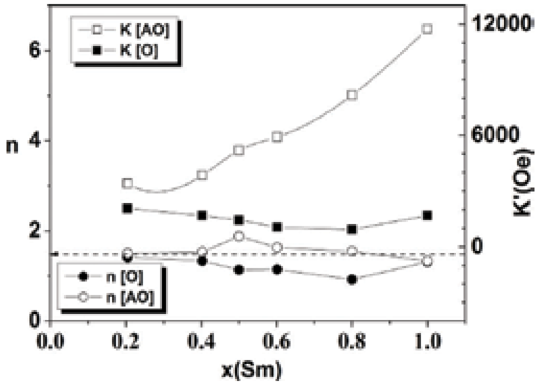

Figure 10. The field K′ and the exponent n as a function of x and heat treatment of $(Y_{1-x}Sm_x)SrBaCu_3O_{6+z}$.

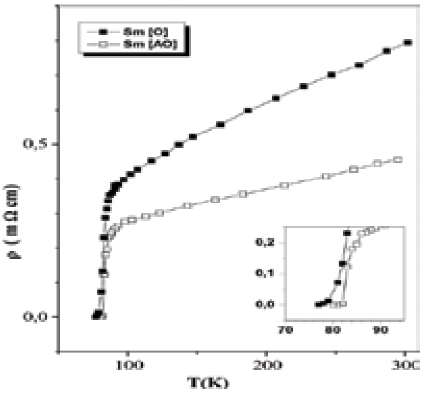

Figure 11. Resistivity ρ(T) of $SmBaSrCu_3O_{6+z}$ as a function of the temperature and heat treatment.

4. Discussions

We saw that the [AO] heat treatment increases the orthorhombic cleaving and eliminated some weak unidentified impurity peaks in **Figure 1(b)**. This indicates a good crystallization and an improvement of crystallographic quality of the samples [AO].

Our samples were prepared in 1 atm of oxygen. Our iodometry measurements show that the total oxygen constant was $6 + z = 6.94 \pm 0.04$ and do not change after the [AO] heat treatment. But for each x, T_c[AO] increased for $x \geq 0.4$. So this increase is not due to z but may lie in some other factor which governs the superconductivity in these samples.

When x increases from 0 to 1, T_c[O] decreases with ε. T_c[AO] decreases with the orthorhombicity ε until x = 0.2 and afterward it increases from 79 to 85 K in $SmSrBaCu_3O_{6+z}$ [AO], as shown in **Figure 12**. When x increases, the parameter b is constant but a (and c) increase

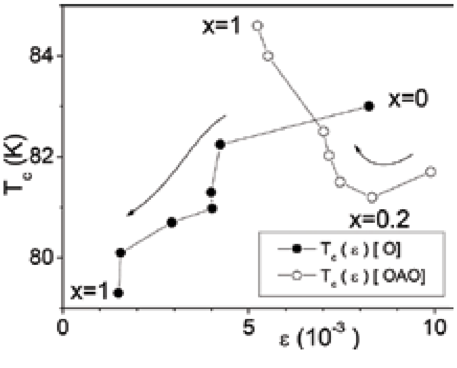

Figure 12. Variation of T_c as a function of the orthorhombicity ε and heat treatments of $(Y_{1-x}Sm_x)SrBaCu_3O_{6+z}$.

indicating an increase of the number of oxygen atoms by chain (NOC) along a axis with a decrease of ε (T_c[O]) from orthorhombic toward tetragonal structure in $SmSrBaCu_3O_{6+z}$ [O].

For each x, the [AO] treatment increases the orthorhombicity ε (for $0 \leq x \leq 1$) and T_c (for $x \geq 0.4$). For each x, the parameter a decreases and b increases after the [AO] heat treatment in the unit cell of **Figure 2**. Some oxygen atoms O(4) go to the vacant site O(5) along b axis. So the (NOC) and the anionic order in the basal plane increases leading to an increase of p_{sh} and T_c for $x \geq 0.4$ in **Figure 15**.

For each $x \geq 0.4$, the thermal parameter of the apical oxygen O(1) decreased from 2.02 to 0.27 $Å^2$ in the sample [AO] leading to a decrease of the cationic disorder; of Y (0.893 Å) (or Sm (0.965 Å) occupying some Ba (1.42 Å)/Sr (1.12 Å) sites along the c axis. Each sample [O] was heated in argon at 850°C. This action removes all the oxygen atoms from the structure and increases the atomic diffusion and the Y/Sm-Sr/Ba-Y/Sm order along c axis in the unit cell of **Figure 2**. In fact, the difference of bond valence (B.V.S.): V(Y)-V(Ba) = 0.77 in $YBa_2Cu_3O_{6.7}$ and 1.00 in $YBa_2Cu_3O_{6.32}$ indicate that the departure from reduced (6 + z) decreases the disorder of Y on the Ba site in $YBa_2Cu_3O_{6+z}$ [16]. So, the argon heat treatment decreases the disorder of Y/Sm on the Ba/Sr site. This is justified by the fact that impurity peaks seen in the [O] samples in **Figure 1(a)** disappeared after the [AO] heat treatment in **Figure 1(b)**.

Our results can be explained by the disorder of the oxygen in the basal plane, on the 0(4) and 0(5) sites along b and a axis, respectively, in **Figure 2**. This order enhanced the orthorhombic symmetry and increased the ratio (b − a)/(b + a). As seen on **Figure 13** when x increases, the interatomic distance d[Cu(1)—(Sr/Ba)] increases for both heat treatments in agreement with the fact that the crystallographic parameter c and the volume of the unit cell increases with x. For each x, the [AO] heat treatment decreases this distance for $x \geq 0.5$ (and increases it for $x < 0.5$). This decreases the distance d[Cu(1)—O(1)] and enhances the transfer of holes from the Cu(1)O chains to the superconducting planes $Cu(2)O_2$ via the apical oxygen O(1) resulting in an increase in the hole density p_{sh} and T_c for $x \geq 0.4$ in **Figure 15**. Such an increase leads to

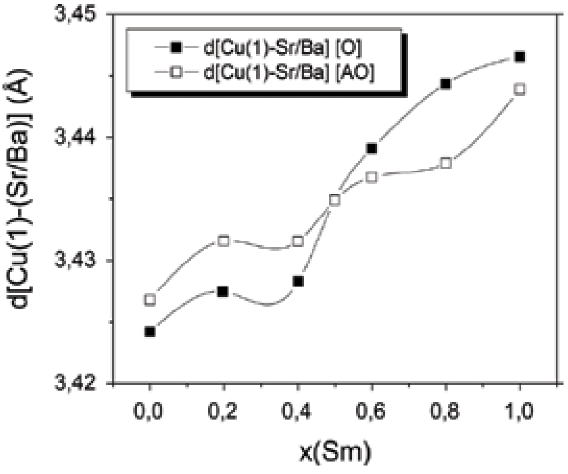

Figure 13. Interatomic distance d[Cu(1)—(Sr/Ba)] as a function of x and heat treatment in $(Y_{1-x}Sm_x)SrBaCu_3O_{6+z}$.

optimum superconducting properties and could account for the observed increase in T_c[AO] in agreement with the model of transfer of charges. This is justified by the fact that, when x increases, the parameter b is constant but a (and c) increase leading to an increase of the number of oxygen atoms by chain (NOC) along a axis with a decrease of ε (T_c[O]) from orthorhombic toward tetragonal structure in **Figure 12**.

When Sm ion occupies Ba (or Sr) site, the same amount of Ba (or Sr) cation is pushed into Y site. Sm is a three-valence ion. It increases the positive charge density around Ba (or Sr) site and the attractive force with oxygen anion. As a result, oxygen vacancies O(5) along the a-axis in the basal plane have higher chance to be filled. On the other hand, Ba^{+2} (or Sr^{+2}) in Y^{+3} (or Sm^{+3}) site decrease the attractive force with oxygen anion in Cu(2) plane. This increases the buckling angle Cu(2)─O(3)─Cu(2) along the a axis. When x increased from 0 to 1, the two changes of cation sites increase the parameter a. For each x, the [AO] heat treatment decreases the parameter a and increases b as shown in **Figure 2**. This increases the number of oxygen atoms by chain (NOC) along b axis leading to an increase of T_c with a decrease of the orthorhombicity ε for $x \geq 0.2$ as seen in **Figure 12**.

In the normal state, the heat treatment [AO] reduced considerably the linear resistivity parameters indicating a diminution of the interaction of carrier charges with phonons. $T_c(\chi')$ and $T_c(\rho = 0)$ were in good agreement.

For each $x > 0.5$, the [AO] heat treatment improved the shielding effect at all $T < T_c$ and for any applied field indicating an enhancement of the quality of the grains and intergranular coupling in the samples [AO]. Also for $x \geq 0.5$, an enhancement of the irreversibility line was noticed in the samples [AO] with an increase of the field K′ showing an improvement in the pinning properties. These results are justified by our XRD spectra, with Rietveld refinement, that showed an improvement of crystallographic quality of the samples [AO] in **Figure 1**.

The two arguments (cationic and anionic disorders) are justified here by the four remarkable correlations observed between $T_c(x)$, the volume of the unit cell V(x) in **Figure 14** and

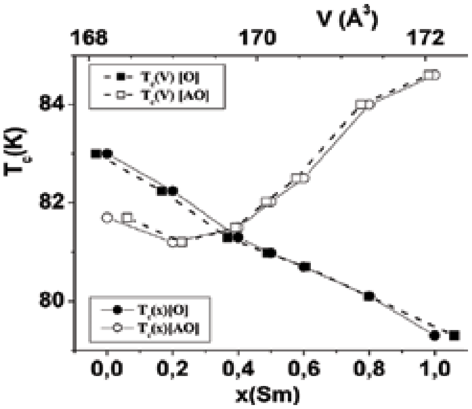

Figure 14. Correlation between T_c and the volume V of the unit cell as a function of x and heat treatment of $(Y_{1-x}Sm_x)SrBaCu_3O_{6+z}$.

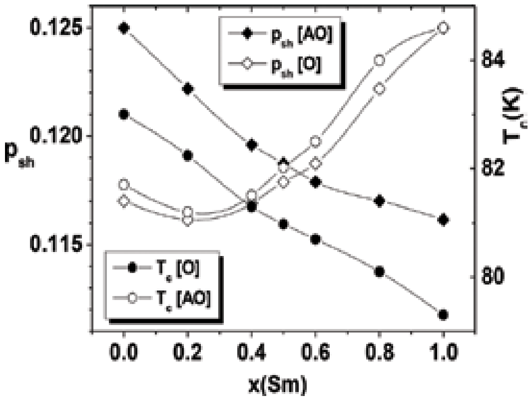

Figure 15. Correlation between p_{sh} and T_c as a function of x and heat treatment of $(Y_{1-x}Sm_x)SrBaCu_3O_{6+z}$.

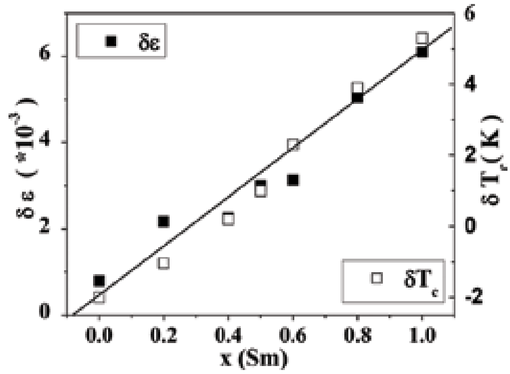

Figure 16. Correlation between $\delta T_c = T_c[AO] - T_c[O]$ and $\delta\varepsilon = \varepsilon[AO] - \varepsilon[O]$ as a function of x and heat treatment of $(Y_{1-x}Sm_x)SrBaCu_3O_{6+z}$.

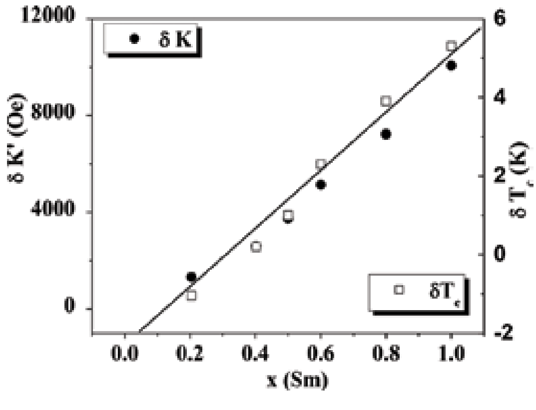

Figure 17. Correlation between δT_c and $\delta K'$ as a function of x and heat treatment of $(Y_{1-x}Sm_x)SrBaCu_3O_{6+z}$.

the number $p_{sh}(x)$ of holes by Cu(2)─O_2 superconducting planes in **Figure 15** (deduced from the undersaturation zone of the universal relation T_c/T_{cmax} (p_{sh}) [17]), and on the other hand, between $\delta T_c(x) = T_c[AO] - T_c[O]$ and $\delta\varepsilon(x)$ in **Figure 16** and between $\delta T_c(x)$ and $\delta K'(x)$ in **Figure 17**. So the structural, electrical and superconducting properties are correlated with the effect of argon heat treatment.

The increase or decrease in T_c must be related to the ionic size of the rare earth Sm, the variation of the Cu(1)-apical oxygen distance, hole density, anionic and cationic disorders, etc.

5. Conclusions

These studies indicate the optimization of the superconducting properties of the high-T_c superconductors $(Y_{1-x}Sm_x)SrBaCu_3O_{6+z}$ by a simple argon heat treatment. These results are a competition between oxygen disorder in basal plane and cationic disorder along c axis. In the samples [O], we are in the presence of a cationic disorder of Y/Sm on (Sr/Ba) sites that induced an anionic disorder of oxygen's chains in basal plane. Anionic order dominates in the samples [AO] in agreement with the previsions of [4, 5]. In the samples [AO], the remarkable improvement in the shielding effect (for $x > 0.5$) and the irreversibility line (for $x \geq 0.5$) are explained, respectively, by the improvement of the quality of the grains and intergranular coupling, and to the improvement of the pinning properties and crystallographic quality of these samples. The structural, magnetic and superconducting properties are correlated with the effect of argon heat treatment.

These results were explained by the effect of the ionic size of the rare earth, the decrease in d[Cu(1)─(Sr/Ba)]; the increase in cationic and chain oxygen ordering; the number of holes $p_{sh}(x)$ by Cu(2)─O_2 superconducting plans and in phase purity for the [AO] samples.

Author details

Abdelhakim Nafidi

Address all correspondence to: nafidi21@yahoo.fr

Laboratory of Condensed Matter Physics and Nanomaterials for Renewable Energy,
University Ibn Zohr, Agadir, Morocco

References

[1] Tokura Y, Takagi H, Uchida S. A superconducting copper oxide compound with electrons as the charge carriers. Nature. 1989;**337**:345-347

[2] Cava RJ. Structural chemistry and the local charge picture of copper oxide superconductors. Science. 1990;**247**:656-662

[3] Raveau B, Michel C, Hervieu M, Grout D. Crystal Chemistry of High-Tc Superconducting Copper Oxides. Berlin: Springer-Verlag; 1991 (Ch. 1-3)

[4] Wada T, Suzuki N, Maeda A, Yabe T, Uchinokura K, Uchida S, Tanaka S. Preparation and properties of superconducting La1+xBa2-xCu3Oy (0 ≤ x ≤ 0.5) ceramics sintered in N2 gas atmosphere. Physical Review B. 1989;**39**(13):9126-9138

[5] Izumi M, Yabe T, Wada T, Maeda A, Uchinokura K, Tanaka S, Asano H. Structural properties of the superconductor LaBa2Cu3-yO7-z in the solid solution system La1+xBa2-xCu3-yO7-z. Physical Review B. 1989;**40**(10):6771-6786

[6] Nikolo M, Hermann AM. Magnetic Susceptibility of Superconductors and Other Spin SystemsHein RA, Francavilla TL, Leinberg DH, editors. New York: Plenum, 1991, p. 553

[7] Van der Pauw LJ. A method of measuring the resistivity and hall coefficient on lamellae of arbitrary shape. Philips Technical Review. 1958;**20**:220-224

[8] Braigue M, Nafidi A, et al. Correlation between enhanced T_c, orthorhombicity and the volume of the unit cell in argon preheated (Y1-xSmx)SrBaCu3O6+z. IEEE Transactions on Applied Superconductivity. 2009;**19**(3):2984-2987

[9] Rietveld HM. A profile refinement method for nuclear and magnetic structures. Journal of Applied Crystallography. 1969;**2**:65-71

[10] Hein RA, Francavilla TL, Leinberg DH, editors. Magnetic Susceptibility of Superconductors and Other Spin Systems. New York: Plenum; 1991

[11] Senoussi S. Review of the critical current densities and magnetic irreversibilities in high Tc superconductors. Journal de Physique III. 1992;**2**:1041-1257

[12] Nafidi A, Suryanarayanan R. Effect of heat treatment on the shielding properties of $NdSrBaCu_3O_{6+z}$. Physica Status Solidi (a). 1994;**146**:29-31

[13] Bellioua M, Nafidi A, Elkaaouachi A, Nafidi A, Suryanarayanan R. Enhancement of orthorhombicity, Tc, shielding and irreversibility line in argon preheated $Sm(SrBa)Cu_3O_{6+z}$. Physica C. 2002;**383**:183-190

[14] El Yakoubi EY, Nafidi A, et al. Correlation between enhanced Tc, AC magnetic irreversibility line and heat treatment in high Tc superconductors. IEEE Transactions on Applied Superconductivity. 2011;**21**(3):2727-2731

[15] Muller KA, Takashige M, Bednorz JG. Flux trapping and superconductive glass state in La_2CuO_{4-y}: Ba. Physical Review Letters. 1987;**58**(11):1143-1146

[16] Brown ID, Altermatt D. Bond-valence parameters obtained from a systematic analysis of the Inorganic Crystal Structure Database. Acta Crystallographica. 1985;**B41**(4):244-247

[17] Zhang H, Sato H. Universal relationship between Tc and the hole content in p-type cuprate superconductors. Physical Review Letters. 1993;**70**(11):1697-1699

Edited by Roberto Zivieri

This book covers some of the most recent advances in the field of superfluids and superconductors. More specifically, it presents some of the most advanced theoretical formulations of superfluidity and superconductivity with special regard to their topological properties and vortex dynamics together with a description of the main experiments carried out via experimental techniques at the forefront to study these two such important phenomena in condensed matter physics. Special emphasis is given to ultracold Fermi gases, to clean liquid helium and to vortex membranes and knots for the class of superfluids and to the emerging superconductivity, to intermediate states in type-I superconductors, and to heat treatments to modulate the critical temperature for the class of superconductors.

Published in London, UK

IntechOpen

ISBN 978-1-83881-513-4
9 781838 815134